

IMPACT MODIFIED POLYAMIDE-ORGANOCLAY NANOCOMPOSITES

A THESIS SUBMITTED TO
THE GRADUATE SCHOOL OF NATURAL AND APPLIED SCIENCES
OF
MIDDLE EAST TECHNICAL UNIVERSITY

BY

IŞIL IŞIK

IN PARTIAL FULFILLMENT OF THE REQUIREMENTS
FOR
THE DEGREE OF DOCTOR OF PHILOSOPHY
IN
CHEMICAL ENGINEERING

MAY 2007

Approval of the Graduate School of Natural and Applied Sciences

Prof. Dr. Canan Özgen
Director

I certify that this thesis satisfies all the requirements as a thesis for the degree of Doctor of Philosophy

Prof. Dr. Nurcan Baç
Head of Department

This is to certify that we have read this thesis and that in our opinion it is fully adequate, in scope and quality, as a thesis for the degree of Doctor of Philosophy.

Assoc. Prof. Dr. Gökür Bayram
Co-Supervisor

Prof. Dr. Ülkü Yılmaz
Supervisor

Examining Committee Members

Prof. Dr. Güngör Gündüz (METU, CHE)

Prof. Dr. Ülkü Yılmaz (METU, CHE)

Prof. Dr. Teoman Tinçer (METU, CHEM)

Prof. Dr. Leyla Aras (METU, CHEM)

Prof. Dr. Nursel Dilsiz (Gazi Univ., CHE)

I hereby declare that all information in this document has been obtained and presented in accordance with academic rules and ethical conduct. I also declare that, as required by these rules and conduct, I have fully cited and referenced all material and results that are not original to this work.

Name, Last name: Işıl, Işık

Signature:

ABSTRACT

IMPACT MODIFIED POLYAMIDE-ORGANOCLAY NANOCOMPOSITES

Işık, Işıl

Ph.D., Department of Chemical Engineering

Supervisor : Prof. Dr. Ülkü Yilmazer

Co-Supervisor: Assoc. Prof. Dr. Göknur Bayram

May 2007, 320 pages

The effects of melt state compounding and addition order of ethylene-butyl acrylate-maleic anhydride (E-BA-MAH), ethylene-glycidyl methacrylate (E-GMA), ethylene-methyl acrylate-glycidyl methacrylate (E-MA-GMA) terpolymer and/or three types of organoclays (Cloisite® 15A, 25A and 30B) on morphology, thermal, mechanical and dynamic mechanical properties of polyamide-6 are investigated. The rheological behavior of nanocomposites is determined via melt flow index (MFI) and parallel disk rheometry. FTIR-ATR spectroscopy is used to determine elastomer/polyamide-6 reactions. XRD patterns show that the interlayer spacing for Cloisite® 15A remained unchanged; however it increased for the organoclays Cloisite® 25A and Cloisite® 30B in both polyamide-6/organoclay binary nanocomposites and in polyamide-6/organoclay/impact modifier ternary systems. TEM analyses indicate that exfoliated-intercalated nanocomposites are formed. Sizes of elastomeric domains in nanocomposites are larger than the domains in their corresponding blends. The MFI results show that incorporation of elastomer reduces the MFI, due to the formation of graft copolymer. Both storage and loss moduli and complex viscosity of polyamide-6 increase with organoclay addition. In DMA measurements, in rubbery region, all nanocomposites show higher storage modulus than the unfilled counterparts. In

general, the organoclays increase tensile and flexural strength, Young's and flexural modulus and elongation at break, but decrease the impact strength, on the contrary, the addition of elastomer has the opposite effect. Generally, Cloisite® 15A containing ternary nanocomposites have higher tensile, flexural and impact strength and Young's and flexural modulus than the ternary nanocomposites prepared with Cloisite® 25A and Cloisite® 30B. In general, nanocomposites processed by adding all the ingredients simultaneously give higher tensile and flexural strength and modulus than the nanocomposites produced by other mixing sequences.

Keywords: Nanocomposite, Polyamide-6, Toughening, Impact Modification, Montmorillonite

ÖZ

DARBE DAYANIMI GELİŞTİRİLMİŞ POLİAMİD-ORGANOKİL NANOKOMPOZİTLERİ

Işık, Işıl

Doktora, Kimya Mühendisliği Bölümü

Tez Yöneticisi : Prof. Dr. Ülkü Yılmaz

Ortak Tez Yöneticisi : Doç. Dr. Gökür Bayram

Mayıs 2007 ,320 sayfa

Bu çalışmada, etilen-butil akrilat-maleik anhidrit (E-BA-MAH), etilen-glisidil metakrilat (E-GMA), etilen-metil akrilat-glisidil metakrilat (E-MA-GMA) terpolimerlerinin ve/veya üç tip organokilin (Cloisite® 15A, 25A ve 30B) poliamid-6 ile eriyik halde karıştırılmasının ve bu malzemelerin karıştırma sıralarının üretilen malzemelerin morfolojilerine, termal, mekanik ve dinamik mekanik özelliklerine olan etkisi araştırılmıştır. Nanokompozitlerin reolojik özellikleri eriyik akış indeksi (EAI) cihazı ve paralel disk reometre kullanılarak incelenmiştir. Poliamid-6/elastomer reaksiyonlarını belirlemek için FTIR-ATR spektroskopisi kullanılmıştır. X-Işını Kırınımı grafikleri, Cloisite® 25A and Cloisite® 30B organokillerinin tabakalar arası uzaklığının poliamid-6/organokil ve poliamid-6/organokil/elastomer nanokompozitlerinde arttığını göstermiştir. TEM analizleri yarı açılmış-dağılmış nanokompozitlerin üretildiğini doğrulamıştır. Polimer matris içinde dağılmış olan küresel elastomer fazının boyutları nanokompozit malzemelerde poliamid-elastomer karışımlarına oranla daha büyüktür. EAI sonuçları, elastomer eklenmesiyle aşırı kopolimerin oluştuğunu ve EAI'nin düştüğünü göstermiştir. Dolgusuz poliamid-6'nın yığılma ve yitirme modülleri ile kompleks viskozitesi organokil varlığında artmıştır. DMA ölçümlerinde nanokompozit malzemeler lastiksi bölgede dolgusuz poliamid-6'dan daha yüksek

yığılma modülü göstermişlerdir. Genelde, organokiller gerilme ve eğilme dayanımlarını, Young ve eğilme modüllerini, kopmadaki uzamayı artırırken darbe dayanımını azaltmış, elastomerler ise tam tersi etkide bulunmuşlardır. Genellikle, Cloisite® 15A içeren üçlü nanokompozitlerin gerilme, eğilme ve darbe dayanımları ile Young ve eğilme modülleri Cloisite® 25A ve Cloisite® 30B içeren üçlü nanokompozitlerden daha yüksektir. Bileşenlerin aynı anda eklenmesiyle elde edilen nanokompozitler, çoğunlukla, diğer ekleme sıralarıyla hazırlanmış nanokompozitlere oranla daha yüksek gerilme ve eğilme dayanımları ve modülleri göstermişlerdir.

Anahtar Sözcükler: Nanokompozit, Poliamid-6, Katılaştırma, Darbe Dayanımı Geliştirilmesi, Montmorillonit

To My Family

ACKNOWLEDGEMENTS

First and foremost, I would like to thank my advisors Prof. Dr. Ülkü Yilmazer and Assoc. Prof. Dr. Göknur Bayram for their encouragement, guidance and advice throughout this work. They were always interested and enthusiastic, and gave many excellent suggestions that improved the thesis. I sincerely appreciate the time and effort they have taken to train me in the methods of conducting successful research.

I thank Prof. Dr. Güngör Gündüz and Prof. Dr. Teoman Tinçer, for serving as committee members, their helpful comments and suggestions.

My sincere acknowledgements go to to Assoc. Prof. Dr. Necati Özkan from METU Central Laboratory for viscoelastic property analysis, Necmi Avcı from Department of Metallurgical Engineering for XRD analysis, Frank Neilen from Holland DSM Explore for TEM analysis, Cengiz Tan from Department of Metallurgical Engineering for SEM analysis, and Mihrican Açıkgöz from Department of Chemical Engineering for DSC analysis. Technical assistance of Machine Shop staff is greatly acknowledged.

My special thanks go to my friends Dr. Güralp Özkoç, Fatma Işık, Saniye Gülersönmez, Mert Kılınç, Sertan Yeşil, Özcan Köysüren, İlknur Çakar, Miray Mert, Elif Alyamaç, Gülsüm Özden, Aslı Tolga and Pelin Toprak.

I am forever grateful for the love and support of my parents, Kezban and Vedat Işık. I am blessed to have them as my family and honored to have my parents as my role models.

I offer sincere thanks to my brother Cem Vedat Işık for his continuous encouragement, patience, advice and support during all stages of my life.

Above all, I am indebted to my fiancée Tamer Gülsaç for his love, support, encouragement, advice and providing the sunshine in my life.

This study was supported by The Scientific and Technological Research Council of Turkey (TUBITAK) under grant no. 104M415 and METU ÖYP-FBE-İM3.

TABLE OF CONTENTS

PLAGIARISM.....	iii
ABSTRACT	iv
ÖZ	vi
ACKNOWLEDGEMENT	ix
TABLE OF CONTENTS.....	xi
LIST OF TABLES	xvii
LIST OF FIGURES	xx
NOMENCLATURE.....	xxxv
CHAPTER	
1. INTRODUCTION.....	1
2. BACKGROUND INFORMATION.....	6
2.1 Composite Materials.....	6
2.1.1 Polymeric Composite Materials.....	7
2.2 Nanocomposite Materials	8
2.2.1 Layered Nanocomposite Structure with Polymeric Matrix ...	9
2.2.1.1 Microcomposite (Conventional) Composite	10
2.2.1.2 Intercalated Nanocomposite.....	10
2.2.1.3 Flocculated Nanocomposite	10
2.2.1.4 Exfoliated (Delaminated) Nanocomposite	10
2.2.2. Synthesis of Polymer-Clay Nanocomposites.....	11
2.2.2.1 In-Situ Polymerization	11
2.2.2.2 Solution Approach.....	12
2.2.2.3 Melt Intercalation.....	13
2.2.2.4 Sol-Gel Technology	16
2.3 Fillers	17
2.3.1 Clay Minerals.....	17
2.3.2 Montmorillonite	18
2.3.2.1 Compatibilizing Agent	20
2.4 Polyamide-6	21
2.4.1 Production of Polyamide-6.....	23

2.4.2 Properties of Polyamide-6	24
2.4.2.1 Physical Properties of Polyamide-6.....	25
2.4.2.2 Reactions of Polyamide-6	26
2.4.2.2.1 Acidolysis, Aminolysis, and Alcoholysis.....	26
2.4.2.2.2 Ammonolysis.....	27
2.4.2.3 Degradation of Polyamide-6.....	28
2.4.2.4 Solvent Resistance of Polyamides	29
2.4.3 Applications of Polyamides.....	29
2.5 Impact Modification of Polyamide-6.....	30
2.6 Polymer Processing	31
2.6.1 Extrusion	32
2.6.2 Injection Molding.....	34
2.7 Characterization of Polymer-Clay Nanocomposites.....	34
2.7.1 X-Ray Diffraction (XRD) Analysis.....	34
2.7.2 Transmission Electron Microscopy (TEM).....	36
2.7.3 Scanning Electron Microscopy (SEM).....	37
2.7.4 Spectroscopic analysis	38
2.7.4.1 Fourier Transform Infrared Spectroscopy - Attenuated Total Reflectance (FTIR-ATR) Analysis.....	38
2.7.5 Thermal Analysis	41
2.7.5.1 Differential Scanning Calorimeter (DSC) Analysis.....	41
2.7.6 Flow characteristics	43
2.7.6.1 Melt Flow Index (MFI) Test	43
2.7.7 Mechanical Analysis	44
2.7.7.1 Impact Properties.....	44
2.7.7.2 Tensile Properties.....	45
2.7.7.3 Flexural Properties.....	46
2.7.8 Thermomechanical Properties	48
2.7.8.1 Dynamic Mechanical Analysis (DMA).....	48
2.7.9 Rheological Properties.....	51
2.8 Previous Studies	54
2.8.1 Previous Studies on Polyamide-6/Clay Nanocomposites....	54
2.8.2 Previous Studies on Impact Modification of Polyamide-6....	56
2.8.3 Previous Studies on Impact Modified Polyamide-6 Nanocomposites.....	58

3. EXPERIMENTAL WORK	62
3.1 Materials.....	62
3.1.1 Polymer Matrix.....	62
3.1.2 Organoclays	62
3.1.3 Elastomers	66
3.2 Nanocomposite Preparation	70
3.2.1 Addition Order of the Components.....	74
3.2.1.1 All-S Mixing Sequence	75
3.2.1.2 PI-C Mixing Sequence	75
3.2.1.3 PC-I Mixing Sequence	75
3.2.1.4 IC-P Mixing Sequence	75
3.3 Characterization Experiments.....	78
3.3.1 Nanocomposite Morphology Determination	78
3.3.1.1 X-Ray Diffraction (XRD) Analysis.....	78
3.3.1.2 Transmission Electron Microscopy (TEM) Analysis....	79
3.3.1.3 Scanning Electron Microscopy (SEM) Analysis	79
3.3.2 Spectroscopic analysis	80
3.3.2.1 Fourier Transform Infrared Spectroscopy - Attenuated Total Reflectance (FTIR-ATR) Analysis.....	80
3.3.3 Thermal Analysis	80
3.3.3.1 Differential Scanning Calorimeter (DSC) Analysis.....	80
3.3.4 Flow characteristics	81
3.3.4.1 Melt Flow Index (MFI) Test	81
3.3.5 Mechanical Analysis	81
3.3.5.1 Impact Tests	82
3.3.5.2 Tensile Tests	83
3.3.5.3 Flexural Tests	84
3.3.6 Viscoelasticity	86
3.3.6.1 Dynamic Mechanical Analysis (DMA).....	86
3.3.6.2 Rheological Properties.....	87
4. RESULTS AND DISCUSSIONS.....	89
4.1 X-Ray Analysis.....	89
4.1.1 X-Ray Analysis Results of Organoclay Cloisite® 15A Containing Nanocomposites.....	89

4.1.2 X-Ray Analysis Results of Organoclay Cloisite® 25A Containing Nanocomposites.....	98
4.1.3 X-Ray Analysis Results of Organoclay Cloisite® 30B Containing Nanocomposites.....	104
4.2 TEM Analysis	110
4.2.1 TEM Analysis Results of Organoclay Cloisite® 15A Containing Nanocomposites.....	111
4.2.2 TEM Analysis Results of Organoclay Cloisite® 25A Containing Nanocomposites.....	113
4.2.3 TEM Analysis Results of Organoclay Cloisite® 30B Containing Nanocomposites.....	115
4.3 SEM Analysis	117
4.3.1 SEM Analysis Results of Elastomer E-BA-MAH Containing Nanocomposites.....	124
4.3.2 SEM Analysis Results of Elastomer E-GMA Containing Nanocomposites.....	129
4.3.3 SEM Analysis Results of Elastomer E-MA-GMA Containing Nanocomposites.....	134
4.4 FTIR Analysis.....	136
4.4.1 Possible Reactions in Polyamide-6/E-BA-MAH Blends.....	138
4.4.2 Possible Reactions in Polyamide-6/E-GMA and Polyamide-6/E-MA-GMA Blends.....	144
4.4.3 Possible Reactions between Organoclay and Elastomers Used	152
4.5 Flow Characteristics-MFI Measurements.....	153
4.5.1 MFI Analysis Results of Polyamide-6/Elastomer Blends.....	153
4.5.2 MFI Analysis Results of Nanocomposites Containing E-BA-MAH Elastomer	154
4.5.3 MFI Analysis Results of Nanocomposites Containing E-GMA Elastomer	156
4.5.4 Analysis Results of Nanocomposites Containing E-MA-GMA Elastomer	158
4.6 DSC Analysis.....	159
4.6.1 DSC Analysis Results of Polyamide-6/Elastomer Blends....	160

4.6.2 DSC Analysis Results of Nanocomposites Containing E-BA-MAH Elastomer	163
4.6.3 DSC Analysis Results of Nanocomposites Containing E-GMA Elastomer	164
4.6.4 Analysis Results of Nanocomposites Containing E-MA-GMA Elastomer	166
4.7 Mechanical Properties.....	167
4.7.1 Impact Properties	167
4.7.1.1 Impact Strength of Polyamide-6/Elastomer Blends	167
4.7.1.2 Impact Strength of E-BA-MAH Elastomer Containing Nanocomposites.....	171
4.7.1.3 Impact Strength of E-GMA Elastomer Containing Nanocomposites.....	175
4.7.1.4 Impact Strength of E-MA-GMA Elastomer Containing Nanocomposites.....	179
4.7.2 Toughness Measurements	180
4.7.3 Tensile Properties.....	183
4.7.3.1 Tensile Properties of Polyamide-6/Elastomer Blends.	184
4.7.3.2 Tensile Properties of E-BA-MAH Elastomer Containing Nanocomposites	190
4.7.3.3 Tensile Properties of E-GMA Elastomer Containing Nanocomposites.....	199
4.7.3.4 Tensile Properties of E-MA-GMA Elastomer Containing Nanocomposites.....	205
4.7.4 Flexural Properties.....	208
4.7.4.1 Flexural Properties of Polyamide-6/Elastomer Blends	209
4.7.4.2 Flexural Properties E-BA-MAH Elastomer Containing Nanocomposites.....	212
4.7.4.3 Flexural Properties of E-GMA Elastomer Containing Nanocomposites.....	217
4.7.4.4 Flexural Properties of E-MA-GMA Elastomer Containing Nanocomposites.....	221
4.7.5 Dynamic Mechanical Analysis	222

4.7.5.1 Dynamic Mechanical Analysis Results of E-BA-MAH Elastomer Containing Nanocomposites	228
4.7.5.2 Dynamic Mechanical Analysis Results of E-GMA Elastomer Containing Nanocomposites	237
4.7.5.3 Dynamic Mechanical Analysis Results of Nanocomposites Containing E-MA-GMA Elastomer	246
4.8 Viscoelastic Properties In the Melt State.....	252
5. CONCLUSIONS.....	267
REFERENCES	272
APPENDICES	
A. DSC ANALYSIS	285
B. TGA ANALYSIS	303
C. MECHANICAL TEST RESULTS	307
D. RHEOLOGICAL PROPERTIES.....	314
VITA	319

LIST OF TABLES

TABLE

3.1 Properties of the Polyamide-6.....	62
3.2 Properties of Organoclays.....	66
3.3 Properties of Elastomeric Materials.....	69
3.4 Drying temperature and time for the materials used in the study.....	72
3.5 Formulation table.....	73
3.6 Formulation table (cont'd).....	74
3.7 Impact Test Specimen Dimensions.....	83
3.8 Tensile Test Specimen Dimensions.....	84
3.9 DMA Specimen Dimensions.....	87
4.1 d-spacing data of polyamide-6/Cloisite® 15A/E-BA-MAH nanocomposites processed by different addition.....	93
4.2 d-spacing data of polyamide-6/Cloisite® 15A/E-GMA nanocomposites processed by different addition order.....	96
4.3 d-spacing data of polyamide-6/Cloisite® 25A/E-BA-MAH nanocomposites processed by different addition orders.....	101
4.4 d-spacing data of nanocomposites containing Cloisite® 30B and E-GMA processed with different addition orders.....	109
4.5. Elastomer domain sizes in polyamide-6/elastomer blends.....	118
4.6 Elastomer domain sizes in polyamide-6/organoclay/E-BA-MAH nanocomposites.....	124
4.7 Elastomer domain sizes in polyamide-6/organoclay/E-GMA nanocomposites.....	129
4.8 Elastomer E-MA-GMA domain size in polyamide-6 nanocomposites.....	134
4.9 Assignment of polyamide-6 FTIR bands.....	136
4.10 Assignment of E-BA-MAH FTIR bands.....	140
4.11 Assignment of E-GMA FTIR bands.....	145

4.12 Assignment of E-MA-GMA FTIR bands.....	145
4.13 MFI measurement results in polyamide-6/elastomer blends.....	154
4.14 MFI measurement results for polyamide-6/organoclay/E-BA-MAH nanocomposites.....	155
4.15 MFI measurement results for polyamide-6/organoclay/E-GMA nanocomposites.....	157
4.16 MFI measurement results for polyamide-6 nanocomposites in All-S sequence with/without E-MA-GMA elastomer	158
4.17 Effect of organoclay type on thermal properties of binary nanocomposites.....	160
4.18 Melting temperatures and % crystallinities in polyamide-6/elastomer polymer blends	161
4.19 Melting temperatures and % crystallinities of polyamide-6/organoclay/E-BA- MAH nanocomposites	164
4.20 Melting temperatures and % crystallinities of polyamide-6/organoclay/E- GMA nanocomposites.....	165
4.21 Melting temperatures and % crystallinities of polyamide-6/organoclay/E-MA- GMA nanocomposites.....	166
4.22 Effect of organoclay type on glass transition temperature of binary nanocomposites.....	224
4.23 Glass transition temperature of polyamide-6/organoclay/E-BA-MAH nanocomposites.....	230
4.24 Glass transition temperatures of polyamide-6/organoclay/E-GMA nanocomposites.....	238
4.25 Glass transition temperatures of polyamide-6/organoclay/E-MA-GMA nanocomposites.....	247
4.26 Storage and Loss Modulus slopes as a function of frequency in double logarithmic scale	258
C.1 Impact Strength data and standard deviations for all the compositions...	307
C.2 Toughness data and standard deviations for all the compositions	308
C.3 Tensile strength data and standard deviations for all the compositions ..	309
C.4 Young's Modulus data and standard deviations for all the compositions	310
C.5 Elongation at Break data and standard deviations for all the compositions	311
C.6 Flexural Strength data and standard deviations for all the compositions.	312

C.7 Flexural Modulus data and standard deviations for all the compositions. 313

LIST OF FIGURES

FIGURE

2.1 Scheme of different types of composite arising from the interaction of layered silicates and polymers.....	9
2.2 Schematic view of in-situ polymerization.....	12
2.3 Schematic view of solution approach.....	13
2.4 Three important parameter affecting clay dispersion and delamination...	15
2.5 Effect of shear on clay platelets.....	15
2.6 Idealized structure of montmorillonite.....	19
2.7 Schematic representation of a cation-exchange reaction between the silicate and an alkylammonium salt.....	21
2.8 Chemical structures for (a) and (b) type polyamides.....	22
2.9 Ring-opening polymerization of ϵ -caprolactam.....	23
2.10 Acidolysis reaction of polyamides.....	26
2.11 Aminolysis reaction of polyamides.....	27
2.12 Ammonolysis reaction of polyamides.....	27
2.13 Thermal decomposition reaction in polyamides by cleavage of amide bond.....	28
2.14 Schematic drawing of extrusion process.....	32
2.15 Intermeshing corotating twin-crew extruder.....	33
2.16 Diffraction of x-rays by planes of atoms.....	35
2.17 Schematic structure of a transmission electron microscope.....	38
2.18 Attenuated total reflectance cell.....	40
2.19 Idealized DSC thermogram of a polymer.....	42
2.20 Schematic drawing of melt flow index apparatus.....	43
2.21 Schematic drawing of notched Charpy impact test.....	44
2.22 Schematic drawing of bending mode.....	48

2.23 Cross-sectional diagram of torsional parallel-plate viscometer	53
3.1 Chemical structure of organic modifier 2M2HT (dimethyl, dihydrogenated tallow quaternary ammonium) and anion (chloride) of Cloisite® 15A.....	63
3.2 Chemical structure of organic modifier 2MHTL8 (dimethyl, hydrogenated tallow, 2-ethylhexyl quaternary ammonium) and anion (methyl sulfate) of Cloisite® 25A.....	64
3.3 Chemical structure of organic modifier MT2EtOH (methyl, tallow, bis-2-hydroxyethyl, quaternary ammonium and anion (chloride) of Cloisite® 30	64
3.4 Clay selection chart based on polymer/monomer chemistry.....	65
3.5 Chemical structure of elastomer E-BA-MAH	67
3.6 Chemical structure of elastomer E-GMA	67
3.7 Chemical structure of elastomer E-MA-GMA.....	68
3.8 Thermo Prism TSE 16 TC twin screw extruder	71
3.9 Daka Instruments injection molding machine	71
3.10 DSM injection molding machine	72
3.11 Generalized flowchart of experimental procedure	77
3.12 Impact Tester.....	82
3.13 Impact Test Specimen	82
3.14 Tensile Test Specimen.....	83
3.15 Three point loading scheme.....	85
3.16 DMA Test Specimen	86
3.17 ARES Rheometer	88
4.1 XRD patterns for (a) Cloisite® 15A (b) Polyamide-6/Cloisite® 15A nanocomposite (c) Polyamide-6/Cloisite® 15A/E-BA-MAH nanocomposite processed by All-S sequence.....	92
4.2 XRD patterns of polyamide-6/Cloisite® 15A/E-BA-MAH nanocomposites processed by different addition orders	94
4.3 XRD patterns for (a) Cloisite® 15A (b) Polyamide-6/Cloisite® 15A nanocomposite (c) Polyamide-6/Cloisite® 15A/E-GMA nanocomposite processed by All-S sequence.....	95
4.4 XRD patterns of polyamide-6/Cloisite® 15A/E-GMA nanocomposites processed by different addition order	97

4.5 XRD patterns for (a) Cloisite® 15A (b) Polyamide-6/Cloisite® 15A nanocomposite (c) Polyamide-6/Cloisite® 15A/E-MA-GMA nanocomposite processed by All-S sequence.....	98
4.6 XRD patterns for (a) Cloisite® 25A (b) Polyamide-6/Cloisite® 25A nanocomposite (c) Polyamide-6/Cloisite® 25A/E-BA-MAH nanocomposite processed by All-S sequence.....	100
4.7 XRD patterns of polyamide-6/Cloisite® 25A/E-BA-MAH nanocomposites processed by different addition orders	102
4.8 XRD patterns for (a) Cloisite® 25A (b) Polyamide-6/Cloisite® 25A nanocomposite (c) Polyamide-6/Cloisite® 25A/E-GMA nanocomposite processed by All-S sequence.....	103
4.9 XRD patterns for (a) Cloisite® 25A (b) Polyamide-6/Cloisite® 25A nanocomposite (c) Polyamide-6/Cloisite® 25A/E-MA-GMA nanocomposite processed by All-S sequence.....	104
4.10 XRD patterns for (a) Cloisite® 30B (b) Polyamide-6/Cloisite® 30B nanocomposite (c) Polyamide-6/Cloisite® 30B/E-BA-MAH nanocomposite processed by All-S sequence.....	106
4.11 XRD patterns for (a) Cloisite® 30B (b) Polyamide-6/Cloisite® 30B nanocomposite (c) Polyamide-6/Cloisite® 30B/E-GMA nanocomposite processed by All-S sequence.....	107
4.12 XRD patterns of nanocomposites containing Cloisite® 30B and E-GMA processed with different addition orders.....	108
4.13 XRD patterns for (a) Cloisite® 30B (b) Polyamide-6/Cloisite® 30B nanocomposite (c) Polyamide-6/Cloisite® 30B/E-MA-GMA nanocomposite processed by All-S sequence.....	110
4.14 TEM micrograph of polyamide-6/Cloisite® 15A nanocomposite.....	112
4.15 TEM micrograph of polyamide-6/Cloisite® 15A/E-BA-MAH nanocomposite processed by All-S sequence.....	112
4.16 TEM micrograph of polyamide-6/Cloisite® 15A/E-GMA nanocomposite processed by All-S sequence.....	113
4.17 TEM micrograph of polyamide-6/Cloisite® 25A nanocomposite.....	114
4.18 TEM micrograph of polyamide-6/Cloisite® 25A/E-BA-MAH nanocomposite processed by All-S sequence.....	114
4.19 TEM micrograph of polyamide-6/Cloisite® 30B nanocomposite.....	116

4.20 TEM micrographs of polyamide-6/Cloisite® 30B/E-GMA nanocomposite processed by All-S sequence.....	116
4.21 Fracture surface of unfilled polyamide-6 sample (a) x300 magnification (b) x3500 magnification	117
4.22 Fracture surface of polyamide-6/5 wt % E-BA-MAH elastomer blend (a) x250 magnification (b) x6000 magnification	120
4.23 Fracture surface of polyamide-6/10 wt % E-BA-MAH elastomer blend (a) x250 magnification (b) x10000 magnification	120
4.24 Fracture surface of polyamide-6/15 wt % E-BA-MAH elastomer blend (a) x250 magnification (b) x10000 magnification	120
4.25 Fracture surface of polyamide-6/5 wt % E-GMA elastomer blend (a) x250 magnification (b) x6000 magnification	121
4.26 Fracture surface of polyamide-6/10 wt % E-GMA elastomer blend (a) x250 magnification (b) x6000 magnification	121
4.27 Fracture surface of polyamide-6/15 wt % E-GMA elastomer blend (a) x250 magnification (b) x6000 magnification	121
4.28 Fracture surface of polyamide-6/5 wt % E-MA-GMA elastomer blend (a) x250 magnification (b) x5000 magnification	122
4.29 Fracture surface of polyamide-6/10 wt % E-MA-GMA elastomer blend (a) x250 magnification (b) x5000 magnification	122
4.30 Fracture surface of polyamide-6/15 wt % E-MA-GMA elastomer blend (a) x250 magnification (b) x5000 magnification	122
4.31 Fracture surface of polyamide-6/Cloisite® 15A nanocomposite (a) x300 magnification (b) x3500 magnification	123
4.32 Fracture surface of polyamide-6/Cloisite® 25A nanocomposite (a) x300 magnification (b) x3500 magnification	123
4.33 Fracture surface of polyamide-6/Cloisite® 30B nanocomposite (a) x300 magnification (b) x3500 magnification	123
4.34 SEM micrograph of Polyamide-6/Cloisite® 15A/E-BA-MAH (All-S) nanocomposite (a) x250 magnification (b) x10000 magnification	126
4.35 SEM micrograph of Polyamide-6/Cloisite® 25A/E-BA-MAH c nanocomposite (a) x250 magnification (b) x10000 magnification	126
4.36 SEM micrograph of Polyamide-6/Cloisite® 30B/E-BA-MAH (All-S) nanocomposite (a) x250 magnification (b) x10000 magnification	126

4.37	SEM micrograph of Polyamide-6/Cloisite® 15A/E-BA-MAH (PI-C) nanocomposite (a) x250 magnification (b) x10000 magnification	127
4.38	SEM micrograph of Polyamide-6/Cloisite® 15A/E-BA-MAH (PC-I) nanocomposite (a) x250 magnification (b) x10000 magnification	127
4.39	SEM micrograph of Polyamide-6/Cloisite® 15A/E-BA-MAH (IC-P) nanocomposite (a) x250 magnification (b) x10000 magnification	127
4.40	SEM micrograph of Polyamide-6/Cloisite® 25A/E-BA-MAH (PI-C) nanocomposite (a) x250 magnification (b) x10000 magnification	128
4.41	SEM micrograph of Polyamide-6/Cloisite® 25A/E-BA-MAH (PC-I) nanocomposite (a) x250 magnification (b) x10000 magnification	128
4.42	SEM micrograph of Polyamide-6/Cloisite® 25A/E-BA-MAH (IC-P) nanocomposite (a) x250 magnification (b) x10000 magnification	128
4.43	SEM micrograph of Polyamide-6/Cloisite® 15A/E-GMA (All-S) nanocomposite (a) x250 magnification (b) x6000 magnification	131
4.44	SEM micrograph of Polyamide-6/Cloisite® 25A/E-GMA (All-S) nanocomposite (a) x250 magnification (b) x6000 magnification	131
4.45	SEM micrograph of Polyamide-6/Cloisite® 30B/E-GMA (All-S) nanocomposite (a) x250 magnification (b) x6000 magnification	131
4.46	SEM micrograph of Polyamide-6/Cloisite® 15A/E-GMA (PI-C) nanocomposite (a) x250 magnification (b) x5000 magnification	132
4.47	SEM micrograph of Polyamide-6/Cloisite® 15A/E-GMA (PC-I) nanocomposite (a) x250 magnification (b) x6000 magnification	132
4.48	SEM micrograph of Polyamide-6/Cloisite® 15A/E-GMA (IC-P) nanocomposite (a) x250 magnification (b) x6000 magnification	132
4.49	SEM micrograph of Polyamide-6/Cloisite® 30B/E-GMA (PI-C) nanocomposite (a) x250 magnification (b) x6000 magnification	133
4.50	SEM micrograph of Polyamide-6/Cloisite® 30B/E-GMA (PC-I) nanocomposite (a) x250 magnification (b) x6000 magnification	133
4.51	SEM micrograph of Polyamide-6/Cloisite® 30B/E-GMA (IC-P) nanocomposite (a) x250 magnification (b) x6000 magnification	133
4.52	SEM micrograph of Polyamide-6/Cloisite® 15A/E-MA-GMA (All-S) nanocomposite (a) x250 magnification (b) x5000 magnification	135
4.53	SEM micrograph of Polyamide-6/Cloisite® 25A/E-MA-GMA (All-S) nanocomposite (a) x250 magnification (b) x5000 magnification	135

4.54 SEM micrograph of Polyamide-6/Cloisite® 30B/E-MA-GMA (All-S) nanocomposite (a) x250 magnification (b) x5000 magnification	135
4.55 FTIR-ATR spectrum for polyamide-6.....	137
4.56 FTIR-ATR spectrum for E-BA-MAH.....	139
4.57 Scheme for the reaction between amine end group of polyamide-6 and maleic anhydride group of E-BA-MAH leading to the formation of amide or imide linkages	140
4.58 Scheme for the reaction between amine end group of polyamide-6 and butyl acrylate of E-BA-MAH	141
4.59 FTIR-ATR spectrum for polyamide-6/50 wt % E-BA-MAH blend	142
4.60 Detailed FTIR-ATR spectrum for polyamide-6/50 wt % E-BA-MAH blend	143
4.61 Scheme for the reaction between amine and carboxyl end groups of polyamide-6 and E-GMA.....	146
4.62 Scheme for the reaction between hydroxyl groups and E-GMA	146
4.63 FTIR-ATR spectrum for E-GMA	147
4.64 FTIR-ATR spectrum for polyamide-6/50 wt % E-GMA blend.....	148
4.65 Scheme for the reaction between amine end group of polyamide-6 and methyl acrylate of E-MA-GMA	149
4.66 FTIR-ATR spectrum for E-MA-GMA.....	150
4.67 FTIR-ATR spectrum for polyamide-6/50 wt % E-MA-GMA blend	151
4.68 Scheme for the reaction between hydroxyl group of organoclay and maleic anhydride group of E-BA-MAH.....	152
4.69 DSC Termogram of pure elastomer E-BA-MAH	162
4.70 DSC Termogram of pure elastomer E-GMA.....	162
4.71 DSC Termogram of pure elastomer E-MA-GMA	163
4.72 Effect of elastomer content on impact strength of E-BA-MAH elastomer toughened polyamide-6 blends.....	168
4.73 Effect of elastomer content on impact strength of E-GMA elastomer toughened polyamide-6 blends	169
4.74 Effect of elastomer content on impact strength of E-MA-GMA elastomer toughened polyamide-6 blends	170
4.75 Effect of organoclay type on impact strength of E-BA-MAH elastomer toughened polyamide-6 nanocomposites.....	172

4.76 Effect of mixing order on impact strength of E-BA-MAH elastomer toughened polyamide-6/Cloisite® 15A nanocomposites.....	173
4.77 Effect of mixing order on impact strength of E-BA-MAH elastomer toughened polyamide-6/Cloisite® 25A nanocomposites.....	174
4.78 Effect of organoclay type on impact strength of E-GMA elastomer toughened polyamide-6 nanocomposites.....	177
4.79 Effect of mixing order on impact strength of E-GMA elastomer toughened polyamide-6/Cloisite® 15A nanocomposites	178
4.80 Effect of mixing order on impact strength of E-GMA elastomer toughened polyamide-6/Cloisite® 30B nanocomposites	179
4.81 Effect of organoclay type on impact strength of E-MA-GMA elastomer toughened polyamide-6 nanocomposites	180
4.82 Effect of elastomer type on toughness of polyamide-6 blends.....	182
4.83 Effect of organoclay type on toughness of polyamide-6 blends.....	182
4.84 Toughness of polyamide-6/organoclay/elastomer ternary nanocomposites	183
4.85 Effect of elastomer content on tensile strength of E-BA-MAH elastomer toughened polyamide-6 blends	185
4.86 Effect of elastomer content on Young's Modulus of E-BA-MAH elastomer toughened polyamide-6 blends	185
4.87 Effect of elastomer content on % elongation at break of E-BA-MAH elastomer toughened polyamide-6 blends.....	186
4.88 Effect of elastomer content on tensile strength of E-GMA elastomer toughened polyamide-6 blends	187
4.89 Effect of elastomer content on Young's Modulus of E-GMA elastomer toughened polyamide-6 blends	187
4.90 Effect of elastomer content on % elongation at break of E-GMA elastomer toughened polyamide-6 blends	188
4.91 Effect of elastomer content on tensile strength of E-MA-GMA elastomer toughened polyamide-6 blends	189
4.92 Effect of elastomer content on Young's Modulus of E-MA-GMA elastomer toughened polyamide-6 blends	189
4.93 Effect of elastomer content on % elongation at break of E-MA-GMA elastomer toughened polyamide-6 blends.....	190

4.94 Effect of organoclay type on tensile strength of E-BA-MAH elastomer toughened polyamide-6 nanocomposites	192
4.95 Effect of organoclay type on Young's Modulus of E-BA-MAH elastomer toughened polyamide-6 nanocomposites	192
4.96 Effect of organoclay type on % elongation at break of E-BA-MAH elastomer toughened polyamide-6 nanocomposites	194
4.97 Effect of mixing order on tensile strength of E-BA-MAH elastomer toughened polyamide-6/Cloisite® 15A nanocomposites	196
4.98 Effect of mixing order on Young's Modulus of E-BA-MAH elastomer toughened polyamide-6/Cloisite® 15A nanocomposites.....	196
4.99 Effect of mixing order on % elongation at break of E-BA-MAH elastomer toughened polyamide-6/Cloisite® 15A nanocomposites.....	197
4.100 Effect of mixing order on tensile strength of E-BA-MAH elastomer toughened polyamide-6/Cloisite® 25A nanocomposites.....	197
4.101 Effect of mixing order on Young's Modulus of E-BA-MAH elastomer toughened polyamide-6/Cloisite® 25A nanocomposites.....	198
4.102 Effect of mixing order on % elongation at break of E-BA-MAH elastomer toughened polyamide-6/Cloisite® 25A nanocomposites.....	198
4.103 Effect of organoclay type on tensile strength of E-GMA elastomer toughened polyamide-6 nanocomposites	200
4.104 Effect of organoclay type on Young's Modulus of E-GMA elastomer toughened polyamide-6 nanocomposites	200
4.105 Effect of organoclay type on % elongation at break of E-GMA elastomer toughened polyamide-6 nanocomposites	201
4.106 Effect of mixing order on tensile strength of E-GMA elastomer toughened polyamide-6/Cloisite® 15A nanocomposites	202
4.107 Effect of mixing order on Young's Modulus of E-GMA elastomer toughened polyamide-6/Cloisite® 15A nanocomposites	203
4.108 Effect of mixing order on % elongation at break of E-GMA elastomer toughened polyamide-6/Cloisite® 15A nanocomposites.....	203
4.109 Effect of mixing order on tensile strength of E-GMA elastomer toughened polyamide-6/Cloisite® 30B nanocomposites	204
4.110 Effect of mixing order on Young's Modulus of E-GMA elastomer toughened polyamide-6/Cloisite® 30B nanocomposites	204

4.111 Effect of mixing order on % elongation at break of E-GMA elastomer toughened polyamide-6/Cloisite® 30B nanocomposites.....	205
4.112 Effect of organoclay type on tensile strength of E-MA-GMA elastomer toughened polyamide-6 nanocomposites	206
4.113 Effect of organoclay type on Young's Modulus of E-MA-GMA elastomer toughened polyamide-6 nanocomposites	207
4.114 Effect of organoclay type on % elongation at break of E-MA-GMA elastomer toughened polyamide-6 nanocomposites.....	207
4.115 Effect of elastomer content on flexural strength of E-BA-MAH elastomer toughened polyamide-6 blends	209
4.116 Effect of elastomer content on flexural modulus of E-BA-MAH elastomer toughened polyamide-6 blends	210
4.117 Effect of elastomer content on flexural strength of E-GMA elastomer toughened polyamide-6 blends	210
4.118 Effect of elastomer content on flexural modulus of E-GMA elastomer toughened polyamide-6 blends	211
4.119 Effect of elastomer content on flexural strength of E-MA-GMA elastomer toughened polyamide-6 blends	211
4.120 Effect of elastomer content on flexural modulus of E-MA-GMA elastomer toughened polyamide-6 blends	212
4.121 Effect of organoclay type on flexural strength of E-BA-MAH elastomer toughened polyamide-6 nanocomposites	214
4.122 Effect of organoclay type on flexural modulus of E-BA-MAH elastomer toughened polyamide-6 nanocomposites	214
4.123 Effect of mixing order on flexural strength of E-BA-MAH elastomer toughened polyamide-6/Cloisite® 15A nanocomposites.....	215
4.124 Effect of mixing order on flexural strength of E-BA-MAH elastomer toughened polyamide-6/Cloisite® 15A nanocomposites.....	215
4.125 Effect of mixing order on flexural strength of E-BA-MAH elastomer toughened polyamide-6/Cloisite® 25A nanocomposites.....	216
4.126 Effect of mixing order on flexural modulus of E-BA-MAH elastomer toughened polyamide-6/Cloisite® 25A nanocomposites.....	216
4.127 Effect of organoclay type on on flexural strength of E-GMA elastomer toughened polyamide-6 nanocomposites	218

4.128 Effect of organoclay type on flexural modulus of E-GMA elastomer toughened polyamide-6 nanocomposites	218
4.129 Effect of mixing order on flexural strength of E-GMA elastomer toughened polyamide-6/Cloisite® 15A nanocomposites	219
4.130 Effect of mixing order on flexural modulus of E-GMA elastomer toughened polyamide-6/Cloisite® 15A nanocomposites	219
4.131 Effect of mixing order on flexural strength of E-GMA elastomer toughened polyamide-6/Cloisite® 30B nanocomposites	220
4.132 Effect of mixing order on flexural modulus of E-GMA elastomer toughened polyamide-6/Cloisite® 30B nanocomposites	220
4.133 Effect of organoclay type on flexural strength of E-MA-GMA elastomer toughened polyamide-6 nanocomposites	221
4.134 Effect of organoclay type on flexural modulus of E-MA-GMA elastomer toughened polyamide-6 nanocomposites	222
4.135 Storage Modulus versus temperature data for pure elastomeric materials	225
4.136 Loss Modulus versus temperature data for pure elastomeric materials	225
4.137 Loss tangent ($\tan \delta$) versus temperature data for pure elastomeric materials	226
4.138 Effect of organoclay type on Storage Modulus versus temperature.....	226
4.139 Effect of organoclay type on Loss Modulus versus temperature.....	227
4.140 Effect of organoclay type on Loss tangent ($\tan \delta$) versus temperature	227
4.141 Storage Modulus versus temperature data for polyamide-6/Cloisite® 15A/E-BA-MAH nanocomposite	231
4.142 Loss Modulus versus temperature data for polyamide-6/Cloisite® 15A/E-BA-MAH nanocomposite.....	231
4.143 Loss tangent ($\tan \delta$) versus temperature data for polyamide-6/Cloisite® 15A/E-BA-MAH nanocomposite	232
4.144 Storage Modulus versus temperature data for polyamide-6/Cloisite® 25A/E-BA-MAH nanocomposite	232
4.145 Loss Modulus versus temperature data for polyamide-6/Cloisite® 25A/E-BA-MAH nanocomposite.....	233
4.146 Loss tangent ($\tan \delta$) versus temperature data for polyamide-6/Cloisite® 25A/E-BA-MAH nanocomposite	233

4.147 Storage Modulus versus temperature data for polyamide-6/Cloisite® 30B/E-BA-MAH nanocomposite	234
4.148 Loss Modulus versus temperature data for polyamide-6/Cloisite® 30B/E-BA-MAH nanocomposite	234
4.149 Loss tangent ($\tan \delta$) versus temperature data for polyamide-6/Cloisite® 30B/E-BA-MAH nanocomposite	235
4.150 Effect of mixing order on storage modulus of polyamide-6/Cloisite® 25A/E-BA-MAH ternary nanocomposites	235
4.151 Effect of mixing order on loss modulus of polyamide-6/Cloisite® 25A/E-BA-MAH ternary nanocomposites	236
4.152 Effect of mixing order on loss tangent ($\tan \delta$) of polyamide-6/Cloisite® 25A/E-BA-MAH ternary nanocomposites.....	236
4.153 Storage Modulus versus temperature data for polyamide-6/Cloisite® 15A/E-GMA nanocomposite.....	239
4.154 Loss Modulus versus temperature data for polyamide-6/Cloisite® 15A/E-GMA nanocomposite.....	239
4.155 Loss tangent ($\tan \delta$) versus temperature data for polyamide-6/Cloisite® 15A/E-GMA nanocomposite.....	240
4.156 Storage Modulus versus temperature data for polyamide-6/Cloisite® 25A/E-GMA nanocomposite.....	240
4.157 Loss Modulus versus temperature data for polyamide-6/Cloisite® 25A/E-GMA nanocomposite.....	241
4.158 Loss tangent ($\tan \delta$) versus temperature data for polyamide-6/Cloisite® 25A/E-GMA nanocomposite.....	241
4.159 Storage Modulus versus temperature data for polyamide-6/Cloisite® 30B/E-GMA nanocomposite.....	242
4.160 Loss Modulus versus temperature data for polyamide-6/Cloisite® 30B/E-GMA nanocomposite.....	242
4.161 Loss tangent ($\tan \delta$) versus temperature data for polyamide-6/Cloisite® 30B/E-GMA nanocomposite.....	243
4.162 Effect of mixing order on storage modulus of polyamide-6/Cloisite® 15A/E-GMA ternary nanocomposites.....	243
4.163 Effect of mixing order on loss modulus of polyamide-6/Cloisite® 15A/E-GMA ternary nanocomposites.....	244

4.164 Effect of mixing order on loss tangent ($\tan \delta$) of polyamide-6/Cloisite® 15A/ E-GMA ternary nanocomposites	244
4.165 Effect of mixing order on storage modulus of polyamide-6/Cloisite® 30B/ E-GMA ternary nanocomposites.....	245
4.166 Effect of mixing order on loss modulus of polyamide-6/Cloisite® 30B/ E-GMA ternary nanocomposites.....	245
4.167 Effect of mixing order on loss tangent ($\tan \delta$) of polyamide-6/Cloisite® 30B/ E-GMA ternary nanocomposites	246
4.168 Storage Modulus versus temperature data for polyamide-6/Cloisite® 15A/E-MA-GMA nanocomposite	248
4.169 Loss Modulus versus temperature data for polyamide-6/Cloisite® 15A/ E-MA-GMA nanocomposite	248
4.170 Loss tangent ($\tan \delta$) versus temperature data for polyamide-6/Cloisite® 15A/E-MA-GMA nanocomposite	249
4.171 Storage Modulus versus temperature data for polyamide-6/Cloisite® 25A/E-MA-GMA nanocomposite	249
4.172 Loss modulus versus temperature data for polyamide-6/Cloisite® 25A/ E-MA-GMA nanocomposite	250
4.173 Loss tangent ($\tan \delta$) versus temperature data for polyamide-6/Cloisite® 25A/E-MA-GMA nanocomposite	250
4.174 Storage modulus versus temperature data for polyamide-6/Cloisite® 30B/E-MA-GMA nanocomposite	251
4.175 Loss modulus versus temperature data for polyamide-6/Cloisite® 30B/ E-MA-GMA nanocomposite	251
4.176 Loss tangent ($\tan \delta$) versus temperature data for polyamide-6/Cloisite® 30B/E-MA-GMA nanocomposite	252
4.177 Influence of strain amplitude on storage modulus for polyamide-6/Cloisite® 25A/E-MA-GMA nanocomposite	253
4.178 Influence of strain amplitude on loss modulus for polyamide-6/Cloisite® 25A/E-MA-GMA nanocomposite	254
4.179 Influence of strain amplitude on complex viscosity for polyamide- 6/Cloisite® 25A/E-MA-GMA nanocomposite	254
4.180 Influence of frequency on storage modulus for polyamide-6/organoclay nanocomposites.....	259

4.181 Influence of frequency on loss modulus for polyamide-6/organoclay nanocomposites.....	260
4.182 Influence of frequency on complex viscosity for polyamide-6/organoclay nanocomposites.....	261
4.183 Loss modulus as a function of storage modulus for polyamide-6/organoclay nanocomposites.....	262
4.184 Influence of frequency on storage modulus for polyamide-6/organoclay/E-MA-GMA nanocomposites	263
4.185 Influence of frequency on loss modulus for polyamide-6/organoclay/E-MA-GMA nanocomposites.....	264
4.186 Influence of frequency on complex viscosity for polyamide-6/organoclay/E-MA-GMA nanocomposites	265
4.187 Loss modulus as a function of storage modulus for polyamide-6/organoclay/E-MA-GMA nanocomposites.....	266
A.1 DSC thermogram of polyamide-6	285
A.2 DSC thermogram of polyamide-6/Cloisite® 15A nanocomposite	286
A.3 DSC thermogram of polyamide-6/Cloisite® 25A nanocomposite	286
A.4 DSC thermogram of polyamide-6/Cloisite® 30B nanocomposite	287
A.5 DSC thermogram of polyamide-6/E-BA-MAH (5 wt %) blend.....	287
A.6 DSC thermogram of polyamide-6/E-BA-MAH (10 wt %) blend.....	288
A.7 DSC thermogram of polyamide-6/E-BA-MAH (15 wt %) blend.....	288
A.8 DSC thermogram of polyamide-6/E-GMA (5 wt %) blend	289
A.9 DSC thermogram of polyamide-6/E-GMA (10 wt %) blend	289
A.10 DSC thermogram of polyamide-6/E-GMA (15 wt %) blend	290
A.11 DSC thermogram of polyamide-6/E-MA-GMA (5 wt %) blend	290
A.12 DSC thermogram of polyamide-6/E-MA-GMA (10 wt %) blend	291
A.13 DSC thermogram of polyamide-6/E-MA-GMA (15 wt %) blend	291
A.14 DSC thermogram of polyamide-6/Cloisite® 15A/E-BA-MAH (All-S) nanocomposite	292
A.15 DSC thermogram of polyamide-6/Cloisite® 15A/E-BA-MAH (PI-C) nanocomposite	292
A.16 DSC thermogram of polyamide-6/Cloisite® 15A/E-BA-MAH (PC-I) nanocomposite	293
A.17 DSC thermogram of polyamide-6/Cloisite® 15A/E-BA-MAH (IC-P) nanocomposite	293

A.18 DSC thermogram of polyamide-6/Cloisite® 25A/E-BA-MAH (All-S) nanocomposite	294
A.19 DSC thermogram of polyamide-6/Cloisite® 25A/E-BA-MAH (PI-C) nanocomposite	294
A.20 DSC thermogram of polyamide-6/Cloisite® 25A/E-BA-MAH (PC-I) nanocomposite	295
A.21 DSC thermogram of polyamide-6/Cloisite® 25A/E-BA-MAH (IC-P) nanocomposite	295
A.22 DSC thermogram of polyamide-6/Cloisite® 30B/E-BA-MAH (All-S) nanocomposite	296
A.23 DSC thermogram of polyamide-6/Cloisite® 15A/E-GMA (All-S) Nanocomposite	296
A.24 DSC thermogram of polyamide-6/Cloisite® 15A/E-GMA (PI-C) Nanocomposite	297
A.25 DSC thermogram of polyamide-6/Cloisite® 15A/E-GMA (PC-I) Nanocomposite	297
A.26 DSC thermogram of polyamide-6/Cloisite® 15A/E-GMA (IC-P) Nanocomposite	298
A.27 DSC thermogram of polyamide-6/Cloisite® 25A/E-GMA (All-S) Nanocomposite	298
A.28 DSC thermogram of polyamide-6/Cloisite® 30B/E-GMA (All-S) nanocomposite	299
A.29 DSC thermogram of polyamide-6/Cloisite® 30B/E-GMA (PI-C) nanocomposite	299
A.30 DSC thermogram of polyamide-6/Cloisite® 30B/E-GMA (PC-I) nanocomposite	300
A.31 DSC thermogram of polyamide-6/Cloisite® 30B/E-GMA (IC-P) nanocomposite	300
A.32 DSC thermogram of polyamide-6/Cloisite® 15A/E-MA-GMA (All-S) nanocomposite	301
A.33 DSC thermogram of polyamide-6/Cloisite® 25A/E-MA-GMA (All-S) nanocomposite	301
A.34 DSC thermogram of polyamide-6/Cloisite® 30B/E-MA-GMA (All-S) nanocomposite	302
B.1 TGA thermogram of Cloisite® 15A organoclay	303

B.2 Isothermal TGA thermogram of Cloisite® 15A organoclay.....	304
B.3 TGA thermogram of Cloisite® 25A organoclay	304
B.4 Isothermal TGA thermogram of Cloisite® 25A organoclay.....	305
B.5 TGA thermogram of Cloisite® 30B organoclay	305
B.6 Isothermal TGA thermogram of Cloisite® 30B organoclay.....	306
D.1 Influence of frequency on storage modulus for polyamide-6/Cloisite® 15A/E-MA-GMA nanocomposite.....	314
D.2 Influence of frequency on loss modulus for polyamide-6/Cloisite® 15A/E-MA-GMA nanocomposite	315
D.3 Influence of frequency on complex viscosity for polyamide-6/Cloisite® 15A/E-MA-GMA nanocomposite.....	315
D.4 Influence of frequency on storage modulus for polyamide-6/Cloisite® 25A/E-MA-GMA nanocomposite.....	316
D.5 Influence of frequency on loss modulus for polyamide-6/Cloisite® 25A/E-MA-GMA nanocomposite	316
D.6 Influence of frequency on complex viscosity for polyamide-6/Cloisite® 25A/E-MA-GMA nanocomposite.....	317
D.7 Influence of frequency on storage modulus for polyamide-6/Cloisite® 30B/E-MA-GMA nanocomposite.....	317
D.8 Influence of frequency on loss modulus for polyamide-6/Cloisite® 30B/E-MA-GMA nanocomposite	318
D.9 Influence of frequency on complex viscosity for polyamide-6/Cloisite® 30B/E-MA-GMA nanocomposite.....	318

NOMENCLATURE

\bar{A}	Average area, μm^2
A_0	Original cross-sectional area before any load is applied, mm^2
A_i	Area of a number of domains in SEM analysis, μm^2
b	Width of the specimen, mm
b_1	Width of the narrow section of tensile test specimen, mm
b_2	Width of overall of tensile test specimen, mm
d	Depth of specimen, mm
d	Interlayer spacing, \AA
\bar{d}	Average domain size, nm
d_p	Depth of penetration, mm
D	Maximum deflection of the centre of the beam, mm
D	Barrel diameter, mm
D	Distance between grips, mm
E	Young's modulus, MPa
E_B	Modulus of elasticity in bending, MPa
E^*	Complex modulus, MPa
E'	Storage modulus, MPa
E''	Loss modulus, MPa
F	Force, N
G^*	Complex dynamic modulus, MPa
G'	Dynamic storage modulus, MPa
G''	Dynamic loss modulus, MPa
h	Thickness of tensile test specimen, mm
h	Gap between the parallel plates, mm
l_1	Length of the narrow section of tensile test specimen, mm
l_2	Length of overall of tensile test specimen, mm
L	Distance between the grips of tensile test specimen, mm
L	Length of impact test specimen, mm
L	Distance between support points, mm
L	Length of the extruder barrel, mm

L_0	Overall length, mm
l_i	Instantaneous length, mm
l_0	Initial gauge length, mm
ΔL	Change in sample length, mm
m	Slope of the tangent to the initial straight line portion of the load deflection curve, N/mm
n	Degree of diffraction
n_1	Refractive Index of the sample
n_2	Refractive index of the crystal
r	Maximum strain in the outer fibers, mm/mm
R	Rate of crosshead motion, mm/min
S	Standard deviation
t	Thickness, mm
T	Torque, J
T_g	Glass transition temperature, °C
T_m	Melting temperature, °C
w_1	Total width, mm
w_2	Unnotched width, mm
W	Width of narrow section in tensile measurements, mm
X	Value of single observation
\bar{X}	Arithmetic mean of the set of observations
Z	Rate of straining of the outer fiber, min^{-1}

Greek Letters

$\dot{\gamma}$	shear rate, cm^{-1}
δ	Phase angle, °
ε	Strain, mm/mm
ε^*	Complex strain, mm/mm
ε^0	Amplitude of the applied strain, mm/mm
ε_b	Strain at break, mm/mm
η	Viscosity, g/cm.s
θ	Diffraction angle, °

λ	Wavelength, nm
σ	Stress, MPa
σ^*	Complex stress, MPa
σ^0	Amplitude of the stress response, MPa
ω	Angular frequency, rad/s
Ω	Angular velocity, rad/s

Abbreviations

ABS	Acrylonitrile-butadiene-styrene
ASTM	American Society for Testing and Materials
CCD	Charge Coupled Device
CEC	Cation Exchange Capacity
C15A	Cloisite® 15A
C25A	Cloisite® 25A
C30B	Cloisite® 30B
DSC	Differential Scanning Calorimetry
DMA	Dynamic Mechanical Analysis
E-BA-MAH	Ethylene-Butyl Acrylate-Maleic Anhydride
EDS	Energy Dispersive X-ray Spectroscopy
EELS	Electron Energy-Loss Spectroscopy
E-GMA	Ethylene-Glycidyl Methacrylate
E-MA-GMA	Ethylene-Methyl Acrylate-Glycidyl Methacrylate
EPM-g-MA	Maleic Anhydride grafted Ethylene-Propylene Rubber
EPR	Poly (ethylene-ran-propylene)
FTIR-ATR	Fourier Transform Infrared Spectroscopy-Attenuated Total Reflectance
HT	Hydrogenated Tallow
ISO	International Organization for Standardization
LDPE	Low Density Polyethylene
MFI	Melt Flow Index
MMA-GMA	Methyl methacrylate-co-glycidyl methacrylate
MMA-MAH	Methyl methacrylate-co-maleic anhydride

MMT	Montmorillonite
NBR	Acrylonitrile-butadiene copolymer
OMMT	Organically Modified Montmorillonite
PA	Polyamide-6
SAXD	Small Angle X-ray Diffraction
SEBS-g-MA	Maleic Anhydride grafted Styrene-Ethylene/Butylene-Styrene triblock copolymer
SEM	Scanning Electron Microscopy
T	Tallow
TEM	Transmission Electron Microscopy
UFPR	Ultra-fine full vulcanized powdered rubber
XRD	X-Ray Diffraction
WAXS	Wide Angle X-ray Diffraction
2210	E-BA-MAH
8840	E-GMA
8900	E-MA-GMA

CHAPTER 1

INTRODUCTION

Polymer-clay nanocomposites are particulate-filled composites in which the reinforcement material is in the form of sheets and have a high aspect ratio with thickness of one to few nanometers and length of hundreds to thousands of nanometers. Layered silicates, especially montmorillonite, are used as filler in polymer-clay nanocomposites. Montmorillonite is a crystalline; 2:1 layered clay mineral in which a central alumina sheet is sandwiched between two silica tetrahedral sheets. There is a charge deficiency on the montmorillonite sheets due to the substitution of ions of different valence and this charge is balanced by exchangeable cations adsorbed between the unit layers and around their edges. Usually, montmorillonite clays are modified by the substitution reaction of alkylammonium ion with surface sodium ions, making the hydrophobic silicate surfaces organophilic. This procedure enables insertion of organic materials to the clay layers. The alkylammonium cations which provide functional groups that can react with the polymer or initiate polymerization of monomers (Isik et al., 2003; Huang et al., 2000; Giannelis 1996).

Investigations on nanocomposite materials have been started by Toyota researchers in which polyamide-6/clay nanocomposites were obtained by the polymerization of ϵ -caprolactam in the interlayer gallery region of organoclay. Polyamide-6 nanocomposite samples showed superior strength, modulus, heat distortion temperature, and water and gas barrier properties in comparison to pure polyamide-6. It is concluded that the enhancement in mechanical properties could be due to the

ionic bonds between polymer and clay and large surface area of silicates (Kojima et al., 1993; Kojima et al., 1994; Usuki et al., 1995).

When layered clay is mixed with polymer matrix, generally, three main kinds of composites may be obtained depending on the preparation method and the nature of the components used. *Intercalated*, in which polymer chains are intercalated between clay layers and a well ordered, alternating polymer/inorganic silicate structure is formed; *flocculated*, where silicate layers are flocculated due to hydroxylated edge–edge interaction of the silicate layers and *delaminated*, in which the silicate layers are exfoliated and dispersed in a continuous polymer matrix (Ray and Okamoto, 2003).

The dispersion of clay and its exfoliation in polymer matrix depends on the initial interlayer spacing and organic modifier of the clay, the viscosity of polymer, and the polymer processing conditions. The clay agglomerates are broken down in processing equipments, such as extruder and injection molding, due to the applied forces by the polymer melt and the diffusion of macromolecules into the organoclay galleries (Fornes et al., 2001). The force applied on the clay agglomerates from the polymer melt depends on the applied shear rate, polymer melt viscosity, surface area of clay, and surface tension between melt and clay interface, whereas the diffusion of macromolecules depends on the melt temperature and chain structure of polymer matrix, interlayer spacing of clay, type/concentration of surfactant modifiers at the clay surface and processing time (Alexandre and Dubois, 2000; Vaia et al., 1995; Vaia and Giannelis, 1997; Balazs et al., 1998).

Mechanical properties, especially modulus, of the polymer-clay nanocomposites increases at low filler loadings compared to the neat polyamide-6, but Izod impact strength decreases and ductile-brittle transition temperature sharply increases as montmorillonite content is increased (Cho and Paul, 2001). The use of nanocomposites, where toughness is important, can be limited by these losses. High toughness can be achieved by incorporating a low modulus, reactive second component to the polymer matrix. Therefore, rubber toughening of nanocomposites becomes interesting.

Polymer matrix used in this study, polyamide-6, is an attractive polymer for engineering applications owing to its high performance characteristics, such as, high melting point, good mechanical strength and ductility, excellent resistance to solvents, fatigue, and abrasion. These properties are utilized in automotive and electrical industries, especially in consumer products. However, for more demanding applications, there has been a need for polyamides with improved toughness, reduced notch sensitivity, and lower ductile-brittle transition temperature, which can not be achieved by unmodified polyamides. Significant investigations have been made on impact modification of polyamides by blending them with reactive or unreactive, low modulus, rubbery type polymers. During processing, two polymers react with each other at the interface generating a block or graft copolymer, in situ, which compatibilizes the blend by reducing interfacial tension and improving interfacial adhesion. If two polymers have no compatibility, functionalized rubbery polymers, such as anhydride and epoxy groups are utilized. Blends of polyamide-6 with poly(phenylene oxide), acrylonitrile-butadiene-styrene (ABS), polyolefins, polycarbonate, ethylene-propylene-diene rubber (EPDM), and ethylene copolymers have been produced to improve its toughness (Campbell et al., 1990; Kudva et al., 1998; González-Montiel et al., 1995; Kudva et al., 1999; Triacca et al., 1991).

There are some studies that combine layered silicate reinforcement and rubber toughening in polyamides. Khatua et al., 2004, studied the effect of organoclay platelets on morphology of polyamide-6 and EPR blends by scanning and transmission electron microscopy. Baldi et al., 2006, investigated rubber toughening of polyamide-6/organoclay nanocomposites both in dry and wet conditions using ethylene-co-propylene maleated rubber. Kelnar et al., 2006 examined the morphological and mechanical properties of polyamide-6/organoclay ternary nanocomposites prepared by different types of both reactive and unreactive elastomers. The effects of clay content and elastomer type were investigated. Chiu et al., 2005 prepared polyamide-6 and maleated polyolefin elastomer based nanocomposites using one type of commercial organoclay. Liu et al. 2001 synthesized polyamide-6/organoclay nanocomposites by in-situ polymerization, then PP-g-MAH/polyamide-6/organoclay nanocomposites were melt-blended in a twin-screw extruder. Mechanical properties, morphology and water absorption were

studied. Ahn and Paul, 2006, processed polyamide-6/EPR-g-MAH nanocomposites. Polyamide-6 and organoclay were mixed in a twin-screw extruder and the nanocomposites were blended with rubber in a single screw extruder.

This study is conducted to investigate nanocomposite formation in polyamide-6 as well as in impact modified polyamide-6 matrices using three different types of elastomers, ethylene-butyl acrylate-maleic anhydride (E-BA-MAH), ethylene-glycidyl methacrylate (E-GMA), ethylene-methyl acrylate-glycidyl methacrylate (E-MA-GMA) and three different types of organoclays, Cloisite® 15A, 25A and 30B. To our best knowledge, no study investigating the effect of organoclay surfactant type in polyamide-6/organoclay/elastomer ternary nanocomposites has been performed. Furthermore, rheological characterization of ternary nanocomposites is performed in this study.

Polyamide-6 has reactive functionality through amine and carboxyl end groups that are capable of reacting to form graft moieties with the elastomers used. E-BA-MAH elastomer has butyl acrylate and maleic anhydride functional groups. Maleic anhydride can react with the amine ends of polyamide-6 chains (Thomas and Groeninckx, 1999). E-GMA and E-MA-GMA elastomers have glycidyl methacrylate groups, which can react both with amine and carboxyl end groups (Tedesco et al., 2001). Also, reactions can take place between the terminal amino groups of polyamide-6 and ester groups of butyl acrylate and methyl acrylate (Raval et al., 1991). In addition to these reactions, some interactions may occur between the clay surfactant and elastomers. Chow et al., 2004, proposed a possible chemical interaction between polyamide-6, polypropylene, organophilic montmorillonite and maleic anhydride grafted polypropylene based on their experimental work.

In order to investigate the effects of component concentrations and addition order of the components on the morphology XRD, TEM and SEM analysis are used. FTIR-ATR technique is used to determine the reactions occurring between polyamide-6 and elastomers. Melting and crystallization behavior of the composites are studied by Differential Scanning Calorimetry (DSC). Flow characteristics are evaluated by

Melt Flow Index (MFI) measurements. Mechanical behavior of nanocomposites is evaluated by measuring impact strength, tensile properties (tensile strength, Young's modulus, % elongation at break) and flexural properties (flexural strength, flexural modulus). Thermomechanical properties are detected by Dynamic Mechanical Analysis (DMA) technique. The research is also focused on the rheological characterization of the polyamide-6 based ternary nanocomposites by parallel disk rheometer, since viscoelastic measurements are highly sensitive to the nanoscale structure of the hybrids and appear to be a powerful method to probe the developed structure of such materials.

CHAPTER 2

BACKGROUND INFORMATION

2.1 Composite Materials

Composite consists of two or more phases that are insoluble in each other on a macroscopic scale, whose mechanical performance and properties are designed to be superior to those of constituent materials acting independently. They may have unique advantages over monolithic materials, such as high strength, high stiffness, long fatigue life, low density, high corrosion and wear resistance, high thermal stability, insulation and conduction. Another important advantage of composite is reduction in life cycle costs (Daniel and Ishai, 1994).

The continuous constituent in the composite is termed as the *matrix*, which governs the mechanical properties of the materials, as the main load-bearing constituent. It can be ceramic, metallic or polymeric.

The second constituent is *reinforcement*, since it reinforces or enhances the mechanical properties of the matrix. In most cases, the reinforcement is stiffer, harder and stronger than the matrix.

Shape and dimensions and also composition of the reinforcements define the mechanical properties of composites. Reinforcements can be fibrous, particulate or laminar. Particulate fillers have dimensions approximately equal in all directions. The arrangement of the particulates may be random or with a preferred orientation.

Mostly, orientation of particles is random for practical purposes. Particulate composites have isotropic properties, whereas, fiber composites may be either isotropic or anisotropic; laminar composites always have anisotropic behavior.

Fibrous reinforcement's length is much greater than its cross-sectional dimension. Composites with continuous reinforcement are divided into two groups; such as single-layer composites (including composites having same orientation and properties in each layer) and multilayered (angle-ply) composites (Matthews and Rawlings, 1996).

The interaction of components at phase boundaries, associated with the existence of a thick interface, i.e. interphase, is also a parameter affecting the properties of polymer composites. It is often considered as a separate phase, which controls adhesion between the components, thus, it can play an important role in controlling the failure mechanisms, fracture toughness and overall stress-strain behaviour of the material (Daniel and Ishai, 1994).

The extent of adhesion at the polymer/filler interface may be related to various parameters associated with adsorption and wetting. Factors affecting adsorption are; interfacial forces (primary, secondary bonds), molecular orientation/conformation at the interface, and polymer mobility. Contact angle, surface tension, and substrate critical surface tension are among factors related to wetting (Xanthos, 2005).

2.1.1 Polymeric Composite Materials

The most common matrix materials for composites are polymeric; as their mechanical properties are inadequate for many structural purposes; also processing them does not involve high pressures and does not require high temperatures. The polymeric matrix material can be thermoset, thermoplastic or rubber.

Polymer composites are mixtures of polymers with inorganic or organic additives having certain geometries, such as fibers, flakes, spheres and particulates.

2.2 Nanocomposite Materials

Nanocomposites are particle-filled polymers, in which at least one dimension of the dispersed particles is in the nanometer range. There are three types of nanocomposites, depending on how many dimensions of the dispersed particles are in the nanometer range.

a. *Nanocomposites with isodimensional nanoparticles*; in which three dimensions of the dispersed particles are in the order of nanometers. Examples are semiconductor nanoclusters, spherical silica nanoparticles obtained by in situ sol-gel methods.

b. *Two dimensions of the dispersed particles are in nanometer scale* and the third is longer, such as in carbon nanotubes or cellulose whiskers. Polymeric nanocomposites containing single-walled or multi-walled carbon nanotubes have been extensively studied. At low loading, they show low density, high mechanical properties and electrical conductivity.

c. The third type of nanocomposites constitute fillers in the form of sheets of one to a few nanometers thick, to hundreds to thousands nanometer long. One only dimension is in the nanometer range. These kinds of composites are called *polymer-layered crystal nanocomposites*. These materials are obtained by the intercalation of a polymer inside the galleries of clay.

Amongst all potential nanocomposites that are discussed above, the third type has been more widely investigated because the intercalation chemistry of clays has been studied for a long time (Alexandre and Dubois, 2000).

These nanocomposites, when compared with conventional composite and base matrix material, exhibit transparency, low density, reduced flammability, low permeability, and enhanced thermal and mechanical properties because of the nanometer-size particles. In order to synthesize polymer-clay nanocomposites, both

thermoplastics and thermosets are used. Mostly used polymeric materials are polyamides, polyolefins, epoxy resins and unsaturated polyesters.

Commercially they are mostly used in automotive (truck mirror housing, engine cover, body and door panels), aerospace, telecommunication, tool housing, coating, electronic and packaging industries (Zanetti et al., 2000).

2.2.1 Layered Nanocomposite Structure with Polymeric Matrix

When layered clay is used, four main kinds of composites may be obtained depending on the method of preparation and the nature of the component used. Idealized structures of these nanocomposites are illustrated in Figure 2.1.

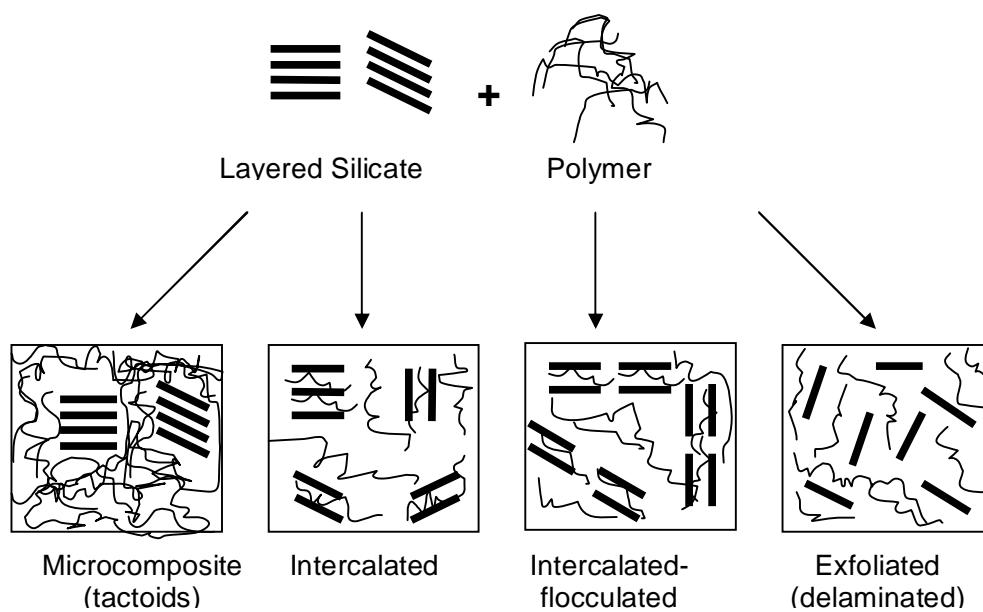


Figure 2.1 Scheme of different types of composite arising from the interaction of layered silicates and polymers

2.2.1.1 Microcomposite (Conventional) Composite

The polymer is unable to intercalate between the silicate sheets in this type of composite. The properties stay in the same range as traditional microcomposites. A phase-separated composite is obtained. Unseparated clay layers are called tactoids (Lan et al., 1995).

2.2.1.2 Intercalated Nanocomposite

In intercalated nanocomposites, the insertion of a polymer matrix into the layered silicate structure occurs in a crystallographically regular fashion, regardless of the clay to polymer ratio. The separation between clay platelets are less than 20-30 Å.

2.2.1.3 Flocculated Nanocomposite

Conceptually, flocculated nanocomposites are similar to intercalated nanocomposites. However, silicate layers are some times flocculated due to hydroxylated edge–edge interaction of the silicate layers (Ray and Okamoto, 2003).

2.2.1.4 Exfoliated (Delaminated) Nanocomposite

When the silicate layers are dispersed in a continuous polymer matrix, uniformly and completely, forming a monolithic structure on the microscale, an exfoliated structure is observed. Polymer separates the clay platelets by 80-100 Å or more. Usually, the clay content of an exfoliated nanocomposite is much lower than that of an intercalated nanocomposite (Alexandre and Dubois, 2000).

2.2.2. Synthesis of Polymer-Clay Nanocomposites

Many strategies have been considered to synthesize polymer-layered silicate nanocomposites. They contain four main processes, described as follows:

2.2.2.1 In-Situ Polymerization

In-situ polymerization can be used to synthesize polymer-clay nanocomposites. A monomer is admitted into a host compound (layered silicates, either natural or modified) containing interplanar spaces (channels or other cavities) and then polymerized. The obtained polymer is called *intercalated* if confined between layers (Zanetti et al., 2000). The polymerization reaction can be initiated by the help of an organic initiator or catalyst, curing agent, heat or radiation.

The driving force of the in-situ polymerization method is related to the polarity of monomer molecules. During the absorption of monomer into the layered silicates, polar monomer molecules are attracted owing to the high surface energy of the clay, thus they can diffuse between clay layers. When the monomer starts to react with the curing agent, polymerization reaction is initiated. The overall polarity of intercalated molecules is lowered. The organic molecules can finally delaminate the clay as this mechanism occurs (Kornmann, 2001). The process is illustrated schematically in Figure 2.2.

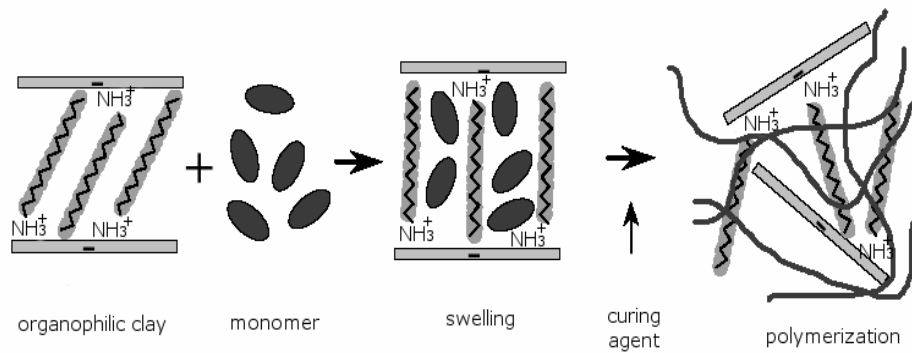


Figure 2.2 Schematic view of in-situ polymerization (Kornmann, 2001)

Nanocomposites based on polyamide-6 are prepared by Toyota Researchers (Usuki et al., 1995). Polymeric nanocomposites using epoxy, unsaturated polyester, polyurethane, and polyethylene terephthalate have been synthesized by this method (Kornmann, 2001).

2.2.2.2 Solution Approach

The layered silicate is exfoliated into single layers using a solvent in which the polymer (or a prepolymer in case of insoluble polymers) is soluble. Then the polymer is absorbed onto the delaminated silicate sheets. The solvent is evaporated and the sheets show an ordered multilayered structure (Alexandre and Dubois, 2000). This process can be seen schematically in Figure 2.3.

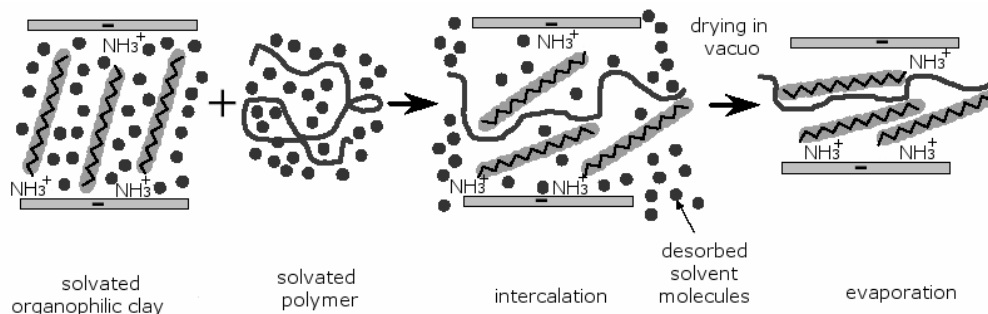


Figure 2.3 Schematic view of solution approach (Kornmann, 2001)

The entropy, which is gained by desertion of the solvent molecules, is the driving force of the solution approach. The decrease in conformational entropy of the intercalated polymer chains is compensated with the entropy gained by desorption of the solvent molecules. For that reason, large number of solvent molecules must be desorbed from the clay to accommodate the incoming polymer chains.

Nanocomposites based on polyimide, and high-density polyethylene and untreated clay based nanocomposites have also been synthesized using this method (Kornmann, 2001).

2.2.2.3 Melt Intercalation

Nanocomposites can be obtained by direct polymer melt intercalation, where molten polymer chains diffuse into the space between the clay layers or galleries (Vaia et al., 1993; Vaia et al., 1995; Vaia and Giannelis, 1997). The mixture is annealed above the glass transition temperature in either static or flow conditions, forming a nanocomposite (Figure 2.4). The main difference between melt processing and other preparation methods is that strong shear forces act on the system. Conventional polymer processing techniques are used to decrease the time to form

nanocomposites by breaking up clay particles. No solvent is required in this technique. If layer surfaces are sufficiently compatible with the polymer, and melt processing conditions are optimized, the polymer can crawl into the interlayer space, and form either intercalated or an exfoliated nanocomposite according to the degree of penetration.

Paul et al. demonstrated that degree of delamination and dispersion of clay layers is affected by clay chemical treatment, as well as type of extruder and its screw design (Cho and Paul, 2001; Dennis et al., 2001; Fornes et al., 2002). They conclude that chemical compatibility between the polymer matrix and clay treatment plays the dominating role for final morphology of nanocomposites. Figure 2.4 shows the parameters affecting clay morphology. When the clay treatment and the resin are compatible, almost any set of processing conditions can be used to produce exfoliated nanocomposites. If organoclay and polymer are marginally compatible, the optimization of the process conditions determines the final morphology of the nanocomposite.

The shear intensity in the extruder can only decrease the tactoid particles or the size of intercalated clay stacks when the chemical compatibility is not strong.

Figure 2.5 shows the possible clay delamination pathway. Clay stacks are decreased in height by sliding platelets apart from each other. When polymer chains enter the clay galleries, end of the platelets are pushed apart. This pathway does not require high shear intensity but involves diffusion of polymer into the clay galleries, which is driven by physical or chemical interactions. Diffusion is facilitated by residence time in the extruder. As more polymer enters and goes further in between clay platelets, they appear to peel apart, especially, near the edge of clay galleries. Top platelet in the stack may be able to curl away as polymer enters from the edge (Dennis et al., 2001).

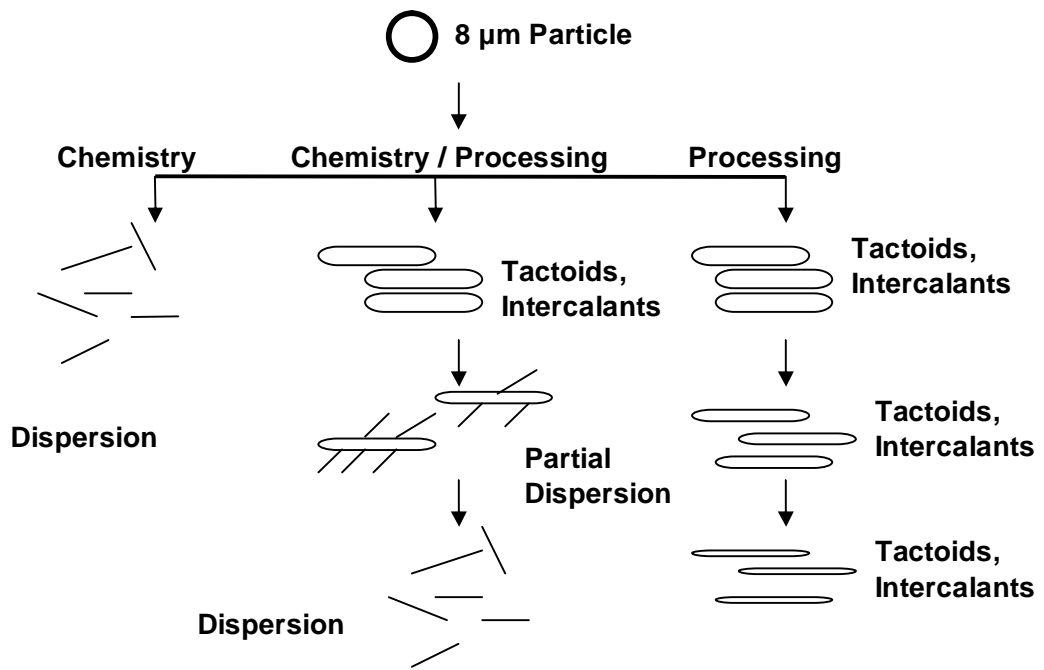


Figure 2.4 Three important parameter affecting clay dispersion and delamination (Dennis et al., 2001)

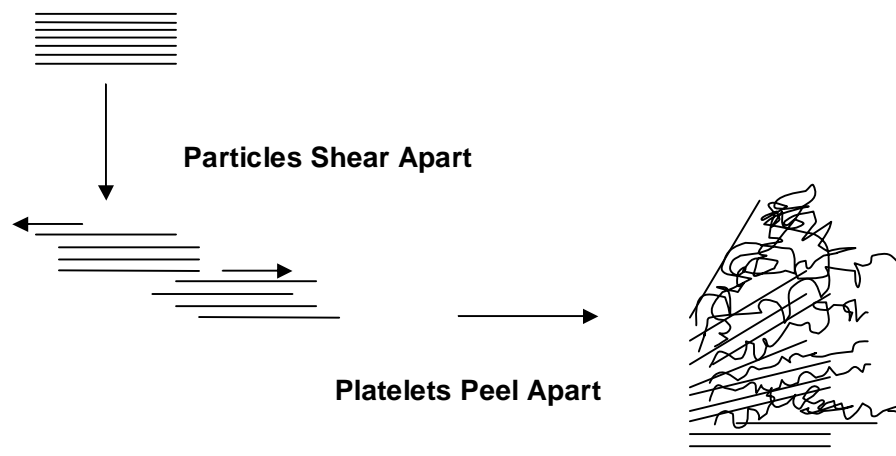


Figure 2.5 Effect of shear on clay platelets (Dennis et al., 2001)

The proposed driving force for melt intercalation is the enthalpic contribution of the polymer, layered silicate interactions during blending and annealing steps. The entropy loss associated with polymer melt confinement does not inhibit nanocomposite formation as it is compensated by the entropy gain associated with layer separation. These results in a zero change in total entropy of the system. Polymer chains exhibit a dramatic loss of conformational entropy during intercalation (Homminga et al., 2005).

A wide range of thermoplastics, from strongly polar polyamide-6 to polystyrene has been intercalated between clay layers by the help of melt intercalation (Alexandre and Dubois, 2000; Zanetti et al., 2000; Kornmann, 2001; Vaia et al., 1995; Cho and Paul, 2001)

2.2.2.4 Sol-Gel Technology

Sol-gel method consists in a direct crystallization of the silicate clays by hydrothermal treatment of a gel containing organics and organometallics, including polymer. As precursor for the clay, silica sol, magnesium hydroxide sol and lithium fluoride are used. This method, without needing the presence of the onium ion, has the potential of promoting the high dispersion of the silicate layers in a one-step process (Zanetti et al., 2000).

This type of nanocomposites is commonly based on polymer matrices reinforced by nanofillers, such as, zeolites, silica beads, and silica-titania oxides.

2.3 Fillers

Fillers add to enhance physical properties such as mechanical, thermal, flame retardancy, processing characteristics, electrical properties, surface properties, and ultraviolet absorption of a polymer or to lower the cost of a polymer. Additional functions may include degradability enhancement, barrier characteristics, anti-aging characteristics, bioactivity, etc (Xanthos, 2005).

They may be organic (carbon and graphite fibers, carbon black, carbon nanotube, wood flour, starch) or inorganic (glass based fillers, silicates, magnesium hydroxide, calcium carbonate and magnesium oxide), or metallic (boron, steel).

In polymer matrix composites, in order to modify the mechanical properties, high aspect ratio (glass fibers, mica, clay minerals, and carbon nanotubes) and low aspect ratio (talc, kaolin, CaCO_3 , glass spheres, and wood flour) fillers are used.

2.3.1 Clay Minerals

Clay is a natural, earthy, fine-grained material, which is composed essentially of alumina, silica, water, and appreciable quantities of iron, alkalis and alkaline earths (Grim, 1968). They have a sheet structure with a thickness of 1 nm and surfaces of 50-150 nm in one dimension, which are physically sorptive and chemically surface active. Several clay types carry an excess negative charge owing to internal substitution of Al^{+3} with Mg^{+2} , which makes clay slightly acidic. A clay deposit contains non-clay minerals as impurities, like quartz, volcanic dust, carbonate minerals, sulfates, sulfides and heavy minerals (Utracki 2004).

Silicon and oxygen are common in all clay minerals, combination with other elements, such as aluminum, magnesium, iron, sodium, calcium and potassium, and the ways in which the elements are linked leads to different structures.

The most important property of clays is their capacity to change volume by absorbing water molecules or other polar ions into their structure which is called swelling property. The cation exchange capacity (CEC) is measured as a function of the number of cations which can be measured on the clay surface once it is washed free of exchange salt solution, measured as milliequivalents per 100 g (meq/100g) (Velde, 1992).

Another important criterion is *basal spacing*, which is the distance between the sheet layers of the crystal structures. X-Ray Diffraction (XRD) patterns of clays give two categories of information on the crystallographic structure. The first one is *basal 001 reflection*, which is the distance between equivalent layers of basal oxygens or oxygen-hydroxyls in a clay structure. It depends on the nature of interlayer cations, the thickness and regularity of water layers between the silica sheets and the presence of other intercalated molecules (such as alkylammonium ions). The second one is *two-dimensional hk diffraction bonds*, which are characteristic of the structure of smectite layers themselves and independent from the basal spacing. These hk bonds are the same in all smectites.

For the preparation of polymeric nanocomposites, 2:1 layered or phyllosilicate type layered silicates such as, montmorillonite, bentonite, hectorite, and saponite are used.

2.3.2 Montmorillonite

Montmorillonite was discovered in 1847 by Damor and Salvetat in France, Montmorillon. Its 2:1 crystalline structure, which is proposed by Hoffmann et al., 1933, consists of two-dimensional layers where a central octahedral sheet of alumina or magnesia is fused to two external silica tetrahedron. Each layer is separated from other layers by van der Waals gaps, which are called gallery. The *d-spacing* or *basal spacing* is 1 nm. These layers form stacks with a regular van der Waals gap in between them, which is called *interlayer*. Isomorphic substitution within

the layers, such as Al^{3+} replaced by Mg^{2+} , generates negative charges. These negative charges are counterbalanced by alkali or alkaline earth cations situated in the interlayer (Alexandre and Dubois, 2000). Crystallographic structure of montmorillonite can be seen in Figure 2.6.

Montmorillonite can hold a large amount of water in its galleries which neutralizes the partial positive charges formed for each cation by ion-dipole interactions (Zanetti et al., 2000). The CEC (cation exchange capacity) of montmorillonite varies from 80 to 150 meq/100g.

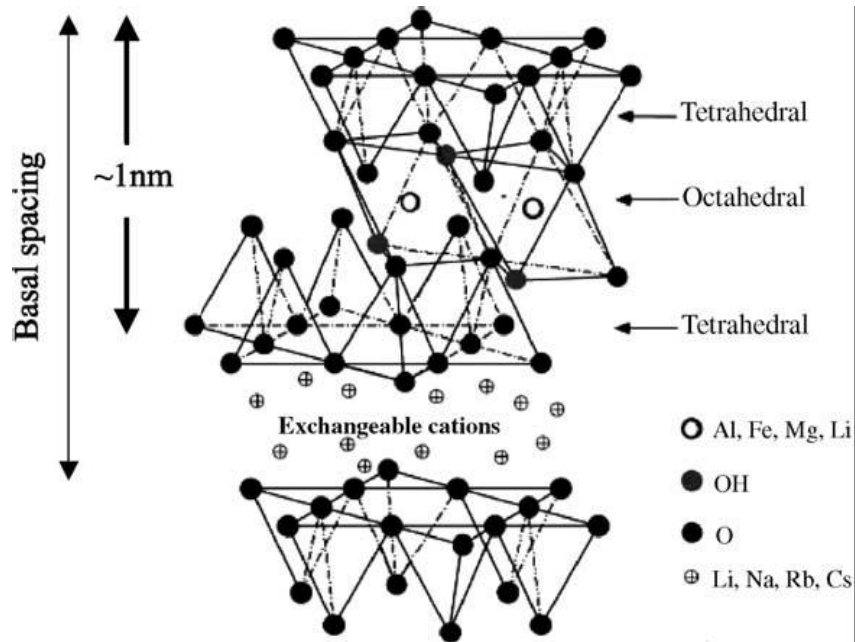


Figure 2.6 Idealized structure of montmorillonite (Ray and Okamoto, 2003)

2.3.2.1 Compatibilizing Agent

In order to make layered silicates miscible with other polymer matrices, one must convert the normally hydrophilic silicate surface to an organophilic one, to ease the intercalation of many engineering polymers. Wide variety of compatibilizing agents has been used in the synthesis of nanocomposites such as silanes, amino acids and alkylammonium ions.

Ion-exchange reactions with cationic surfactants including primary, secondary, tertiary, and quaternary alkylammonium or alkylphosphonium cations make the clay surface organophilic. Alkylammonium or alkylphosphonium cations in the organosilicates lower the surface energy of the inorganic host and improve the wetting characteristics of the polymer matrix, and result in a larger interlayer spacing. Additionally, the alkylammonium or alkylphosphonium cations can provide functional groups that can react with the polymer matrix, or initiate the monomer polymerization to improve the strength of the interface between the inorganic and the polymer matrix (Krishnamoorti et al., 1996; Ray and Okamoto, 2003).

The most widely used alkylammonium ions are based on primary alkylamines put in an acidic medium to protonate the amine function. Alkylammonium ions have basic formula such as $\text{CH}_3\text{-(CH}_2\text{)}_n\text{NH}_3^+$, n varies between 1 and 8. When the hydrated cations are ion-exchanged with alkylammonium ions, the result is a larger interlayer spacing as illustrated in Figure 2.7. The spacing increases by about 10 Å by this procedure.

Amino acids are one group of the compatibilizing agents, which consist of a basic amino group ($-\text{NH}_2$) and an acidic carboxyl group ($-\text{COOH}$). The clay becomes organophilic by cation-exchange between a cation (Na^+ , K^+ , ...) and $-\text{NH}_3^+$ function, which is produced by the transfer of a proton from the $-\text{COOH}$ group to the intramolecular $-\text{NH}_2$ group.

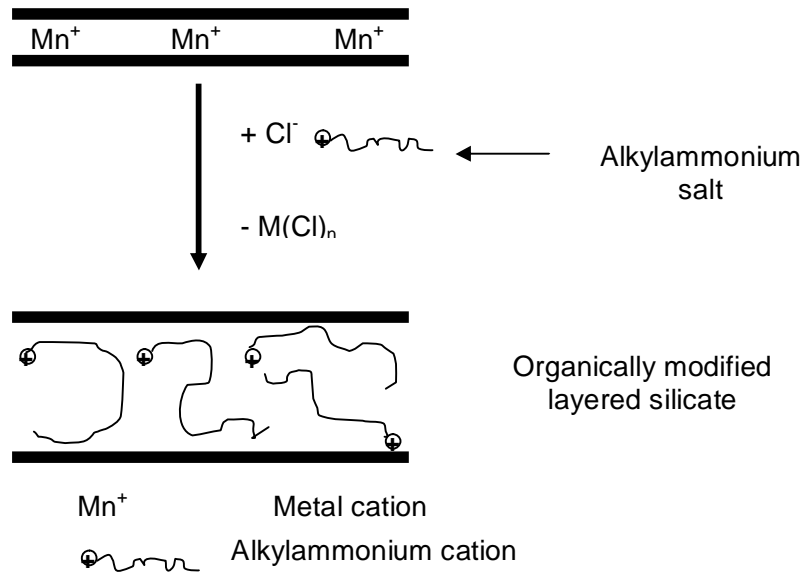


Figure 2.7 Schematic representation of a cation-exchange reaction between the silicate and an alkylammonium salt (Zanetti et al., 2000)

2.4 Polyamide-6

Polyamides, often also referred to as nylons, are polymers which contain the amide repeat linkage in the polymer backbone. They have high performance characteristics such as high melting points, good mechanical strength and ductility, as well as their excellent resistance to solvents, fatigue and abrasion.

The regularity of the amide linkages along the polymer chain defines two classes of polyamides.

a) Polyamides derived from the melt polymerization of ω -amino acids or lactam monomers, such as polyamide-6, polyamide-11 and polyamide-12. All the amide linkages have the same orientation along the backbone in this type.

b) Polyamides derived from the melt polymerization of salts of diamines and dicarboxylic acids, such as polyamide-6,6, polyamide-4,6, polyamide-6,12. Amide linkages alternate in orientation along the backbone. The R and R' groups in these structures are hydrocarbon radicals and can be aliphatic, aromatic, or mixed (Kirk-Othmer Encyclopedia of Chemical Technology, 2001).

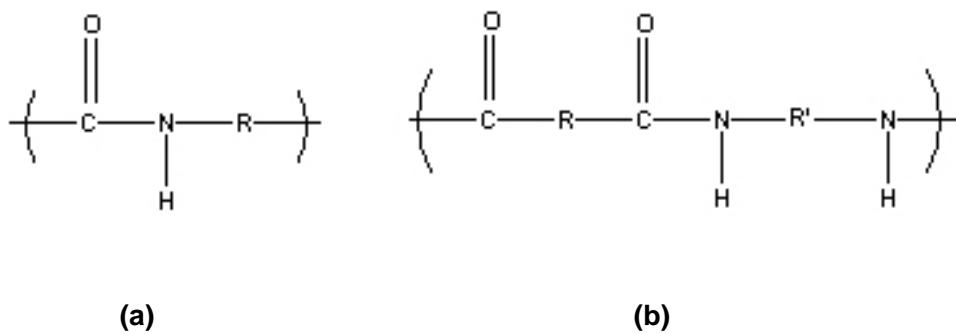


Figure 2.8 Chemical structures for (a) and (b) type polyamides

Repeating amide functionality (-CONH-) in their backbone imparts hydrogen bonding capability favoring strong intra- and inter-chain segmental association and crystallinity to polyamides. These hydrogen bonding and crystallinity characteristics of polyamides account for their generally high solvent resistance, heat resistance and mechanical strength.

Polyamide-6 and polyamide-6,6 are commercially more important because of their large volume production and widespread use in fibers, films, and engineering plastics applications, such as electrical, automotive and consumer industries.

2.4.1 Production of Polyamide-6

Wallace H. Carothers synthesized polyamide-6,6 in 1937 for DuPont Company, a few years later, polyamide-6,6 was commercialized as the first synthetic fiber. In less than one year, DuPont scientists and engineers built the first commercial plant in Seaford, Delaware, which began production in 1939.

In 1941 P. Schlack at I. G. Farbenindustrie in Germany issued a patent for polyamide-6, based on the polymerization of caprolactam.

Polyamide-6 is produced commercially by the ring-opening polymerization of ϵ -caprolactam. The polymerization reaction can be initiated by acids, bases or water. The hydrolytic process (initiated by water) is the most predominantly used method because it is easier to control and better adapted for large-scale production. Figure 2.9 shows this reaction schematically.

The hydrolytic process for polyamide-6 involves (a) ϵ -caprolactam and additives addition, (b) hydrolysis, (c) addition, (d) condensation, (e) pelletizing (for remelt processing), (f) leaching/extraction of monomers, (g) drying, and (h) packaging (for pellet sales). The polymerization process for polyamide-6 via the hydrolytic mechanism can be batch or continuous.

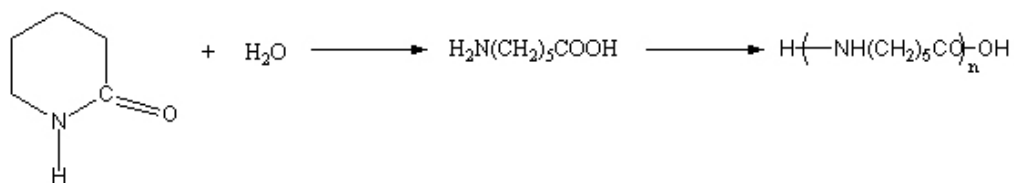


Figure 2.9 Ring-opening polymerization of ϵ -caprolactam

Batch processing of polyamide-6 is generally used only for the production of specialty polymers such as very high molecular weight polymer or masterbatch polymers for special additives. In a typical modern batch process, the caprolactam is mixed in a holding tank with the desired additives, and then charged to an autoclave with a small amount of water. During the two-stage polymerization cycle, the temperature is raised from 80 to 260 °C. In the first stage, water is held in the reactor, the pressure rises, and the hydrolysis and addition steps occur. After a predetermined time the pressure is released and the final condensation reaction step occurs. The molecular weight of the polymer can be increased by means of a vacuum finishing step. The final polymer is then drained, often with a forcing pressure of inert gas, through a die to form ribbons of polymer, which are then cooled in water and cut into pellets. High monomer and oligomer contents are extracted to increase the quality of final product. The pellets, are then, dried because excess water decreases the molecular weight of the polymer during subsequent melt processing.

In the continuous polymerization process for polyamide-6, the three steps of polymerization can be made to take place in a series of connected vessels or in a single long, vertical, tubular reactor (Kirk-Othmer Encyclopedia of Chemical Technology, 2001).

2.4.2 Properties of Polyamide-6

Polyamide-6 is a semi-crystalline material, which is a combination of ordered crystalline regions and more random amorphous areas having a much lower concentration of hydrogen bonding. The regular spatial alignment of amide groups allows a high degree of hydrogen bonding to be developed when chains are aligned together, giving rise to a crystalline structure in that region.

The crystalline regions contribute to the stiffness, strength, chemical resistance, creep resistance, temperature stability, and electrical properties; whereas

amorphous areas contribute to the impact resistance and high elongation at break (Mark, 2003).

2.4.2.1 Physical Properties of Polyamide-6

Strong hydrogen bonding between the chains and the crystal structure leads to high melting points. The melting point is mainly related to the degree of hydrogen bonding between the chains, which depends on the density of amide groups.

A characteristic property of a polyamide is the ability to absorb significant amounts of water. This is related to the polar amide groups around which water molecules can become coordinated. Water absorption is generally concentrated in the amorphous regions of the polymer, where it interrupts the hydrogen bonding, making it more flexible and increasing the impact strength. Moisture absorption is reduced with increasing length of aliphatic groups in the chain.

Polyamides are reasonably good insulators at low temperatures and humidities and are generally suitable for low frequency, moderate voltage applications.

Most nylons are self-extinguishing within a certain time scale under the conditions of the test.

The semicrystalline structure of most commercial polyamides imparts a high strength (tensile, flexural, compressive, and shear) as a result of the crystallinity and good toughness (impact strength) due to the amorphous region. The properties of the material are affected by the type of polyamide, molecular weight, moisture content, temperature, and the presence of additives. Strength and modulus (stiffness) are increased by increasing density of amide groups and crystallinity in aliphatic nylons; impact strength and elongation are decreased.

Generally, polyamides are notch-sensitive, and the unnotched impact strength is dramatically reduced when a notch or flaw is introduced into the material. The notch sensitivity can be reduced by incorporating impact modifiers. For the most effective of these materials, the notched impact strength approaches the unnotched impact performance of the unmodified resin.

Polyamides show particular advantages in abrasion resistance and coefficient of friction over most of the polymers.

2.4.2.2 Reactions of Polyamide-6

2.4.2.2.1 Acidolysis, Aminolysis, and Alcoholysis

When heated, polyamides react with monofunctional acids, amines, or alcohols, especially above the melt temperature, to undergo rapid loss of molecular weight, as in acidolysis (Figure 2.10) e. g. with acetic acid or aminolysis (Figure 2.11) with an aliphatic amine:



Figure 2.10 Acidolysis reaction of polyamides



Figure 2.11 Aminolysis reaction of polyamides

2.4.2.2.2 Ammonolysis

In a reaction closely related to aminolysis, ammonia reacts with polyamides, usually under pressure and at elevated temperatures. Lewis acids are effective catalysts for this reaction.



Figure 2.12 Ammonolysis reaction of polyamides

Polyamide can also undergo transamidation and transesteramidation reactions. Transamidation is the mutual exchange of chain fragments in a polyamide, whereas transesteramidation resembles transamidation, except that a polyamide is mixed with polyester rather than another polyamide. This is often a convenient route to produce polyesteramides.

2.4.2.3 Degradation of Polyamide-6

The polymerization of polyamide is a reversible process and the material can either hydrolyze or polymerize further, depending on the conditions. Below the critical moisture content, where rate of hydrolysis equal to the rate of polymerization, the melt polymerizes, and its viscosity increases. Above it, hydrolysis occurs with reduction in viscosity and molecular weight. Polyamides also undergo solid-state polymerization if they are heated above 100°C in the absence of water.

Although polyamides have good thermal stability, they tend to degrade in the melt when held for long periods of time or at high temperatures. Along with reduction of molecular weight, cross-linking also occurs, and the material eventually sets into an intractable gel. The general thermal decomposition reaction in polyamides, which is the cleavage of the amide bond to eventually form an olefin and a nitrile, results in chain cleavage and thus a loss in molecular weight.

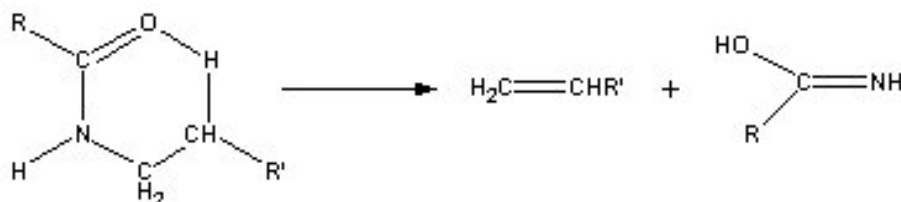


Figure 2.13 Thermal decomposition reaction in polyamides by cleavage of amide bond (Kirk-Othmer Encyclopedia of Chemical Technology, 2001)

Also, reequilibration reaction leading to production of the starting lactam can be viewed as the decomposition of the polyamides into cyclic products.

All polyamides are susceptible to oxidation, which involves the initial formation of a free radical on the alpha carbon next to the NH group, to form a peroxy radical with

subsequent chain reactions leading to chain scission and yellowing. Similarly, nylon parts exposed to high temperature in air lose their properties with time as a result of oxidation.

Polyamides can undergo a free-radical aging process when exposed to sunlight and UV rays.

2.4.2.4 Solvent Resistance of Polyamides

Generally, polyamides tend to be particularly resistant to nonpolar materials such as hydrocarbons. Resistance is least to strong acids and phenols which are most effective in disrupting the hydrogen bonding and they can sometimes dissolve the polyamide-6. They are soluble in formic acid, chloral hydrate, mineral acids, and fluorinated alcohols (Kirk-Othmer Encyclopedia of Chemical Technology, 2001).

2.4.3 Applications of Polyamides

Polyamides are used in automotive industry, especially in underhood (radiator end tanks, filter housings, fuel rails, fans, thermostat housings, valve and engine covers), interior (seat belt components, air bag containers, pedals, pedal boxes) and exterior (sun roof surrounds, door handles, fuel filler flaps) applications.

Another application area is electrical and electronics industry. Uses include cable ties, connectors, light housings, plugs, and switches.

Impact modified polyamides are also used in a number of consumer applications, power tool housings, such as sport equipments (ski boots, ski bindings, ice or roller skates, sports shoe soles, and tennis rackets). Other miscellaneous applications

include lighters, kitchen utensils, toothbrush filaments, chair bases and arms, sewing thread, and packaging film.

2.5 Impact Modification of Polyamide-6

To overcome the notched Izod impact strength deficiency, significant investigations have been made on the concept of impact modification of polyamides by blending it with various types of low-modulus, rubbery polymers. Through the development of reactive extrusion techniques, impact modification of polyamides involves polymer blending and compatibilization with rubbery polymers containing polar or reactive functionalities. Compatibility is defined as the ability of the rubber modifier to disperse itself into the polyamide matrix to form stable rubber particle dispersions with reduced interfacial tension and improved adhesion.

Generally, impact modified polyamides are based on blending polyamides with either;

- (a) polar functional, ethylene copolymers such as ethylene-ethyl acrylate, ethylene-acrylic acid copolymers, ionomers based on zinc neutralized, ethylene-methacrylic copolymers, and terpolymers, or;
- (b) reactive functional rubbers having a low T_g, such as the maleic-anhydride grafted ethylene-propylene copolymer or terpolymers (m-EPR or m-EPDM) and maleic anhydride grafted styrene-ethylene/butylene-styrene block copolymer rubbers (m-SEBS), often in combination with the unmodified EPR and SEBS rubbers (Akkapeddi, 2001).

The graft copolymer formed at the interface reduces the interfacial tension and increases the interfacial adhesion through the entanglement of the polymer chains enough to achieve a high level of fracture toughness and morphology stability.

The increase in impact strength of the reactive rubber modified polyamides is attributed to the small particle size of rubber dispersion and their adhesion to the polyamide matrix through the interfacially generated graft copolymer links. The studies established that there is a correlation between the rubber particle size and ductile-brittle transition in impact modified polyamides (Wu 1985; Wu 1988; Borggreve et al., 1987; Borggreve et al., 1989). Wu proposed that inter-particle distance (critical matrix ligament thickness) is a very important parameter defining the toughness mechanism. Small inter-particle distance suppresses craze or crack growth and facilitates the overlap of the stress fields around the adjacent rubber particles. By this way, local shear yielding is promoted and high impact energies are absorbed.

2.6 Polymer Processing

Polymer processing is the operation by which solid or liquid polymers are converted to finished products. It consists of several steps, such as, pre-shaping, shaping (molding, casting, die-forming, calendaring etc.), post-shaping (decorating, fastening, sealing, welding, dyeing, printing, etc.). Pre-shaping involves melting and softening, pressurization and pumping of the polymer melt, homogeneous mixing and devolatilization and stripping of residual monomers, solvents, contaminants (Xanthos, 2005).

In this study, extrusion and injection molding are used to process the nanocomposites.

2.6.1 Extrusion

Extrusion is defined as continuously forcing a molten material through a shaping device. Extruders are the most common machines in the plastics processing industry. They permit multiple process steps in a single machine, including melting, metering, mixing, reacting, side-stream addition, and venting. Schematic diagram of extrusion process is given in Figure 2.14.

There are three main extruder types; the screw extruder, the ram extruder and the drum or disk extruder. In a screw extruder, which used in this study, two screws rotate in a cylinder; the rotation of the screws creates a pumping action.

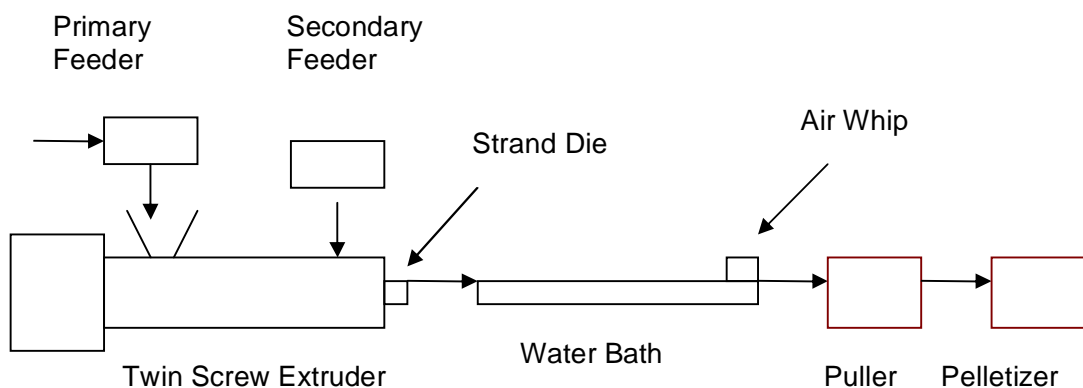


Figure 2.14 Schematic drawing of extrusion process

Twin-screw extruders are classified as being tangential and or intermeshing, and the latter as being counter or corotating. In co-rotating twin screw extruders, both screws rotate in the same direction. If the screws of a twin screw extruder rotate in opposite direction, it is called counter-rotating twin screw extruder. Generally, twin screw extruders are intermeshing. These extruders are generally supplied with slip-on conveying and kneading screw elements and segmented barrels. These elements

give the processor improved mixing and pumping versatility (Mark, 2003). In Figure 2.15 drawing of intermeshing corotating twin-screw extruder is given. In this figure, A stands for motor, B is gear box, C is feed port, d is clam shell barrel, E is vent port, F is for screw shafts, G shows conveying screws, H kneading paddels, I barrel valve and J is blister rings.

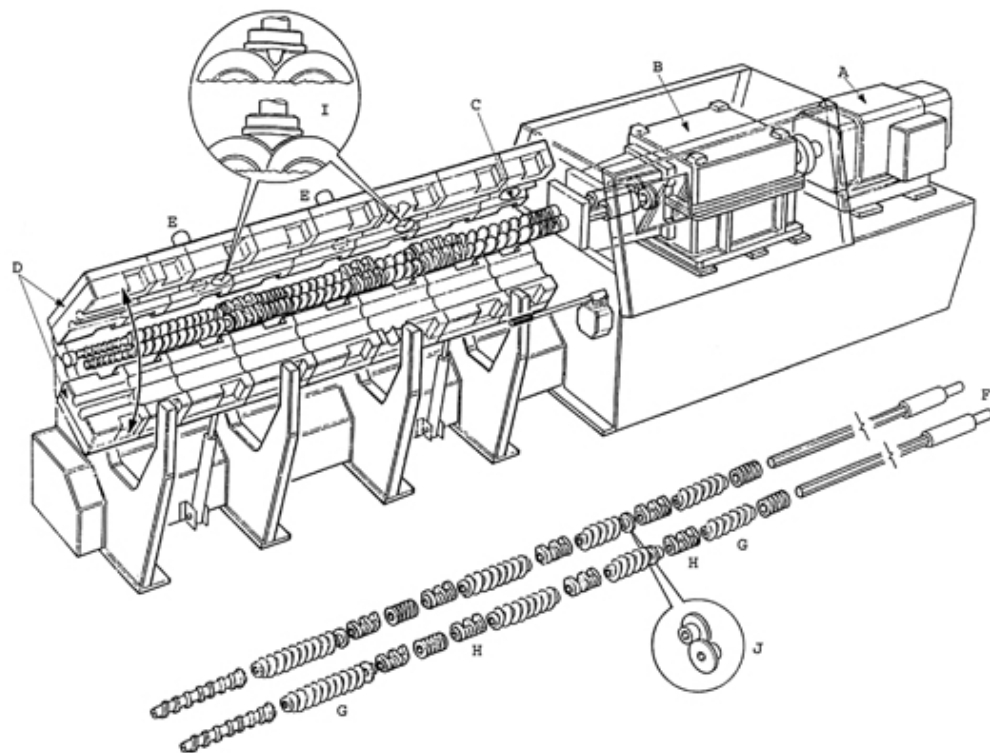


Figure 2.15 Intermeshing corotating twin-crew extruder ((Kirk-Othmer Encyclopedia of Chemical Technology, 2001).

2.6.2 Injection Molding

In injection molding, a molten thermoplastic is injected under high pressure into a steel mold. After the plastic solidifies, the mold is opened and a part in the shape of the mold cavity is removed.

The injection molding machine consists of an injection unit and a clamp unit. In industry, the injection unit consists of usually a reciprocating screw extruder that melts the plastic and injects it into the mold. The melt polymer is rammed into a mold under high pressure by a hydraulic power. The clamp unit opens, closes, and holds the mold closed against the pressure of injection (Mark, 2003).

2.7 Characterization of Polymer-Clay Nanocomposites

In order to observe the effects of component concentrations and addition order of the components on the final properties and morphology; spectroscopic, thermal, mechanical, rheological and thermomechanical characterization methods are used.

2.7.1 X-Ray Diffraction (XRD) Analysis

X-ray diffraction is used to define the crystallographic structure determination, such as crystal lattice spacings, crystal size and perfection, the crystallinity and the degree of preferred orientation in polycrystalline samples.

XRD equipments are mainly divided into two types, wide angle (WAXD) and small angle (SAXD). Since newer WAXD instruments are able to scatter at low angles, they are commonly used to probe the nanocomposite structure and to study the kinetics of polymer melt intercalation. By observing the position, shape, and intensity

of basal reflections from the distributed silicate layers, the nanocomposite structure may be identified. For example, in an exfoliated nanocomposite, the extensive layer separation associated with the delamination of the original silicate layers in the polymer matrix results in the disappearance X-ray peaks. On the other hand, for intercalated nanocomposites, the finite layer expansion associated with polymer intercalation results in the appearance of a new basal reflection corresponding to larger gallery height.

X-ray is a form of electromagnetic radiation that has high energy and short wavelength i.e., on the order of the atomic spacing for solids. When a beam of x-rays impinges on a solid material, a portion of this beam will be scattered in all directions by the electrons associated with each atom or ion that lies within the beam's path.

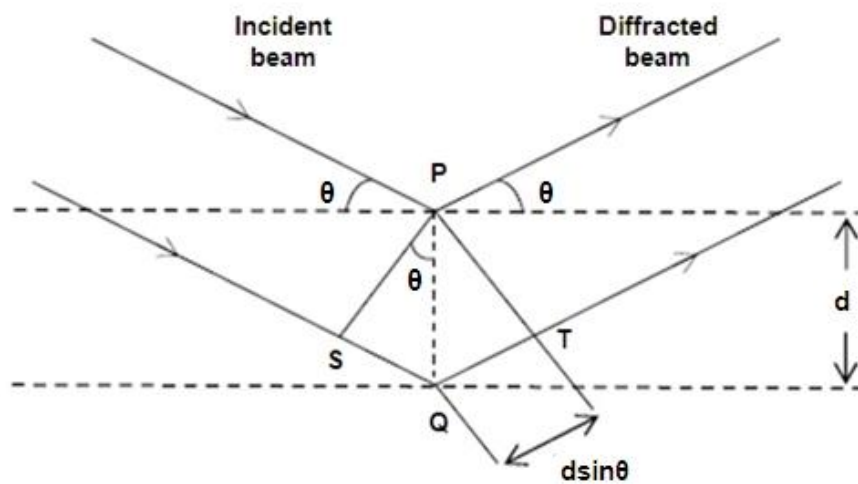


Figure 2.16 Diffraction of x-rays by planes of atoms (Callister, 1997)

Figure 2.16 shows the two scattering planes of atoms, which may be either two consecutive clay layers or other crystallographic planes of the layers themselves that are separated by the interplanar spacing. A parallel beam of x-rays of wavelength λ

is incident on these two planes at an angle θ . Two rays in this beam are scattered by atoms. Constructive interference of the scattered rays occurs also at an angle θ to the planes. The distance between SQ+QT is equal to a whole number, n , of wavelengths. The angles opposite SQ and QT are also θ , as the direction of d is normal to the planes, and the wave normal is normal to the wavelets. Thus, $\sin \theta = SQ/d = QT/d$ so that $(SQ+QT) = 2d\sin\theta$ (Callister, 1997).

The condition for diffraction, which characterized by Bragg's Law, is;

$$n\lambda = 2d\sin\theta \quad (2.1)$$

2.7.2 Transmission Electron Microscopy (TEM)

During XRD analysis, the disappearance of organoclay peak does not always mean that exfoliated nanocomposite is produced. Many factors, such as concentration and orientation of the clay, sampling problems and poor calibration of most XRD instruments at very low angles can influence the XRD patterns of layered silicates, thus, TEM analysis is needed. TEM allows a qualitative understanding of the internal structure, distribution of the various phases, and views of the defect structure through direct visualization at levels down to atomic dimensions.

TEM, as seen in Figure 2.17, is composed of an illumination system, a specimen stage, an objective lens system, magnification system, data recording system and chemical analysis system. The electron gun is used in the illumination system. It also includes condenser lenses that are vitally important for forming a fine electron probe. The objective lens is the heart of a TEM, which determines the limit of image resolution. The magnification system consists of intermediate lenses and projection lenses, and it gives a magnification up to 1.5 million. The data recording system tends to be digital with the use of a charge coupled device (CCD), allowing

quantitative data processing and quantification. Finally, chemical analysis system is the energy dispersive X-ray spectroscopy (EDS) and electron energy-loss spectroscopy (EELS) (Wang, 2001).

Since solid materials are highly absorptive to electron beams, specimen to be examined must be prepared in the form of a very thin foil (less than 100 nm thick). By this way, appreciable fraction of the incident beam transmission through the specimen is ensured (Callister, 1997).

2.7.3 Scanning Electron Microscopy (SEM)

In SEM analysis, the surface of a specimen to be examined is scanned with an electron beam, and the reflected (or back-scattered) beam of electrons is collected, and then displayed at the same scanning rate on a cathode ray tube. The image on the screen, which may be photographed, represents the surface features of the specimen. The surface must be electrically conductive; therefore a very thin metallic surface coating must be applied to nonconductive materials. Magnifications ranging from 10 to in excess of 50000 diameters are possible (Callister, 1997).

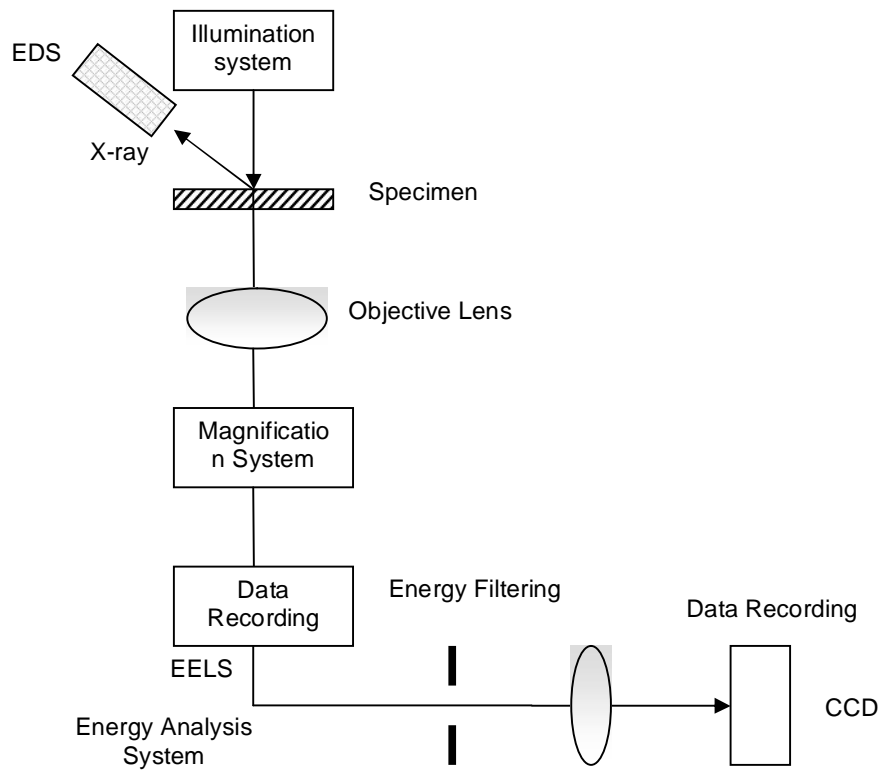


Figure 2.17 Schematic structure of a transmission electron microscope (Wang, 2001)

2.7.4 Spectroscopic analysis

2.7.4.1 Fourier Transform Infrared Spectroscopy - Attenuated Total Reflectance (FTIR-ATR) Analysis

Fourier transform infrared (FTIR) is one of the most commonly used analysis methods for determining the composition of polymers. It's used in the analysis of

fingerprinting contaminants, characterizing chemical property gradients, or detecting physical property anisotropy.

FTIR technique corresponds to the vibrational energies of atoms or specific groups of atoms within a molecule as well as rotational energies. It identifies components by comparing the spectrum of a sample to reference spectra.

An IR spectrum is commonly obtained by passing IR radiation through a sample and determining what fraction of the incident radiation is absorbed at a particular energy. The energy, at which any peak in an absorption spectrum appears, corresponds to the frequency of a vibration of a part of a sample molecule.

For a molecule to show IR absorptions, it must possess a specific feature: An electric dipole moment of the molecule must change during the movement. The interactions of IR radiation with matter may be understood in terms of changes in molecular dipoles associated with vibrations and rotations. The atoms in molecules can move relative to one another, i.e., bond lengths can vary or one atom can move out of its present plane. This is a description of stretching and bending movements, i.e. vibrations. Vibrations can involve either a change in bond length (stretching) or bond angle (bending). Some bonds can stretch in-phase (symmetrical stretching) or out-of-phase (asymmetric stretching). If a molecule has different terminal atoms the amount of coupling will vary. Varying proportions of the stretching motion of each group is observed.

Reflectance techniques may be used for samples that are difficult to analyze by the conventional transmittance methods. Attenuated total reflectance spectroscopy (ATR) utilizes the phenomenon of total internal reflection (Figure 2.18). ATR-FTIR can be readily performed on most commercial FTIR spectrometers through the use of an attachment for ATR spectroscopy. In these devices, a beam of radiation entering a crystal will undergo total internal reflection when the angle of incidence at the interface between the sample and crystal is greater than the critical angle. The critical angle is a function of the refractive indices of the two surfaces. The beam penetrates a fraction of a wavelength beyond the reflecting surface, and when a

material that selectively absorbs radiation is in close contact with the reflecting surface, the beam loses energy at the wavelength where the material absorbs. The resultant attenuated radiation is measured and plotted as a function of wavelength by the spectrometer and gives rise to the absorption spectral characteristics of the sample. The depth of penetration in ATR is a function of wavelength, λ , the refractive index of the crystal, n_2 , and the angle of incident radiation, θ . The depth of penetration, d_p , for a nonabsorbing medium is given by the following formula:

$$d_p = (\lambda/n_1)/(2\pi[\sin^2\theta - (n_1/n_2)^2]^{1/2}) \quad (2.2)$$

where n_1 is the refractive index of the sample. The crystals used in ATR cells are made from materials that have low solubility in water and are of a very high refractive index. Such materials include zinc selenide (ZnSe), germanium (Ge), and thallium/iodide (KRS-5) (Kirk-Othmer Encyclopedia of Chemical Technology, 2001).

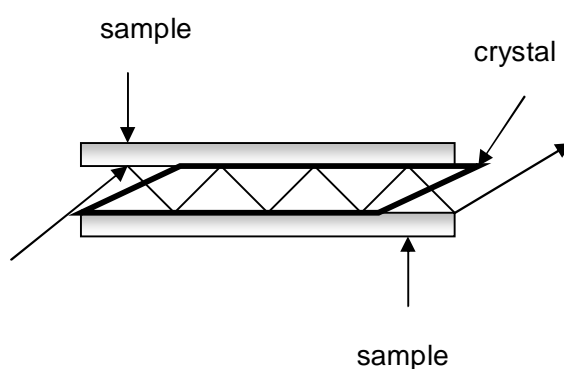


Figure 2.18 Attenuated total reflectance cell

2.7.5 Thermal Analysis

2.7.5.1 Differential Scanning Calorimeter (DSC) Analysis

Differential scanning calorimetry (DSC), is a technique of nonequilibrium calorimeter, in which the heat flow into or away from the polymer is compared with the heat flow into or away from a reference which is measured as a function of temperature. In DSC, an average-temperature circuit measures and controls the temperature of sample and reference holders (one that undergoes no transitions in the temperature range of interest) to conform to a predetermined time-temperature program. This temperature is plotted on one axis of an x-y recorder. At the same time, a temperature-difference circuit compares the temperatures of the sample and reference holders and proportions power to the heater in each holder so that the temperatures remain equal. The thermodynamic property monitored here is the enthalpy. When the sample undergoes a thermal transition, the power to the two heaters is adjusted to maintain their temperatures, and a signal proportional to the power difference is plotted on the second axis of the recorder. The area under the resulting curve is a direct measure of the heat of transition. T_g and T_m of polymers can easily be determined by using this method (Billmeyer, 1984; Rosen, 1982).

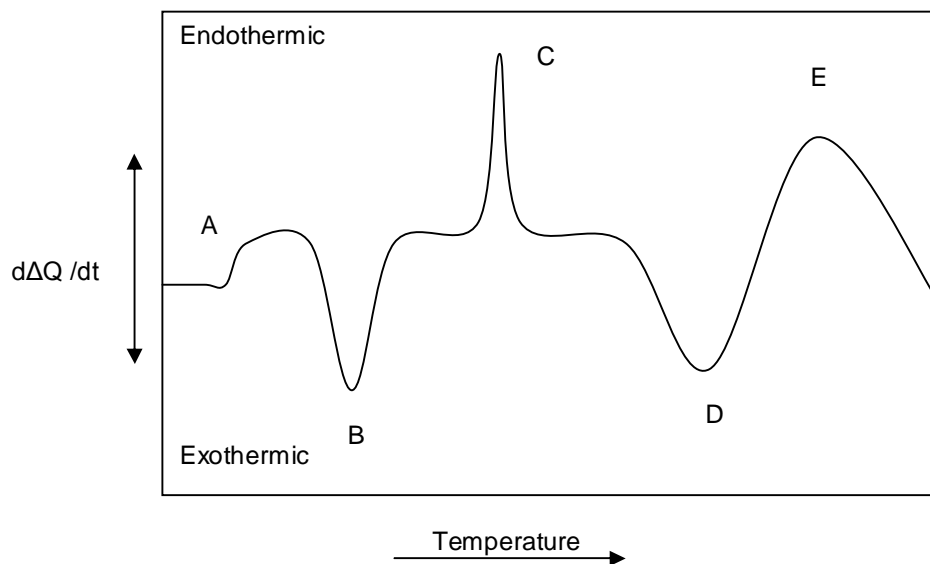


Figure 2.19 Idealized DSC thermogram of a polymer

Figure 2.19 shows an idealized DSC diagram illustrating types of transitions. The glass-transition, T_g , is the transition from the metastable glassy state to the liquid or rubbery state. It appears as an endothermic step change (A), and commonly the midpoint is taken as T_g . Crystallization exotherm (B), melting endotherm (C), reaction exotherm (D), and decomposition (E) follow the glass-transition temperature. Thermodynamically, melting is the temperature at which the crystal and the melt are in equilibrium. Melting peak temperature, T_m , is regarded as the highest temperature at which the largest and most perfect crystals disappear. The decomposition of polymeric material in an inert atmosphere is usually endothermic; however, it may show exothermic processes due to the oxidation reaction in the presence of air (Simon, 2003).

2.7.6 Flow characteristics

2.7.6.1 Melt Flow Index (MFI) Test

The melt index, also known as melt flow rate (MFR) measures the rate of extrusion of a thermoplastic material through an orifice of specific length and diameter, under prescribed temperature and load conditions. The test is especially used to measure the uniformity of the flow rate of material (Shah, 1998).

During the characterization experiments, melt index apparatus (Figure 2.20) is preheated to a specified temperature. The material is loaded into the cylinder and a specified weight is placed on a piston. Then the material is allowed to flow through the die. Depending on the flow rate of materials, at different time intervals, samples are taken. The extrudate is weighed and MFI values are reported in grams per ten minutes.

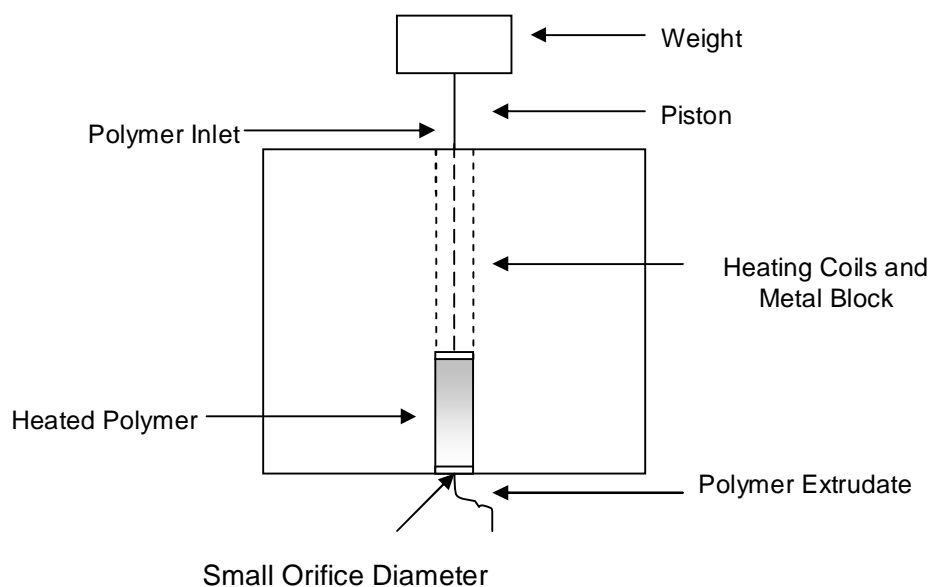


Figure 2.20 Schematic drawing of melt flow index apparatus

2.7.7 Mechanical Analysis

2.7.7.1 Impact Properties

Impact tests are high-speed fracture tests that measure the energy to break a specimen. In the Izod and Charpy impact tests a pendulum with hammerlike weight strikes a specimen (a notched or unnotched bar), and the energy required to break the specimen is determined from the loss in kinetic energy of the weight (ISO 179-2:1997).

In the Charpy experiment, the specimen is supported on both ends and struck in the middle. The notch is on the side away from the striker. The hammer is released and allowed to strike through the specimen (see Figure 2.21).

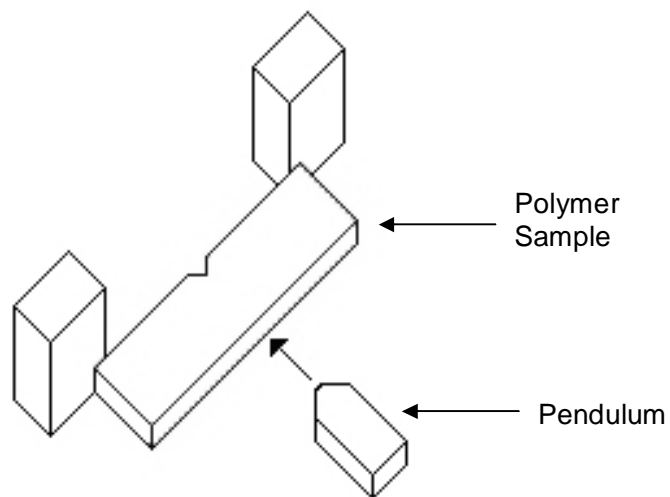


Figure 2.21 Schematic drawing of notched Charpy impact test

2.7.7.2 Tensile Properties

In tensile tests, a specimen is deformed, usually to fracture, with a gradually increasing tensile load that is applied uniaxially along the long axis of a specimen.

The tensile test machine is designed to elongate the specimen at a constant rate, and to continuously and simultaneously measure the instantaneous applied load (with a load cell) and the resulting elongations.

The output of such a tensile test is recorded on a strip chart as load or force versus elongation. Load and elongation are normalized to the respective parameters of *engineering stress* or *engineering strain*.

Engineering stress σ is defined by the relationship:

$$\sigma = \frac{F}{A_0} \quad (2.3)$$

In which F is the instantaneous load applied perpendicular to the specimen cross section in Newtons, and A_0 (mm^2) is the original cross-sectional area before any load is applied.

Engineering strain ε is defined according to:

$$\varepsilon = \frac{l_i - l_0}{l_0} = \frac{\Delta l}{l_0} \quad (2.4)$$

where l_0 is the initial gauge length (mm), l_i is instantaneous length (mm) and ΔL is the change in sample length (mm).

Tensile strength (MPa) is the maximum tensile stress, which a material is capable of developing. It is calculated from the maximum load carried during a tension test and the original cross-section area of the specimen (Callister, 1997).

Tensile Modulus (Young's Modulus) (MPa) is the ratio of stress to corresponding strain below the proportional limit of a material (ASTM D638-03, 2004).

$$\sigma = \epsilon E \quad (2.5)$$

2.7.7.3 Flexural Properties

In flexural tests, a rod specimen having either a circular or rectangular cross-section is bent until fracture following a three-or-four-point loading technique.

In three-point loading, which applied in this thesis, the top surface of the specimen is placed in a state of compression, whereas the bottom surface is in tension. Stress is computed from the specimen thickness, the bending moment, and the moment of inertia of the cross section. The maximum tensile stress exists at the bottom specimen surface directly below the point of load application.

The maximum stress using the flexure test is known as the *flexural strength*. For a rectangular cross-section, the flexural strength is equal to:

$$\sigma_{fs} = \frac{3F_f L}{2bd^2} \quad (2.6)$$

where F_f is the load (N), L is the distance between support points (mm), b is the width of the specimen (mm), and d is the depth of specimen (mm).

The maximum strain in the outer fibres that occurs at midspan, is calculated as follows:

$$r = \frac{6Dd}{L^2} \quad (2.7)$$

where r is the maximum strain in the outer fibers (mm/mm), D is the maximum deflection of the center of the beam (mm), L is support span (mm) and d is the depth of specimen (mm). Strain at break was calculated in the thesis, so D was taken as the point where specimen breaks.

Tangent modulus of elasticity (flexural modulus) is the ratio, within the elastic limit of stress to corresponding strain and shall be expressed as MPa. It is calculated by drawing a tangent to the steepest initial straight-line portion of the load-deflection curve and by using Equation (2.8)

$$E_B = \frac{L^3 m}{4bd^3} \quad (2.8)$$

where E_B is modulus of elasticity in bending (MPa), L is the length of support span (mm), b is the width of the beam tested (mm), d is the depth of beam tested (mm), and m is the slope of the tangent to the initial straight-line portion of the load deflection curve, N/mm of deflection (ASTM D790-03, 2003).

2.7.8 Thermomechanical Properties

2.7.8.1 Dynamic Mechanical Analysis (DMA)

In the dynamic mechanical analysis (DMA), the sample is deformed cyclically, usually under forced vibration conditions. By monitoring the stress-strain relationship while changing temperature, information can be obtained about the relaxation behavior of the test piece. There are some loading options for dynamic mechanical testing, such as reversed bending, axial tension, torsion and shear. The technique used in this study is bending. Schematic drawing of bending mode can be seen in Figure 2.22. During the tests, applied vibration to the sample is usually sinusoidal. If the amplitude is sufficiently small, a sinusoidal load gives rise to a sinusoidal deformation (Campbell et al., 2000).

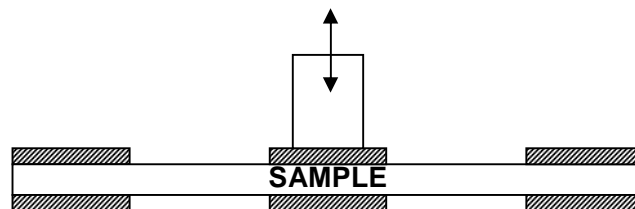


Figure 2.22 Schematic drawing of bending mode

Polymers are typically viscoelastic in nature, and have a dynamic response to the oscillatory stress, which is controlled by the viscous component. Strain continues to increase until the stress is removed and is not recoverable. The other component is the elastic response, which reacts instantaneously to the applied stress and is completely recovered if the stress is removed. In polymeric materials, strain lags behind the stress, by an amount δ . Phase angle (δ) depends on the relative elastic

and viscous nature of the material. It is a measure of the viscous response of the material to dynamic strain.

A sinusoidal stress applied to an ideal elastic material produces a sinusoidal strain proportional to the stress amplitude and in phase with it. For ideal viscous materials the stress and strain are out of phase by 90°. The amplitude of the deformation (strain) in response to the stress is proportional to that of the stress, but lags behind the strain curve by some angle, δ , between 0 and 90°, depending on the elastic/viscous characteristic of the material. This behavior is usually analyzed by the use of complex variables to represent stress and strain. These variables, complex stress and complex strain, ie, σ^* and ε^* , respectively, are vectors in complex planes. They can be resolved into real (in phase) and imaginary (90° out of phase) components (Kirk-Othmer Encyclopedia of Chemical Technology, 2001).

For a tensile strain, which is a sinusoidal function of time, t, the strain function may be expressed as:

$$\varepsilon^* = \varepsilon^0 \exp(i\omega t) \quad (2.9)$$

where, ε^* and ε^0 are complex strain and the amplitude of the applied strain, respectively, ω is the angular frequency of oscillation (rad/s).

The stress resulting from the applied sinusoidal strain is expressed as follows:

$$\sigma^* = \sigma^0 \exp[i(\omega t + \delta)] \quad (2.10)$$

where σ^* and σ^0 are complex stress and the amplitude of the stress response, respectively, δ is the phase angle between the stress and strain.

Complex modulus, E^* is described as the ratio of complex stress to complex strain as:

$$E^* = \frac{\sigma^*}{\varepsilon^*} = \left(\frac{\sigma^0}{\varepsilon^0} \right) \exp(i\delta) \quad (2.11)$$

The complex modulus can be resolved into two components, which one is *in phase* (E') and the other one is *out of phase* (E'') with the applied strain. Applying necessary mathematical substitutions into Equation 2.11 gives,

$$E^* = \left(\frac{\sigma^0}{\varepsilon^0} \right) \cos \delta + i \left(\frac{\sigma^0}{\varepsilon^0} \right) \sin \delta \quad (2.12)$$

Here;

E' is called storage modulus, which proportional to the peak energy that is stored per cycle of oscillation in the material, expressed as;

$$E' = \left(\frac{\sigma^0}{\varepsilon^0} \right) \cos \delta \quad (2.13)$$

and E'' is called loss modulus, that associated with the dissipation of energy as heat, expressed as;

$$E'' = \left(\frac{\sigma^0}{\varepsilon^0} \right) \sin \delta \quad (2.14)$$

The ratio of loss and storage moduli gives $\tan \delta$, which is a measure of the ratio of energy dissipated to energy stored given by;

$$\tan \delta = \frac{\sin \delta}{\cos \delta} = \frac{E''}{E'} \quad (2.15)$$

The two primary uses are for determination of morphology including glass transitions and meltings, and checking polymer behavior at conditions simulating the end use while maintaining temperature equilibrium. This method detects α (first-order or glass) transitions, β (side-chain motions) transitions, and γ (crankshaft rotation of main-chain segments or single bond flips) transitions, and has about a 1000 times greater sensitivity than DSC for amorphous polymers (Kirk-Othmer Encyclopedia of Chemical Technology, 2001).

2.7.9 Rheological Properties

Rheology is the science of the deformation and flow of matter. It is concerned with the response of materials to applied stress. That response may be irreversible viscous flow, reversible elastic deformation, or a combination of the two. Viscoelastic materials show both flow and elasticity.

The dynamic response of viscoelastic materials to cyclic stresses or strains is also important, partly because cyclic motion occurs in many processing operations and applications, and partly because so much rheological information can be gained from dynamic measurements. By subjecting a specimen to oscillatory stress and determining the response, both the elastic and viscous or damping characteristics can be obtained. Elastic materials store energy, whereas liquids dissipate it as heat. This dissipation results in highly damped motion. Viscoelastic materials exhibit both

elastic and damping behavior. The latter causes the deformation to be out of phase with the stress applied in the dynamic measurement.

The theory behind is mentioned in Section 2.9.8, but the nomenclature is different here.

Complex dynamic modulus is represented as G^* , instead of E^* in DMA analysis, which is the ratio of the complex stress and complex strain. G' (dynamic storage modulus) and G'' (dynamic loss modulus) are used rather than E' and E'' .

The value of G' is high when a polymer is in its glassy state, but drops with increasing temperature as the polymer goes through the glass transition and becomes soft and rubbery. For viscoelastic melts it is common practice to associate G' with the ability of a melt to recover from a deformation. G'' is associated with viscous energy dissipation, ie, damping. The ratio of G'' and G' gives loss tangent;

$$\tan \delta = \frac{G''}{G'} \quad (2.16)$$

Rheometers may be separated into three main types: capillary, rotational, (bob and cup), parallel-plate, cone and plate, etc.) and, moving body (falling ball viscometer).

Plate-plate rheometer is used in this study, instead of cone and plate rheometer, since slinging of material from the gap is observed in the latter.

The shear rate, cm^{-1} , caused by the torsional flow between parallel plates (see Figure 2.23), is given by Equation 2.17, where R is the radius of the plate and h the distance between the two plates and Ω is the relative angular velocity in radians per second (Barnes et al., 1989).

$$\dot{\gamma} = \frac{\Omega R}{h} \quad (2.17)$$

It is this shear rate that finds its way into the interpretation of experimental data for torsional flow.

The viscosity is given by equation 2.18, where T is the torque.

$$\eta = \frac{T / 2\pi R^3}{\dot{\gamma}} \left[3 + \frac{d \ln(T / 2\pi R^3)}{d \ln \dot{\gamma}} \right] \quad (2.18)$$

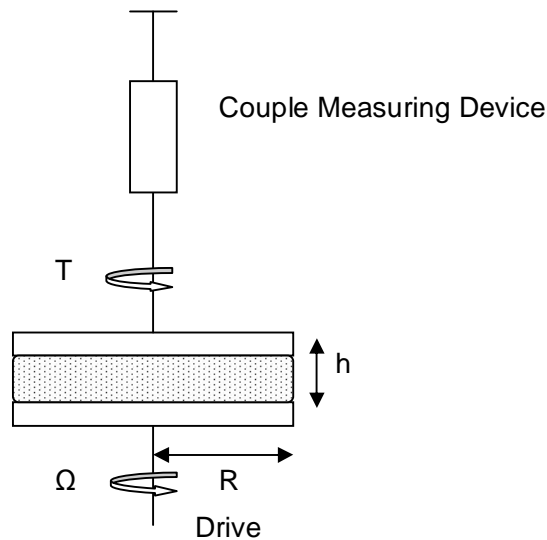


Figure 2.23 Cross-sectional diagram of torsional parallel-plate rheometer

2.8 Previous Studies

2.8.1 Previous Studies on Polyamide-6/Clay Nanocomposites

Investigations on nanocomposite materials were started by Toyota researchers in which polyamide-6/clay nanocomposites were obtained by the polymerization of ϵ -caprolactam in the interlayer gallery region of organoclay. The polyamide-6 nanocomposite samples showed superior strength, modulus, heat distortion temperature, and water and gas barrier properties in comparison to pure polyamide-6. Their composite showed major improvements in physical and mechanical properties even at very low clay content. With the addition of only 4 % of delaminated clay, tensile strength and modulus of polyamide 6 increased by 55 and 90 %, respectively. It was concluded that the enhancement in mechanical properties could be due to the large surface area and to the ionic bonds between the organic polymer and the inorganic silicate (Kojima et al., 1993; Kojima et al., 1994; Usuki et al., 1995).

Liu et al. in 1999 processed polyamide-6/clay nanocomposites by melt intercalation. XRD and DSC results showed that the crystal structure and crystallization behavior of the nanocomposites were different from polyamide-6. Mechanical and thermal testing showed that the properties of the nanocomposites were superior to polyamide-6, in terms of the heat-distortion temperature, strength, and modulus without sacrificing their impact strength.

Cho and Paul, 2001, prepared nylon-6/organoclay nanocomposites by melt compounding using a conventional twin screw extruder. The mechanical properties and morphology of these nanocomposites were compared with the nanocomposites prepared by in-situ polymerization.

Fornes et al., 2001 investigated the effect of matrix molecular weight in nylon 6 nanocomposites. Nanocomposites based on higher molecular weight polyamides

yielded superior composite properties, having higher degrees of clay exfoliation, higher stiffness and yield strength values, than low molecular weight polyamide. The differences in properties were attributed to differences in melt rheologies.

Effect of melt processing conditions on the extent of exfoliation in polyamide-6/organoclay nanocomposites were evaluated via XRD, TEM and mechanical property tests by Dennis et al., 2001. Two types of clay treatments were added to polyamide-6 using four different multiple screw design extruders. It was stated that degree of delamination and dispersion of layered silicates in a polymer matrix depends on clay chemical treatment, type of extruder and its screw design. Non-intermeshing twin-screw extruder yielded the best delamination and dispersion results, in comparison to co-rotating and counter-rotating intermeshing ones.

Effect of organoclay surfactant structure on polyamide-6 nanocomposite morphology and properties was examined by Fornes et al., 2002. Methyl groups, rather than hydroxy-ethyl and decreasing number of long alkyl tails from two to one tallows led to greater extents of silicate platelet exfoliation, increased moduli, higher yield strengths and lower elongation at break.

Morphology and properties of nylon 6 and nylon 6,6 organoclay nanocomposites processed through melt processing in twin screw extruder were compared by Chavarria and Paul, 2004. WAXD and TEM results showed that polyamide-6 nanocomposites were better exfoliated than polyamide-6,6 nanocomposites, which exhibited a mixture of intercalated and exfoliated structures. Polyamide-6 nanocomposites had superior mechanical properties than polyamide-6,6 nanocomposites .

Devaux et al., 2002 studied the crystallization behavior of polyamide-6 organoclay nanocomposites. They showed that montmorillonite induces the crystallization of polyamide-6 in γ -form, melting temperature of polyamide-6 decreased whereas crystallization temperature increased, since reinforcing material acted as a nucleating agent. Crystallization was not spherulitic and the macromolecules were oriented in the vicinity of clay.

The mechanical behavior of compression-molded polyamide-6 reinforced with 2 wt% of organo-nanoclay was studied and compared to that of PA6 by Bureau et al., 2002. The strength and the Young's modulus of the PA6/clay were 15% higher than those of PA6. DSC, FTIR and XRD analysis showed that the crystalline structures of PA6 and PA6/clay differed considerably. A crystallinity of 25% with a dual structure composed of the α and γ forms was obtained in PA6/clay, while a crystallinity of 31% with the α form as the dominant crystalline structure was obtained in PA6.

Crystallization behavior was also investigated by Homminga et al., 2006, in terms of matrix molecular weight, montmorillonite type and concentration. The silicate layer nucleating power was poor in nanocomposites made by melt extrusion, since stable PA-6 crystallization precursors are generated during melt-extrusion. In most of the nanocomposites, dispersed silicate layers decreased polyamide-6 crystallization rate, because silicate layers hindered the diffusion of polymer chains to the crystal growth front. Moderate nucleation effects were observed when montmorillonite amount was low and there was a poor degree of exfoliation.

Processing degradation of polyamide-6/montmorillonite clay nanocomposites and clay organic modifier was examined by Davis et al, 2003. In-situ polymerized polyamide-6/montmorillonite nanocomposite significantly degraded at 300 °C in 12.5 min, during typical processing techniques. A four-fold increase in ϵ -caprolactam monomer and reduction in average molecular mass was observed. Degradation was believed to occur via peptide bond scission, following water attack released from the polymer and montmorillonite clay surface. Under identical injection molding conditions, within experimental uncertainties, number average molecular mass of unfilled polyamide-6 did not decrease.

2.8.2 Previous Studies on Impact Modification of Polyamide-6

Generally, impact modification of polyamides is based on blending them with ethylene copolymers such as ethylene-ethyl acrylate, ethylene-acrylic acid

copolymers and ethylene-methacrylic copolymers, and terpolymers. Also, maleic-anhydride or glycidyl methacrylate containing reactive elastomers are used. There are several studies about impact modification of polyamides, thus a brief summary will be given.

Blends of low density polyethylene and polyamide-6 with poly (ethylene-co-acrylic acid) and ethylene-glycidylmethacrylate copolymer in the LDPE/compatibilizer or PA6/compatibilizer systems were prepared by Minkova et al., 2002. The morphology, crystal structure, isothermal crystallization behavior and microhardness of the blends were studied. Results indicated that the compatibilization efficiency of acrylic acid towards polyamide-6 is higher than that of glycidylmethacrylate.

Fracture behavior of nylon 6/SEBS-g-MA blends was investigated by Kayano et al., 1997. High speed fracture behaviour of nylon 6/SEBS-g-MA blends with rather small rubber particles, near the lower limit for rubber toughening, was characterized by the standard Izod impact tests. All blends examined showed four different regions, i.e. an extensive shear yield zone, a shear yield zone, a cavitation zone and an apparent non-deformed zone within a visible whitened zone.

The grafting efficiency on different nylons (6, 11, 12, 6,10 and 6,12) of ethylene-glycidyl methacrylate copolymer (PE-g-GMA) and ethylene-ethyl acrylate copolymer at a composition of 85/15, when melt mixed under optimum conditions, was investigated by Koulouri et al., 1997. Using dynamic mechanical analysis, tensile testing, differential scanning calorimetry, scanning electron microscopy and Fourier transform infra-red spectroscopy techniques, it was shown that the most efficient grafting occurred in the case of nylon 11/PE-g-GMA blends. The formation of a copolymer was confirmed by extraction experiments. The existence of both polymers in the isolated copolymers was proved by FTIR and thermal analysis.

A reactive route was employed to compatibilize ethylene-propylene rubber (EPM) and nylon 6 blends by the addition of maleic anhydride grafted EPM (EPM-g-MA). In this reactive route, the maleic anhydride group of EPM reacts with the amino end group of nylon forming a graft copolymer of nylon and EPM (nylon-g-EPM) at the

blend interface which decreases the interfacial tension and reduces the coalescence. The influence of the concentration of EPM-g-MA, blend composition, molecular weight of nylon 6, mode of addition of EPM-g-MA and mixing time on the phase morphology of the blends were studied quantitatively by scanning electron microscopy and image analysis. It was found that the addition of EPM-g-MA reduces the domain size of the dispersed phase followed by a levelling off at high concentrations; the levelling off is an indication of interfacial saturation (Thomas and Groeninckx, 1999).

The ductile–brittle transition temperatures were determined for compatibilized nylon 6/acrylonitrile-butadiene-styrene (PA6/ABS) copolymer blends by Araújo et al., 2003. The compatibilizers used for those blends were methyl methacrylate-co-maleic anhydride (MMA-MAH) and MMA-co-glycidyl methacrylate (MMA-GMA). The ductile–brittle transition temperatures were found to be lower for blends compatibilized through maleic acid modified acrylic polymers. At room temperature, the PA6/ABS binary blend was essentially brittle, whereas the ternary blends with MMA-MAH compatibilizer were supertough and showed a ductile–brittle transition temperature at -10°C. The blends compatibilized with maleated copolymer exhibited impact strengths of up to 800 J/m. However, the blends compatibilized with MMA-GMA showed poor toughness at room temperature and failed in a brittle manner at subambient temperatures.

2.8.3 Previous Studies on Impact Modified Polyamide-6 Nanocomposites

There are some studies that combine layered silicate reinforcement and rubber toughening in polyamides.

Liu et al. 2001 synthesized polyamide-6/organoclay nanocomposites by in-situ polymerization, then PP-g-MAH/polyamide-6/organoclay nanocomposites were melt-blended in a twin-screw extruder. Mechanical properties, morphology and water absorption were studied.

Khatua et al., 2004, studied the effect of organoclay platelets on morphology of polyamide-6 and poly(ethylene-ran-propylene) (EPR) blends by scanning and transmission electron microscopy. They observed that dispersed domain size of EPR phase in 20 wt % EPR containing blends decreased significantly even if a small amount of organoclay was added. The extent of the decrease in domain size was similar to polyamide-6/EPR-g-MA blends. Their results indicated that if the clay becomes exfoliated in the polymer matrix, the exfoliated clay platelets prevent the coalescence of the dispersed domains.

Tjong and Bao, 2005, investigated the impact fracture toughness of polyamide-6/montmorillonite nanocomposites toughened with a maleated styrene/ethylene butylene/styrene elastomer. Their results showed that SEBS-g-MA addition improved the tensile ductility and impact strength of polyamide-6/montmorillonite nanocomposites at the expense of its tensile strength and ductility.

Chiu et al., 2005 prepared polyamide-6 and maleated polyolefin elastomer (POEMA) based nanocomposites using one type of commercial organoclay. XRD results showed that both organoclay and polyolefin elastomer induce the formation of γ form crystal. Storage modulus, Young's Modulus and tensile strength increased after organoclay addition. However, these properties declined after further incorporation of elastomer.

SEBS-MA (up to 40 wt %) toughened polyamide-6 nanocomposites with 3 wt % organoclay are studied by González et al., 2006. The morphology of polyamide-6 matrix did not change on blending with elastomer. However, rubber particle sizes in nanocomposites were larger than their corresponding blends. Super-tough nanocomposites were obtained with 30 wt % SEBS-MA. In another study, the authors investigated the effect of clay loading on morphology and mechanical properties of the same material combinations (González et al., 2006). The elastomer content was selected as 30 wt %. The interactions between the organoclay surfactant and elastomer maleic anhydride groups, led to a decrease in compatibility, thus decreased the particle size.

Ahn and Paul, 2006, processed polyamide-6/EPR-g-MAH nanocomposites. Polyamide-6 and organoclay were mixed in a twin-screw extruder and the nanocomposites were blended with rubber in a single screw extruder. They observed that, the addition of clay affected the dispersion of the rubber phase resulting in larger and more elongated rubber particles.

Kelnar et al., 2006 examined the morphology and mechanical properties of polyamide-6/organoclay ternary nanocomposites prepared by different types of both reactive and unreactive elastomers, such as EPR-MA, EPR, SEBS-MA, SEBS, E-MA-GMA, E-MA and NBR. The effects of clay content and elastomer type were investigated. They found that mechanical properties of the system were influenced by elastomer type and particle size, clay localization and its degree of ordering.

Baldi et al., 2006, investigated rubber toughening of polyamide-6/organoclay nanocomposites both in dry and wet conditions using ethylene-co-propylene maleated rubber. Their results showed that toughening action of rubber strongly depended on the degree of humidity of the material. In slightly wet conditions, they found that the addition of small amounts of rubber increased the fracture resistance of polyamide-6/layered silicate nanocomposites without impairing the material stiffness.

Polyamide-6/unmodified montmorillonite/rubber nanocomposites were prepared by Dong et al., 2006, on the basis of three compound powders of ultra-fine full-vulcanized powdered rubber (UFPR), butadiene-styrene vinyl-pyridine (VP-UFPR), acrylate UFPR (A-UFPR) and silicone UFPR (S-UFPR). First, montmorillonite was mixed with rubber latex, and then the mixture was melt blended with polyamide-6. Different UFPRs led to different superior properties of the three nylon-6 nanocomposites. Nylon-6/S-UFPR nanocomposite exhibited superior flame retardance, good flowability and high thermal stability, whereas Nylon-6/UV-UFPR nanocomposite showed much higher toughness.

Polyamide-6/maleated propylene blend based nanocomposites were studied by Chow et al. (Chow et al., 2003; Chow et al., 2004; Chow et al., 2005).

Nanocomposite morphology, mechanical, thermal and dynamic mechanical properties were investigated. Clay surface was modified by octadecylamine, and the authors claimed that H-bonding between amine groups of octadecylamine intercalant of the clay and carbonyl groups of polyamide-6 and polyamide-6-g-polypropylene favors exfoliation.

CHAPTER 3

EXPERIMENTAL WORK

3.1 Materials

3.1.1 Polymer Matrix

The polymer matrix, polyamide-6 (Teklamid) is purchased from Polyone Company in the form of pellets. Typical properties of polyamide-6 obtained from the producer are listed in Table 3.1.

Table 3.1 Properties of the Polyamide-6

Property	Value
Density at 23 °C (g/cm ³) – ISO 1183	1.13
Melting Range (°C)	220-225
Tensile Strength (MPa) – ISO 527	75
Charpy Notched Impact Strength (kJ/m ²) – ISO	6.5

3.1.2 Organoclays

The layered silicates used in this study are montmorillonites Cloisite® 15A, Cloisite® 25A, and Cloisite® 30B that were produced by a cation exchange

reaction between sodium montmorillonite and various quaternary alkyl ammonium salts by Southern Clay Products (USA). Organic modifier chemical structures for Cloisite® 15A, Cloisite® 25A, and Cloisite® 30B are given in Figures 3.1, 3.2 and 3.3, respectively. Table 3.2 shows physical properties of organic modifiers that are used in this study. Due to the nature of organic modifier, surface hydrophobicities are different from one organoclay to another. According to Figure 3.4, surface hydrophobicity is highest in Cloisite® 15A and least in 30B. Cloisite® 25A is in the middle of the two.

Cloisite® 15A was modified by the cation dimethyl, dehydrogenated tallow quaternary ammonium (2M2HT) at a concentration of 125 meq/100g clay, and the anion is chloride.

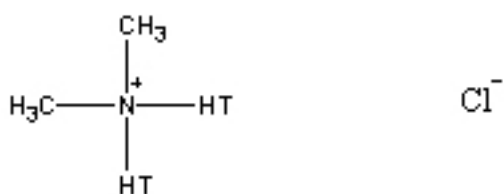


Figure 3.1 Chemical structure of organic modifier 2M2HT (dimethyl, dihydrogenated tallow quaternary ammonium) and anion (chloride) of Cloisite® 15A

Cloisite® 25A was modified by the cation dimethyl, hydrogenated tallow and a C-8 hydrocarbon chain quaternary ammonium (2MHTL8) with a concentration of 95 meq/100g clay, and the anion is methyl sulfate.

Cloisite® 30B was modified by the cation methyl, tallow, bis-2-hydroxyethyl quaternary ammonium (MT2EtOH) with a concentration of 90 meq/100g clay, and the anion is chloride.

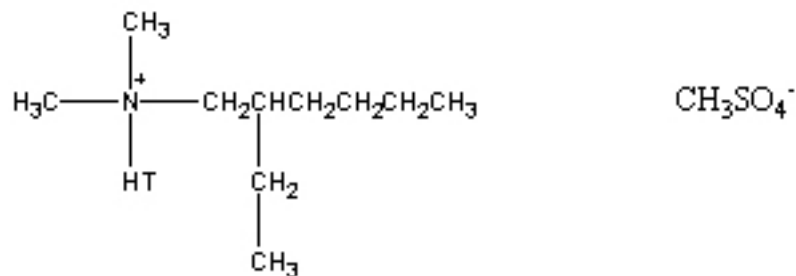


Figure 3.2 Chemical structure of organic modifier 2MHTL8 (dimethyl, hydrogenated tallow, 2-ethylhexyl quaternary ammonium) and anion (methyl sulfate) of Cloisite® 25A

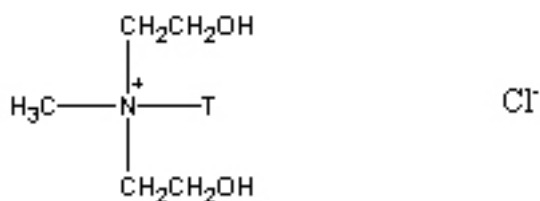


Figure 3.3 Chemical structure of organic modifier MT2EtOH (methyl, tallow, bis-2-hydroxyethyl, quaternary ammonium and anion (chloride) of Cloisite® 30B

HT and T in Figures 3.1, 3.2 and 3.3 stand for hydrogenated tallows, long organic molecules having ~65% C18; ~30% C16; ~5% C14.

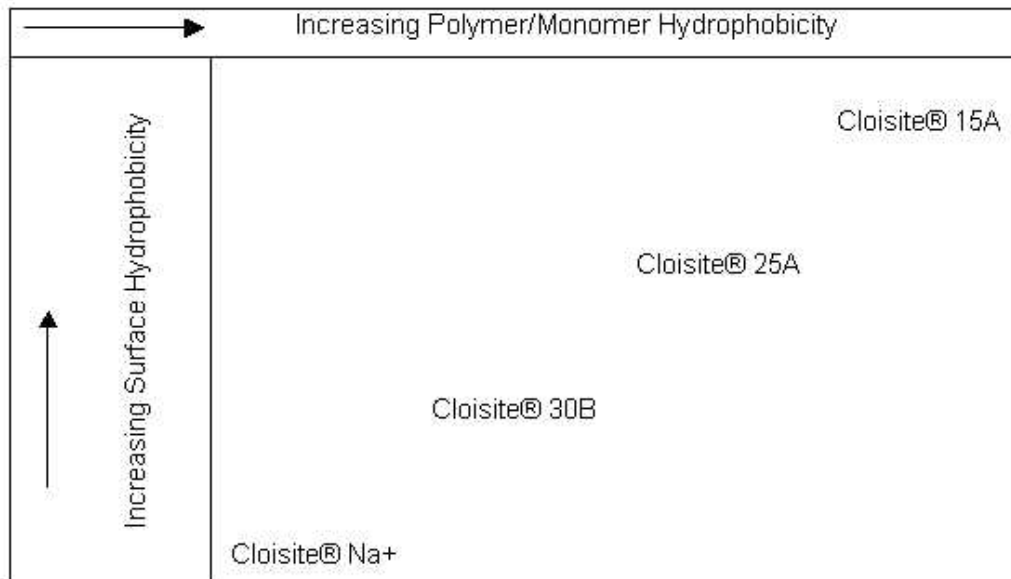


Figure 3.4 Clay selection chart based on polymer/monomer chemistry (www.nanoclay.com)

Table 3.2 Properties of Organoclays

Organoclay	Cloisite® 15A	Cloisite® 25A	Cloisite® 30B
% Moisture	< 2 %		
% Weight Loss on Ignition	43 %	34 %	30 %
Typical Dry Particle Sizes (microns, by volume)	10% less than : 2 μ 50% less than : 6 μ 90% less than : 13 μ		
Color	Off white		
Specific gravity (g/cc)	1.66	1.87	1.98
Loose Bulk (lbs/ft ³)	10.79	12.08	14.25
Packed Bulk (lbs/ft ³)	18.64	20.48	22.71
d-spacing	d ₀₀₁ =31.5Å	d ₀₀₁ =18.6Å	D ₀₀₁ =18.5Å

3.1.3 Elastomers

Three different types of elastomeric materials; Lotader 2210, ethylene-butyl acrylate-maleic anhydride (E-BA-MAH), Lotader AX 8840, ethylene-glycidyl methacrylate (E-GMA) and Lotader AX 8900, ethylene-methyl acrylate- glycidyl methacrylate (E-MA-GMA) are purchased from Arkema Chemicals, France. Their chemical structures can be seen in Figures 3.5-3.7.

Elastomers used have functional groups which enable them react with hydroxyl, amine and carboxylic acid groups. These functional groups reduce crystallinity and increase polarity compared to polyethylene. The elastomers have excellent

heat stability allowing high processing temperatures. Some important specifications of terpolymers are given in Table 3.3.

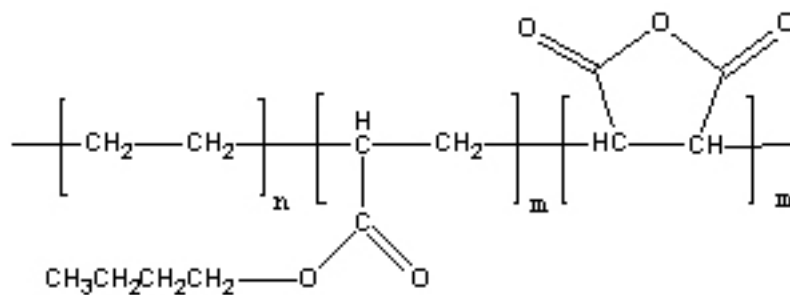


Figure 3.5 Chemical structure of elastomer E-BA-MAH

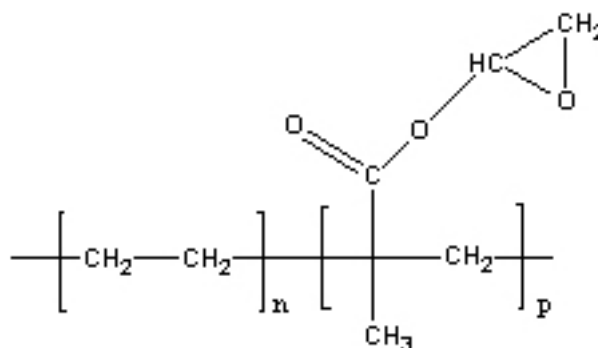


Figure 3.6 Chemical structure of elastomer E-GMA

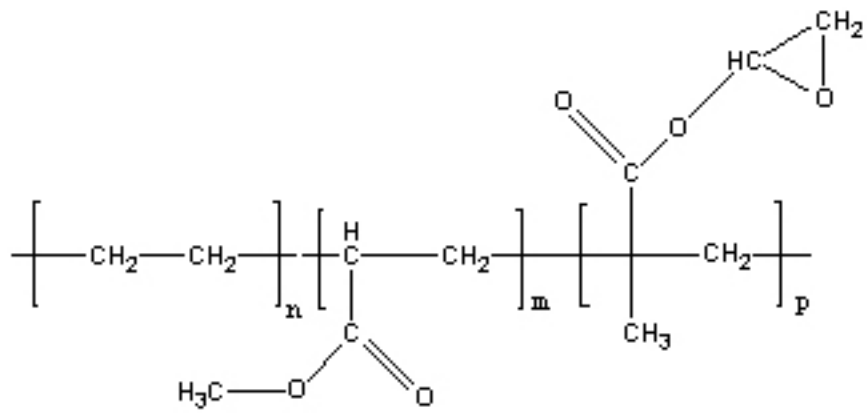


Figure 3.7 Chemical structure of elastomer E-MA-GMA

Table 3.3 Properties of Elastomeric Materials (www.lotader.com)

Typical Properties	E-BA-MAH	E-GMA	E-MA-GMA
MAH content (wt %)	2.6	-	-
GMA content (wt %)	-	8	8
Ester content (wt %)	8	-	25
Melt Index (g/10 min) 190 °C, 2.16 kg. (ASTM D1238)	3	5	6
Vicat Point (°C) (ASTM D 1525)	80	87	<40
Melting Point (°C)	107	105	60
Tensile Strength at Break (MPa) (ASTM D638)	12	8	4
Elongation at Break (%) (ASTM D638)	600	420	1100
Hardness (ASTM D2240)	46 (Shore D)	92 (Shore A)	70 (Shore A)

3.2 Nanocomposite Preparation

Organically treated montmorillonite (2 weight %), elastomer (5 weight %) and polyamide-6 nanocomposites are prepared by melt compounding in a Thermoprism TSE 16 TC, co-rotating, intermeshing twin-screw extruder (D = 16 mm, L = 384 mm) at a screw speed of 250 rpm with a feed rate of 25 g/min. Figure 3.8 shows the extruder used in this study. The temperature profile of the barrel is 220-240-240-240-240 °C from hopper to the die. Twice extruded pellets are dried and injection molded (Microinjector, Daga Instruments) at barrel temperature of 240 °C and mold temperature of 30 °C. For impact tests, DSM Micro 10 cc Injection Molding Machine is used at the same barrel and mold temperatures. Injection molding machines are shown in Figures 3.9 and 3.10. Pure polyamide-6, polyamide-6/organoclay binary nanocomposites and polyamide-6/elastomer blends are also prepared with the same process conditions for comparison. Prior to processing, polyamide-6, organically modified montmorillonites, elastomers and extruded samples are dried under vacuum. Drying conditions are given in Table 3.4. Addition order of the components is changed in some ternary nanocomposites. Some ternary nanocomposites are prepared by four different addition orders. Table 3.5 and 3.6 show the all the compositions processed in this study. After injection molding, the samples are immediately sealed in polyethylene bags and stored in vacuum desiccators for at least 24 h prior to characterization experiments.



Figure 3.8 Thermo Prism TSE 16 TC twin screw extruder

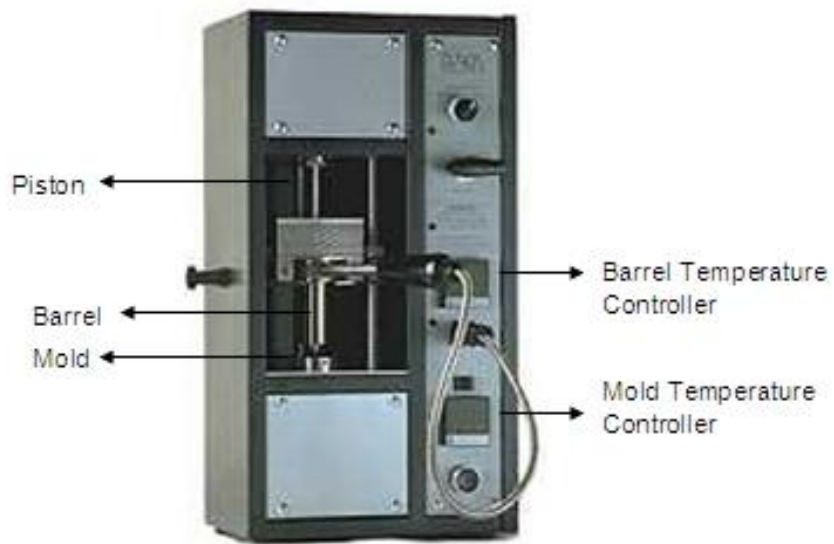


Figure 3.9 Daka Instruments injection molding machine



Figure 3.10 DSM injection molding machine

Table 3.4 Drying temperature and time for the materials used in the study

Material	Drying Temperature (°C)	Drying Time (h)
Before RUN 1 Extrusion		
Polyamide-6	80	24
Organoclays	80	12
Elastomers	40	12
Before RUN 2 Extrusion		
Polyamide-6	80	24
Polyamide-6 + Elastomer	80	24
Elastomer + Organoclay	40	12
Polyamide-6 + Elastomer + Organoclay	80	24
Before Injection Molding		
All samples	80	24

Table 3.5 Formulation table

Composition	Concentration (wt %)		
	Polyamide-6	Organoclay	Elastomer
Polyamide-6	100	-	-
Polyamide-6/Elastomer Blends			
Polyamide-6+E-BA-MAH	95	-	5
Polyamide-6+E-BA-MAH	90	-	10
Polyamide-6+E-BA-MAH	85	-	15
Polyamide-6+E-GMA	95	-	5
Polyamide-6+E-GMA	90	-	10
Polyamide-6+E-GMA	85	-	15
Polyamide-6+E-MA-GMA	95	-	5
Polyamide-6+E-MA-GMA	90	-	10
Polyamide-6+E-MA-GMA	85	-	15
Polyamide-6/Organoclay Binary Nanocomposites			
Polyamide-6+C15A	98	2	-
Polyamide-6+C25A	98	2	-
Polyamide-6+C30B	98	2	-
Polyamide-6/Organoclay/Elastomer Ternary Nanocomposites (All-S)			
Polyamide-6+C15A+E-BA-MAH	93	5	2
Polyamide-6+C25A+E-BA-MAH	93	5	2
Polyamide-6+C30B+E-BA-MAH	93	5	2
Polyamide-6+C15A+E-GMA	93	5	2
Polyamide-6+C25A+E-GMA	93	5	2
Polyamide-6+C30B+E- GMA	93	5	2
Polyamide-6+15A+E-MA-GMA	93	5	2
Polyamide-6+C25A+E-MA-GMA	93	5	2
Polyamide-6+C30B+E-MA-GMA	93	5	2

Table 3.6 Formulation table (cont'd)

Composition	Concentration (wt %)		
	Polyamide-6	Organoclay	Elastomer
Polyamide-6/Organoclay/Elastomer Ternary Nanocomposites (PI-C)			
Polyamide-6+C15A+E-BA-MAH	93	5	2
Polyamide-6+C25A+E-BA-MAH	93	5	2
Polyamide-6+C15A+E-GMA	93	5	2
Polyamide-6+C30B+E-GMA	93	5	2
Polyamide-6/Organoclay/Elastomer Ternary Nanocomposites (PC-I)			
Polyamide-6+C15A+E-BA-MAH	93	5	2
Polyamide-6+C25A+E-BA-MAH	93	5	2
Polyamide-6+C15A+E-GMA	93	5	2
Polyamide-6+C30B+E-GMA	93	5	2
Polyamide-6/Organoclay/Elastomer Ternary Nanocomposites (IC-P)			
Polyamide-6+C15A+E-BA-MAH	93	5	2
Polyamide-6+C25A+E-BA-MAH	93	5	2
Polyamide-6+C15A+E-GMA	93	5	2
Polyamide-6+C30B+E-GMA	93	5	2

3.2.1 Addition Order of the Components

In this study, polyamide-6/organoclay/elastomer ternary nanocomposites are prepared by four different addition orders. For the polyamide-6 based ternary nanocomposites having Cloisite® 15A/E-BA-MAH, Cloisite® 25A/E-BA-MAH, Cloisite® 15A/E-GMA and Cloisite® 30B/E-GMA, effect of addition order of the components are investigated. P, I and C stand for polyamide-6, impact modifier (elastomer) and clay, respectively. Generalized flowchart of experimental procedure is given in Figure 3.11.

3.2.1.1 All-S Mixing Sequence

In RUN 1, dry blended polyamide-6 and E-BA-MAH inside the main feeder and organoclay inside the second feeder are fed to the extruder simultaneously from the first feed port. In RUN 2, the product is pelletized, dried and fed to the extruder from the main feeder and extruded once more.

3.2.1.2 PI-C Mixing Sequence

In RUN 1, polyamide-6 and elastomer pellets are dry blended and added to the extruder from the main feeder. In RUN 2, precompounded polyamide-6/elastomer blend (run 1) pellets are fed to the extruder from the main feeder whereas, organoclay is given inside to the melt stream from the second feeder.

3.2.1.3 PC-I Mixing Sequence

In RUN 1, polyamide-6 pellets are fed to the extruder from the main feeder. At the same time, organoclay particles inside the second feeder are added to the molten polymer. In RUN 2, pellets of precompounded polyamide-6/organoclay nanocomposites (run 1) are dry blended with elastomer pellets and added to the system from the main feeder.

3.2.1.2 IC-P Mixing Sequence

In RUN 1, elastomer pellets are fed to the extruder from the main feeder. Organoclay particles are added to the molten stream at the second feed port. In RUN 2, polyamide-6 pellets are dry blended with pellets of precompounded

organoclay/elastomer mixture (run 1). In the first run of the mixing sequence 1 (IC-P), temperatures are adjusted based on the processing temperature of elastomer. Thus, the barrel temperature profile is 170-190-190-190-200°C.

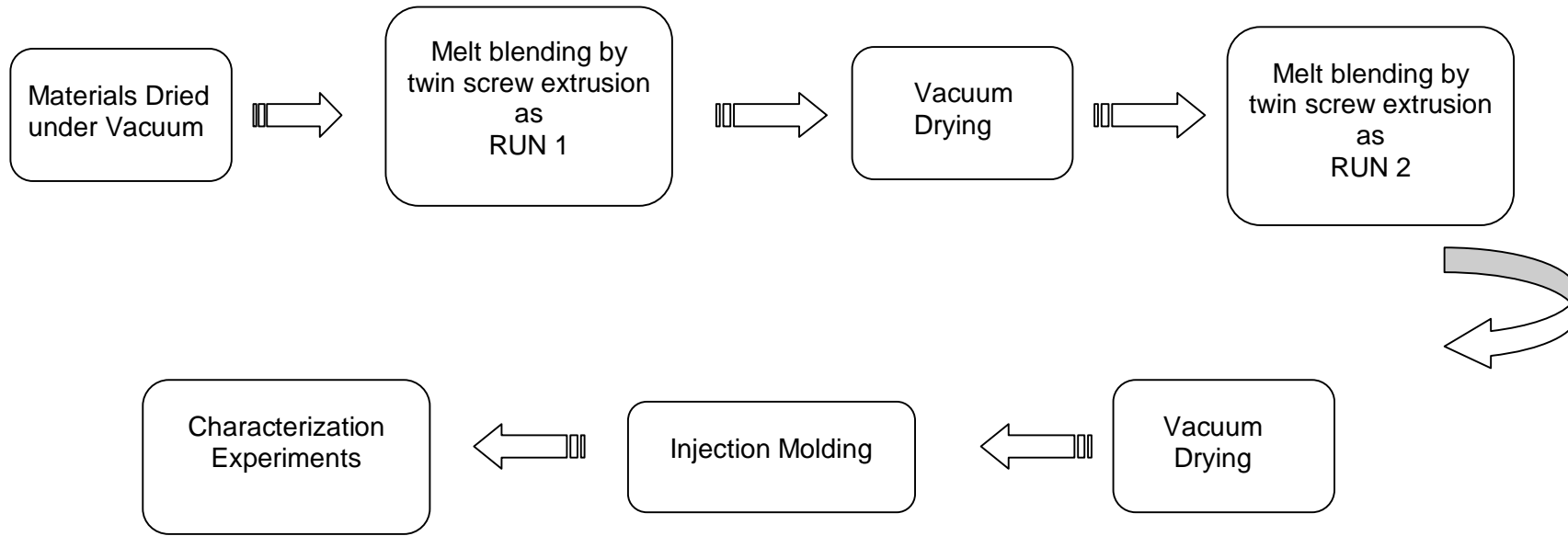


Figure 3.11 Generalized flowchart of experimental procedure

3.3 Characterization Experiments

In order to investigate the effects of component concentrations and addition order of the components on the final properties of ternary nanocomposites composed of polyamide-6, three types of organoclays and three types of elastomers, X-Ray, TEM and SEM analysis are used for morphological characterization. FTIR-ATR technique is used to determine the reactions occurring between polyamide-6 and elastomers. Melting and crystallization behavior of the composites are studied by Differential Scanning Calorimetry (DSC). Flow characteristics are evaluated by Melt Flow Index (MFI) measurements. Mechanical behavior of nanocomposites is evaluated by measuring impact strength, tensile properties (tensile strength, Young's modulus, % elongation at break) and flexural properties (flexural strength, flexural modulus). Thermomechanical properties are detected by Dynamic Mechanical Analysis (DMA) technique. The research is also focused on the rheological characterization of the polyamide-6 based nanocomposites by parallel disk rheometer.

3.3.1 Nanocomposite Morphology Determination

3.3.1.1 X-Ray Diffraction (XRD) Analysis

The composites are analyzed by using a RIGAKU D/MAX 2200/PC X-ray diffractometer. Cu K α ($\lambda = 1.54 \text{ \AA}$) radiation, generated at a voltage of 40 kV and current of 40 mA is used as the X-Ray source. The diffraction angle 2θ is scanned from 1° to 10° at a scanning rate of $1^\circ/\text{min}$ and a step size of 0.01° . XRD analysis is performed on tensile bars except for the organoclay which is in powder form.

3.3.1.2 Transmission Electron Microscopy (TEM) Analysis

Philips CM200 Transmission Electron Microscope (TEM) in DSM Research, Holland is used at an acceleration voltage of 120 kV to examine the samples. Ultra thin sections of 70 nm in thickness are cryogenically cut with a diamond knife at a temperature of $-100\text{ }^{\circ}\text{C}$. All samples are trimmed parallel to the molding direction.

3.3.1.3 Scanning Electron Microscopy (SEM) Analysis

The fracture surfaces of the materials obtained by impact testing are examined by a low voltage Scanning Electron Microscope (JEOL JSM-6400). Polyethylene based elastomeric material phase from the blends and ternary systems is selectively etched in hot xylene. The sample surfaces are coated with gold to avoid electrostatic charging during examination.

Domain sizes of 100-250 elastomers are analyzed by Image J software by NIH (Image Processing and Analysis in Java). Calculation of the average domain size is carried out by using the area of domains (A_i) obtained by the program for a number of the domains (n_i) in Equations 3.1 and 3.2.

$$\bar{A} = \frac{\sum n_i A_i}{\sum n_i} \quad (3.1)$$

$$\bar{d} = \sqrt{\frac{4 \times \bar{A}}{\pi}} \quad (3.2)$$

3.3.2 Spectroscopic analysis

3.3.2.1 Fourier Transform Infrared Spectroscopy - Attenuated Total Reflectance (FTIR-ATR) Analysis

FTIR-ATR analysis is used to obtain qualitative information about the reactions occurring between polyamide-6 and elastomers.

Spectra are recorded at ambient temperature on a Bruker Optics Tensor Series spectrometer equipped with an internal reflection element of diamond by applying the same pressure of the crystal on the surface in each sample. The samples are scanned from 4000 cm^{-1} to 600 cm^{-1} with a resolution of 32 scans.

3.3.3 Thermal Analysis

3.3.3.1 Differential Scanning Calorimeter (DSC) Analysis

The melting temperature and crystallinity of the nanocomposites are determined with a 910 S Dupont TA Differential Scanning Calorimeter. The samples are heated from 40 °C to 300 °C at a heating rate of 10 °C/min under nitrogen atmosphere. DSC measurements for elastomers are carried out by using Perkin-Elmer Diamond DSC with heating from -75 °C to 200 °C at a heating rate of 20 °C/min under nitrogen atmosphere. The percent crystallinity of the polyamide phase is calculated as the ratio of the heat of fusion of the sample (ΔH_f), divided by the weight fraction of polyamide in the nanocomposite and the heat of fusion of the pure crystalline form of polyamide-6 (ΔH_f^0). The ΔH_f^0 value for polyamide-6 matrix is taken as 190.9 J/g (Inoue, 1963).

3.3.4 Flow characteristics

3.3.4.1 Melt Flow Index (MFI) Test

Melt flow index (MFI) measurements are carried out according to ASTM D1238-04c using an Omega Melt Flow Indexer. Conditions of temperature and load are selected as 235 °C and 2.16 kg respectively, as indicated in standards. The method is based on determining melt index, defined as the amount of polymer passing through a specified capillary in ten minutes.

3.3.5 Mechanical Analysis

All mechanical tests are performed at 23 °C. Impact, tensile and flexural properties reported represent the average of the results on at least five samples. For each type of composite, arithmetic means with standard deviations are reported.

$$s = \sqrt{\frac{\sum X^2 - n\bar{X}^2}{n-1}} \quad (3.3)$$

where s is the estimated standard deviation, X is the value of single observation; n is the number of observations and \bar{X} is the arithmetic mean of the set of observations (ASTM D638-03, 2004).

3.3.5.1 Impact Tests

Charpy impact strength of one sided notched specimens is measured by pendulum Ceast Resil Impactor according to ISO 179-2, which shown in Figure 12. The shape and dimensions of the specimens are given in Figure 3.13 and Table 3.7, respectively.

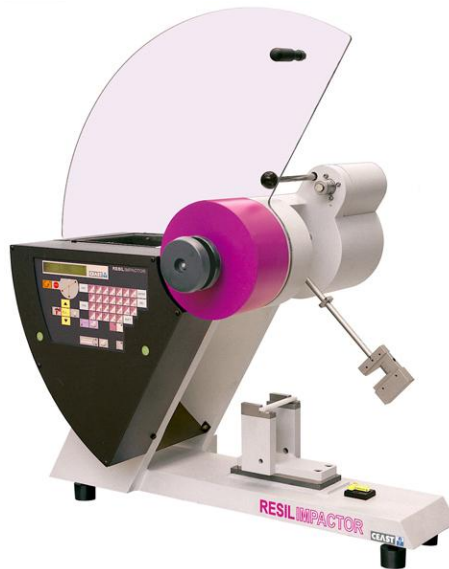


Figure 3.12 Impact Tester

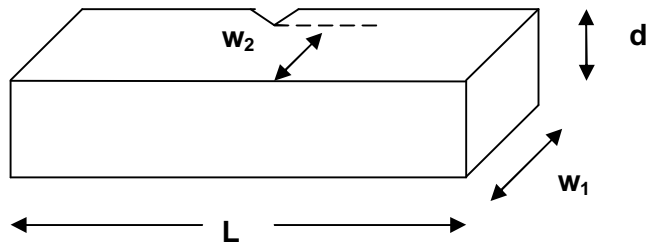


Figure 3.13 Impact Test Specimen

Table 3.7 Impact Test Specimen Dimensions

Term	Specimen Dimensions (mm)
Length, L	80
Thickness, t	4
Total Width, w_1	10
Unnotched Width, w_2	8
Notch Type and Angle	v, 45°

3.3.5.2 Tensile Tests

Tensile tests are performed using a testing machine (Lloyd 30K), according to ASTM D638-03. The strain rate is 0.1 min^{-1} . The shape and dimensions of the specimens are given in Figure 3.14 and Table 3.8, respectively. Tensile strength, Young's modulus, % elongation at break and toughness values are determined using stress-strain curves.

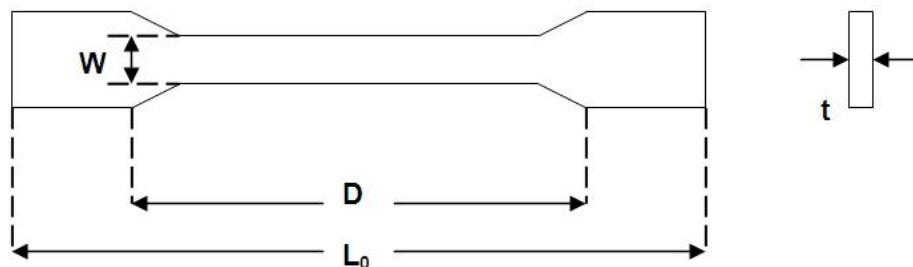


Figure 3.14 Tensile Test Specimen

Table 3.8 Tensile Test Specimen Dimensions

Term	Specimen Dimensions (mm)
Distance Between Grips, D	80
Overall Length, L ₀	112
Thickness, t	2.1
Width of Narrow Section, W	7.5

3.3.5.3 Flexural Tests

Three-point bending tests were performed according to Procedure A of ASTM D790-03 with Lloyd 30K Universal Test Machine. A three-point loading scheme is illustrated in Figure 3.15. Support span and strain rate are taken as 50 mm and 0.1 min⁻¹, respectively. Cross-head speed is calculated as 19.84 mm/min according to Equation 3.4,

$$R = \frac{ZL^2}{6d} \quad (3.4)$$

where;

R = rate of crosshead motion, mm/min,

L = support span, mm,

d = depth of beam, mm, and

Z = rate of straining of the outer fiber, min⁻¹

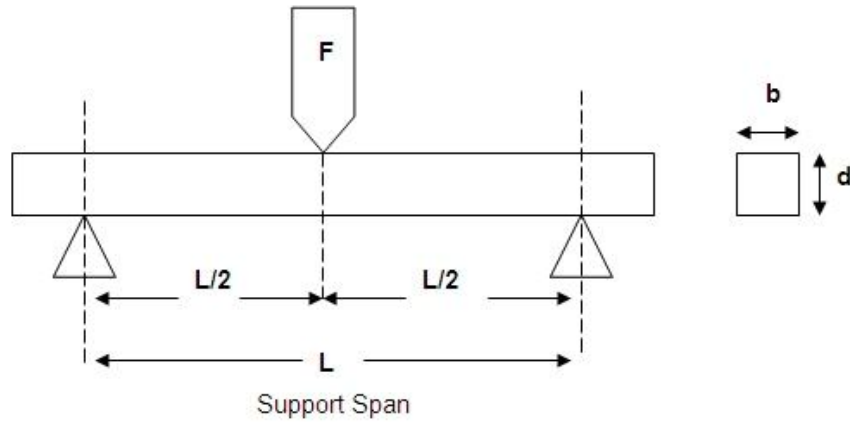


Figure 3.15 Three point loading scheme

Flexural strength (σ_{fs}) and modulus (E_B) are determined using Equations 3.5 and 3.6, respectively. No fracture occurred in polyamide-6, polyamide-6/elastomer blends and nanocomposites. The test is ended after maximum degree of bending is reached for the specimen fixed between two supports.

$$\sigma_{fs} = \frac{3F_f L}{2bd^2} \quad (3.5)$$

where F_f is the maximum load at fracture (N), L is the distance between support points (mm), b is the width of the specimen (mm), and d is the depth of specimen (mm).

$$E_B = \frac{L^3 m}{4bd^3} \quad (3.6)$$

where E_B is modulus of elasticity in bending (MPa), L is the length of support span (mm), b is the width of the beam tested (mm), d is the depth of beam tested

(mm), and m is the slope of the tangent to the initial straight-line portion of the load deflection curve, N/mm of deflection.

3.3.6 Viscoelasticity

3.3.6.1 Dynamic Mechanical Analysis (DMA)

Perkin Elmer Pyris Diamond DMA is used in dynamic mechanical property analysis. Spectra are recorded in the bending mode, with oscillation amplitude of $1\ \mu\text{m}$, a frequency of 1 Hz and a heating rate of $5\ ^\circ\text{C}/\text{min}$ in the range of -100 to $200\ ^\circ\text{C}$. The storage modulus, E' , loss modulus, E'' , and loss tangent, $\tan \delta$, are measured for each sample in this temperature range. The shape and dimensions of injection molded specimens can be seen in Figure 3.16 and Table 3.9, respectively.

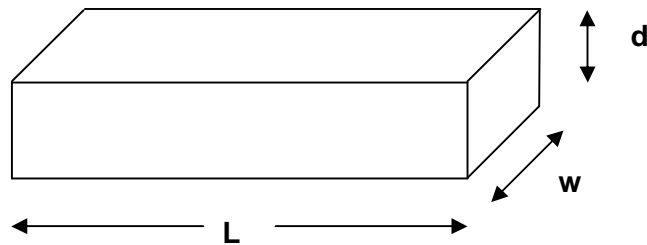


Figure 3.16 DMA Test Specimen

Table 3.9 DMA Specimen Dimensions

Term	Specimen Dimensions (mm)
Overall Length, L	50
Depth, d	2.1
Width, w	7.5

3.3.6.2 Rheological Properties

Dynamic rheological measurements are performed using a Rheometric Scientific rotational rheometer (Advanced Rheometric Expansion System). Rheometer is shown in Figure 3.17. Rheological properties of polyamide-6, elastomer E-MA-GMA, polyamide-6/organoclay binary nanocomposites, and polyamide-6/organoclay/E-MA-GMA ternary nanocomposites are measured using 25 mm diameter parallel plates in oscillatory shear mode. Dynamic storage modulus, G' , dynamic loss modulus G'' and complex viscosity, η^* , are recorded as functions of angular frequency, ω , at 240 °C. The frequency test range is from 1 to 100 rad/s. For rheological analysis, extruded pellets are compression molded at 250 °C, for 4 min in order to obtain disks having diameter of 25 mm and thickness of 1 mm. For polyamide-6/Cloisite® 25A/E-MA-GMA nanocomposite, strain is swepted 1 to 20 % at 240 °C and 5 rad/s angular frequency, then storage modulus, loss modulus and complex viscosity versus percentage strain are obtained. These values remain constant in the studied strain range. Thus, in the analysis 5% strain amplitude is selected to ensure that experiments are performed in linear viscoelastic region. Experiments are conducted under nitrogen atmosphere in order to prevent oxidative degradation.



Figure 3.17 ARES Rheometer

CHAPTER 4

RESULTS AND DISCUSSIONS

4.1 X-RAY ANALYSIS

XRD analysis is used to probe the structure of polyamide-6/clay nanocomposites. The patterns are very useful to make qualitative observations, however XRD may not be regarded as being the most sensitive technique for describing the degree of intercalation/exfoliation of organoclay aggregates in a polymer matrix.

4.1.1 X-Ray Analysis Results of Organoclay Cloisite® 15A Containing Nanocomposites

Figure 4.1 shows XRD patterns of pure Cloisite® 15A, polyamide-6/Cloisite® 15A binary nanocomposite and polyamide-6/Cloisite®15A/E-BA-MAH ternary nanocomposite. XRD diffractogram of Cloisite® 15A organoclay shows two diffraction peaks. The d-spacing data for pure Cloisite® 15A and nanocomposites are calculated by using Bragg's Equation from the first peak (d_1) and second peak (d_2) diffraction peaks in the figure. The second peak can result from a second silicate layer if 2θ is approximately twice the value of the first characteristic peak of the clay or it may be due to a reflection from a portion of the clay where the inorganic cations of the smectite clay are not fully replaced by the organic ions if 2θ is about 2θ for unmodified clay (Mehrabzadeh and Kamal, 2004; Finnigan et al., 2005). In the $2\theta=1-10^\circ$ interval, polyamide-6 shows no peaks. It can be seen from Figure 4.1 that, d-spacing calculated from d_1 diffraction peak did not significantly change when Cloisite® 15A was melt blended with polyamide-6 and

impact modified polyamide-6. The d_2 d-spacing of Cloisite® 15A in powder form corresponds to the d_1 d-spacing of Cloisite® Na⁺ according to Southern Clay Products. Thus, it corresponds to clay which is not modified by the quarternary ammonium salt. It is observed that, d_2 peak is shifted to lower angles when Cloisite® 15A is mixed with polymers indicating a few polymer chains are intercalated between the clay lers. Initial d_2 interlayer spacing of pure Cloisite® 15A (12.8 Å) is increased to 17.0 Å and 15.7 Å when mixed with polyamide-6 and polyamide-6/elastomer blend, respectively. Since d_2 is not exactly half of d_1 , it is thought that d_2 is observed by intercalation of polymer into unmodified clay layers. This is supported by the fact that the peak at 12.8 Å is not observed in the nanocomposites.

Polyamide-6 is a relatively polar polymer that is capable of making high degree of hydrogen bonding, and it also has a relatively good affinity for the polar surface of the montmorillonite (Fornes et al., 2002). According to suppliers' data, Cloisite® 15A has the most hydrophobic surface among the organoclays studied with no polar groups on its modifier. Thus, it would be expected that Cloisite® 15A is the least compatible with polyamide-6.

Figure 4.2 shows XRD patterns of polyamide-6/Cloisite® 15A/E-BA-MAH nanocomposites processed by different addition orders whereas Table 4.1 shows d-spacing data of the same materials. As it is seen from table, original d_1 d-spacing of organoclay Cloisite® 15A, which is 31.5 Å, did not change significantly and d_2 diffraction peak is shifted to lower angles when it was mixed with polyamide-6 and E-BA-MAH elastomer in all addition orders. It is known that the external force applied on the clay agglomerates from the polymer melt depends on shear rate, melt viscosity of polymer matrix, surface area of clay, and surface tension at the interface (between melt and clay), whereas the diffusion of macromolecules relies among others on the melt temperature, chain structure, interlayer spacing, time, and type/concentration of surfactant modifiers at the clay surface (Vaia et al. 1995; Vaia and Giannelis, 1997; Balazs at al, 1998). From the experimental results obtained in this study, chemical compatibility between the polymer matrix and organoclay, and also the chemistry of the clay treatment are understood to be very important factors in intercalation/exfoliation mechanism. The shear intensity in the extruder can only decrease the tactoid particles or the

size of intercalated clay stacks when the chemical compatibility is not strong enough (Cho and Paul, 2001).

Figure 4.3 shows XRD patterns of pure Cloisite® 15A, polyamide-6/Cloisite® 15A binary nanocomposite and polyamide-6/Cloisite®15A/E-GMA ternary nanocomposite. Similar to the polyamide-6 based nanocomposites containing Cloisite® 15A and E-BA-MAH, organoclay d_1 d-spacing in Figure 4.3 is not changed in the presence of polyamide-6 and E-GMA elastomer. d_2 d-spacing for this organoclay increased from 12.8 Å to 17.0 Å and 16.2 Å when mixed with polyamide-6 and polyamide-6/E-GMA elastomer blend, respectively. Again, in this case Table 4.2 indicates that Cloisite® 15A powder has layer which are not modified by the quaternary ammonium salt and thus gives an interlayer spacing of 12.8 Å. When this powder is melt blended, polymer molecules enter the unmodified layers and increase the d-spacing to 15.7 Å or 17.0 Å. Cloisite® 15A has two long aliphatic tails and these tails limit the access of polyamide-6 segments to the silicate surface. Vaia and Giannelis, in their lattice model of polymer melt intercalation, conclude that maximization of the number of favorable polymer-silicate interactions and minimization of unfavorable non-polar interactions between polymer and alkyl type surfactants on the silicate, leads to desirable changes in interaction energies. Favorable interactions are believed to be the driving force for polymer intercalation and sustain exfoliation (Vaia and Giannelis, 1997).

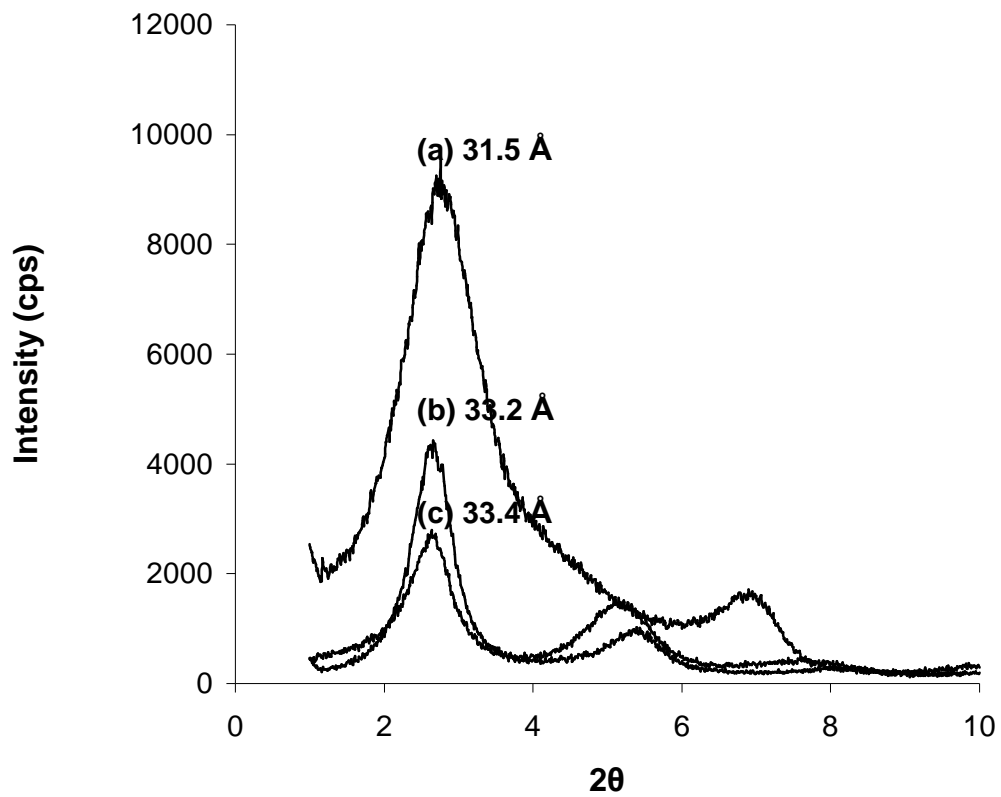


Figure 4.1 XRD patterns for (a) Cloisite® 15A (b) Polyamide-6/Cloisite® 15A nanocomposite (c) Polyamide-6/Cloisite® 15A/E-BA-MAH nanocomposite by All-S sequence

Table 4.1 d-spacing data of polyamide-6/Cloisite® 15A/E-BA-MAH nanocomposites processed by different addition orders

	d ₁ d-spacing (Å)	d ₂ d-spacing (Å)
Pure Cloisite® 15A in powder form	31.5	12.8
Polyamide-6 + Cloisite® 15A	33.2	17.0
Polyamide-6 + Cloisite® 15A + E-BA-MAH (All-S)	33.4	15.7
Polyamide-6 + Cloisite® 15A + E-BA-MAH (PI-C)	31.6	15.9
Polyamide-6 + Cloisite® 15A + E-BA-MAH (PC-I)	30.6	15.8
Polyamide-6 + Cloisite® 15A + E-BA-MAH (IC-P)	30.6	15.6

Figure 4.4 shows XRD patterns of polyamide-6/Cloisite® 15A/E-GMA nanocomposites processed by different addition orders whereas Table 4.2 shows d-spacing data of the same materials. As it is observed from table, original d₁ and d₂ d-spacing of organoclay Cloisite® 15A did not change significantly when it was blended with polyamide-6 and E-GMA elastomer in all addition orders, like the nanocomposites having Cloisite® 15A and E-BA-MAH. The same phenomena is observed here, thus, the same explanations are valid for this system. According to Homminga et al., formation of a polymer/clay nanocomposite is mostly dependent on the favourable chemical compatibility of its constituents. At sufficient compatibility, the polymer can intercalate the clay layer stacks. The shear forces acting on clay platelets, resulting from addition order of the components, is not effective in intercalation/exfoliation if the polymer matrix and organoclay is marginally compatible. The role of the shear forces in this situation, is particularly to facilitate the intercalation process by breaking-up the original clay agglomerates and large primary clay particles into smaller sized primary clay particles (Homminga, et al., 2005).

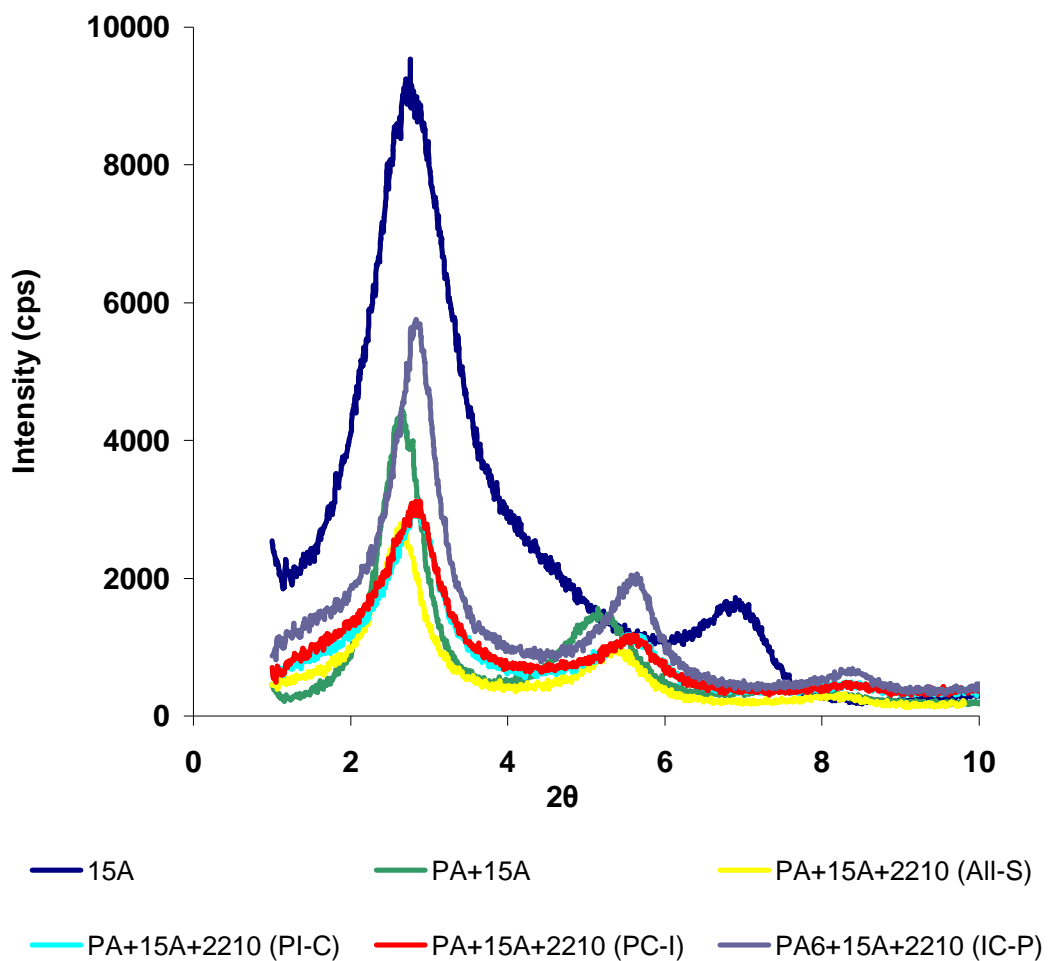


Figure 4.2 XRD patterns of polyamide-6/Cloisite® 15A/E-BA-MAH nanocomposites processed by different addition orders

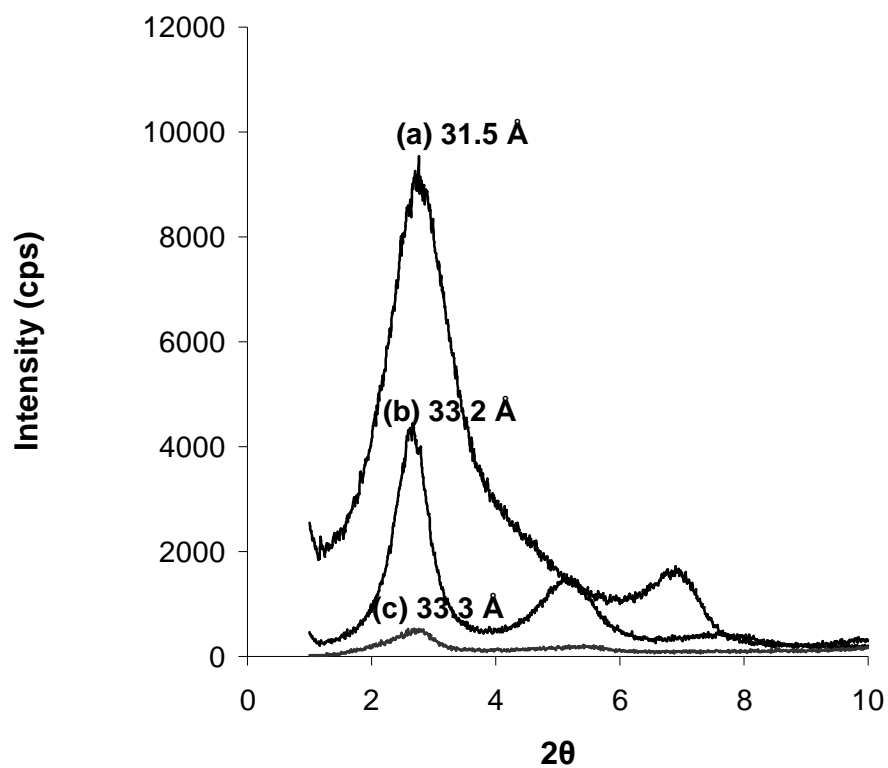


Figure 4.3 XRD patterns for (a) Cloisite® 15A (b) Polyamide-6/Cloisite® 15A nanocomposite (c) Polyamide-6/Cloisite® 15A/E-GMA nanocomposite processed by All-S sequence

Table 4.2 d-spacing data of polyamide-6/Cloisite® 15A/E-GMA nanocomposites processed by different addition order

	d ₁ d-spacing (Å)	d ₂ d-spacing (Å)
Pure Cloisite® 15A in powder form	31.5	12.8
Polyamide-6 + Cloisite® 15A	33.2	17.0
Polyamide-6 + Cloisite® 15A + E-GMA (All-S)	33.3	16.2
Polyamide-6 + Cloisite® 15A + E-GMA (PI-C)	31.7	15.7
Polyamide-6 + Cloisite® 15A + E-GMA (PC-I)	31.6	15.8
Polyamide-6 + Cloisite® 15A + E-GMA (IC-P)	31.4	15.8

Figure 4.5 shows XRD patterns of pure Cloisite® 15A, polyamide-6/Cloisite® 15A binary nanocomposite and polyamide-6/Cloisite®15A/E-MA-GMA ternary nanocomposite. It is seen from the figure that organoclay d₁ d-spacing is increased from 31.5 Å to 37.9 Å in nanocomposites containing polyamide-6 and E-MA-GMA elastomer. In ternary systems containing polyamide-6/Cloisite® 15A and elastomeric material, E-MA-GMA gives the best results in terms of d-spacing. This may be due to the relatively higher compatibility of organoclay 15A with the resulting polyamide-6/E-MA-GMA polymer blend. Organoclay second diffraction peak is shifted to lower angles for polyamide-6/Cloisite® 15A/E-MA-GMA ternary nanocomposites as seen in Figure 4.5, interlayer spacing is increased to 18.1 Å.

It is seen from Figures 4.1, 4.3 and 4.5 that intensity of both the first and second peak of pure organoclay 15A decreases, indicating transformation of large silicate agglomerates into small tactoids as a result of increased viscosity and shear intensity. Extrusion of polymer matrix twice helped overcome the cohesive forces between the clay layers by the hydrodynamic separation forces of the polymer matrix and provided easier diffusion of polymer chains into the organoclay gallery. Decrease in intensity can be associated with the decrease in the number of layers of individual clay particles (Lee et al., 2005).

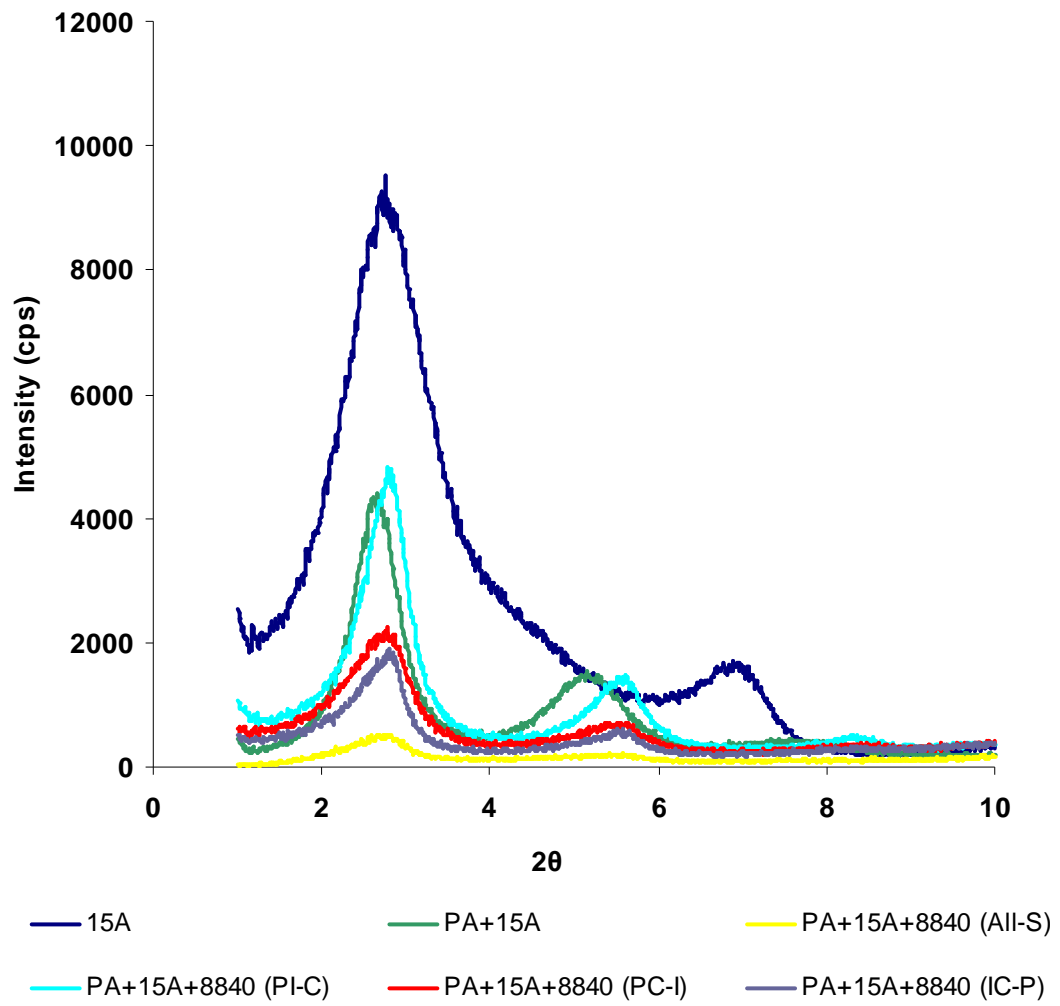


Figure 4.4 XRD patterns of polyamide-6/Cloisite® 15A/E-GMA nanocomposites processed by different addition order

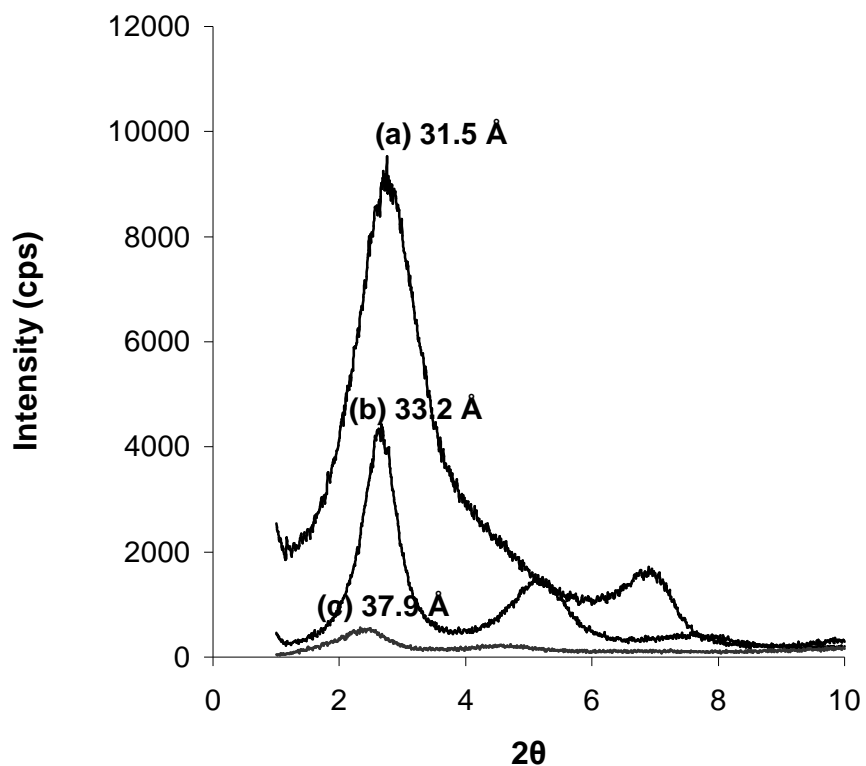


Figure 4.5 XRD patterns for (a) Cloisite® 15A (b) Polyamide-6/Cloisite® 15A nanocomposite (c) Polyamide-6/Cloisite® 15A/E-MA-GMA nanocomposite processed by All-S sequence

4.1.2 X-Ray Analysis Results of Organoclay Cloisite® 25A Containing Nanocomposites

Figure 4.6 shows XRD patterns of pure Cloisite® 25A, binary nanocomposite containing Polyamide-6/Cloisite® 25A and ternary nanocomposite of polyamide-6/ Cloisite® 25A/E-BA-MAH. The organoclay XRD pattern reveals an intense peak at around $2\theta = 4.75^\circ$ corresponding to basal spacing of 18.6 Å. The XRD patterns of binary as well as ternary nanocomposites show that the characteristic peak of the pure organoclay is shifted to lower angles, indicating that polymer

chains are intercalated between the clay galleries. For intercalated nanocomposites, the expansion associated with the polymer intercalation results in the appearance of a new basal reflection corresponding to larger gallery height, which are 30.8 Å (65.6 % increase) and 34.2 Å (83.8 % increase) for polyamide-6/Cloisite® 25A and polyamide-6/Cloisite® 25A/E-BA-MAH nanocomposites, respectively. Also, as it can be seen in Figure 4.6, the peaks of the organoclay in both nanocomposites are very broad. However, peak broadening and intensity changes are very difficult to study systematically in XRD measurements. This, along with the TEM data shown later, indicates that the organoclay used is partly intercalated and partly exfoliated, both in the presence of pure polyamide-6 and E-BA-MAH.

Figure 4.7 shows XRD patterns of polyamide-6/Cloisite® 25A/E-BA-MAH nanocomposites processed by different addition orders, whereas, Table 4.3 shows d-spacing data of the same materials. Organoclay 25A d-spacing is increased in all mixing sequences. All-S and PI-C addition orders give nearly the same d-spacing. This suggests that mixing the three components simultaneously or blending polyamide-6 and E-BA-MAH prior to mixing with clay makes no difference in resulting d-spacing. PC-I sequence, in which polyamide-6/organoclay nanocomposite is prepared first, and then melt blended with elastomer E-BA-MAH, gives the best result in terms of interlayer spacing. In this mixing sequence, polymer-organoclay interactions are maximized. Organoclay interlayer spacing increase in IC-P sequence is relatively lower than the other mixing sequences, mixing organoclay with elastomer prior to polyamide-6 blending may hinder the polymer diffusion into the clay galleries. The diffusion, in which driving force is physical or chemical affinity of the polymer for the organoclay surface, is facilitated by residence time in extruder. In IC-P addition order, organoclay and polyamide-6 interactions are lower than the other addition orders, since clay is extruded with polyamide-6 only once

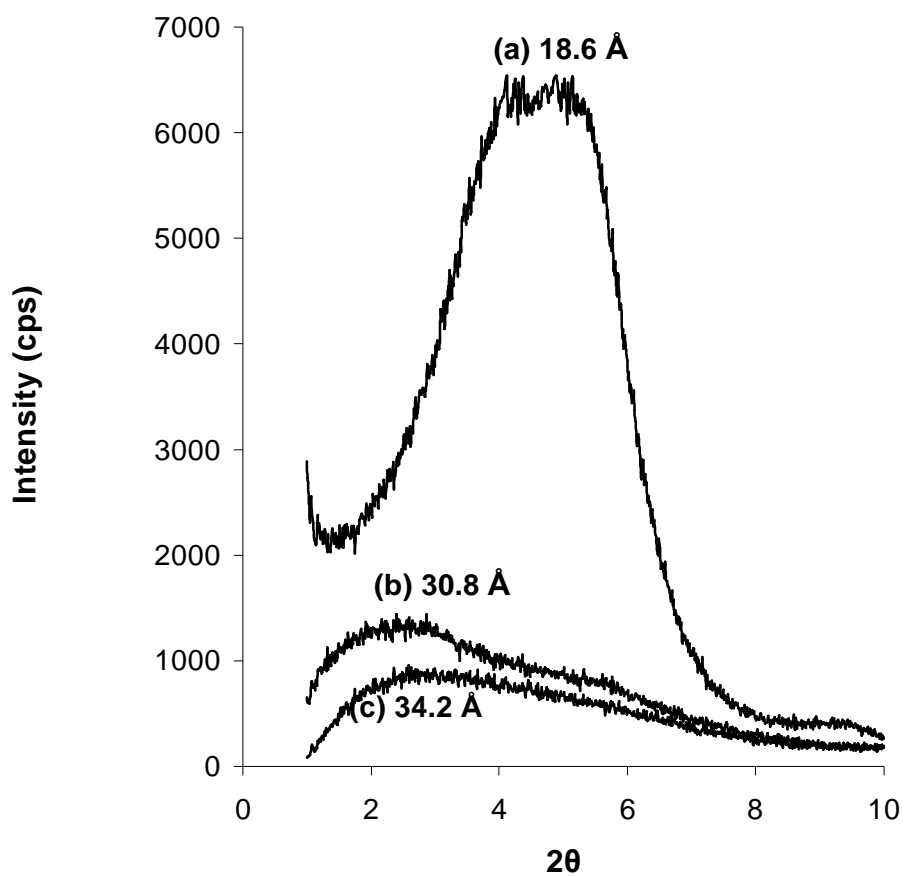


Figure 4.6 XRD patterns for (a) Cloisite® 25A (b) Polyamide-6/Cloisite® 25A nanocomposite (c) Polyamide-6/Cloisite® 25A/E-BA-MAH nanocomposite processed by All-S sequence

Table 4.3 d-spacing data of polyamide-6/Cloisite® 25A/E-BA-MAH nanocomposites processed by different addition orders

	d-spacing (Å)
Pure Cloisite® 25A in powder form	18.6
Polyamide-6 + Cloisite® 25A	30.8
Polyamide-6 + Cloisite® 25A + E-BA-MAH (All-S)	34.2
Polyamide-6 + Cloisite® 25A + E-BA-MAH (PI-C)	34.3
Polyamide-6 + Cloisite® 25A + E-BA-MAH (PC-I)	45.7
Polyamide-6 + Cloisite® 25A + E-BA-MAH (IC-P)	30.4

Figure 4.8 shows XRD spectra of pure Cloisite® 25A, binary nanocomposite containing polyamide-6/Cloisite® 25A and ternary nanocomposite of polyamide-6/ Cloisite® 25A/E-GMA. The interlayer spacing of the clay in ternary nanocomposite is increased nearly 16 Å (85.5 % increase), as compared to the neat organically modified clay, showing that polyamide-6/E-GMA polymer blend chains have entered the clay galleries.

Figure 4.9 shows XRD spectra of pure Cloisite® 25A, binary nanocomposite containing polyamide-6/Cloisite® 25A and ternary nanocomposite of polyamide-6/ Cloisite® 25A/E-MA-GMA. XRD spectra for this ternary nanocomposite shows a very broad characteristic. This result suggests the interlayer spacing of organoclay 25A is mostly expanded over 58.8 Å or the layered-structure of 25A hardly exists in the sample. If Figures 4.6, 4.8 and 4.9 are compared, in ternary nanocomposite systems, it can be seen that d-spacing is increased mostly in the presence of elastomer E-MA-GMA, like the data in Figure 4.5. Due to the relatively higher compatibility of organoclay 25A with the resulting polyamide-6/E-MA-GMA polymer blend, level of intercalation/exfoliation is higher than the other nanocomposites containing organoclay 25A.

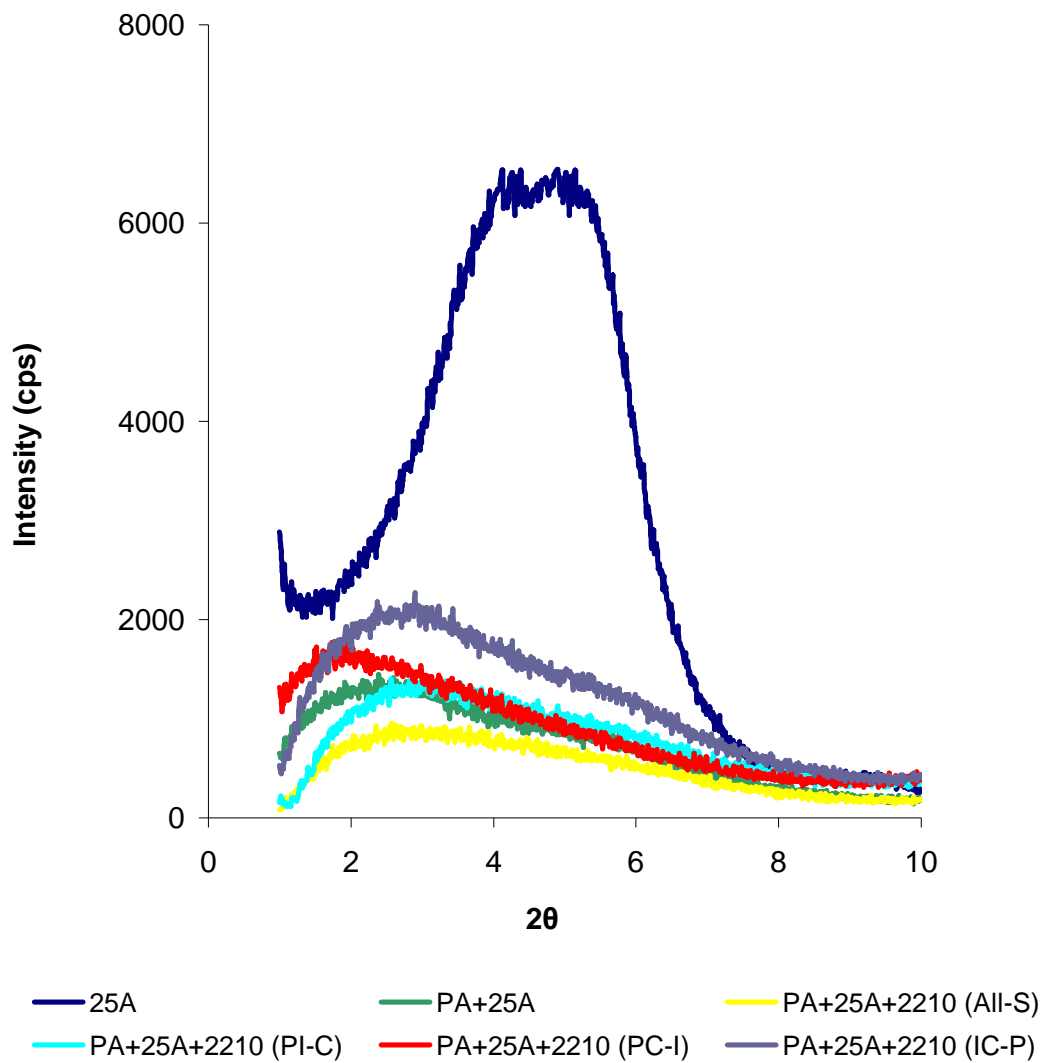


Figure 4.7 XRD patterns of polyamide-6/Cloisite® 25A/E-BA-MAH nanocomposites processed by different addition orders

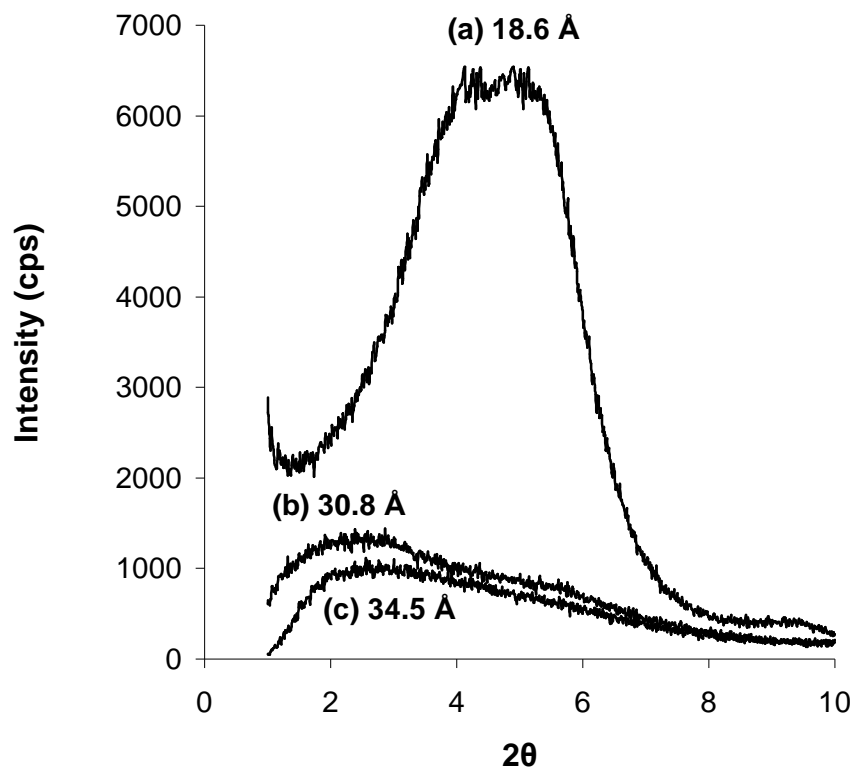


Figure 4.8 XRD patterns for (a) Cloisite® 25A (b) Polyamide-6/Cloisite® 25A nanocomposite (c) Polyamide-6/Cloisite® 25A/E-GMA nanocomposite processed by All-S sequence

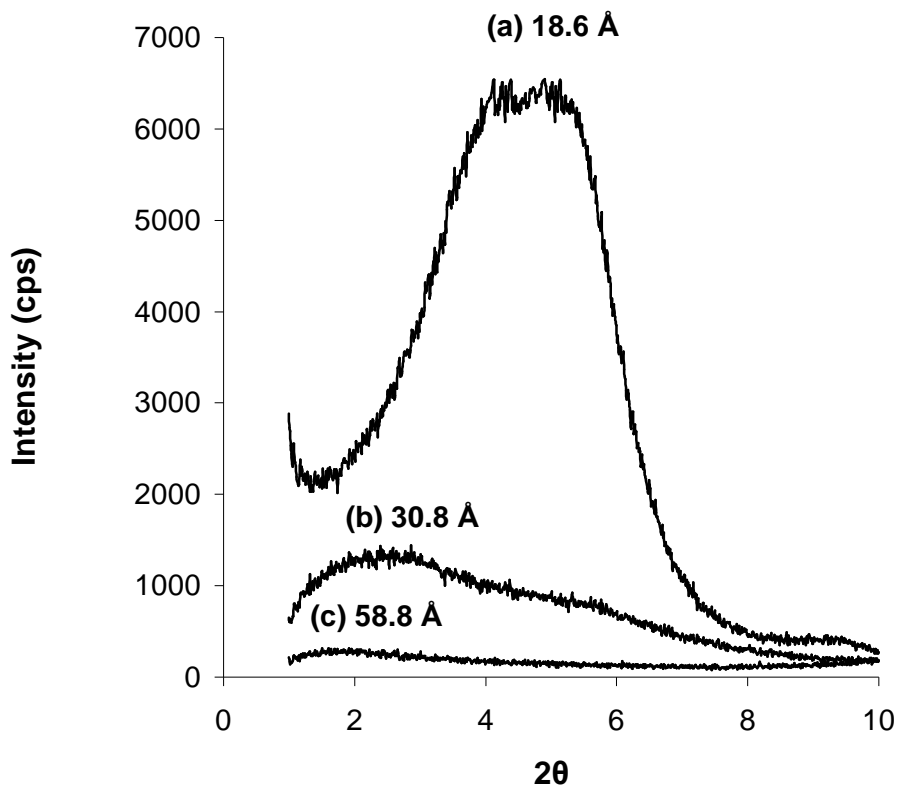


Figure 4.9 XRD patterns for (a) Cloisite® 25A (b) Polyamide-6/Cloisite® 25A nanocomposite (c) Polyamide-6/Cloisite® 25A/E-MA-GMA nanocomposite processed by All-S sequence

4.1.3 X-Ray Analysis Results of Organoclay Cloisite® 30B Containing Nanocomposites

Figure 4.10 shows XRD spectra of pure Cloisite® 30B, binary nanocomposite containing polyamide-6/Cloisite® 30B and ternary nanocomposite of polyamide-6/ Cloisite® 30B/E-BA-MAH. Organoclay d-spacing is increased from 18.5 Å to approximately 41.4 Å (123.8 % increase) and 43.5 Å (135.1 % increase) when melt blended with polyamide and impact modified polyamide-6, respectively. Similar to Figures 4.6, 4.8 and 4.9, XRD patterns for these nanocomposites

exhibit very broad peaks indicating that partially intercalated and partially exfoliated nanocomposites are obtained. Although the initial interlayer spacing for Cloisite® 15A is higher than those of Cloisite® 25A and 30B, no significant change is observed in the d-spacings of nanocomposites with Cloisite® 15A. It might be expected that larger initial d-spacings may lead to easier exfoliation since platelet–platelet attraction is reduced, and diffusion of polymer chains inside the clay galleries is less hindered owing to increased spacing. This process may ultimately lead to improved exfoliation. In part 3.1.3 factors affecting intercalation/exfoliation are discussed. Among the other factors, here, it is observed that compatibility between the clay surface modifier and polymer matrix is essential to get an intercalated/exfoliated nanocomposite.

Figure 4.11 shows XRD spectra of pure Cloisite® 30B, binary nanocomposite containing polyamide-6/Cloisite® 30B and ternary nanocomposite of polyamide-6/ Cloisite® 30B/E-GMA. d-spacing of polyamide-6/Cloisite® 30B/E-GMA nanocomposite is increased by 22.7 Å (122.7 % increase) over the d-spacing of Cloisite® 30B, indicating intercalation. According to suppliers' data, Cloisite® 30B with -OH groups on its modifier, has the least hydrophobic surface among the other organoclays studied. This organoclay is proposed to be the most compatible among the others. XRD analysis reveal this phenomena, the % increase in d-spacing is higher in the nanocomposites containing organoclay 30B than the other organoclays used. This observation suggests that, generally, the degree of intercalation/exfoliation of Cloisite® 30B aggregates in polyamide-6 matrix might be higher than that of Cloisite® 25A and 15A aggregates in polyamide-6. TEM analysis, reported in section 4.2, corroborate the XRD results. This relatively high degree of dispersion of Cloisite® 30B in nanocomposites can be attributed to the existence of attractive interactions via hydrogen bonding between polyamide-6 and Cloisite® 30B organic modifier.

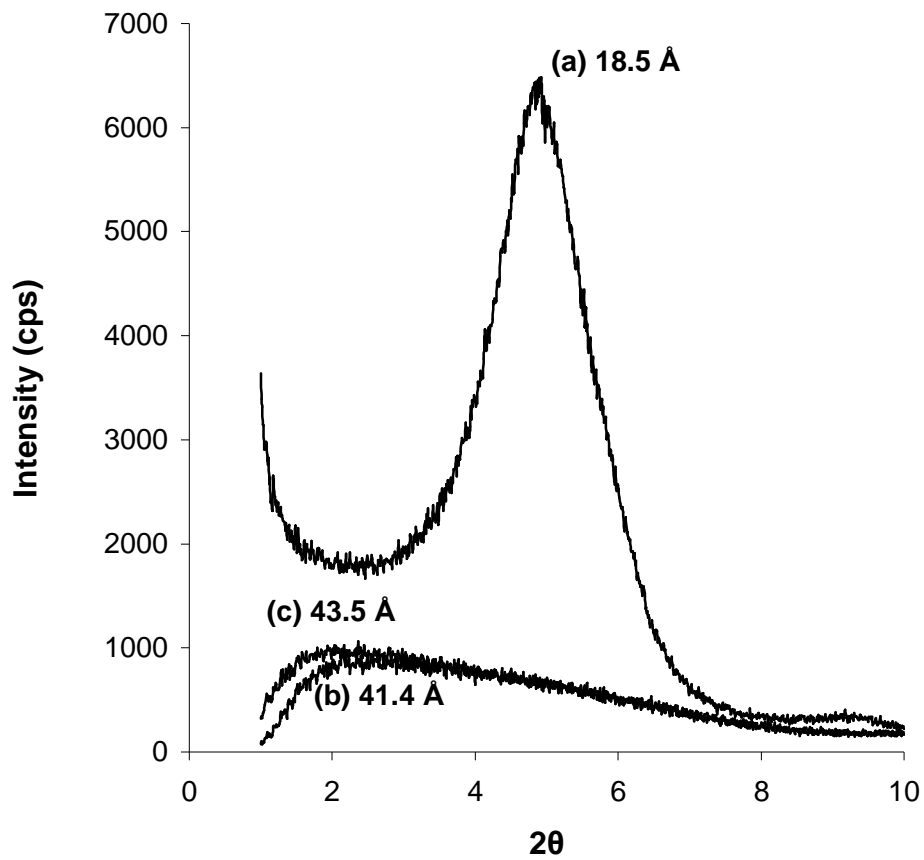


Figure 4.10 XRD patterns for (a) Cloisite® 30B (b) Polyamide-6/Cloisite® 30B nanocomposite (c) Polyamide-6/Cloisite® 30B/E-BA-MAH nanocomposite processed by All-S sequence

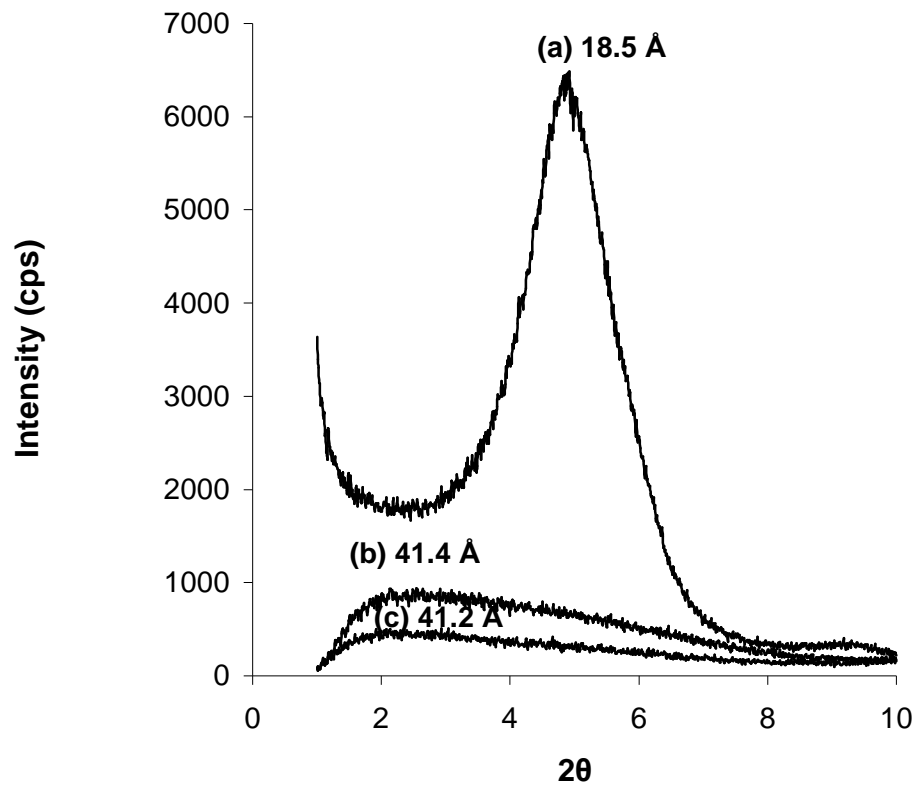


Figure 4.11 XRD patterns for (a) Cloisite® 30B (b) Polyamide-6/Cloisite® 30B nanocomposite (c) Polyamide-6/Cloisite® 30B/E-GMA nanocomposite processed by All-S sequence

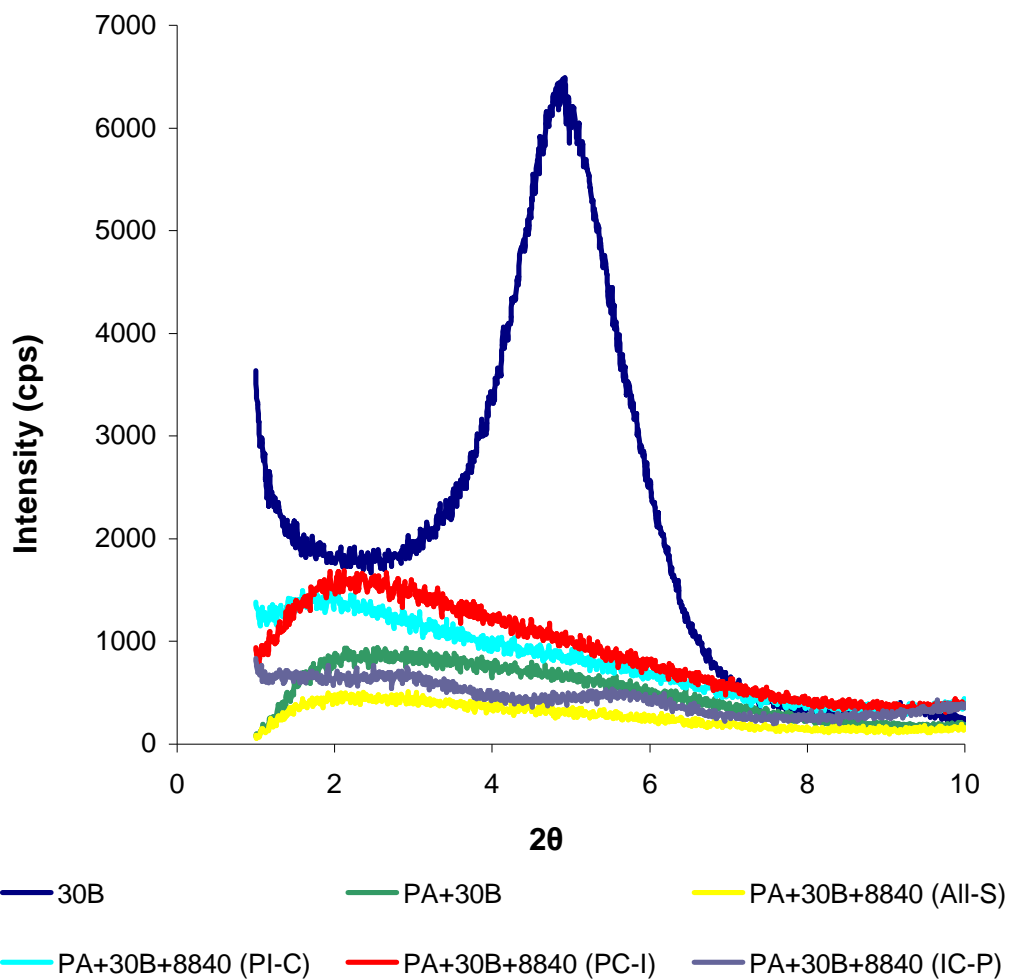


Figure 4.12 XRD patterns of nanocomposites containing Cloisite® 30B and E-GMA processed with different addition orders

Figure 4.12 shows XRD patterns of polyamide-6/Cloisite® 30B/E-GMA nanocomposites processed by different addition orders whereas Table 4.4 shows d-spacing data of the same materials. All-S and PC-I addition orders give nearly the same d-spacing. PI-C and IC-P sequences give the highest d-spacing values. IC-P sequence, in which organoclay/elastomer E-GMA mixture is prepared first, then melt blended with polyamide-6, gives the best result in terms of intercalation/exfoliation. The absence of diffraction peaks corresponding to the interlayer spacing means that ordered clay morphology in the polymer matrix is disrupted and an exfoliated nanostructure is obtained (Usuki et al.,2002). As it is mentioned before, Cloisite® 30B is the only organoclay containing -OH functional

groups on its modifier surface. In this mixing sequence, during organoclay and elastomer mixing, there might be a reaction between GMA and -OH functional groups. Due to these strong interactions, and the compatibility of organoclay with polyamide-6 exfoliated nanostructure is obtained.

Table 4.4 d-spacing data of nanocomposites containing Cloisite 30B and E-GMA processed with different addition orders

	d-spacing (Å)
Pure Cloisite® 30B in powder form	18.5
Polyamide-6 + Cloisite® 30B	41.4
Polyamide-6 + Cloisite® 30B + E-GMA (All-S)	41.2
Polyamide-6 + Cloisite® 30B + E-GMA (PI-C)	55.5
Polyamide-6 + Cloisite® 30B + E-GMA (PC-I)	41.6
Polyamide-6 + Cloisite® 30B + E-GMA (IC-P)	88.23 / exfoliation

Figure 4.13 shows XRD spectra of pure Cloisite® 30B, binary nanocomposite containing polyamide-6/Cloisite® 30B and ternary nanocomposite of polyamide-6/ Cloisite® 30B/E-MA-GMA. According to the spectra, it is seen that Cloisite® 30B is intercalated between the polymer matrix. The presence of these peaks indicated that the organoclay morphology can not be fully exfoliated. However, with such a peak it can not be excluded that the morphology contains both intercalated stacks and exfoliated individual silicate layers. d-spacing of organoclay 30B is higher in polyamide-6/Cloisite® 30B/E-MA-GMA nanocomposite than the polyamide-6/Cloisite® 30B/E-BA-MAH, polyamide-6/Cloisite® 30B/E-GMA and polyamide-6/organoclay/E-MA-GMA nanocomposites.

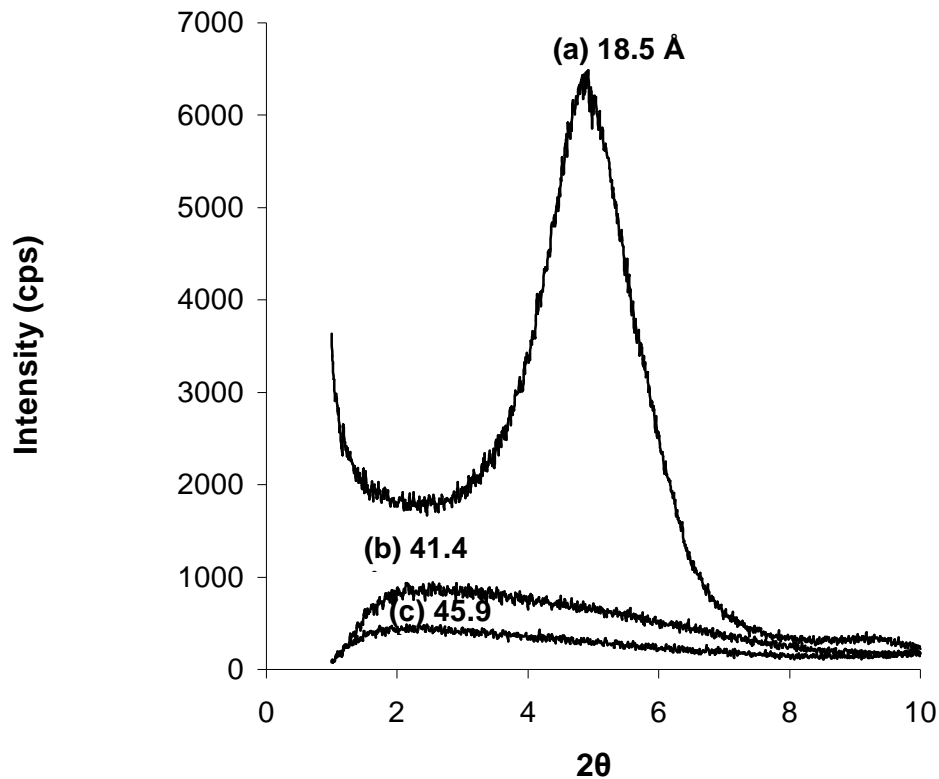


Figure 4.13 XRD patterns for (a) Cloisite® 30B (b) Polyamide-6/Cloisite® 30B nanocomposite (c) Polyamide-6/Cloisite® 30B/E-MA-GMA nanocomposite processed by All-S sequence

4.2 TEM ANALYSIS

It is hard to comment about the distribution of the silicate layers or any structural non-homogeneity in nanocomposites by XRD analysis. Conclusions about the formation mechanism of nanocomposites and their structure based on XRD patterns are only tentative. On the other hand, TEM allows a qualitative understanding of the internal structure, distribution of the various phases, and views of the defect structure through direct visualization.

4.2.1 TEM Analysis Results of Organoclay Cloisite® 15A Containing Nanocomposites

TEM micrograph of polyamide-6 nanocomposite sample having no elastomer but 2 weight % Cloisite® 15A is shown in Figure 4.14. In the micrographs, the dark lines represent the thickness of individual clay layers or their agglomerates (tactoids) whereas the gray/white areas represent the polymer matrix. Several dark lines are observed indicating stacked silicate layers that are formed due to clustering and agglomeration. From XRD analysis it is noted that little change is observed in Cloisite® 15A clay d-spacing when melt blended with polyamide-6.

Figure 4.15 shows the TEM micrograph of polyamide-6/Cloisite® 15A/E-BA-MAH nanocomposite processed by All-S mixing sequence, whereas Figure 4.16 shows TEM micrograph of polyamide-6/Cloisite® 15A/E-GMA ternary nanocomposite sample processed in the same mixing sequence. In these two micrographs stacked silicate layers as darker lines can be easily seen. This finding is consistent with the XRD analysis as no change in d-spacing of pure organoclay is observed in ternary nanocomposites composed of polyamide-6 and elastomer.

If Figures 4.14 through 4.16 are evaluated, it can be observed that nanocomposites with Cloisite® 15A contain small fraction of dispersed features involving one or two layered silicate layers as well as large fraction of intercalated multi-layered clay platelet stacks. It is interesting to note that the morphology seen by TEM is somewhat different than that predicted by XRD. TEM figures indicate the presence of both intercalated structures and some delaminated platelets; while XRD results in Figures 4.2 and 4.3 suggest only a low degree of intercalation, since delaminated layers can not be observed in TEM analysis.

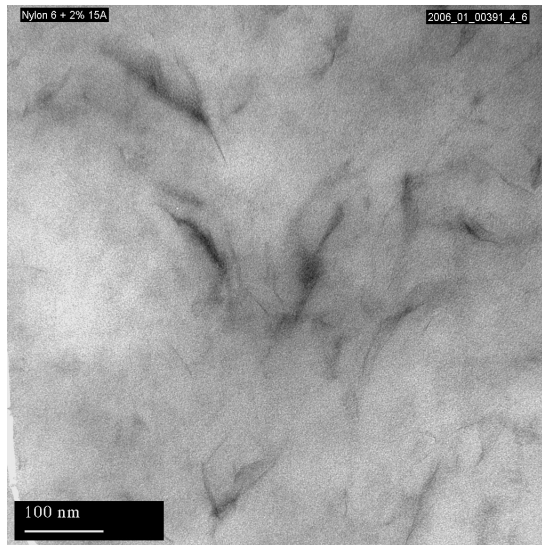


Figure 4.14 TEM micrograph of polyamide-6/Cloisite® 15A nanocomposite

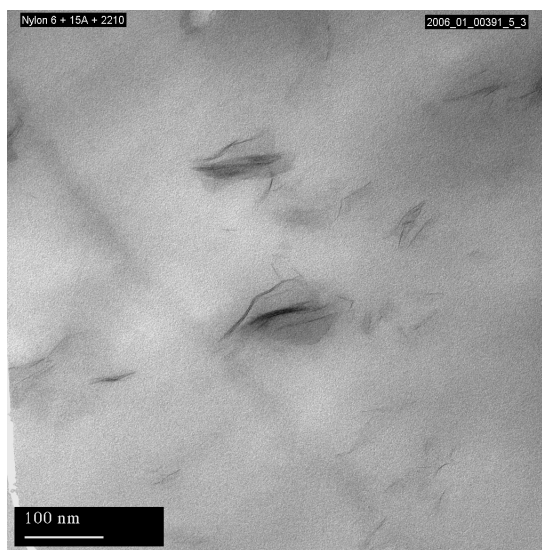


Figure 4.15 TEM micrograph of polyamide-6/Cloisite® 15A/E-BA-MAH nanocomposite processed by All-S sequence

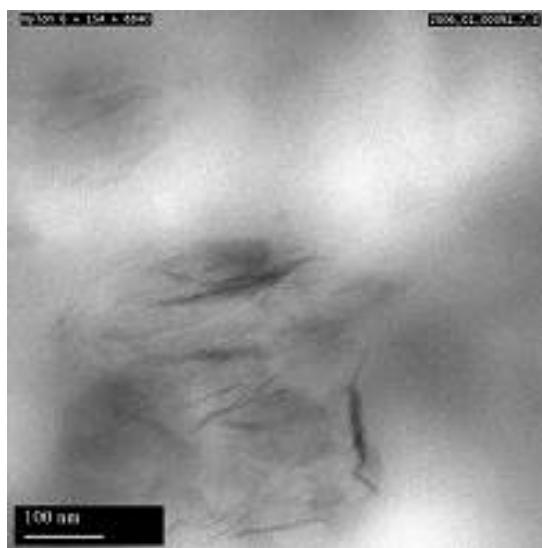


Figure 4.16 TEM micrograph of polyamide-6/Cloisite® 15A/E-GMA nanocomposite processed by All-S sequence

4.2.2 TEM Analysis Results of Organoclay Cloisite® 25A Containing Nanocomposites

Figure 4.17 shows TEM micrograph of polyamide-6 nanocomposite sample having 2 weight % Cloisite® 25A and no elastomer. The micrograph reveals that organoclay is uniformly dispersed and exfoliated in the polyamide-6 matrix. The average thickness of clay appears to be just a few nanometers, whereas the average length is approximately 100 nm. From XRD analysis, it is found that characteristic clay diffraction peak for Cloisite® 25A is shifted to lower 2θ angles indicating intercalation. Thus, it can be concluded that polyamide-6/Cloisite® 25A nanocomposite has a partially exfoliated and partially intercalated structure.

Figure 4.18 shows the TEM micrograph of polyamide-6/Cloisite® 25A/E-BA-MAH ternary nanocomposite sample. In the micrograph, both individual clay layers or their agglomerates (tactoids) and some stacked silicate layers, which are formed due to clustering, can be observed. The addition of elastomeric material hardly altered the organoclay 25A dispersibility in the nanocomposites. The white dispersed domains correspond to elastomer phases in the micrograph. In

agreement with the results reported by Khatua et al., (2004) and Baldi et al., (2006), clay platelets are not seen in the elastomer domains. Although minor amount of clay might be incorporated in the elastomer phase, it may be assumed that most of the platelets are contained in the polyamide-6 matrix.

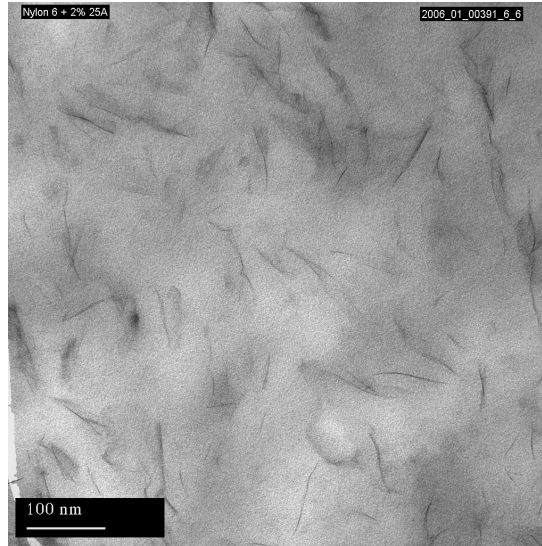


Figure 4.17 TEM micrograph of polyamide-6/Cloisite® 25A nanocomposite

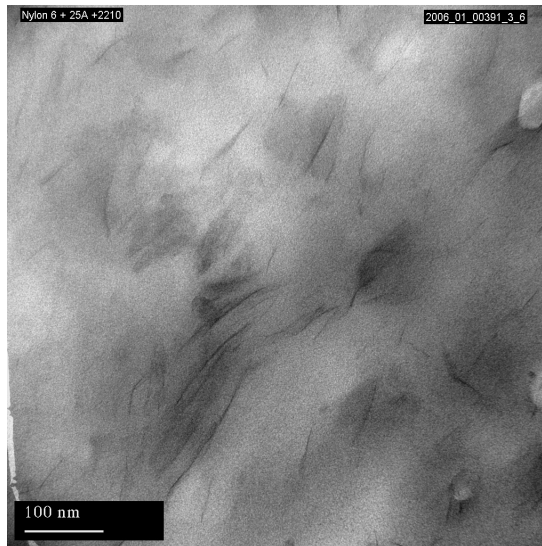


Figure 4.18 TEM micrograph of polyamide-6/Cloisite® 25A/E-BA-MAH nanocomposite processed by All-S sequence

4.2.3 TEM Analysis Results of Organoclay Cloisite® 30B Containing Nanocomposites

Figure 4.19 shows TEM micrograph of polyamide-6 nanocomposite sample having 2 weight % Cloisite® 30B and no elastomer. According to the micrograph, Cloisite® 30B is uniformly dispersed and exfoliated in polyamide-6 matrix. XRD analysis reveal that when Cloisite® 30B is melt blended with polyamide-6, a significantly intercalated structure is obtained. Thus, it can be concluded that polyamide-6/Cloisite® 30B nanocomposite has a mixed morphological structure, i.e. combination of intercalated stacks and exfoliated particles. If a comparison is made between Figures 4.14 , 4.17 and 4.19, it can be seen that degree of dispersion of Cloisite® 25A and 30B layers in polyamide-6 matrix is higher than the degree of dispersion of Cloisite® 15A layers in polyamide-6. The above observation is consistent with the X-ray data and is attributed to the higher compatibility of these organoclays with the polymer matrix.

Figure 4.20 shows TEM micrograph of polyamide-6/Cloisite® 30B/E-GMA ternary nanocomposite sample. Similar to the observation seen in Figure 4.18, white dispersed domains correspond to elastomer phases in the micrograph. Clay platelets are not seen in the elastomer domains. Rubber particles seem to affect the alignment of clay platelets in the nearby region. Organoclay 30B is observed to be partially exfoliated into a thinner multi-layered structure or even single layer in the micrographs. But thicknesses of clay platelets seem to be higher than the polyamide-6/Cloisite® 30B nanocomposite with no elastomer. If Figures 4.19 and 4.20 are compared, slightly altered organoclay dispersibility with the addition of elastomeric material can be observed. The presence of reactively formed copolymer suppresses the exfoliation in and near the interfacial area. Similar results are observed by Kelnar et al. (2006).

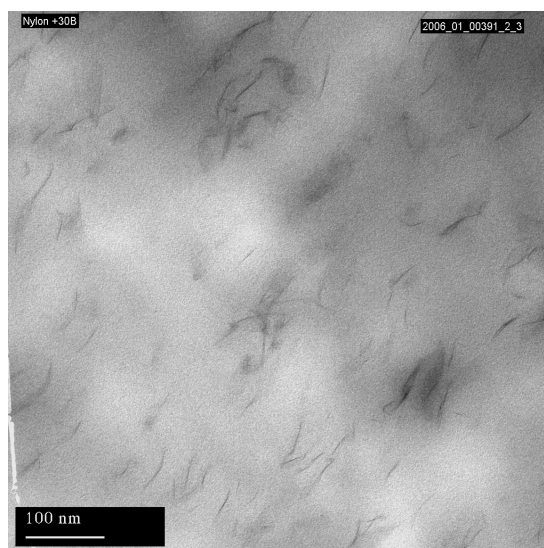


Figure 4.19 TEM micrograph of polyamide-6/Cloisite® 30B nanocomposite

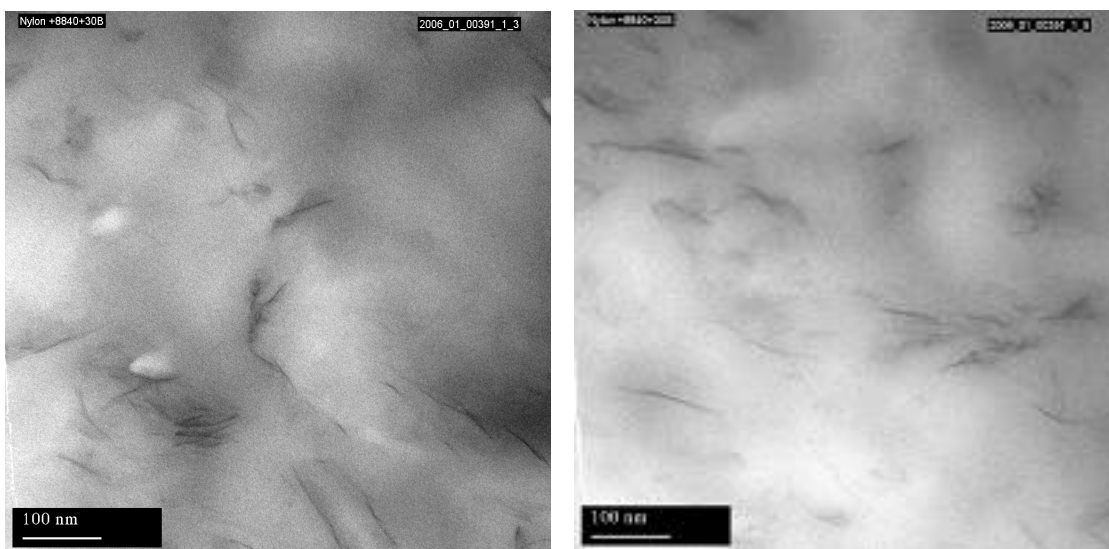


Figure 4.20 TEM micrographs of polyamide-6/Cloisite® 30B/E-GMA nanocomposite processed by All-S sequence

4.3 SEM ANALYSIS

SEM analysis is performed to determine the particle size and the distribution of elastomer particles in the polymer matrix, since these factors, along with the interparticle distance, are very important parameters in toughening mechanism. Figure 4.21 represents the fracture surfaces of unfilled polyamide-6 at magnitude of x300. The surface is featureless and few straight crack lines can easily be seen, indicative of low impact strength.

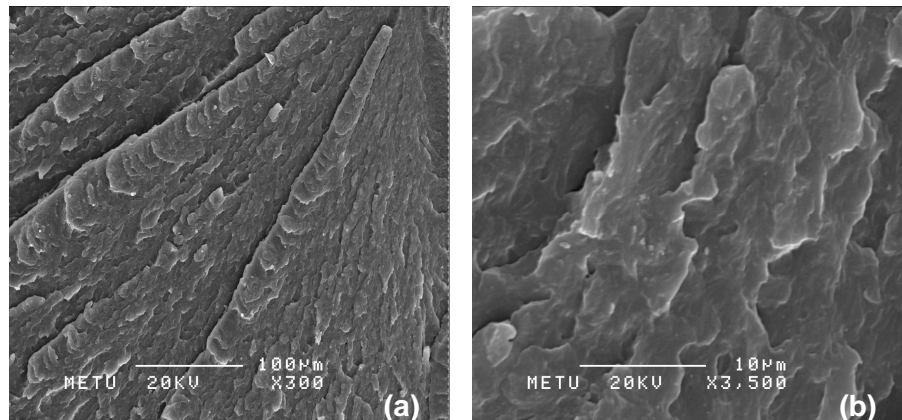


Figure 4.21 Fracture surface of unfilled polyamide-6 sample (a) x300 magnification (b) x3500 magnification

Figures 4.22-4.24 show the micrographs of binary blends containing 5, 10 and 15-wt % E-BA-MAH but no organoclay, respectively. It is obvious that featureless structure of unfilled polyamide-6 disappears when melt blended with elastomeric material. The micrographs show two-phase, particle-in-matrix morphology. Some voids have regular spherical shape while others are ellipsoidal, they are scattered throughout the matrix. The dispersion of minor phase during melt blending involves the stretching of drop-like particles until fibers are formed; then, filaments rupture to form smaller drops, after that these drops coalesce to create larger ones. The balance of these processes determine the final particle size, which is controlled by the viscosity and melt elasticity of the components, shear stresses and rates, the mobility of the interface, and the surface tension. Lower

tension promotes the stretching of smaller drops producing a very fine morphology (Contreras et al., 2006). Wu et al., 1985, proposed that there must be some degree of adhesion or coupling between the rubber and matrix phases. By this way, necessary adhesion is provided. The maleic anhydride groups of E-BA-MAH elastomer can react with polyamide amine end groups and form a graft copolymer at rubber matrix interface, which will be shown in Section 4.4.1. Table 4.5 shows elastomer domain sizes in polyamide-6/elastomer blends. It is seen that as the elastomer amount increases domain size decreases in polyamide-6/E-BA-MAH blends.

Table 4.5. Elastomer domain sizes in polyamide-6/elastomer blends

	Domain size (nm)
Polyamide-6 / 5 weight % E-BA-MAH	53.7 ± 5.6
Polyamide-6 / 10 weight % E-BA-MAH	47.3 ± 4.9
Polyamide-6 / 15 weight % E-BA-MAH	45.7 ± 5.9
Polyamide-6 / 5 weight % E-GMA	106.1 ± 5.0
Polyamide-6 / 10 weight % E-GMA	176.6 ± 9.2
Polyamide-6 / 15 weight % E-GMA	182.3 ± 9.6
Polyamide-6 / 5 weight % E-MA-GMA	85.4 ± 6.7
Polyamide-6 / 10 weight % E-MA-GMA	135.2 ± 6.0
Polyamide-6 / 15 weight % E-MA-GMA	151.9 ± 9.6

The decrease in domain size upon increasing amount of E-BA-MAH is ascribed to the formation of graft copolymer during the blending process by the imidation reactions. This graft copolymer either forms or migrates to the interface between the two components, lowering the interfacial energy and improving the interfacial adhesion. In this way, it contributes to the stability of the dispersed phase against segregation during further processing (MacKnight et.al., 1985). Reaction reduces interfacial tension and retards particle coalescence (Carone Jr et. al., 2000). The rubber domain size is probably the most critical factor to achieve effective

toughening. It is recognized that rubber domains must be smaller than 1 μm to give super-tough polyamide materials (Oshinski et al., 1992, Oshinski et al., 1996). Figures 4.25-4.27 show the micrographs of binary blends containing 5, 10 and 15 wt % E-GMA but no organoclay, respectively. It is seen that as elastomer amount increases in the polymer matrix, domain sizes increase, similar to polyamide-6/E-GMA blends seen in the Figures 4.28-4.30.

It is seen from Tables 4.5 that MAH based elastomer domains are much more smaller than the GMA based elastomer domains. According to Takeda et al., 1992, the size of rubber particles in reactive blends depends on the rubber or polyamide functionality. Since GMA can react with both amine and acid ends of polyamide-6, unlike MAH, these grafting reactions may lead to some crosslinking which may inhibit elastomeric domain breakdown in the extruder (Kudva et al., 1998, Majumdar et al., 1997).

Figure 4.31 shows the micrographs of a sample containing 2 % organoclay Cloisite® 15A but no elastomer. Crack lines going top right to bottom left in the surface structure and homogenous dispersion of clay particles are observed. Considerable surface roughness indicates that the cracks progressed along a more tortuous path. This increases the fracture surface area and the toughness, tensile strength and Young's Modulus. Figure 4.32 and 4.33 show the micrographs of a sample containing 2 % organoclay Cloisite® 25A and 30B but no elastomer, respectively. Crack lines can be easily observed in the micrographs.

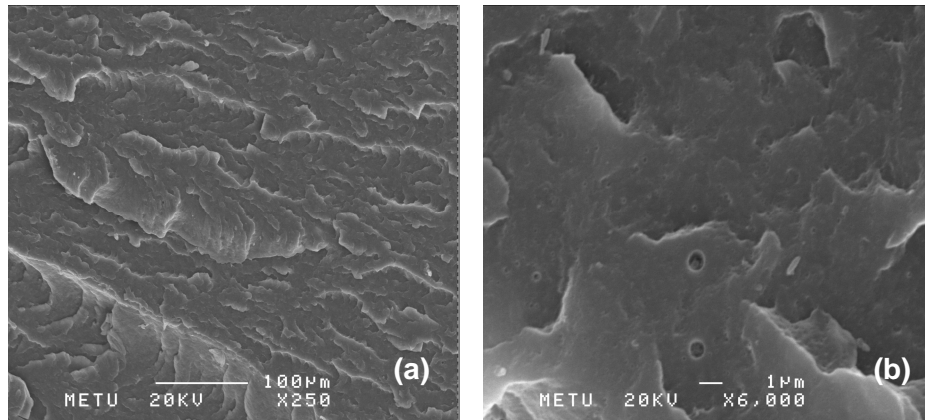


Figure 4.22 Fracture surface of polyamide-6/5 wt % E-BA-MAH elastomer blend
 (a) x250 magnification (b) x6000 magnification

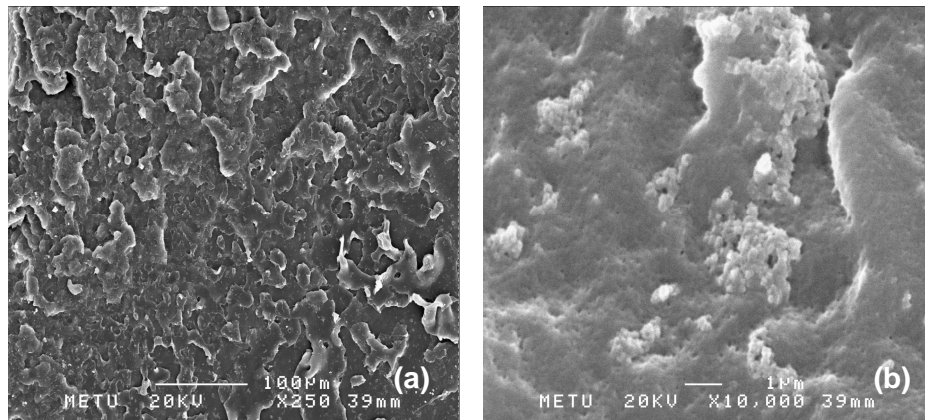


Figure 4.23 Fracture surface of polyamide-6/10 wt % E-BA-MAH elastomer blend
 (a) x250 magnification (b) x10000 magnification

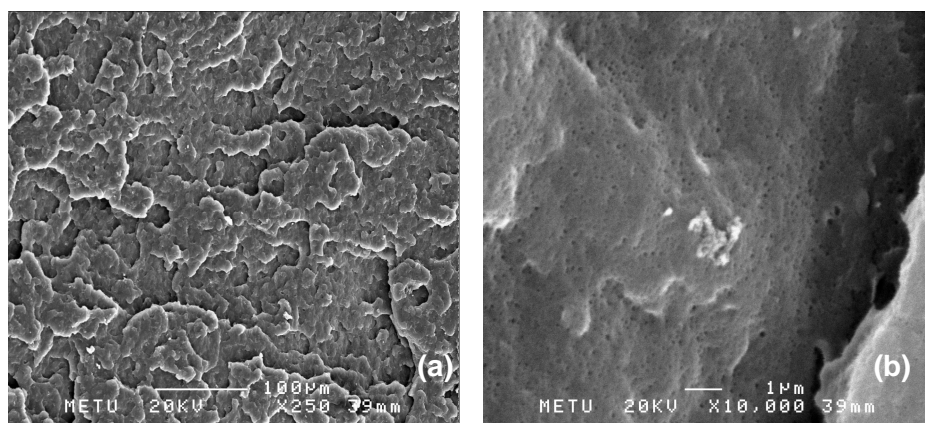


Figure 4.24 Fracture surface of polyamide-6/15 wt % E-BA-MAH elastomer blend
 (a) x250 magnification (b) x10000 magnification

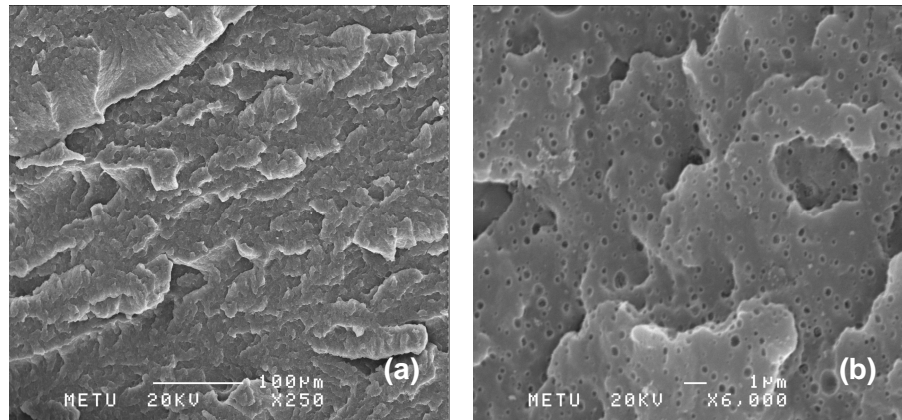


Figure 4.25 Fracture surface of polyamide-6/5 wt % E-GMA elastomer blend (a) x250 magnification (b) x6000 magnification

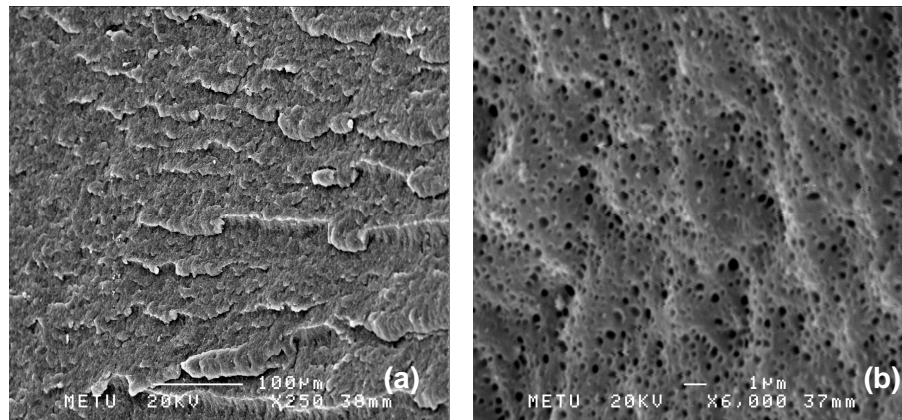


Figure 4.26 Fracture surface of polyamide-6/10 wt % E-GMA elastomer blend (a) x250 magnification (b) x6000 magnification

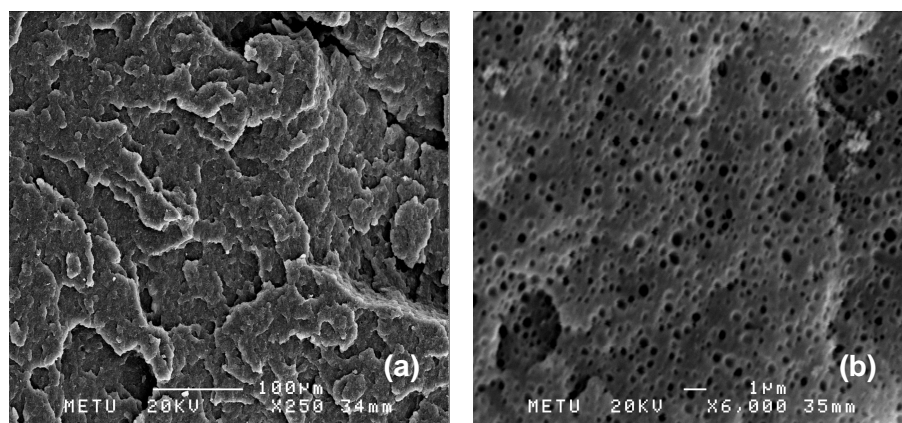


Figure 4.27 Fracture surface of polyamide-6/15 wt % E-GMA elastomer blend (a) x250 magnification (b) x6000 magnification

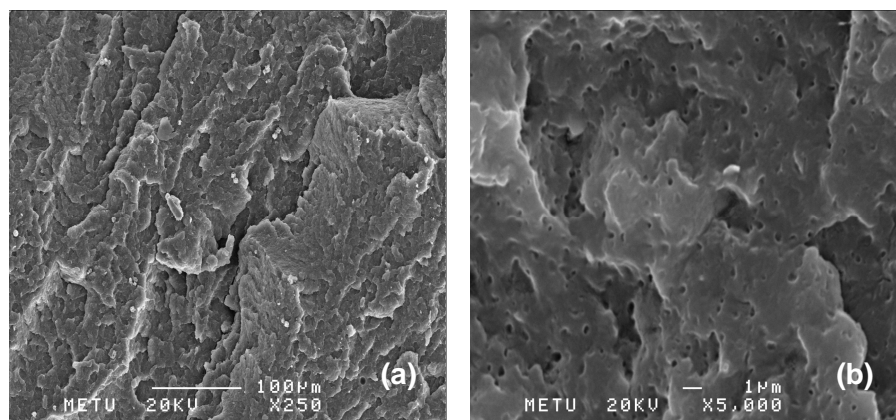


Figure 4.28 Fracture surface of polyamide-6/5 wt % E-MA-GMA elastomer blend (a) x250 magnification (b) x5000 magnification

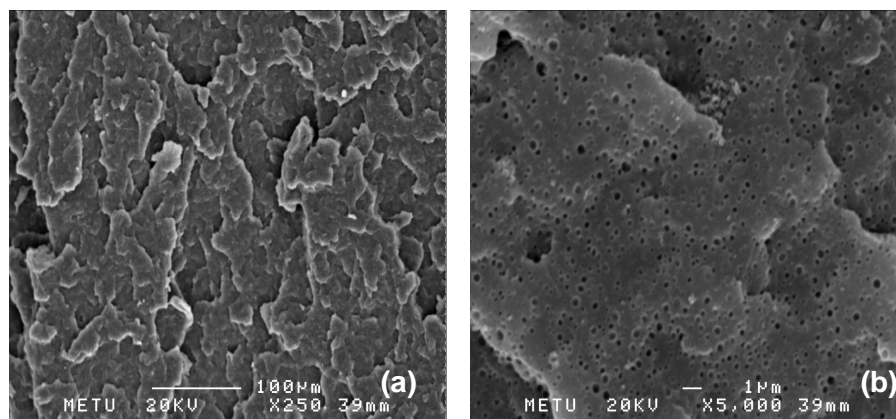


Figure 4.29 Fracture surface of polyamide-6/10 wt % E-MA-GMA elastomer blend (a) x250 magnification (b) x5000 magnification

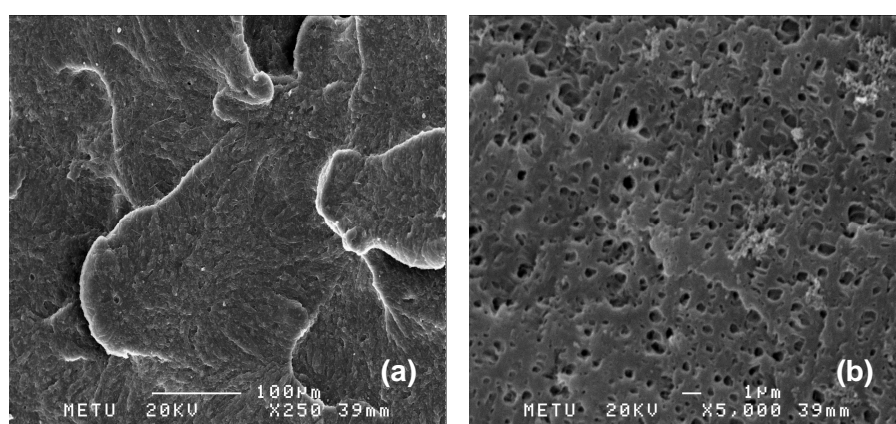


Figure 4.30 Fracture surface of polyamide-6/15 wt % E-MA-GMA elastomer blend (a) x250 magnification (b) x5000 magnification

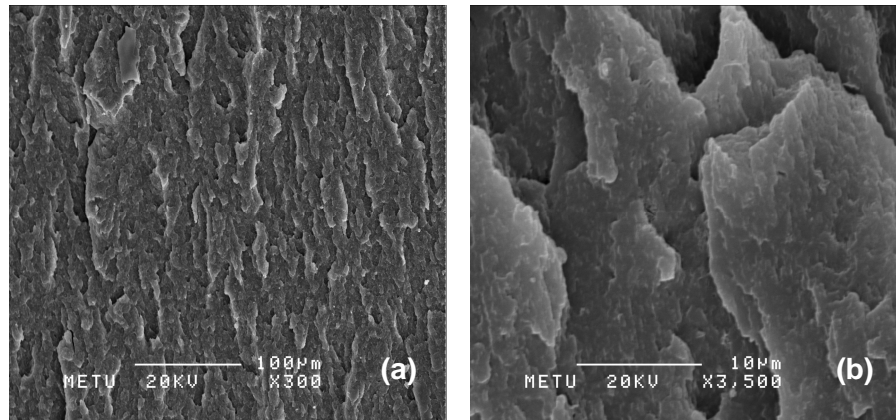


Figure 4.31 Fracture surface of polyamide-6/Cloisite® 15A nanocomposite (a) x300 magnification (b) x3500 magnification

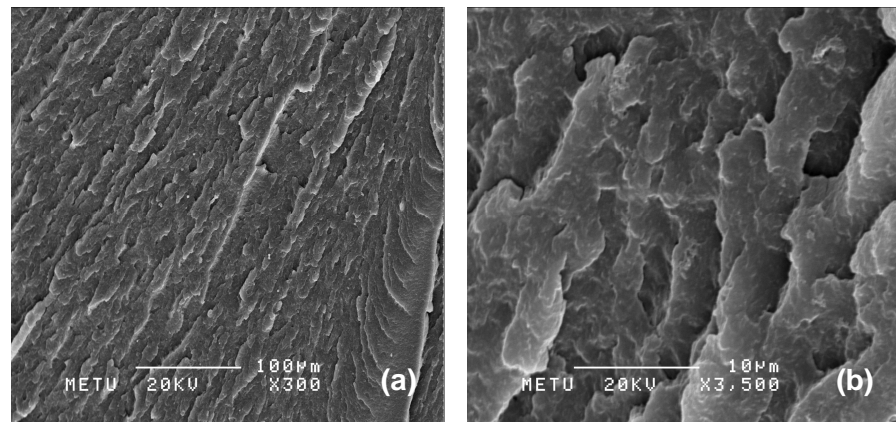


Figure 4.32 Fracture surface of polyamide-6/Cloisite® 25A nanocomposite (a) x300 magnification (b) x3500 magnification

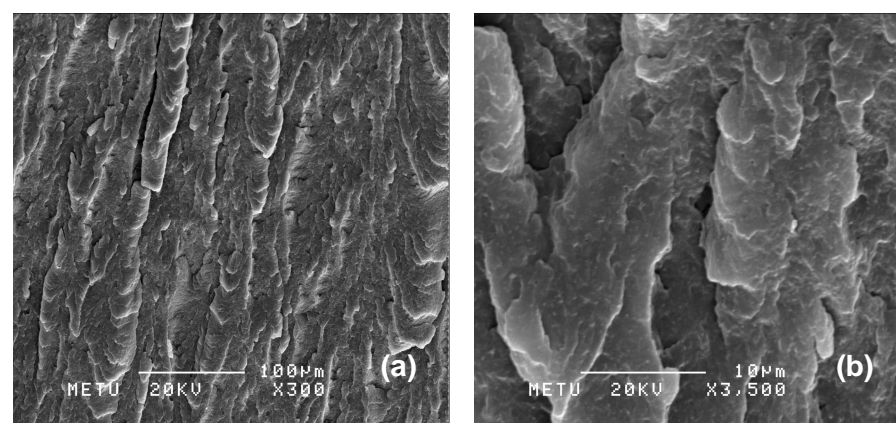


Figure 4.33 Fracture surface of polyamide-6/Cloisite® 30B nanocomposite (a) x300 magnification (b) x3500 magnification

4.3.1 SEM Analysis Results of Elastomer E-BA-MAH Containing Nanocomposites

Figures 4.34 through 4.36 show fracture surfaces of polyamide-6/Cloisite® 15A/E-BA-MAH, polyamide-6/Cloisite® 25A/E-BA-MAH and polyamide-6/Cloisite® 30B/E-BA-MAH nanocomposites, respectively. Domain sizes of elastomeric phases can be observed in Table 4.6. Data reveal that clay surfactant type affects domain size, since particle size is smaller in Cloisite® 30B containing ternary nanocomposites than the others. Interaction between elastomer maleic anhydride groups and organoclay hydroxyethyl groups may lead to an increase in viscosity and to a decrease in particle size. MFI measurements analyzed later showed that this ternary nanocomposite has higher viscosity than the ternary system having E-BA-MAH elastomer and processed by All-S sequence (see Table 4.14).

Table 4.6 Elastomer domain sizes in polyamide-6/organoclay/E-BA-MAH nanocomposites

	Domain size (nm)
Polyamide-6 + E-BA-MAH (5 wt %)	53.7 ± 5.6
Polyamide-6 + Cloisite® 15A + E-BA-MAH (All-S)	52.4 ± 6.3
Polyamide-6 + Cloisite® 25A + E-BA-MAH (All-S)	52.0 ± 4.8
Polyamide-6 + Cloisite® 30B + E-BA-MAH (All-S)	45.5 ± 7.3
Polyamide-6 + Cloisite® 15A + E-BA-MAH (PI-C)	58.6 ± 9.4
Polyamide-6 + Cloisite® 15A + E-BA-MAH (PC-I)	60.7 ± 5.6
Polyamide-6 + Cloisite® 15A + E-BA-MAH (IC-P)	62.5 ± 8.3
Polyamide-6 + Cloisite® 25A + E-BA-MAH (PI-C)	49.6 ± 7.0
Polyamide-6 + Cloisite® 25A + E-BA-MAH (PC-I)	67.2 ± 9.2
Polyamide-6 + Cloisite® 25A + E-BA-MAH (IC-P)	55.3 ± 6.1

Figures 4.37-4.39 represent SEM micrographs polyamide-6/Cloisite® 15A/E-BA-MAH ternary nanocomposites processed by different mixing orders. In these nanocomposites, clay tactoids can be observed in SEM micrographs at x250 magnification, supporting XRD results. As shown in the figures, dispersed rubber particles are very small, their size range from 50 to 60 nm (Table 4.6). Their shape seems to be either spherical in most cases or with some imperfections. According to Table 4.6, IC-P sequence, in which elastomer and organoclay are mixed prior to polyamide-6, gives the highest domain size in comparison to other mixing orders in polyamide-6/Cloisite® 15A/E-BA-MAH nanocomposites. Mixing elastomer with polyamide-6 in the second extrusion step, only once, limited its dispersion.

SEM micrographs polyamide-6/Cloisite® 25A/E-BA-MAH ternary nanocomposites processed by different mixing orders can be observed in Figures 4.40-4.42. In the micrographs, crack lines and also distribution and cavitation effect of elastomer are observed. Table 4.6 shows the effect of mixing order on E-BA-MAH domains in polyamide-6/Cloisite® 25A nanocomposites. In PC-I mixing sequence, elastomer domain size is bigger than the other sequences. As processing conditions are the same for all the samples, the viscosity of the matrix and the interfacial tension are the main parameters responsible for the change in particle size observed in Table 4.6 (González, et al., 2006). Table 4.14 shows the effect of mixing order on MFI of polyamide-6/Cloisite® 25A/E-BA-MAH ternary nanocomposites. According to the Tables 4.6 and 4.14, as MFI increases, i.e. viscosity decreases, the domain size also increases. The decrease in viscosity in the presence of clay can be attributed to the higher clay platelet alignment, smaller particle sizes, and/or matrix molecular weight degradation (Fornes et al, 2001). Table 4.3 in XRD analysis shows that PC-I mixing sequence in polyamide-6/ Cloisite® 25A/E-BA-MAH nanocomposite also gives the highest d-spacing among the others.

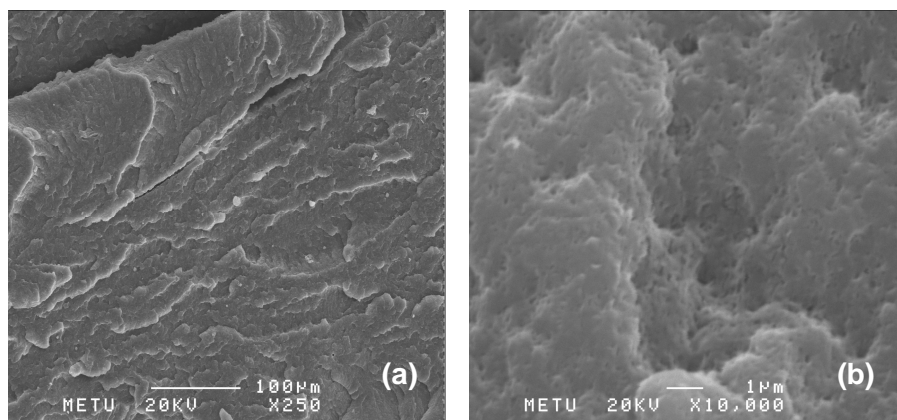


Figure 4.34 SEM micrograph of Polyamide-6/Cloisite® 15A/E-BA-MAH (All-S) nanocomposite (a) x250 magnification (b) x10000 magnification

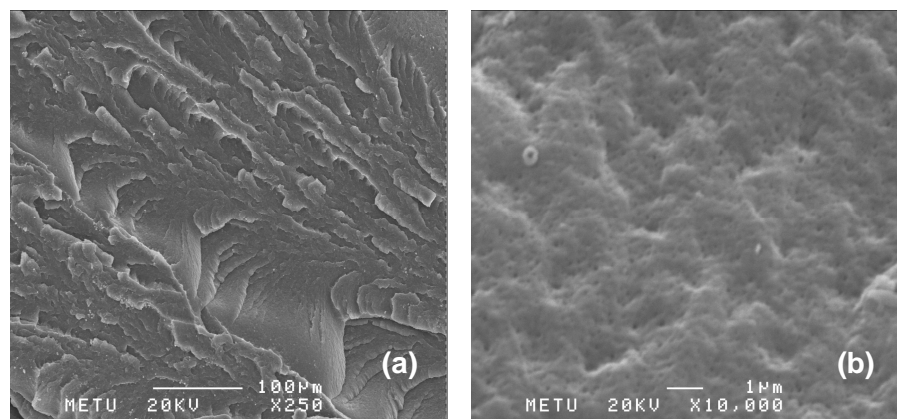


Figure 4.35 SEM micrograph of Polyamide-6/Cloisite® 25A/E-BA-MAH (All-S) nanocomposite (a) x250 magnification (b) x10000 magnification

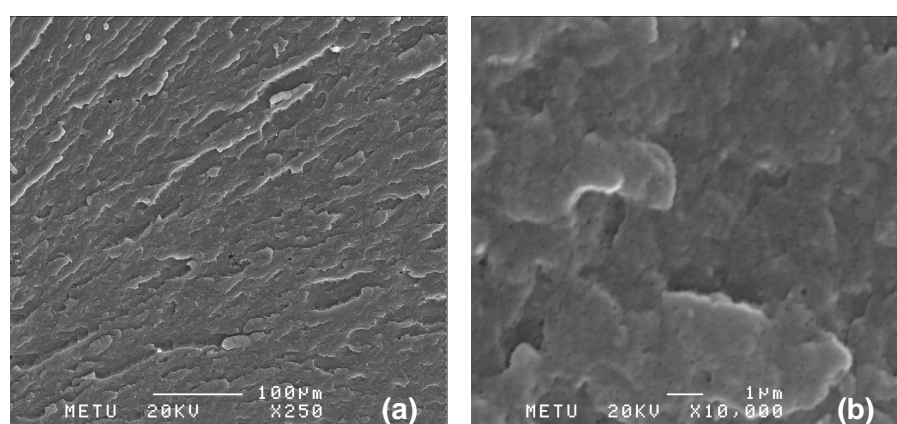


Figure 4.36 SEM micrograph of Polyamide-6/Cloisite® 30B/E-BA-MAH (All-S) nanocomposite (a) x250 magnification (b) x10000 magnification

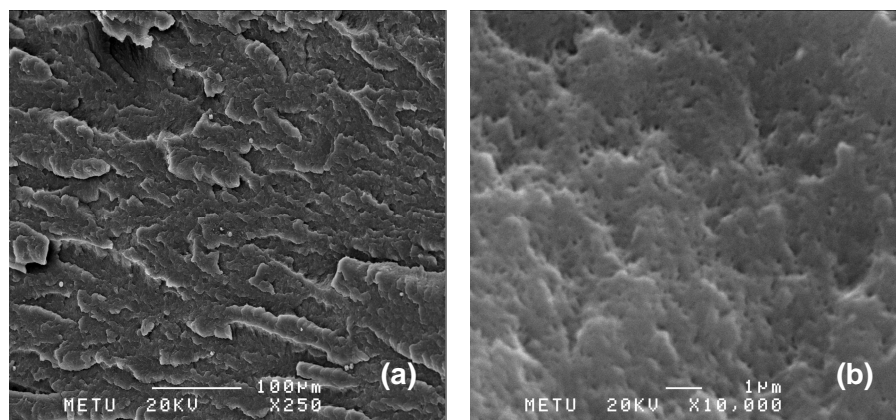


Figure 4.37 SEM micrograph of Polyamide-6/Cloisite® 15A/E-BA-MAH (PI-C) nanocomposite (a) x250 magnification (b) x10000 magnification

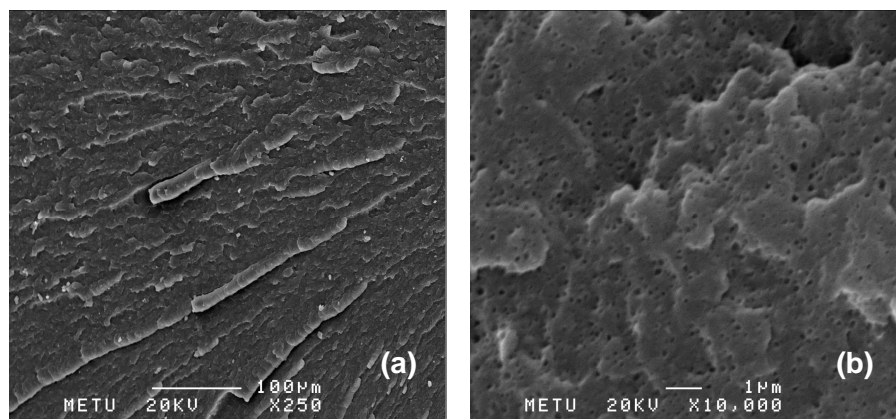


Figure 4.38 SEM micrograph of Polyamide-6/Cloisite® 15A/E-BA-MAH (PC-I) nanocomposite (a) x250 magnification (b) x10000 magnification

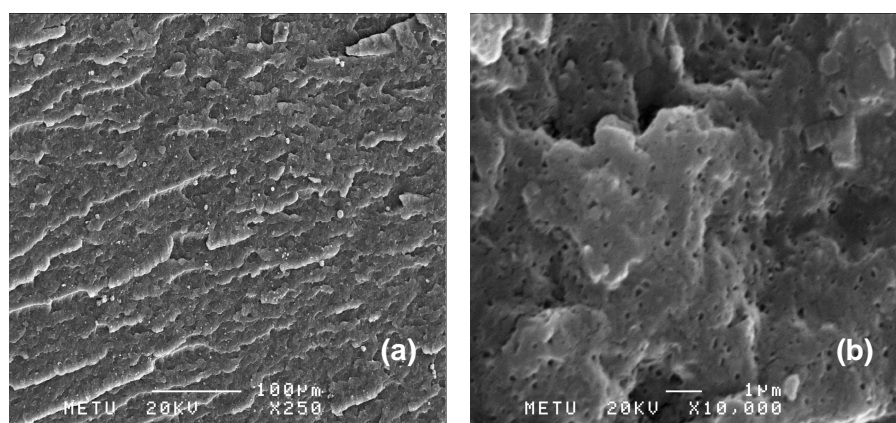


Figure 4.39 SEM micrograph of Polyamide-6/Cloisite® 15A/E-BA-MAH (IC-P) nanocomposite (a) x250 magnification (b) x10000 magnification

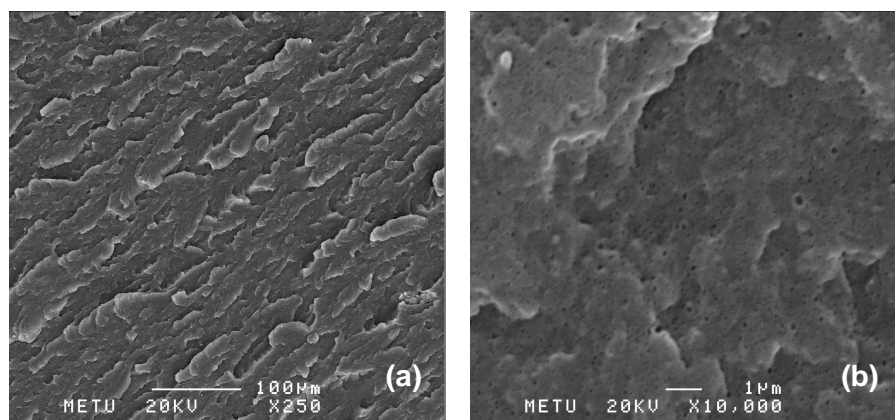


Figure 4.40 SEM micrograph of Polyamide-6/Cloisite® 25A/E-BA-MAH (PI-C) nanocomposite (a) x250 magnification (b) x10000 magnification

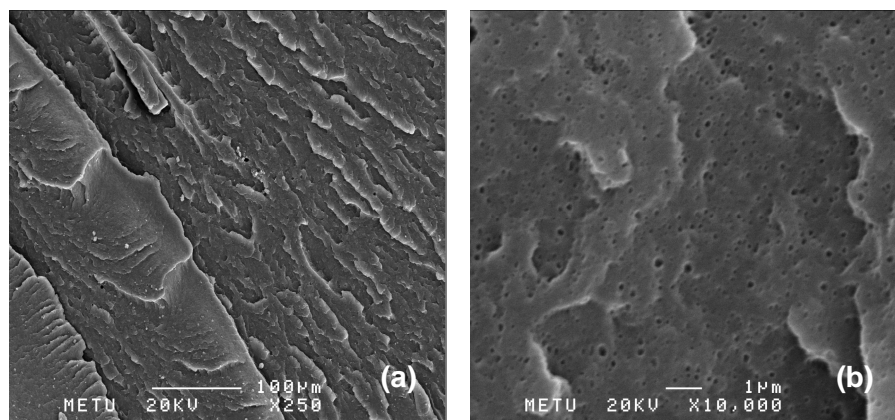


Figure 4.41 SEM micrograph of Polyamide-6/Cloisite® 25A/E-BA-MAH (PC-I) nanocomposite (a) x250 magnification (b) x10000 magnification

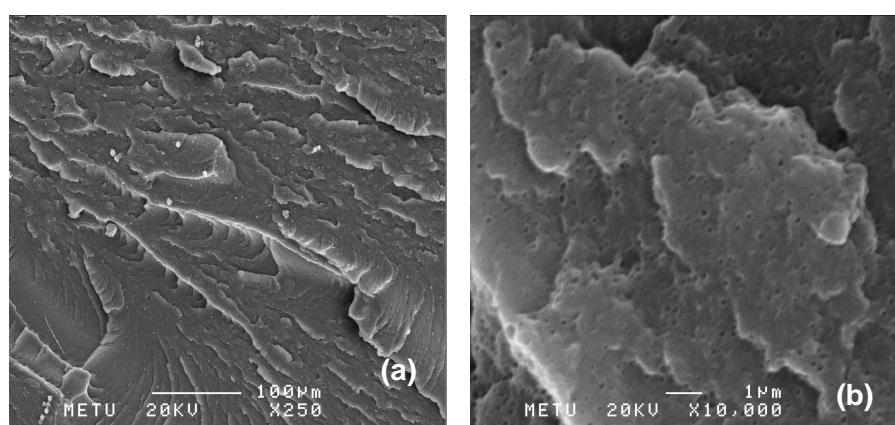


Figure 4.42 SEM micrograph of Polyamide-6/Cloisite® 25A/E-BA-MAH (IC-P) nanocomposite (a) x250 magnification (b) x10000 magnification

4.3.2 SEM Analysis Results of Elastomer E-GMA Containing Nanocomposites

SEM micrographs for polyamide-6/Cloisite® 15A/E-GMA, polyamide-6/Cloisite® 25A/E-GMA and polyamide-6/Cloisite® 30B/E-GMA nanocomposites are given in Figures 4.43, 4.44 and 4.45, respectively. Domain sizes of the elastomeric phases can be observed in Table 4.7. Elastomers show uniformly dispersed particles in the matrix in all ternary nanocomposites. The micrographs of deformed samples suggests the cavitation of the rubber particles. Rubber cavitation is believed to precede and induce shear yielding of the matrix.

Table 4.7 Elastomer domain sizes in polyamide-6/organoclay/E-GMA nanocomposites

	Domain size (nm)
Polyamide-6 + E-GMA (5 wt %)	106.1 ± 5.0
Polyamide-6 + Cloisite® 15A + E-GMA (All-S)	126.9 ± 8.6
Polyamide-6 + Cloisite® 25A + E-GMA (All-S)	147.6 ± 9.2
Polyamide-6 + Cloisite® 30B + E-GMA (All-S)	142.7 ± 7.0
Polyamide-6 + Cloisite® 15A + E-GMA (PI-C)	119.4 ± 6.0
Polyamide-6 + Cloisite® 15A + E-GMA (PC-I)	155.7 ± 7.5
Polyamide-6 + Cloisite® 15A + E-GMA (IC-P)	175.4 ± 12.3
Polyamide-6 + Cloisite® 30B + E-GMA (PI-C)	122.9 ± 6.1
Polyamide-6 + Cloisite® 30B + E-GMA (PC-I)	122.5 ± 7.8
Polyamide-6 + Cloisite® 30B + E-GMA (IC-P)	114.3 ± 5.0

It can be observed that the presence of the organoclay does not seem to substantially modify the dispersion of the rubber domains. This observation is unexpected since higher viscosity of the nanocomposite matrix should lead to a lower dispersed phase size, considering that the rest of the parameters that should influence the domain size does not change. Baldi et al., 2006, Ahn and

Paul, 2006, and González et al., 2006, observed similar results to the ones obtained in this study. The presence of organoclay helps coalescence of rubber domains. The increase in particle size is attributed to chemical and physical interactions between the organic modifier of the clay dissolved in the matrix and the functional groups of the elastomer, that should hinder the compatibilizing effect of the latter.

Figures 4.46 through 4.48 show the fracture surfaces of polyamide-6/Cloisite® 15A/E-GMA ternary nanocomposites processed by different mixing orders. Table 4.7 shows the domain sizes of these samples. It is seen that domain size is increased for all nanocomposites regardless of mixing sequence, due to the presence of organoclay in the structure. Similar to the data presented in Table 4.6, IC-P sequence gives the highest domain size in polyamide-6/Cloisite® 15A/E-GMA nanocomposites. Mixing elastomer with polyamide-6 in the second extrusion step limited its dispersion. According to Table 4.15, which shows the MFI results of polyamide-6/Cloisite® 15A/E-GMA samples, sample processed by IC-P sequence also gives the highest MFI value (lowest viscosity), corroborating this observation.

Fracture surfaces of polyamide-6/Cloisite® 30B/E-GMA ternary nanocomposites processed by different mixing orders can be observed in Figures 4.49 through 4.51. Elastomer domain size in nanocomposites is increased for all mixing sequences with respect to polyamide-6/elastomer blend, like in the domain sizes of polyamide-6/organoclay/E-BA-MAH nanocomposites shown in Table 4.6.

IC-P mixing sequence gives the lowest domain size in polyamide-6/Cloisite® 30B/E-GMA ternary nanocomposites as seen Table 4.7. Interactions between elastomer glycidyl methacrylate groups and organoclay hydroxyethyl groups may reduce the interfacial tension leading to a decrease in domain size. According to Table 4.15, MFI of polyamide-6/Cloisite® 30B/E-GMA (IC-P) sample is lower than polyamide-6/Cloisite® 15A/E-GMA (IC-P) sample, indicating the presence of interactions between organoclay surfactant and E-GMA elastomer.

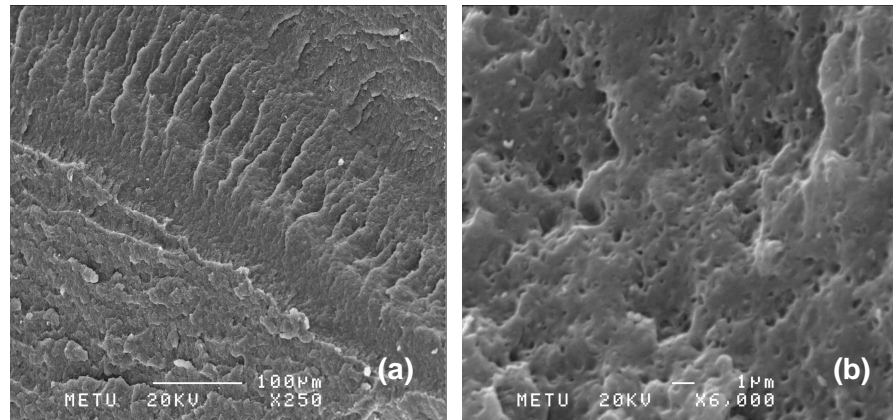


Figure 4.43 SEM micrograph of Polyamide-6/Cloisite® 15A/E-GMA (All-S) nanocomposite (a) x250 magnification (b) x6000 magnification

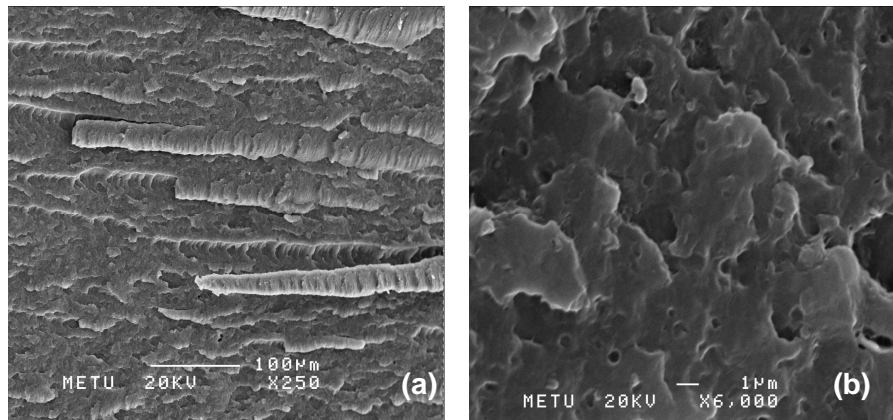


Figure 4.44 SEM micrograph of Polyamide-6/Cloisite® 25A/E-GMA nanocomposite (All-S) (a) x250 magnification (b) x6000 magnification

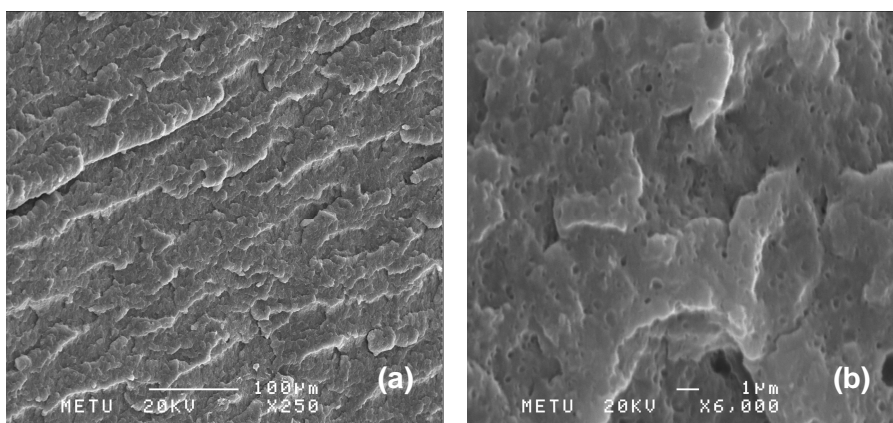


Figure 4.45. SEM micrograph of Polyamide-6/Cloisite® 30B/E-GMA (All-S) nanocomposite (a) x250 magnification (b) x6000 magnification

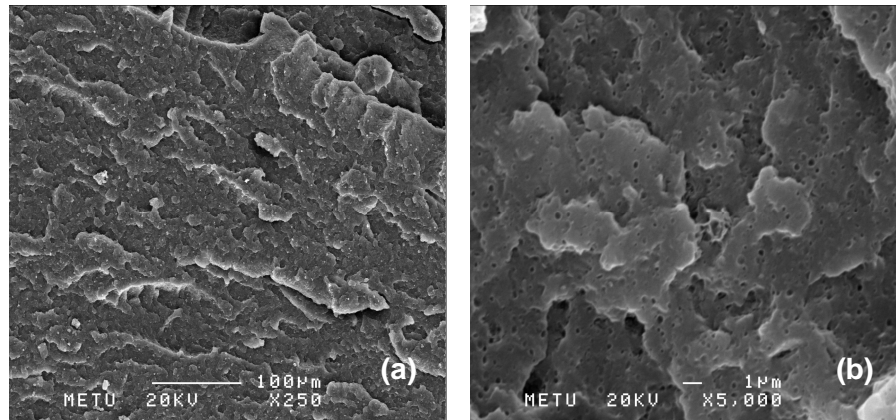


Figure 4.46 SEM micrograph of Polyamide-6/Cloisite® 15A/E-GMA (PI-C) nanocomposite (a) x250 magnification (b) x5000 magnification

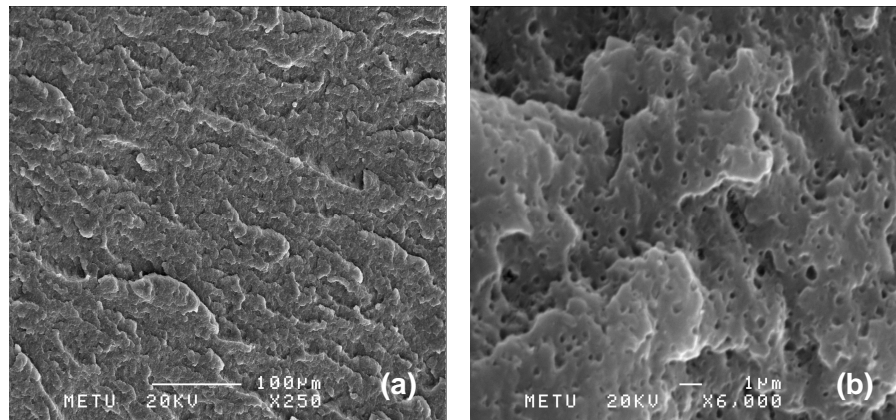


Figure 4.47 SEM micrograph of Polyamide-6/Cloisite® 15A/E-GMA (PC-I) nanocomposite (a) x250 magnification (b) x6000 magnification

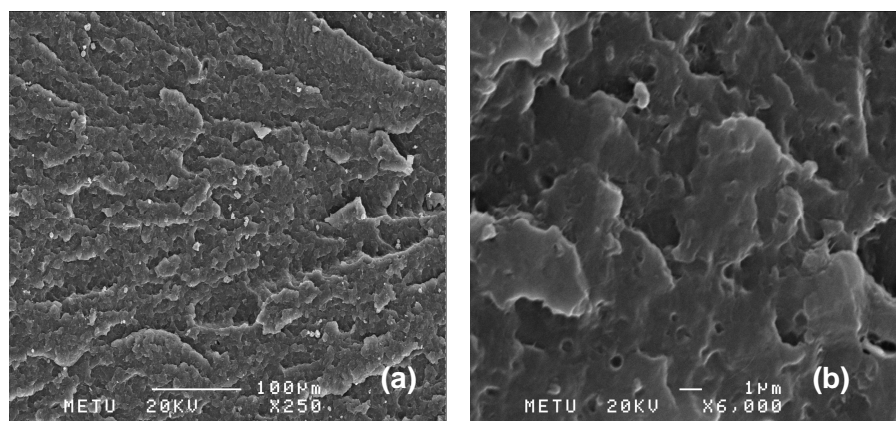


Figure 4.48 SEM micrograph of Polyamide-6/Cloisite® 15A/E-GMA (IC-P) nanocomposite (a) x250 magnification (b) x6000 magnification

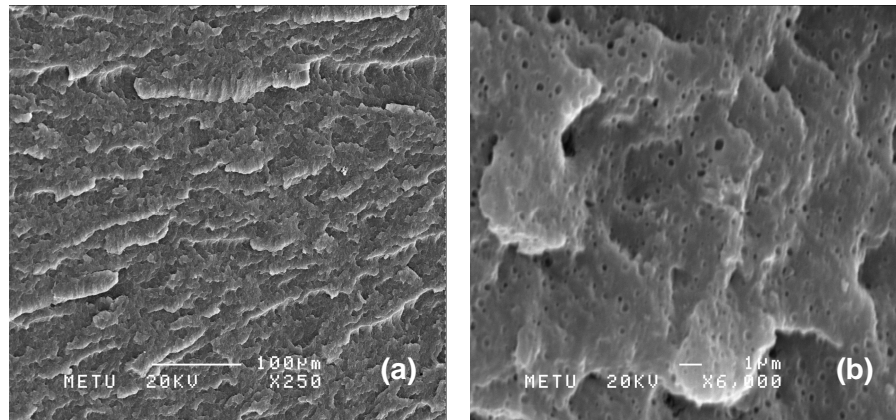


Figure 4.49 SEM micrograph of Polyamide-6/Cloisite® 30B/E-GMA nanocomposite (PI-C) (a) x250 magnification (b) x6000 magnification

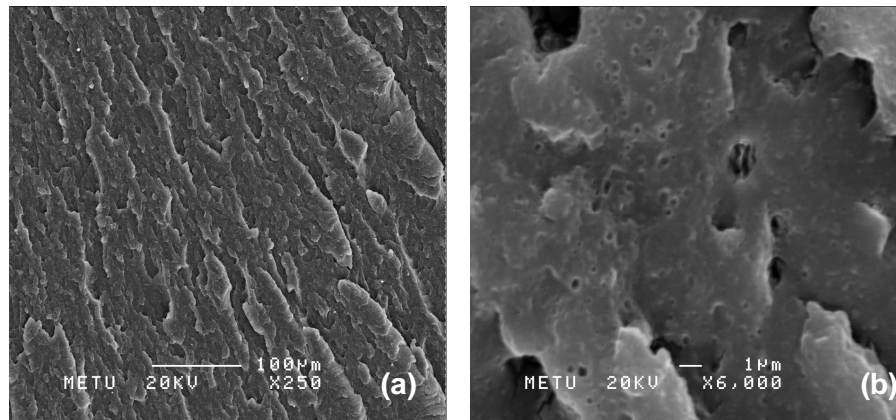


Figure 4.50 SEM micrograph of Polyamide-6/Cloisite® 30B/E-GMA (PC-I) nanocomposite (a) x250 magnification (b) x6000 magnification

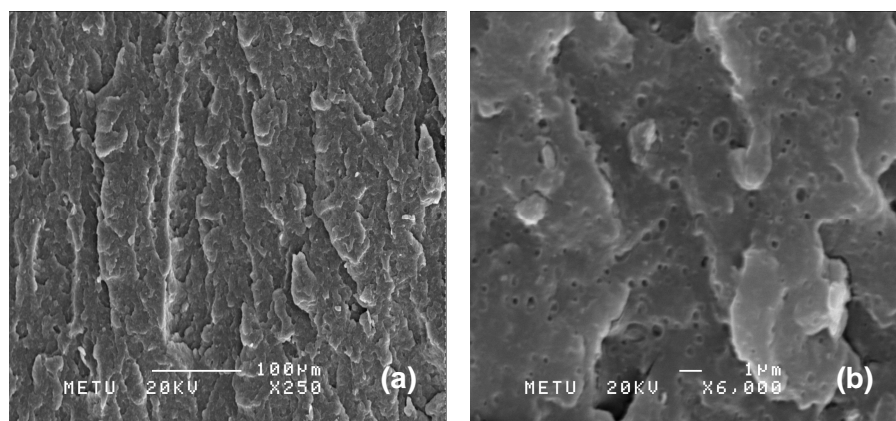


Figure 4.51 SEM micrograph of Polyamide-6/Cloisite® 30B/E-GMA (IC-P) nanocomposite (a) x250 magnification (b) x6000 magnification

4.3.3 SEM Analysis Results of Elastomer E-MA-GMA Containing Nanocomposites

SEM micrographs of ternary nanocomposites in which E-MA-GMA elastomer is the dispersed phase are shown in Figures 4.52-4.54. The rubber domain size data are summarized in Table 4.8. Because the interfacial tension between the matrix and the dispersed phase might be changed in the presence of organoclay, rubber domain sizes are larger in nanocomposites than their corresponding polyamide-6/elastomer blends. Also, unless there is a large affinity between the matrix and organoclay, some organoclay particles might be located at the interphase, resulting in increase in domain size.

Table 4.8 Elastomer E-MA-GMA domain size in polyamide-6 nanocomposites

	Domain size (nm)
Polyamide-6 + E-MA-GMA (5 wt %)	85.4 ± 6.7
Polyamide-6 + Cloisite® 15A + E-MA-GMA (All-S)	102.1 ± 6.4
Polyamide-6 + Cloisite® 25A + E-MA-GMA (All-S)	99.0 ± 6.0
Polyamide-6 + Cloisite® 30B + E-MA-GMA (All-S)	108.0 ± 6.6

Effect of organoclay type on domain size of E-MA-GMA containing nanocomposites is shown in Table 4.8. Nanocomposite with Cloisite® 30B has higher domain size than the others. Grafting reactions between E-MA-GMA/polyamide-6 and organoclay may lead some crosslinking which may inhibit rubber domain breakdown in the extruder.

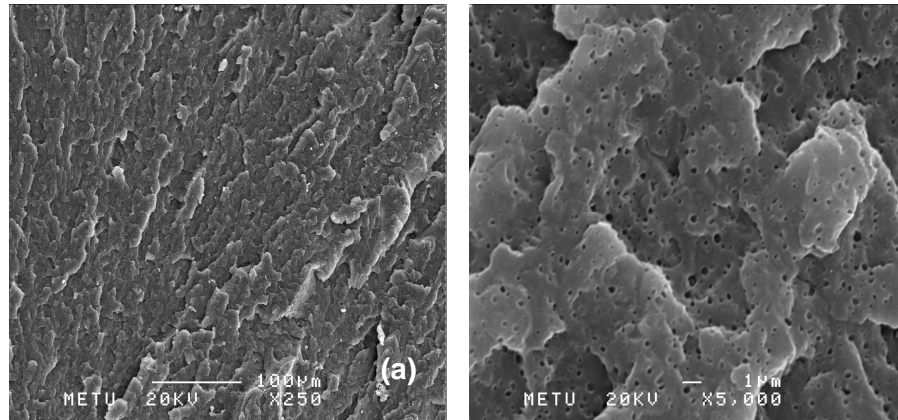


Figure 4.52 SEM micrograph of Polyamide-6/Cloisite® 15A/E-MA-GMA (All-S) nanocomposite (a) x250 magnification (b) x5000 magnification

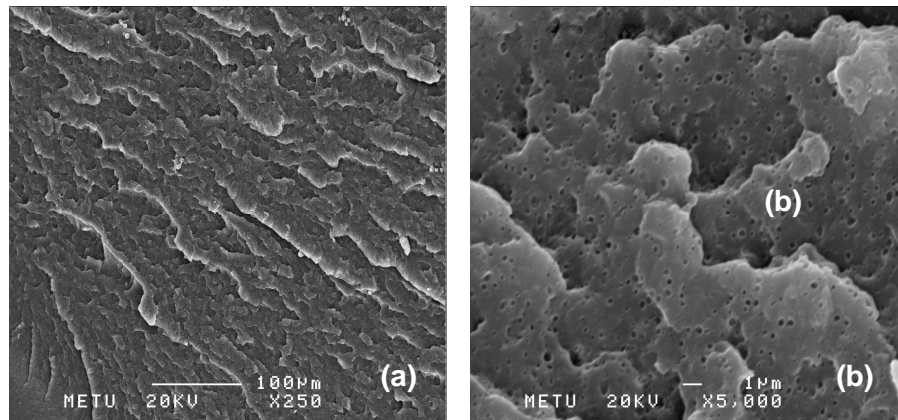


Figure 4.53 SEM micrograph of Polyamide-6/Cloisite® 25A/E-MA-GMA (All-S) nanocomposite (a) x250 magnification (b) x5000 magnification

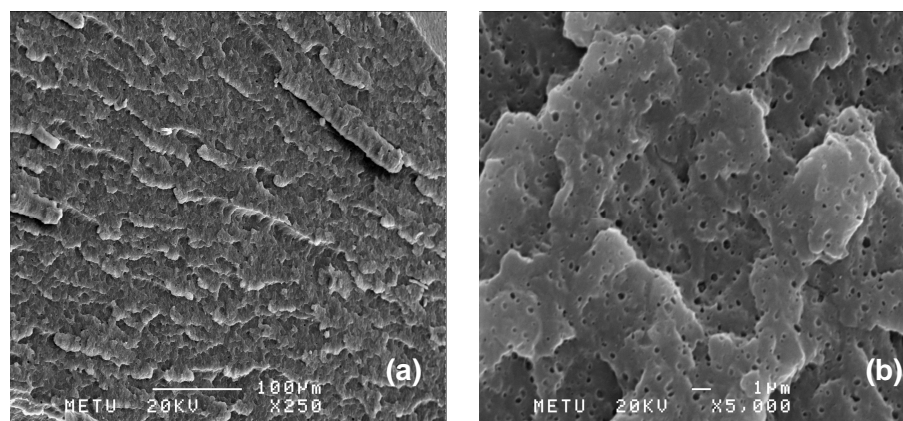


Figure 4.54 SEM micrograph of Polyamide-6/Cloisite® 30B/E-MA-GMA (All-S) nanocomposite (a) x250 magnification (b) x5000 magnification

4.4 FTIR ANALYSIS

Polyamide-6 has reactive functionality through amine and carboxyl end groups that are capable of reacting to form graft moieties with the elastomers used.

The potential chemical reactions between functional groups of elastomers and end-groups of polyamide-6 are investigated by FTIR-ATR technique.

The FTIR spectrum for polyamide-6 is shown in Figure 4.55. The peaks at 1625 cm^{-1} and 1537 cm^{-1} are attributed to the amide I and amide II bands, respectively. Absorption bands at 676 cm^{-1} , 964 cm^{-1} , 1363 cm^{-1} , 1465 cm^{-1} , 2850 cm^{-1} , and 2916 cm^{-1} indicated various absorptions of -C-H group. C-N stretching vibrations are located in 1112 cm^{-1} and 1168 cm^{-1} bands. Table 4.9 shows the assignment of peaks shown in Figure 4.55.

Table 4.9 Assignment of polyamide-6 FTIR bands

Wavenumber (cm^{-1})	Assignment
676	C-H wagging vibration
964	C-H out of plane deformation vibration
1064	C-N stretching vibrations in $-\text{CH}_2\text{-NH-}$
1112	C-N stretching vibrations in $-\text{CH-NH-}$
1168	C-N stretching vibrations in $-\text{R-NH-CO-}$
1255	Coupled C-N and C-O stretching vibration
1363	C-H deformation vibration in $-\text{N-CH}_2\text{-}$
1465	C-H scissor vibration in $-\text{CH}_2\text{-}$
1537	N-H bending absorption (Amide II band)
1625	C=O stretching vibration (Amide I band)
2850	C-H symmetrical stretching vibration
2916	C-H asymmetrical stretching vibration
3068	N-H stretch vibration
3284	O-H stretching vibration in $-\text{COOH}$

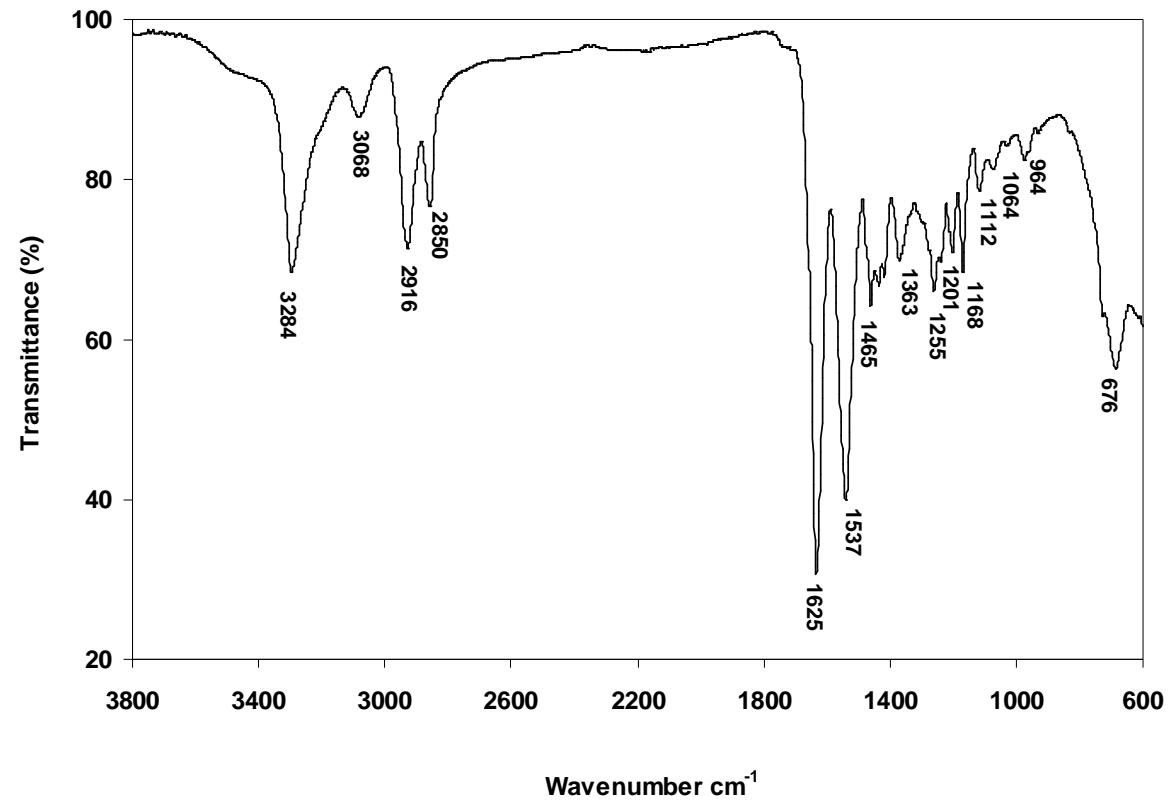


Figure 4.55 FTIR-ATR spectrum for polyamide-6

4.4.1 Possible Reactions in polyamide-6/E-BA-MAH blends

The FTIR spectrum for elastomer E-BA-MAH is shown in Figure 4.56. C=O stretching vibrations at 1778 cm^{-1} and C=O bending at 719 cm^{-1} are the characteristic bands for maleic anhydride groups. The other FTIR peaks seen in spectra of E-BA-MAH are explained in Table 4.10.

Possible reaction scheme between maleic anhydride functional groups of E-BA-MAH and polyamide-6 can be seen in Figure 4.57. Reaction between the butyl acrylate functional groups and polyamide-6 is given in Figure 4.58.

Researchers have reported that the grafted anhydride groups can be transformed to acid, ester, and amide (or imide) groups by their reactions with water, alcohols, and amines, respectively. At low temperatures ($T < 120\text{ }^{\circ}\text{C}$), amidic linkages are reported to be dominant, whereas at high temperatures, almost only imidic bonds are present as revealed by FTIR analysis (Greco et al., 1987; Martuscelli et al., 1985). The anhydride-amine reaction is one of the most effective reactions in polymer blend compatibilization since it is very fast and achieved within short melt mixing time (Sundararaj and Macosko, 1995).

According to Akkapeddi (2001), amine end-group reactivity with esters are very slow and negligible. Thus, butyl acrylate is used only as co-diluent.

Figure 4.59 shows FTIR-ATR spectra for polyamide-6/50 wt % E-BA-MAH blend, in Figure 4.60, detailed spectra of the same blend in $1690\text{-}1790\text{ cm}^{-1}$ region is given. The blend spectra show the typical bands of imide group at 1770 cm^{-1} , corresponding to imide carbonyl asymmetric stretching. The presence of that band indicates that imidation reaction took place between polyamide-6 amine end groups and maleic anhydride groups of E-BA-MAH. The peak at 1714 cm^{-1} (C=O symmetric stretching) indicate that the reaction shown in Figure 4.57 also took place. In addition, unreacted carboxyl end groups and elastomer ester groups can be related to the peak at 1732 cm^{-1} (Bhattacharyya and Pötschke, 2006).

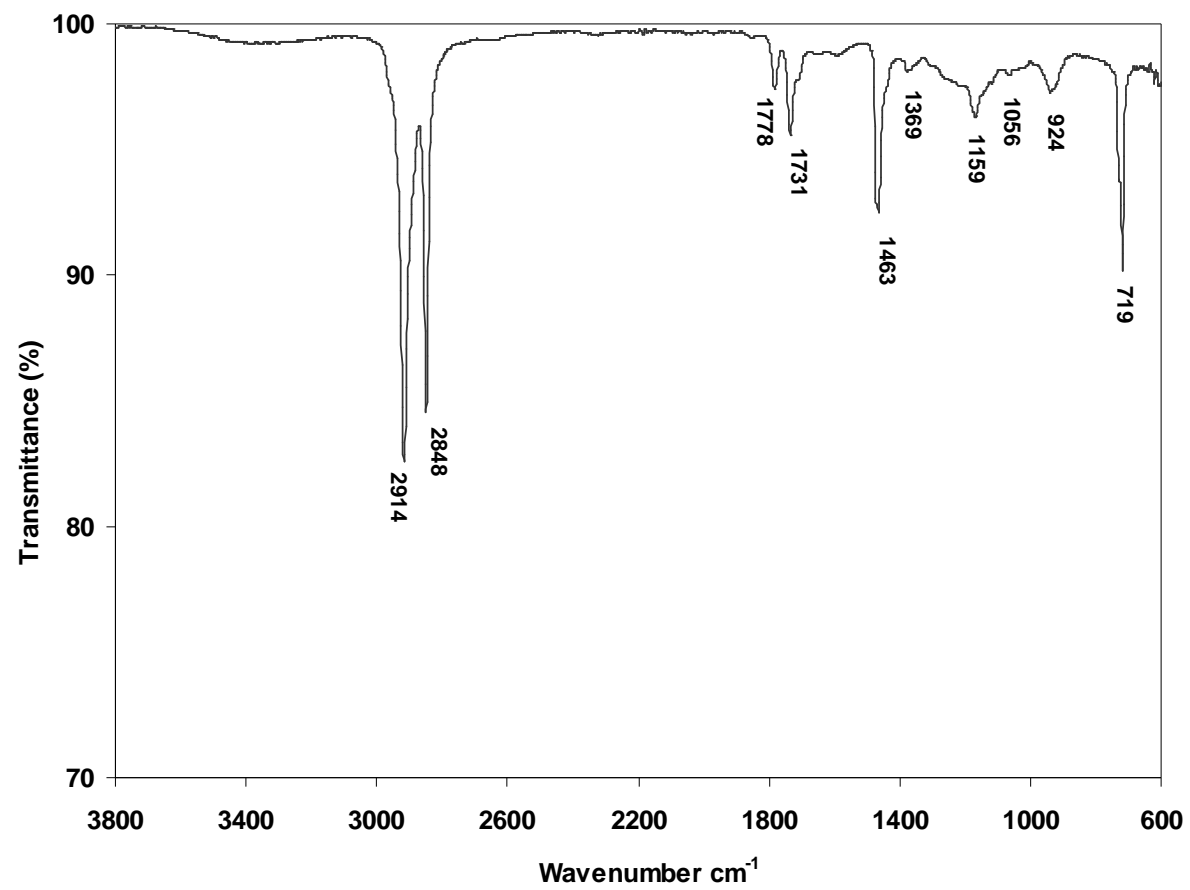


Figure 4.56 FTIR-ATR spectrum for E-BA-MAH

Table 4.10 Assignment of E-BA-MAH FTIR bands

Wave number (cm ⁻¹)	Assignment
719	C-C skeleton vibration (rocking) in -(CH ₂) _n -
924	C-H deformation vibration
1056	C-O-C symmetric stretching vibration in R ₁ -O-(C=O)-R
1159	C-O-C symmetric stretching vibration R ₁ - (C=O)- O-R
1369	C-H symmetrical deformation vibration in R-CH ₃
1463	CH ₂ symmetrical deformation vibration in esters
1731	C=O stretching vibrations in -(C=O)-(C=O)-C-
1778	C=O asymmetrical stretching vibration in anhydrides
2848	C-H stretching vibration in -CH ₂ -
2914	C-H asymmetrical stretching vibration

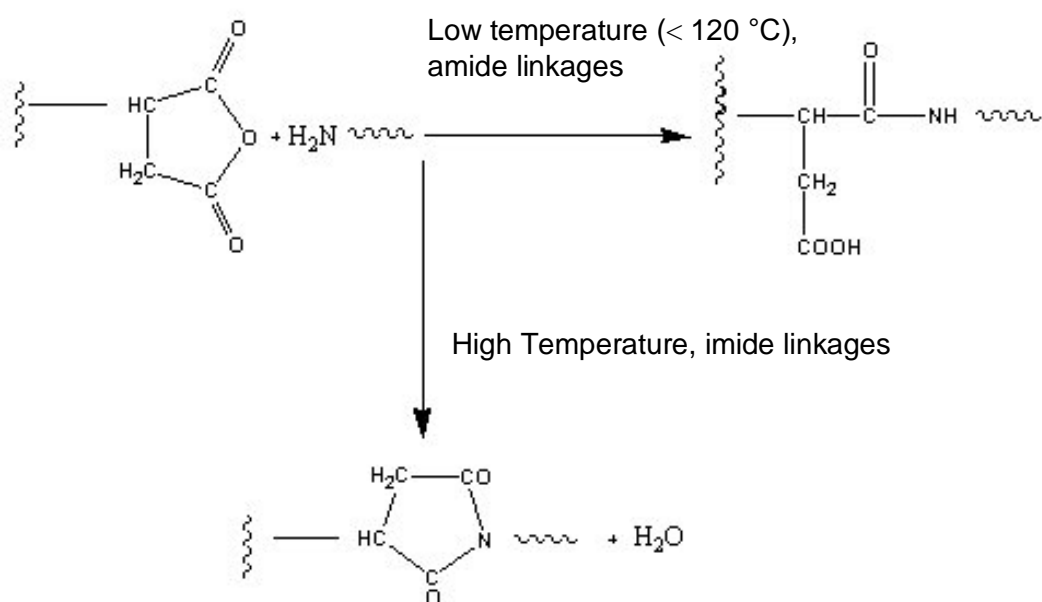


Figure 4.57 Scheme for the reaction between amine end group of polyamide-6 and maleic anhydride group of E-BA-MAH leading to the formation of amide or imide linkages (Thomas and Groeninckx, 1999)

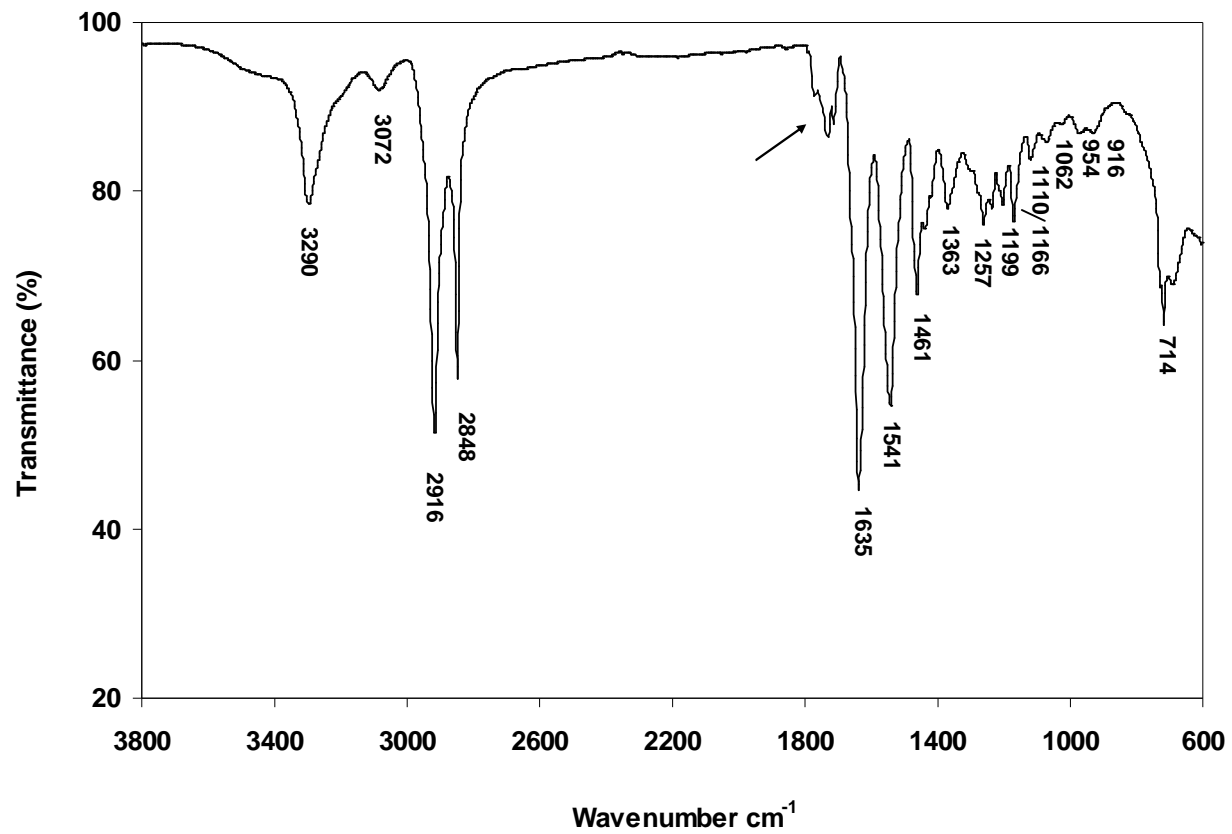


Figure 4.59 FTIR-ATR spectrum for polyamide-6/50 wt % E-BA-MAH blend

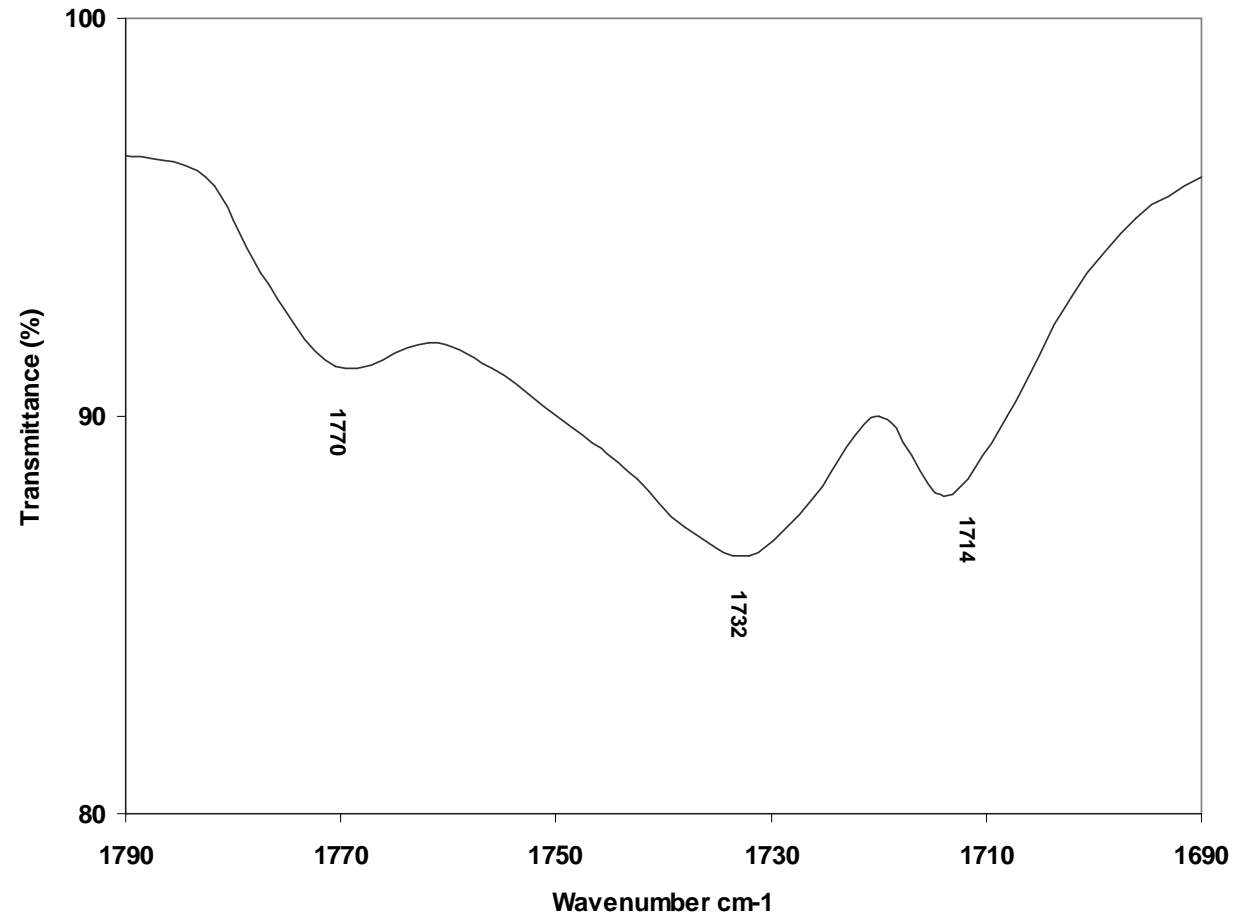


Figure 4.60 Detailed FTIR-ATR spectrum for polyamide-6/50 wt % E-BA-MAH blend

4.4.2 Possible Reactions in polyamide-6/E-GMA and polyamide-6/E-MA-GMA blends

The FTIR spectra for elastomers E-GMA and E-MA-GMA are shown in Figures 4.63 and 4.66, respectively. Oxirane ring vibration at 908 cm^{-1} that corresponds to epoxy group is observed in the figures. Other FTIR peaks are explained in Tables 4.11 and 4.12.

Previous studies demonstrated that both amines (Duffy et al., 1987; Glover et al., 1988; Kalal et al., 1974) and carboxylic acids (Kalal et al., 1974; Shechter et al., 1956) are capable of reacting with epoxide groups. In addition to these reactions, the epoxide group can also undergo a ring-opening polymerization in the presence of acid, amine and hydroxyl end groups.

The kinetics of epoxide ring reactions with amine and acid groups under melt processing conditions are studied by Kudva et al. (1998). They concluded that both reactions in Figure 4.61 take place easily and rapidly in the blending conditions. On the other hand, hypothetical reactions of epoxy ring with hydroxyl functionalities, which can be seen in Figure 4.62, generated by amine-epoxide and acid-epoxide reactions are not found to play a significant role, and those with the secondary amines produced by the amine-epoxide to be quite slow relative to the time scale of reactive processing. Reaction between the methyl acrylate functional groups and polyamide-6 is given in Figure 4.65. Methyl acrylate group in E-MA-GMA elastomer is used only as co-diluent, since ester group reactions with polyamide-6 are very slow and negligible (Akkapeddi M. K., 2001).

Since GMA can react with both end groups of polyamide-6, it is capable of yielding cross-linked products. In order to avoid cross-linking, low concentration of elastomers are used in this study.

FTIR spectra of polyamide-6/E-GMA and polyamide-6/E-MA-GMA blends in Figures 4.64 and 4.66 showed that absorption band for ring vibration of oxirane group at 910 cm^{-1} is disappeared.

Table 4.11 Assignment of E-GMA FTIR bands

Wave number (cm ⁻¹)	Comment
719	C-C skeleton vibration (rocking) in $-(CH_2)_n-$
757	Trisubstitue epoxy ring vibration
838	Monosubstitue epoxy ring vibration
908	Oxiraine ring vibration
991	C-H out-of-plane deformation vibration in $COCH=CH_2$
1139	C-O-C symmetrical streching vibration
1238	Epoxy C-O stretching vibration
1375	C-H symmetrical deformation vibration in R-CH ₃
1463	C-H asymmetrical deformation vibration in R-CH ₃
1731	C=O stretching vibrations
2846	C-H stretching vibration in $-CH_2-$
2914	C-H asymmetrical stretching vibration

Table 4.12 Assignment of E-MA-GMA FTIR bands

Wave number (cm ⁻¹)	Assignment
719	C-C skeleton vibration (rocking) in $-(CH_2)_n-$
762	CH ₂ rocking vibration
908	Oxiraine ring vibration
1101	C-O stretching vibration
1370	C-H symmetrical deformation vibration in R-CH ₃
1460	C-H asymmetrical deformation vibration in R-CH ₃
1731	C=O stretching vibrations
2848	C-H stretching vibration in $-CH_2-$
2916	C-H asymmetrical stretching vibration
3363	O-H stretching vibration in -COOH

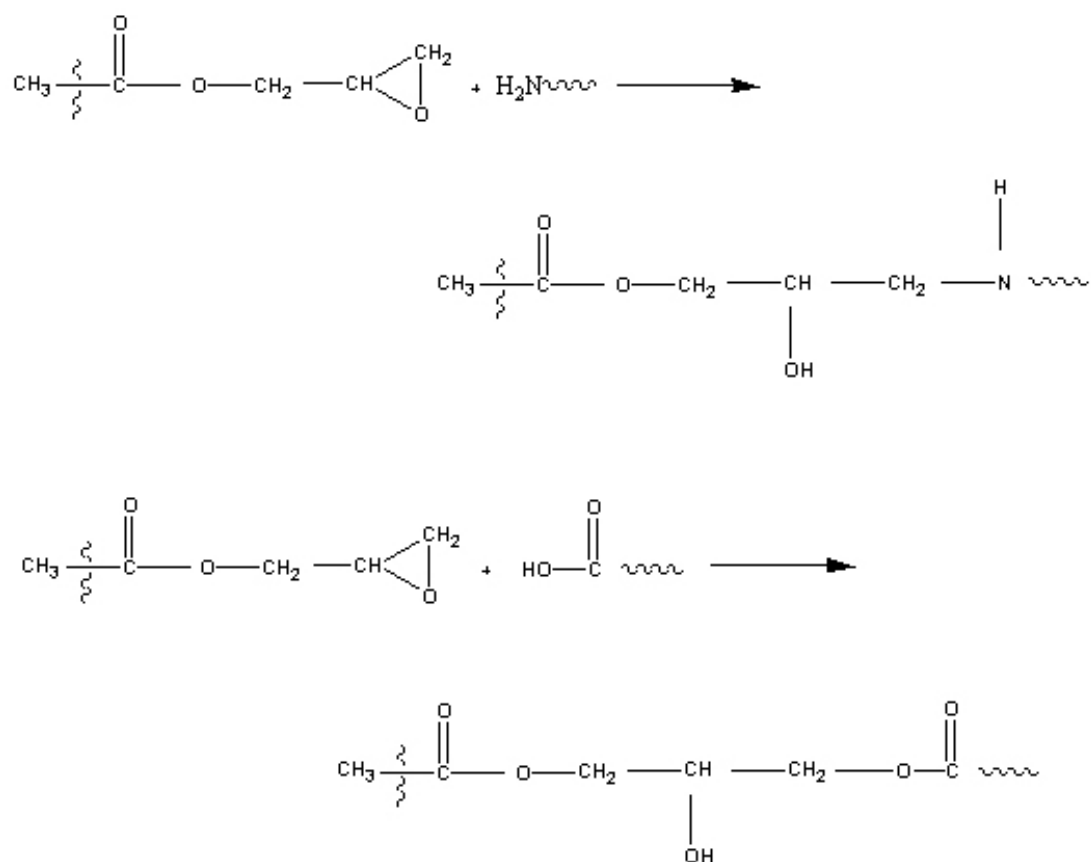


Figure 4.61 Scheme for the reaction between amine and carboxyl end groups of polyamide-6 and E-GMA (Chiono et al., 2003)

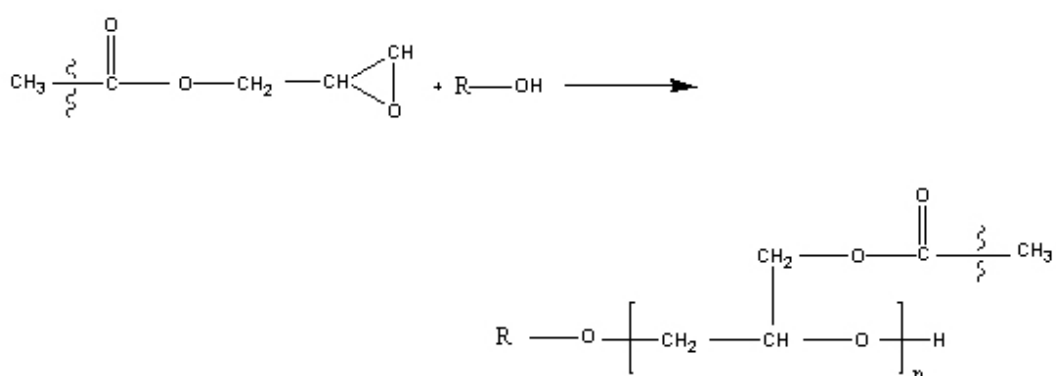


Figure 4.62 Scheme for the reaction between hydroxyl groups and E-GMA

147

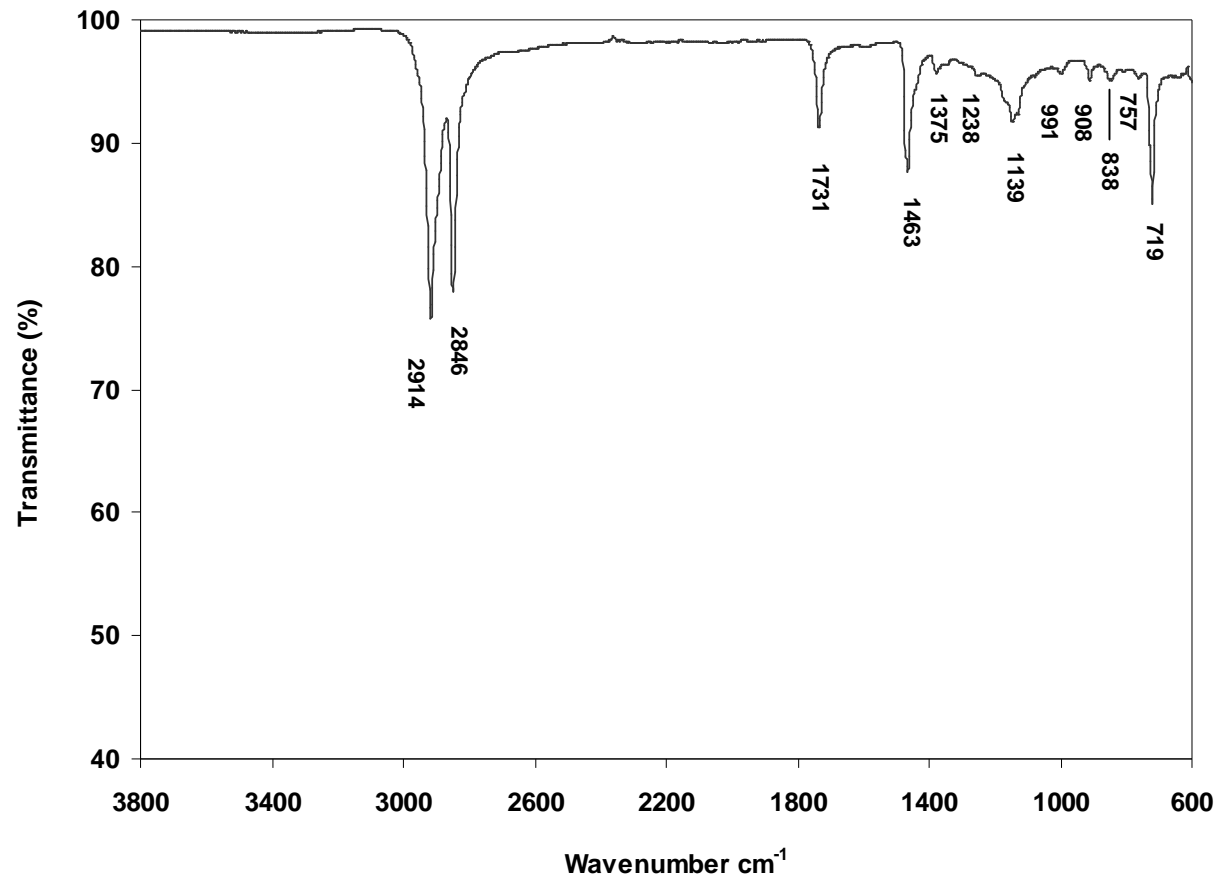


Figure 4.63 FTIR-ATR spectrum for E-GMA

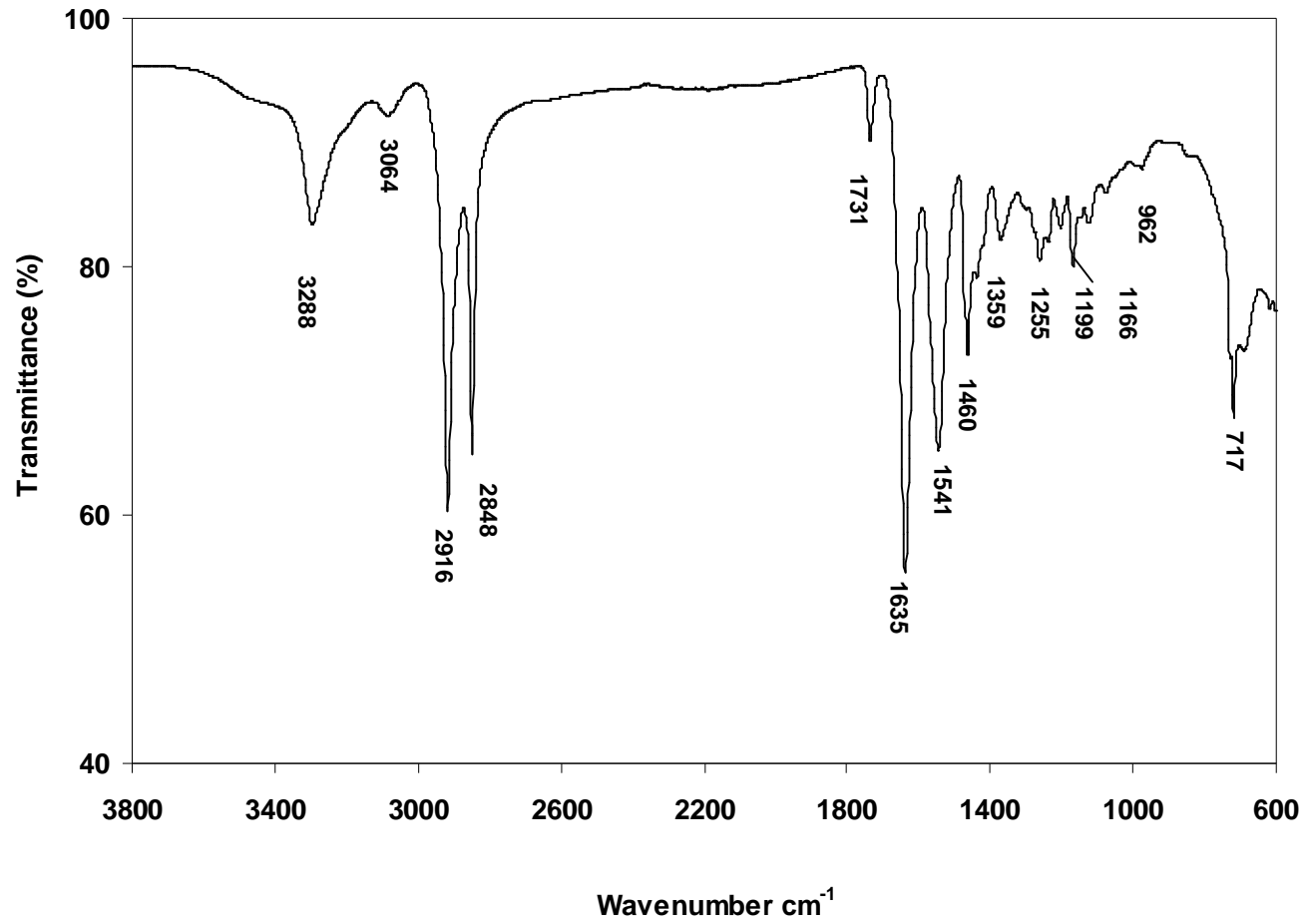


Figure 4.64 FTIR-ATR spectrum for polyamide-6/50 wt % E-GMA blend

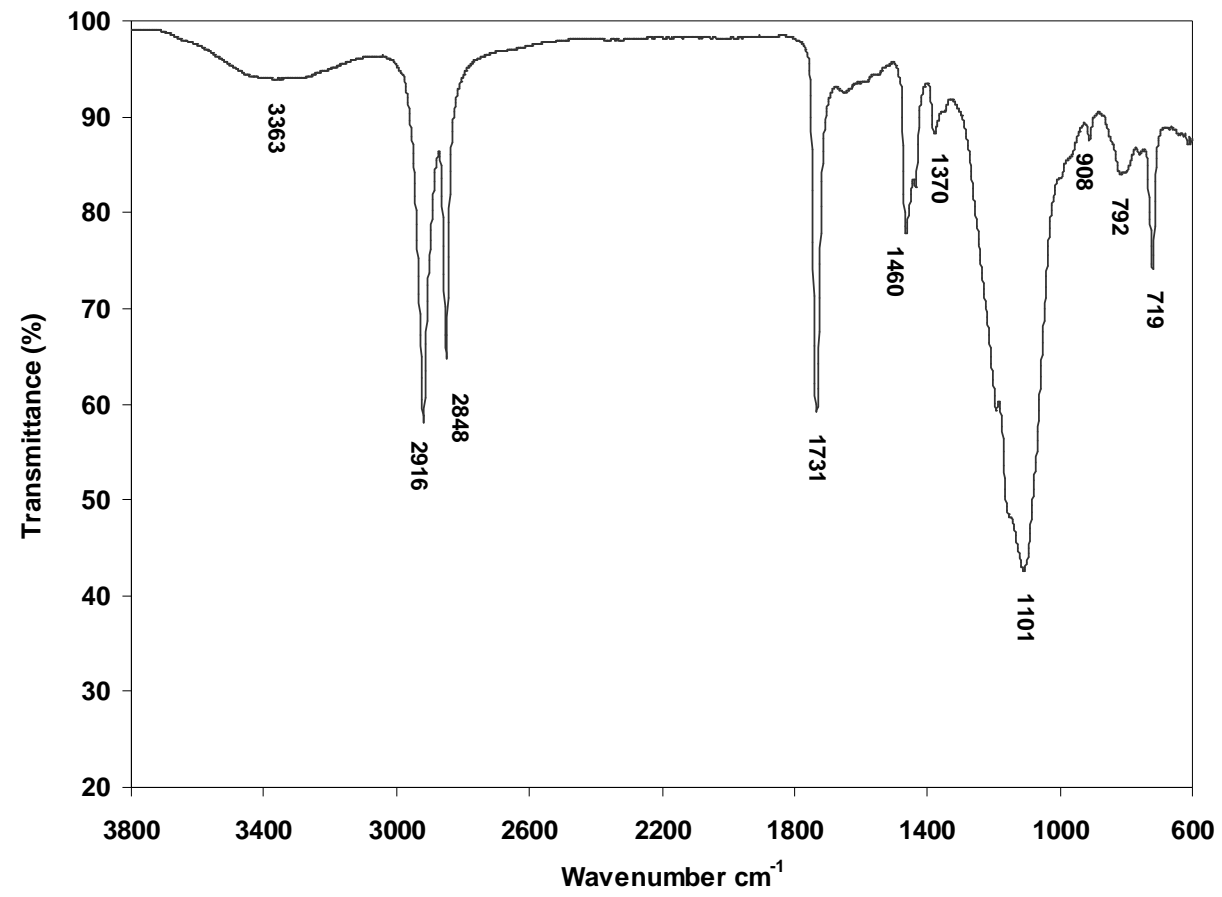


Figure 4.66 FTIR-ATR spectrum for E-MA-GMA

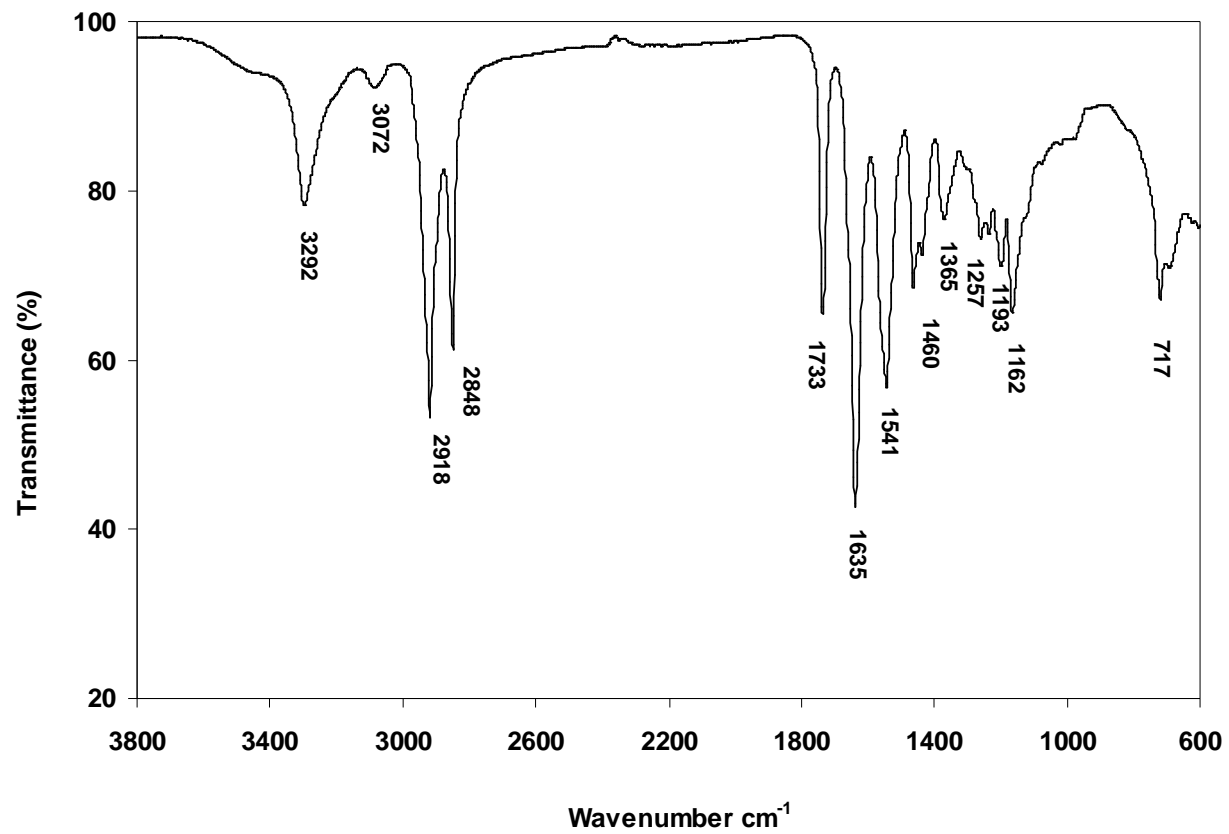


Figure 4.67 FTIR-ATR spectrum for polyamide-6/50 wt % E-MA-GMA blend

4.4.3 Possible Reactions between organoclay and elastomers used

Among the organoclays used in this study, only Cloisite® 30B has reactive groups on its surfactant. Hydroxyl groups may react with epoxy and maleic anhydride functional groups as seen in Figure 4.62 and 4.68, respectively.

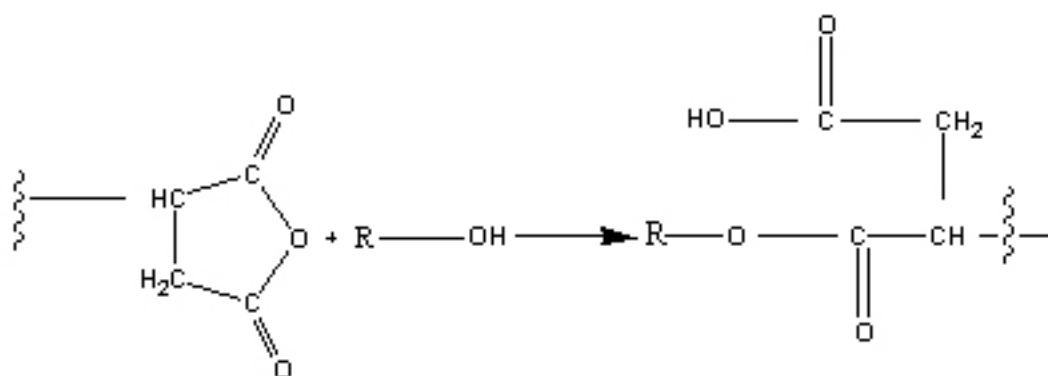


Figure 4.68 Scheme for the reaction between hydroxyl group of organoclay and maleic anhydride group of E-BA-MAH (Loyens and Groeninckx, 2002)

Due to the low amount of organoclay in the nanocomposites, these interactions can not be observed in FTIR analysis.

4.5 FLOW CHARACTERISTICS-MFI MEASUREMENTS

4.5.1 MFI Analysis Results of Polyamide-6/Elastomer Blends

The MFI results of polyamide-6/E-BA-MAH elastomer blends, polyamide-6/E-GMA elastomer blends and polyamide-6/E-MA-GMA elastomer blends are given in Table 4.13. As it can be observed in the Table, MFI of polyamide-6 decreases (viscosity increases) upon addition of elastomer and as the amount of elastomer increases, MFI of blends decrease. This is due to the high viscosities of these elastomers. Another reason is the possible reactions between MAH and GMA functional groups of elastomers and polyamide-6 (Liu et.al., 2001, Ahn and Paul, 2006). Polyamide-6 has reactive functionality through amine and carboxyl end groups that are capable of reacting to form graft moieties with the elastomers used. GMA contains epoxide functionality capable of reacting with both the acid and amine end groups of polyamide-6 (Tedesco et al., 2001). The anhydrides can react only with the amine ends of polyamide-6 chains (Thomas and Groeninckx, 1999). In addition to the above reactions, terminal amino groups of polyamide-6 and ester groups of butyl acrylate or methyl acrylate may react with each other (Raval et al., 1991).

Table 4.13 MFI measurement results in polyamide-6/elastomer blends

	MFI (g/10 min)
Polyamide-6	34.3 ± 0.9
E-BA-MAH Elastomer	17.2 ± 1.6
Polyamide-6 / 5 weight % E-BA-MAH	19.9 ± 0.5
Polyamide-6 / 10 weight % E-BA-MAH	8.8 ± 0.1
Polyamide-6 / 15 weight % E-BA-MAH	2.5 ± 0.2
E-GMA Elastomer	15.9 ± 1.6
Polyamide-6 / 5 weight % E- GMA	24.4 ± 0.4
Polyamide-6 / 10 weight % E- GMA	16.5 ± 0.3
Polyamide-6 / 15 weight % E- GMA	8.7 ± 0.4
E-MA-GMA Elastomer	14.6 ± 1.4
Polyamide-6 / 5 weight % E-MA-GMA	23.1 ± 0.5
Polyamide-6 / 10 weight % E-MA-GMA	18.7 ± 0.2
Polyamide-6 / 15 weight % E-MA-GMA	7.9 ± 0.6

4.5.2 MFI Analysis Results of Nanocomposites Containing E-BA-MAH Elastomer

In binary polyamide-6/organoclay nanocomposites, the addition of organoclay increases the MFI slightly (decreases the viscosity) in Cloisite® 25A and 30B organoclays as seen in Table 4.14. The viscosity decrease in the presence of clay can be attributed to the higher clay platelet alignment and/or matrix molecular weight degradation (Fornes et al, 2001). The decrease of MFI value with Cloisite® 15A is basically due to large clusters formed by the organoclay. Increase in viscosity with rigid filler addition is balanced with the flow alignment of exfoliated clay and the polymer, which may cause an increase in MFI hence dynamic viscosity. This is observed in case of Cloisite® 25A and 30B organoclays.

The viscosity of polymer matrix should play an important role in exfoliating organoclay aggregates, since intercalation and/or exfoliation of organoclay aggregates require the diffusion of polymer molecules into the galleries of layered silicates or peel away of the top and bottom layers as promoted by the polymer adsorption and by the application of shear stress (Lee and Han, 2003). As the melt viscosity increases, the shear stress applied to the clay agglomerates increases, which may facilitate separation of clay platelets.

Table 4.14 MFI measurement results for polyamide-6/organoclay/E-BA-MAH nanocomposites

	MFI (g/10 min)
Polyamide-6	34.3 ± 0.9
Polyamide-6 + Cloisite® 15A	31.2 ± 0.2
Polyamide-6 + Cloisite® 25A	35.3 ± 2.9
Polyamide-6 + Cloisite® 30B	35.5 ± 3.4
Polyamide-6 + E-BA-MAH Blend (5 weight %)	19.9 ± 0.5
Polyamide-6 + Cloisite® 15A+ E-BA-MAH (All-S)	17.7 ± 0.2
Polyamide-6 + Cloisite® 15A+ E-BA-MAH (PI-C)	19.1 ± 0.3
Polyamide-6 + Cloisite® 15A+ E-BA-MAH (PC-I)	24.6 ± 0.1
Polyamide-6 + Cloisite® 15A+ E-BA-MAH (IC-P)	19.0 ± 0.4
Polyamide-6 + Cloisite® 25A+ E-BA-MAH (All-S)	17.2 ± 0.2
Polyamide-6 + Cloisite® 25A+ E-BA-MAH (PI-C)	18.8 ± 0.3
Polyamide-6 + Cloisite® 25A+ E-BA-MAH (PC-I)	27.1 ± 1.1
Polyamide-6 + Cloisite® 25A+ E-BA-MAH (IC-P)	17.9 ± 0.6
Polyamide-6 + Cloisite® 30B+ E-BA-MAH (All-S)	16.3 ± 1.3

As seen from Table 4.14 incorporation of elastomer reduced the MFI of the nanocomposites, owing to the formation of graft copolymer and the high viscosity of the elastomers. Also, interactions between clay organic modifier and elastomer cannot be excluded. In these ternary nanocomposites, generally, the addition of clay leads to a decrease in MFI with respect to the MFI of the polyamide-6/elastomer blends (MFI=19.9 g/10 min), since the presence of elastomer suppresses the organoclay dispersion as seen in TEM Figures 4.15 and 4.18. The decrease in MFI may also be attributed to the flow hindrance by organoclay particles and interactions between the organoclay and polyamide-6 (Chow et al., 2005).

Table 4.14 shows the MFI values of ternary nanocomposites containing Cloisite® 15A/E-BA-MAH and Cloisite® 25A/E-BA-MAH processed by different addition orders, respectively. MFI decreases in the presence of elastomer in all the samples. It is seen that, MFI is higher in PC-I sequence and lower in All-S sequence, independent of organoclay type. Mixing polymer with organoclay prior to elastomer blending leads to a decrease in viscosity, since organoclay may obstruct the graft polymer formation and prevent increase in polymer molecular weight. Polyamide-6/Cloisite® 30B/E-BA-MAH nanocomposite has the lowest MFI among the polyamide-6/organoclay/E-BA-MAH nanocomposites, since there should be interactions between organoclay hydroxyethyl groups and elastomer.

4.5.3 MFI Analysis Results of Nanocomposites Containing E-GMA Elastomer

Table 4.15 shows the MFI results of the nanocomposites prepared with polyamide-6, E-GMA and various organoclays. Incorporation of elastomer reduces the MFI of the nanocomposites. In these ternary nanocomposites, generally, the addition of clay leads to a decrease in MFI with respect to the MFI of the polyamide-6/elastomer blend (MFI=24.4 g/10 min), since the presence of elastomer suppresses the organoclay dispersion as seen in TEM Figure 4.20. MFI decrease may also be attributed to the flow hindrance caused by the presence of organoclay particles.

Table 4.15 shows the MFI data in polyamide-6 based Cloisite® 15A/E-GMA and Cloisite® 30B/E-GMA nanocomposites processed by different addition orders. MFI is lower in PI-C sequence for both material combinations, since blending polymer and elastomer followed by addition of organoclay promotes the formation of polyamide-6-co-E-GMA copolymer more than the other mixing sequences. The effect of impact modifier is more pronounced than the effect of organoclay on the melt viscosity of all the blending sequences. According to Table 4.15, MFI of polyamide-6/Cloisite® 30B/E-GMA (IC-P) sample is lower than polyamide-6/Cloisite® 15A/E-GMA (IC-P) sample, indicating interactions between organoclay surfactant and E-GMA elastomer, in addition to E-GMA and polyamide-6 interactions.

Table 4.15 MFI measurement results for polyamide-6/organoclay/E-GMA nanocomposites

	MFI (g/10 min)
Polyamide-6	34.3 ± 0.9
Polyamide-6 + Cloisite® 15A	31.2 ± 0.2
Polyamide-6 + Cloisite® 25A	35.3 ± 2.9
Polyamide-6 + Cloisite® 30B	35.5 ± 3.4
Polyamide-6 + E-GMA Blend (5 weight %)	24.4 ± 0.4
Polyamide-6 + Cloisite® 15A + E-GMA (All-S)	25.6 ± 0.2
Polyamide-6 + Cloisite® 15A + E-GMA (PI-C)	24.7 ± 0.4
Polyamide-6 + Cloisite® 15A + E-GMA (PC-I)	27.7 ± 0.6
Polyamide-6 + Cloisite® 15A + E-GMA (IC-P)	28.6 ± 0.3
Polyamide-6 + Cloisite® 25A + E-GMA (All-S)	20.2 ± 0.1
Polyamide-6 + Cloisite® 30B + E-GMA (All-S)	22.7 ± 0.3
Polyamide-6 + Cloisite® 30B + E-GMA (PI-C)	19.9 ± 0.1
Polyamide-6 + Cloisite® 30B + E-GMA (PC-I)	23.7 ± 0.1
Polyamide-6 + Cloisite® 30B + E-GMA (IC-P)	21.1 ± 0.3

4.5.4 MFI Analysis Results of Nanocomposites Containing E-MA-GMA Elastomer

Table 4.16 shows the MFI measurement results for polyamide-6 nanocomposites in All-S sequence with/without E-MA-GMA elastomer. MFI of unfilled polyamide-6 is observed to decrease in polyamide-6/E-MA-GMA blends and in ternary nanocomposites. The reasons are similar to the ones discussed in Sections 4.5.1, 4.5.2 and 4.5.3.

Table 4.16 MFI measurement results for polyamide-6 nanocomposites in All-S sequence with/without E-MA-GMA elastomer

	MFI (g/10 min)
Polyamide-6	34.3 ± 0.9
Polyamide-6 + Cloisite® 15A	31.2 ± 0.2
Polyamide-6 + Cloisite® 25A	35.3 ± 2.9
Polyamide-6 + Cloisite® 30B	35.5 ± 3.4
Polyamide-6 + E-MA-GMA Blend (5 weight %)	23.1 ± 0.5
Polyamide-6 + Cloisite® 15A + E-MA-GMA (All-S)	24.9 ± 0.4
Polyamide-6 + Cloisite® 25A + E-MA-GMA (All-S)	21.3 ± 0.2
Polyamide-6 + Cloisite® 30B + E-MA-GMA (All-S)	25.7 ± 0.1

4.6 DSC ANALYSIS

DSC thermograms of pure polyamide-6, polyamide-6/elastomer blends, binary and ternary nanocomposites are listed in Appendix A, Figures A. 1 through A.34. Tables 4.17-4.21 provide a summary of the results.

Table 4.17 shows the effect of organoclay type on thermal properties of binary nanocomposites. The T_g values are not changed significantly owing to the low amount of organoclay in the system. Melting of the nanocomposites occur at a slightly lower temperature than that of unfilled polyamide-6. This may be related to a slight reduction in crystallite size in the presence of fillers (Ogata et al., 1997). The percent crystallinity of the polyamide phase is calculated as the ratio of the heat of fusion of the sample (ΔH_f), divided by the weight fraction of polyamide in the nanocomposite and the heat of fusion of the pure crystalline form of polyamide-6 (ΔH_f^0). The ΔH_f^0 value for polyamide-6 matrix is taken as 190.9 J/g (Inoue, 1963). According to Table 4.17, it can be seen that the crystallinity slightly decreases in the presence of Cloisite® 25A and Cloisite® 30B organoclays. The study performed by Devaux et al. showed that crystallization rate of the nanocomposite material is definitely lower than that of the polyamide-6 alone when the two materials are crystallized under identical cooling conditions (Devaux et al., 2002). This unexpected result, combined with the fact that melting temperature is slightly decreased in the nanocomposites, shows that polyamide-6 macromolecules may be oriented in the vicinity of clay. The changes in melting temperatures and % crystallinities are not so significant, because, nucleation effect of organoclays may be counteracted by the clay particles since crystal growth can be terminated by clay particles (Fornes and Paul, 2003).

Table 4.17 Effect of organoclay type on thermal properties of binary nanocomposites

	T_g (°C)	T_m (°C)	%Crystallinity
Polyamide-6	67.7	223.5	30.7
Polyamide-6 / Cloisite® 15A Nanocomposite	68.2	222.1	31.0
Polyamide-6 / Cloisite® 25A Nanocomposite	66.7	221.7	25.6
Polyamide-6 / Cloisite® 30B Nanocomposite	67.8	221.6	29.6

4.6.1 DSC Analysis Results of Polyamide-6/Elastomer Blends

Melting temperatures and % crystallinities in polyamide-6/elastomer polymer blends can be observed in Table 4.18. T_g is not detected in polyamide-6/elastomer blends and in polyamide-6/organoclay/elastomer ternary nanocomposites. DSC thermograms for elastomers E-BA-MAH, E-GMA and E-MA-GMA elastomers can be seen in Figures 4.69, 4.70 and 4.71, and melting temperatures for these elastomers are 107.2 °C, 104.5 °C and 68.6 °C, respectively. Two melting temperatures are observed for blends and composites processed by using E-BA-MAH and E-GMA elastomers in DSC thermograms, indicating two-phase morphology, which is seen from SEM micrographs. Melting temperature of elastomer E-MA-GMA can not be observed in blends and ternary nanocomposites. The crystallinity of the polyamide-6 phase slightly decreases with increasing amounts of E-BA-MAH, E-GMA and E-MA-GMA elastomers, according to Table 4.18. The decrease in % crystallinities is due to the difficulties in polymer chain arrangement and restricted movement by the branched chains which are formed by the reactions between elastomer functional groups and polyamide-6 (Sathe et al., 1996).

Table 4.18 Melting temperatures and % crystallinities in polyamide-6/elastomer polymer blends

	T_{m1} / T_{m2} (°C)	% crystallinity
Polyamide-6	- / 223.5	30.7
Polyamide-6 / 5 weight % E-BA-MAH	104.8 / 221.9	30.5
Polyamide-6 / 10 weight % E-BA-MAH	104.2 / 221.8	27.6
Polyamide-6 / 15 weight % E-BA-MAH	103.9 / 221.7	24.7
Polyamide-6 / 5 weight % E-GMA	103.6 / 225.6	28.4
Polyamide-6 / 10 weight % E-GMA	101.2 / 223.2	27.7
Polyamide-6 / 15 weight % E-GMA	101.5 / 222.5	26.5
Polyamide-6 / 5 weight % E-MA-GMA	- / 222.3	29.3
Polyamide-6 / 10 weight % E-MA-GMA	- / 222.6	28.8
Polyamide-6 / 15 weight % E-MA-GMA	- / 222.6	25.5

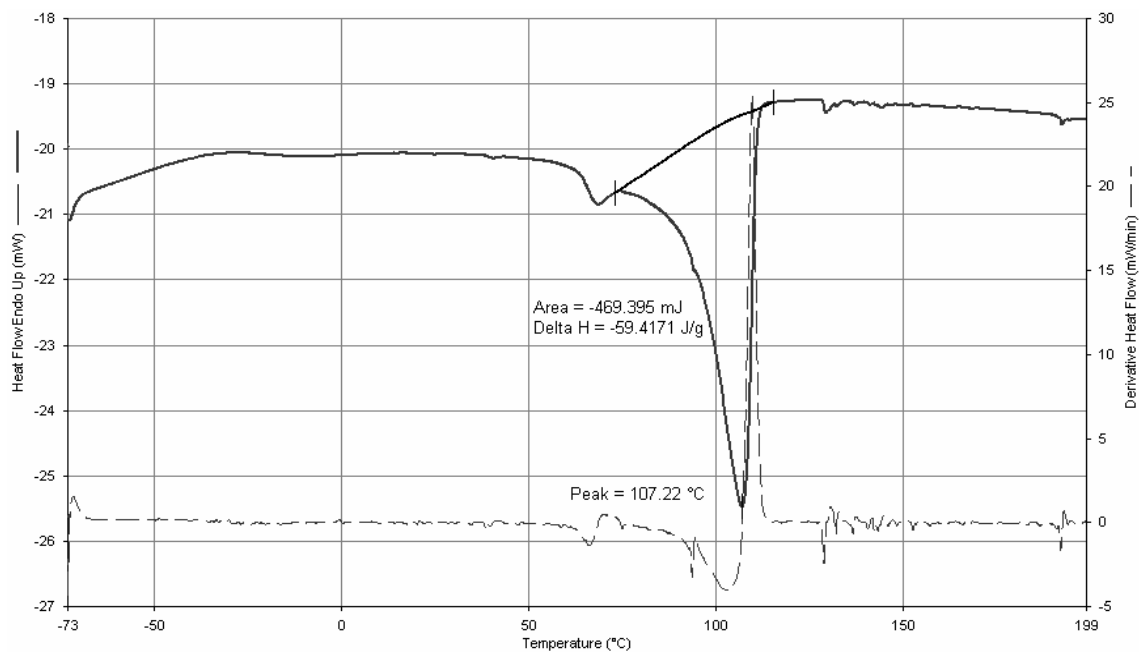


Figure 4.69 DSC Termogram of pure elastomer E-BA-MAH

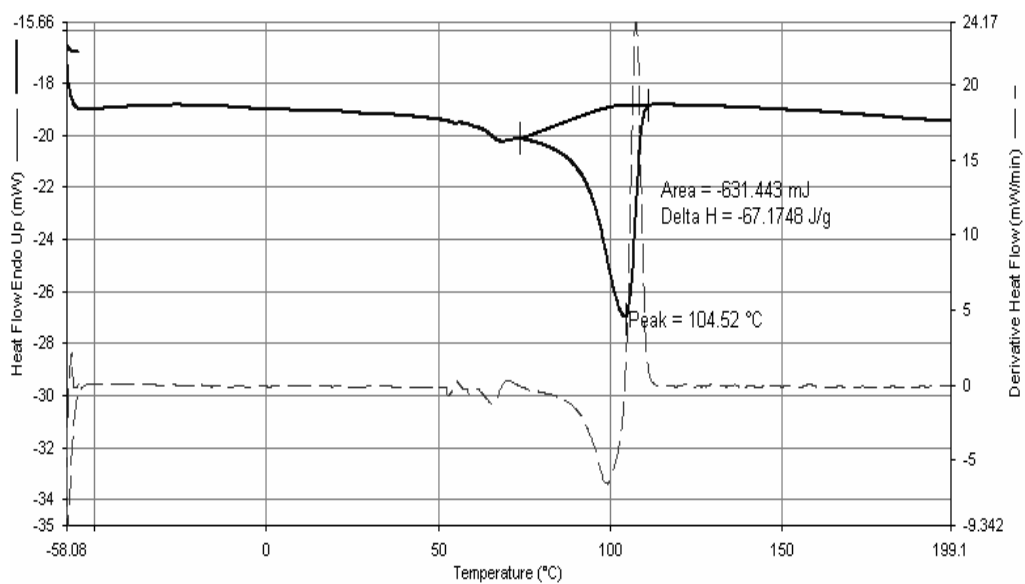


Figure 4.70 DSC Termogram of pure elastomer E-GMA

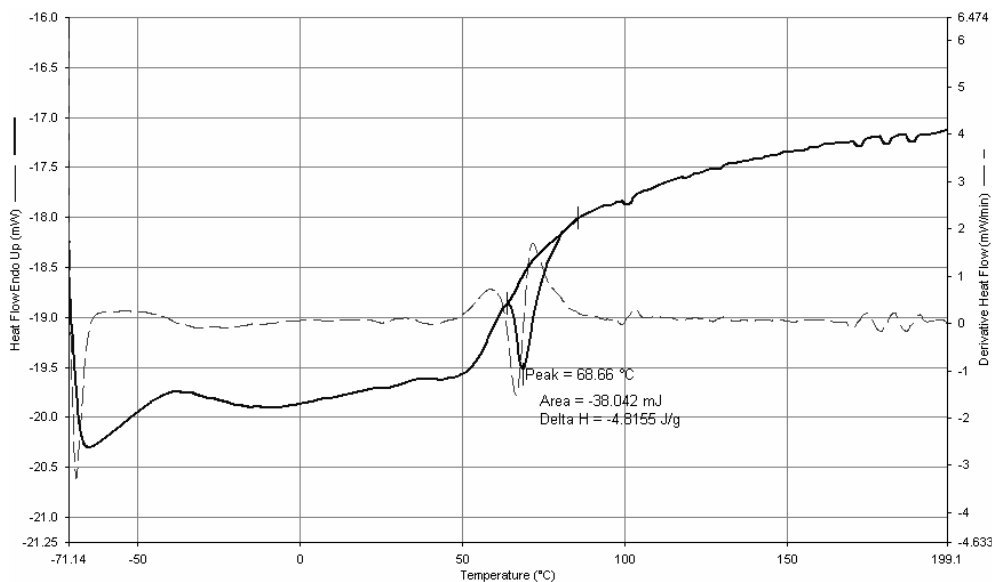


Figure 4.71 DSC Termogram of pure elastomer E-MA-GMA

4.6.2 DSC Analysis Results of Nanocomposites Containing E-BA-MAH Elastomer

The effects of organoclay type and elastomer E-BA-MAH on melting temperature and % crystallinity of polyamide-6 can be observed in Table 4.19. In ternary nanocomposites, melting temperatures for polyamide-6 show no significant change with respect to binary blends of elastomer and binary nanocomposites. In ternary nanocomposites, crystallinities are lower than those of polyamide-6/organoclay binary nanocomposites. This effect may be attributed to the possible interactions among the elastomeric material, polyamide-6 and the organoclay.

Table 4.19 also shows the effect of mixing orders on melting temperatures and % crystallinities of polyamide-6/Cloisite® 15A/E-BA-MAH and polyamide-6/Cloisite® 25A/E-BA-MAH nanocomposites. Melting temperatures and % crystallinities are generally the same for all mixing orders. Variations in blending sequences do not result in significant changes in crystallinity.

Table 4.19 Melting temperatures and % crystallinities of polyamide-6/organoclay/E-BA-MAH nanocomposites

	T_{m1} / T_{m2} (°C)	% crystallinity
Polyamide-6	- / 223.5	30.7
Polyamide-6 + Cloisite® 15A	- / 222.1	31.0
Polyamide-6 + Cloisite® 25A	- / 221.7	25.6
Polyamide-6 + Cloisite® 30B	- / 221.6	29.6
Polyamide-6 / 5 weight % E-BA-MAH	104.8 / 221.9	30.5
Polyamide-6 + Cloisite® 15A+ E-BA-MAH (All-S)	104.8 / 222.5	28.3
Polyamide-6 + Cloisite® 15A+ E-BA-MAH (PI-C)	103.7 / 221.4	26.8
Polyamide-6 + Cloisite® 15A+ E-BA-MAH (PC-I)	102.4 / 221.5	26.2
Polyamide-6 + Cloisite® 15A+ E-BA-MAH (IC-P)	103.1 / 221.2	27.2
Polyamide-6 + Cloisite® 25A+ E-BA-MAH (All-S)	103.9 / 221.8	25.0
Polyamide-6 + Cloisite® 25A+ E-BA-MAH (PI-C)	104.3 / 220.7	25.3
Polyamide-6 + Cloisite® 25A+ E-BA-MAH (PC-I)	103.1 / 221.8	23.1
Polyamide-6 + Cloisite® 25A+ E-BA-MAH (IC-P)	103.1 / 220.9	25.2
Polyamide-6 + Cloisite® 30B+ E-BA-MAH (All-S)	105.2 / 221.3	26.9

4.6.3 DSC Analysis Results of Nanocomposites Containing E-GMA Elastomer

Melting temperatures and % crystallinities of polyamide-6/organoclay/E-GMA nanocomposites in All-S sequence can be observed in Table 4.20. The effect of elastomer on crystallinity is dominant over the effect of organoclay. Except for Cloisite® 25A containing nanocomposites, crystallinity of polyamide-6 phase in binary nanocomposites decreases when elastomer is added. The decrease in crystallinity in the presence of elastomer, resulting from the restricted movement of branched chains can be attributed to the interactions between GMA groups and polyamide-6.

Table 4.20 also shows the effect of mixing orders on melting temperatures and % crystallinities of polyamide-6/Cloisite® 15A/E-GMA and polyamide-6/Cloisite® 30B/E-GMA nanocomposites. Melting temperatures and % crystallinities are generally the same for all mixing orders. It is interesting to notice that crystallinity in polyamide-6/Cloisite® 30B/E-GMA nanocomposites is lower than the polyamide-6/Cloisite® 15A/E-GMA nanocomposites. The difference can be attributed to the difficulty in polymer chain arrangement due to the interactions between hydroxyl groups on Cloisite® 30B surface and GMA functional group.

Table 4.20 Melting temperatures and % crystallinities of polyamide-6/organoclay/E-GMA nanocomposites

	T_{m1} / T_{m2} (°C)	% crystallinity
Polyamide-6	- / 223.5	30.7
Polyamide-6 + Cloisite® 15A	- / 222.1	31.0
Polyamide-6 + Cloisite® 25A	- / 221.7	25.6
Polyamide-6 + Cloisite® 30B	- / 221.6	29.6
Polyamide-6 / 5 weight % E-GMA	103.6 / 225.6	28.4
Polyamide-6 + Cloisite® 15A+ E-GMA (All-S)	103.7 / 223.1	30.7
Polyamide-6 + Cloisite® 15A+ E-GMA (PI-C)	100.5 / 221.8	30.9
Polyamide-6 + Cloisite® 15A+ E-GMA (PC-I)	99.8 / 221.5	28.5
Polyamide-6 + Cloisite® 15A+ E-GMA (IC-P)	102.4 / 221.7	28.5
Polyamide-6 + Cloisite® 25A+ E-GMA (All-S)	102.4 / 222.4	28.8
Polyamide-6 + Cloisite® 30B+ E-GMA (All-S)	102.4 / 221.9	27.6
Polyamide-6 + Cloisite® 30B+ E-GMA (PI-C)	101.8 / 221.5	26.6
Polyamide-6 + Cloisite® 30B+ E-GMA (PC-I)	99.2 / 221.7	27.2
Polyamide-6 + Cloisite® 30B+ E-GMA (IC-P)	99.2 / 221.8	29.4

4.6.4 DSC Analysis Results of Nanocomposites Containing E-MA-GMA Elastomer

Melting temperatures of polyamide-6/organoclay/E-MA-GMA nanocomposites in All-S sequence are demonstrated in Table 4.21. It can be seen that in the presence of both elastomer and organoclay melting temperatures of polyamide-6/organoclay/E-MA-GMA nanocomposites remain nearly the same when compared with polyamide-6/E-MA-GMA blend and binary polyamide-6/organoclay nanocomposites. % crystallinity of polyamide-6 phase in binary nanocomposites decreases when elastomer is added.

Table 4.21 Melting temperatures and % crystallinities of polyamide-6/organoclay/E-MA-GMA nanocomposites

	T_{m1} / T_{m2} (°C)	% crystallinity
Polyamide-6	- / 223.5	30.7
Polyamide-6 + Cloisite® 15A	- / 222.1	31.0
Polyamide-6 + Cloisite® 25A	- / 221.7	25.6
Polyamide-6 + Cloisite® 30B	- / 221.6	29.6
Polyamide-6 / 5 weight % E-MA-GMA	- / 222.3	29.3
Polyamide-6 + Cloisite® 15A + E-MA-GMA (All-S)	- / 222.8	28.7
Polyamide-6 + Cloisite® 25A + E-MA-GMA (All-S)	- / 222.7	29.6
Polyamide-6 + Cloisite® 30B + E-MA-GMA (All-S)	- / 222.7	28.5

4.7 MECHANICAL PROPERTIES

4.7.1 Impact Properties

4.7.1.1 Impact Strength Results of Polyamide-6/Elastomer Blends

Polyamides have great industrial importance because of their excellent tensile properties, chemical and abrasion resistance and high melting point. However, their use is limited by low impact strength especially below the glass transition temperature, poor dimensional stability due to high hygroscopy and poor processability. Blends of polyamide-6 with rubbers and polyamide-6 based composite materials have been extensively studied in order to improve its physical properties (Campbell et al., 1990; Kudva et al., 1998; González-Montiel et al., 1995; Kudva et al., 1999; Triacca et al., 1991). In semicrystalline polymers, the predominant mechanism for toughening is the shear banding, but rubber phase cavitation and shear yielding of the polymer phase are also important (Ramsteiner and Heckmann, 1985, Majumdar et al., 1994). All studies conclude that toughening of semicrystalline polymers is a complex mechanism including the initial elastic loading of the matrix/rubber blend, the internal or external cavitation of the dispersed rubber particles, followed by craze initiation and shear banding of the matrix (Karayannidis et.al., 2002).

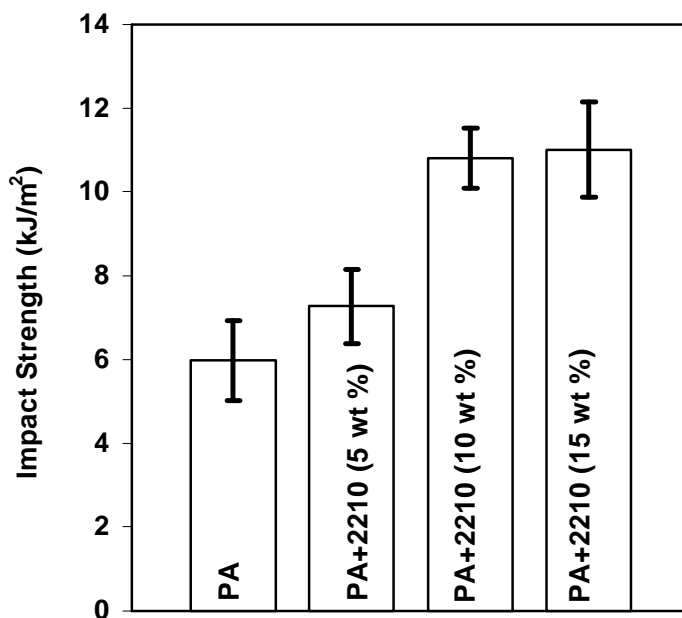


Figure 4.72 Effect of elastomer content on impact strength of E-BA-MAH elastomer toughened polyamide-6 blends

The effects of elastomer content on impact strengths of polyamide-6/E-BA-MAH, polyamide-6/E-GMA and polyamide-6/E-MA-GMA blends are shown in Figures 4.72-4.74. Impact strength of polyamide-6 increases when melt blended with elastomer and it is approximately proportional to the elastomer content. It is known that with increasing rubber content the brittle-ductile transition temperature is shifted to lower temperatures which promote toughening (van der Wal et.al. 1990). Also, SEM micrographs show that these elastomers formed a second phase in polymer matrix. Rubber particles are responsible for void initiation internally on the particles or at the rubber-matrix boundary (Bucknall et al., 1989). The rubber particles act as stress concentrators in producing crazes. A very large surface area is produced during crazing and dewetting process, thus high energy can be absorbed. Reactions occurring between polyamide-6 and elastomers are also important since there should be a good adhesion between the polyamide-6 and elastomer.

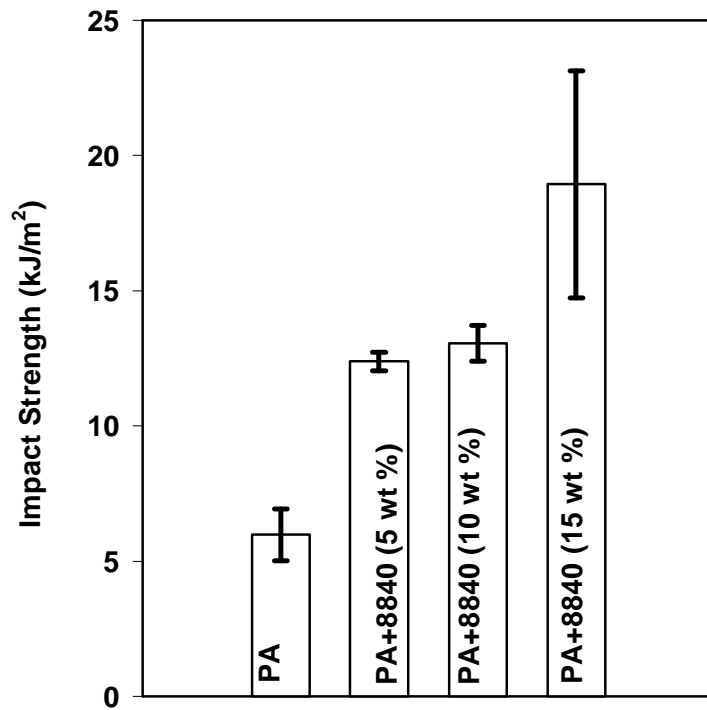


Figure 4.73 Effect of elastomer content on impact strength of E-GMA elastomer toughened polyamide-6 blends

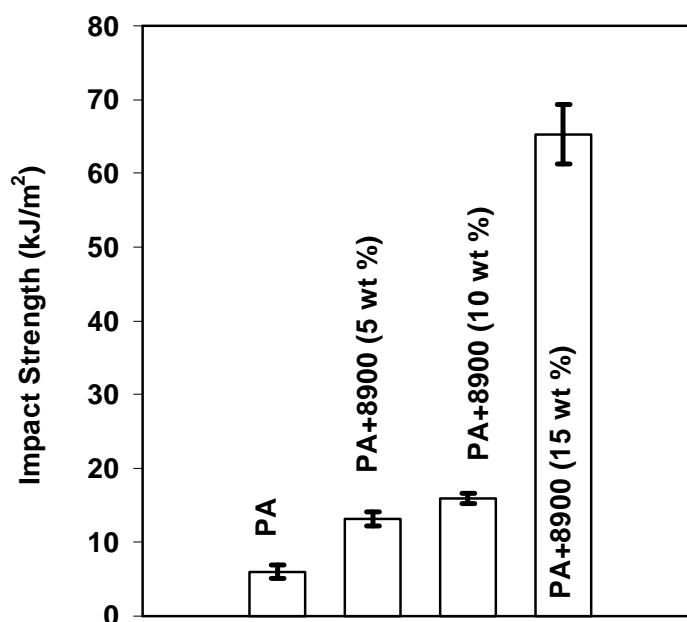


Figure 4.74 Effect of elastomer content on impact strength of E-MA-GMA elastomer toughened polyamide-6 blends

Polyamide-6/E-BA-MAH blends have lower impact strengths than E-GMA and E-MA-GMA containing blends. It is seen from Tables 4.5 through 4.7 that MAH based elastomer domains are around 50-60 nm and much smaller than the GMA based elastomer domains. It is known that toughening occurs in a specific size range and effective toughening may not be favorable on nanolength scales. Rubber particles must be smaller than 1 μm to obtain super-tough polyamide materials (Oshinski et al., 1992, Oshinski et al., 1996). Rubber particle size higher than 100 nm, is one of the critical factors to achieve effective toughening (Kelnar et al., 2005). GMA can react with both amine and acid ends of polyamide-6, unlike MAH, thus, interfacial adhesion might be higher in GMA containing blends resulting high impact strength.

4.7.1.2 Impact Strength Results of Nanocomposites Containing E-BA-MAH Elastomer

Impact strength of polyamide-6/organoclay/E-BA-MAH nanocomposites can be seen in Figure 4.75. Incorporation of E-BA-MAH to a matrix increases the impact strength, due to the cavitation of the dispersed rubber particles and craze initiation and shear banding of polymer matrix.

The addition of organoclay to polyamide-6 decreases its impact strength, acting as a crack initiator. Thus, impact modification of these binary nanocomposites with an impact modifier would be desirable. In ternary systems, impact strength is higher in comparison to binary nanocomposites with no elastomer. SEM micrographs of the ternary nanocomposites containing polyamide-6/organoclay/E-BA-MAH shown in Figure 4.34-4.36 explain the mechanism of impact modification. The energy spent on surface separation upon impact provides high impact strength. According to Table 4.19, which shows % crystallinities for polyamide-6/organoclay/E-BA-MAH nanocomposites in All-S sequence, crystallinity decreases as elastomer is introduced to the nanocomposites, this may lead to an increase in impact strength.

Rubber concentration, rubber particle size, shear modulus of rubber, interfacial adhesion and nylon matrix structure are the parameters that may affect the notched impact strength. The structure of the matrix does not change significantly with type, size and amount of rubber and is regarded as constant when varying the rubber concentration and particle size (Borggreve et al., 1985).

It should be noted that, Cloisite® 15A containing ternary nanocomposite has the highest impact strength in comparison to the impact strengths of ternary nanocomposites prepared with Cloisite® 25A and Cloisite® 30B. Table 4.8 shows the elastomer E-BA-MAH domain size in polyamide-6 nanocomposites in All-S sequence, largest domain size is observed in polyamide-6/Cloisite® 15A/E-BA-MAH nanocomposite. Domain size is important in toughness mechanism since small particles are not effective in hindering crack propagation.

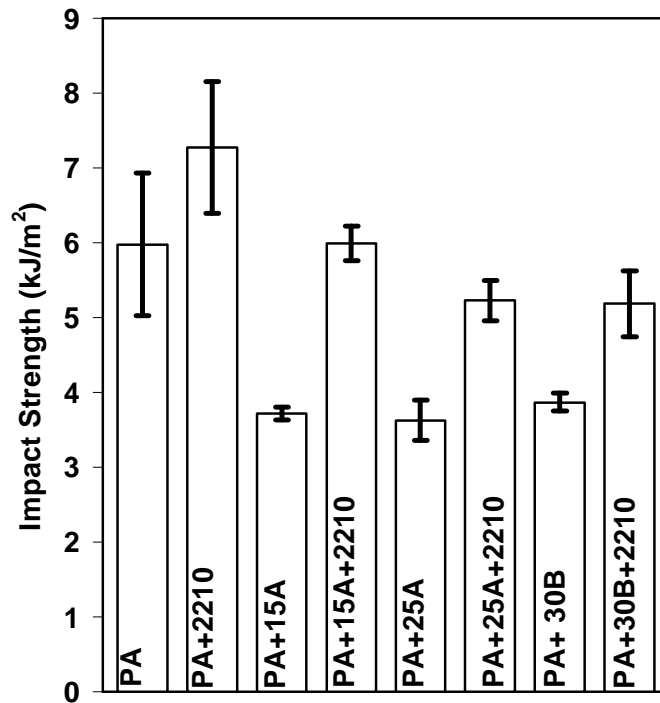


Figure 4.75 Effect of organoclay type on impact strength of E-BA-MAH elastomer toughened polyamide-6 nanocomposites

Wu suggested that the key parameter in toughening polyamides is interparticle distance rather than particle size, regardless of rubber type (Wu 1985). Critical interparticle distance depends on some extrinsic (impact speed, test temperature, mode of deformation) and intrinsic (interfacial adhesion, modulus of matrix, modulus of matrix/modulus of rubber ratio) parameters (Jiang et al., 1998; Borggreve et al., 1987; Liu et al., 2001). Interfacial adhesion is the main parameter that influences critical interparticle distance. The presence of organoclays modified with different surfactants should influence the interfacial adhesion, since the TEM micrograph in Figure 4.18 shows clay layers at the interphase. Interparticle distance of domains seems to be closer in 15A and 25A containing nanocomposites than in 30B containing nanocomposite.

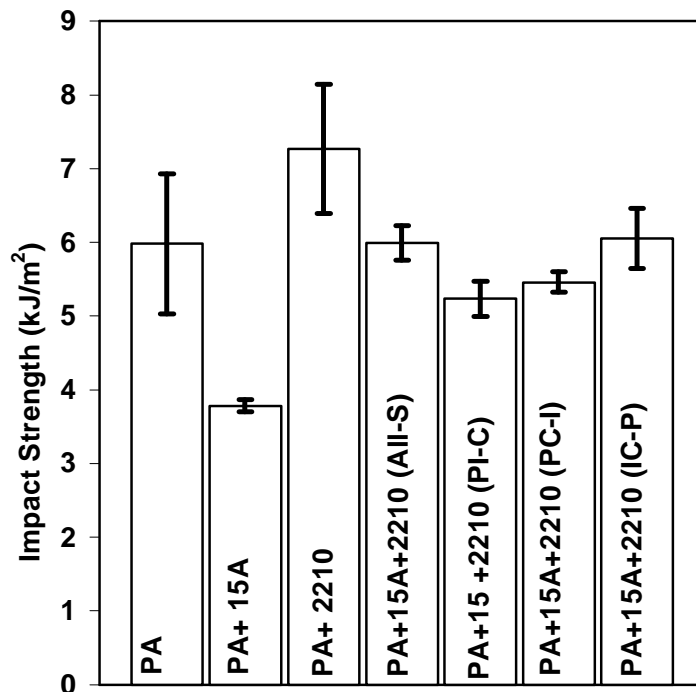


Figure 4.76 Effect of mixing order on impact strength of E-BA-MAH elastomer toughened polyamide-6/Cloisite® 15A nanocomposites

Figures 4.76 and 4.77 show effect of mixing order on impact strength of E-BA-MAH toughened polyamide-6/Cloisite® 15A and polyamide-6/Cloisite® 25A nanocomposites, respectively. Tables 4.1 and 4.3 show the d-spacing of these nanocomposites, whereas Tables 4.9 and 4.10 show the effect of mixing order on domain size of E-BA-MAH domains. Impact strength of polyamide-6/Cloisite® 15A/E-BA-MAH nanocomposites in all mixing sequences, increase with respect to its binary nanocomposite, regardless of d-spacing, as this organoclay and polyamide-6 are incompatible. All-S and IC-P sequence give nearly the same impact strength.

In polyamide-6/Cloisite® 25A/E-BA-MAH nanocomposites, PC-I mixing sequence gives the highest impact strength among the other mixing sequences within the experimental error limits. According to Table 4.10, elastomer domain size is bigger and the nanocomposite has the highest d-spacing, i.e highest contact surface of

organoclay with polymer matrix, as it can be observed in Table 4.3. In this mixing sequence, organoclay is first intercalated/exfoliated due to its affinity with polyamide-6 and a strong interaction may exist between them. Then, E-BA-MAH elastomer is added, maximizing polymer-organoclay interactions.

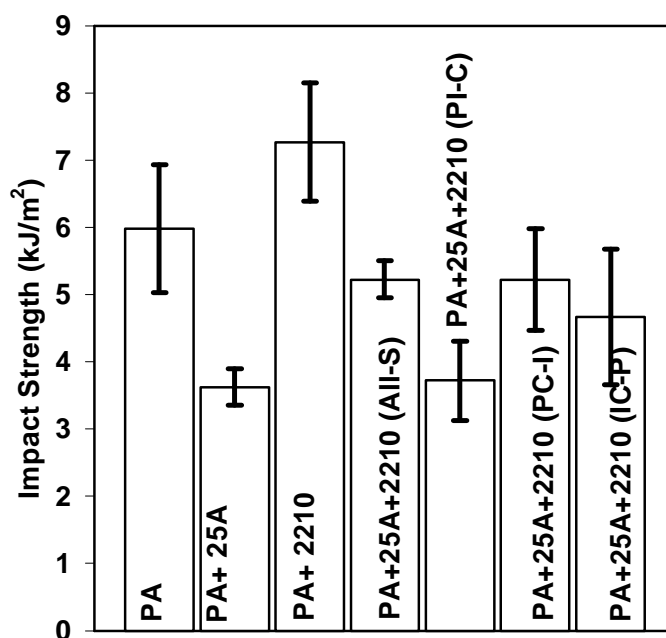


Figure 4.77 Effect of mixing order on impact strength of E-BA-MAH elastomer toughened polyamide-6/Cloisite® 25A nanocomposites

PI-C mixing sequence, independent of organoclay type, domain size and d-spacing data, give the lowest impact strength in Figures 4.76 and 4.77. In PI-C mixing order, the organoclay is extruded only once, thus the organoclay agglomerates may have been dispersed to a lower extent in this mixing sequence.

4.7.1.3 Impact Strength Results of Nanocomposites Containing E-GMA Elastomer

Figure 4.78 shows the effect of organoclay type on impact strength of E-GMA elastomer toughened polyamide-6 nanocomposites. E-GMA domains, which are shown in SEM Figures 4.25 and 4.43 through 4.45, increase the impact strength of polyamide-6 and binary nanocomposites, due to cavitation of elastomer particles, the associated matrix shear yielding mechanisms and their low glass transition temperatures. Impact strength decreases in binary polyamide-6/organoclay nanocomposites, regardless of surfactant type. Rigid fillers act as stress concentrators in a polymer matrix and generally, they increase the brittle-to-tough transition temperature, thus, impact strength at room temperature decreases. In ternary systems, impact strength is higher in comparison to binary nanocomposites with no elastomer. % crystallinities, as shown in Table 4.16, decrease as elastomer is introduced to the nanocomposites; this may lead to an increase in impact strength. Cloisite® 15A containing ternary nanocomposites show the highest impact strength in comparison to the impact strengths of ternary nanocomposites prepared with Cloisite® 25A and Cloisite® 30B, similar to the ternary nanocomposites having elastomer E-BA-MAH. According to Figures 4.43-4.45, it can be seen that interparticle distance is closer in Cloisite® 15A and 30B organoclay containing nanocomposites. Interfacial adhesion, which influences the interparticle distance, varies with respect to organoclay surfactant polarity and functional groups on it.

Figures 4.79 and 4.80 show effect of mixing order on impact strength of E-GMA toughened polyamide-6/Cloisite® 15A and polyamide-6/Cloisite® 30B nanocomposites, respectively. Tables 4.2 and 4.4 show the d-spacing of these nanocomposites, whereas Tables 4.12 and 4.13 show the effect of mixing order on domain size of E-GMA domains. Impact strength of polyamide-6 is increased in all mixing orders for the produced nanocomposites. As observed in Figure 4.79, impact strength is highest in All-S sequence, when all three components blended simultaneously. In-situ formed polyamide-6/elastomer copolymer helps in finely

dispersing the elastomer phase as shown in Figure 4.43, hence improving interfacial interaction and leading to an increase in the impact strength.

PC-I mixing sequence gives the highest impact strength in polyamide-6/Cloisite® 30B/E-GMA nanocomposites. According to suppliers' data, Cloisite® 30B with -OH groups on its modifier has the least hydrophobic surface among the organoclays studied. Interactions occur via hydrogen bonding between polyamide-6 and Cloisite® 30B organic modifier, thus, this organoclay is thought to be the most compatible among the others. Mixing polyamide-6 with organoclay 30B prior to blending with elastomer, may lead to an increase in impact strength due to the compatibility of polyamide-6 with the organoclay.

PI-C mixing sequence gives the lowest impact strength, as it is observed in Figure 4.80, since the organoclay is extruded only once in this mixing sequence, it may be intercalated/exfoliated to a lower extent.

Although 30B and polyamide-6 are compatible, organoclay incorporation in the second extrusion may hinder the polyamide-6/E-GMA interactions resulting decrease in impact strength.

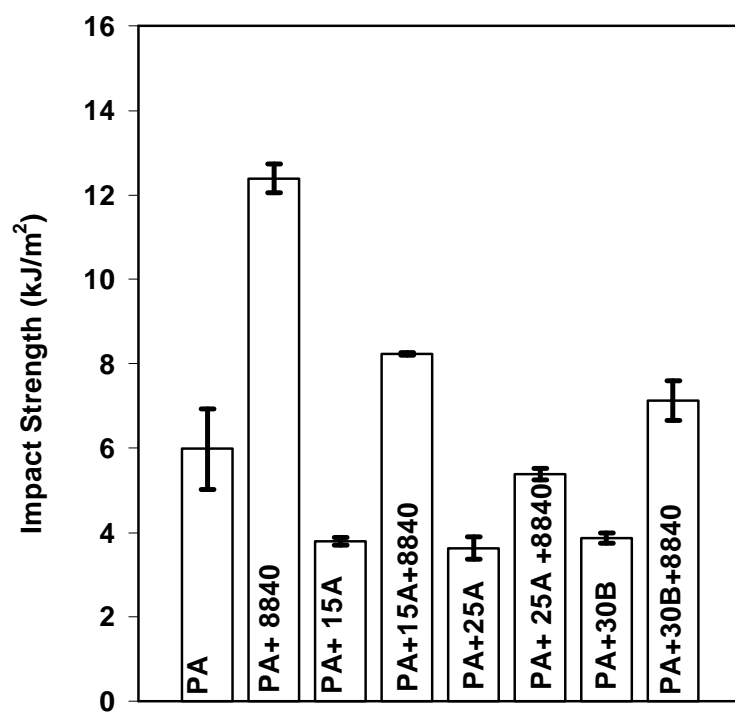


Figure 4.78 Effect of organoclay type on impact strength of E-GMA elastomer toughened polyamide-6 nanocomposites

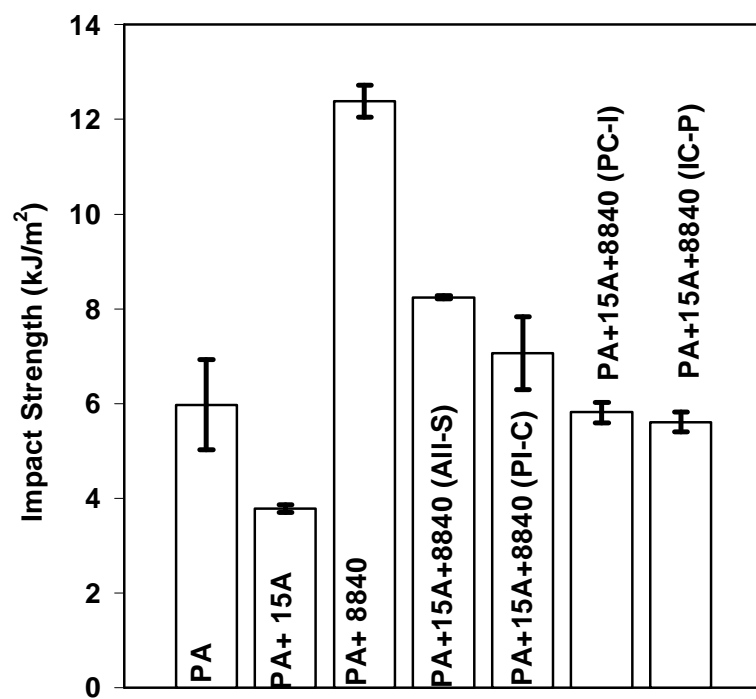


Figure 4.79 Effect of mixing order on impact strength of E-GMA elastomer toughened polyamide-6/Cloisite® 15A nanocomposites

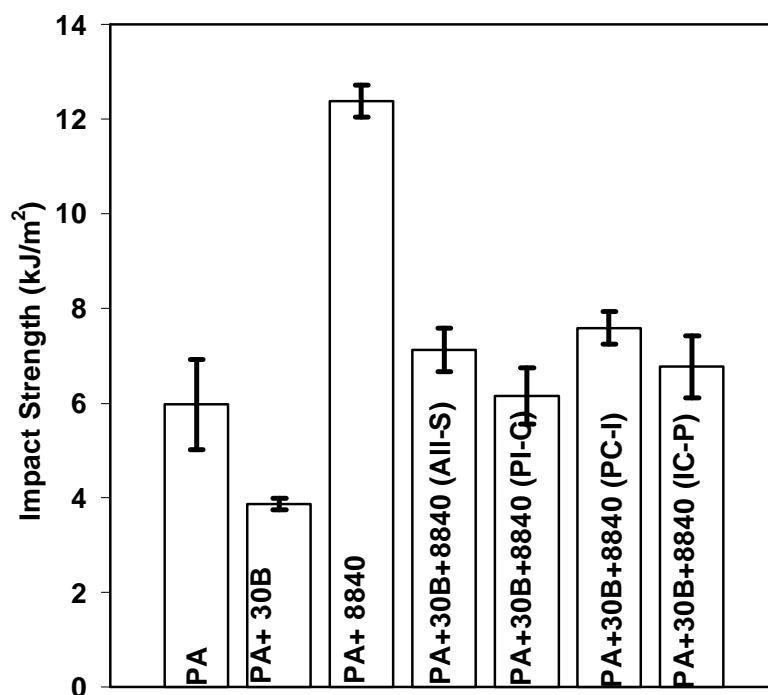


Figure 4.80 Effect of mixing order on impact strength of E-GMA elastomer toughened polyamide-6/Cloisite® 30B nanocomposites

4.7.1.4 Impact Strength Results of Nanocomposites Containing E-MA-GMA Elastomer

Figure 4.81 shows the effect of organoclay type on impact strength of E-MA-GMA elastomer toughened polyamide-6 nanocomposites. Organoclay decreases impact strength, whereas elastomer incorporation to polyamide-6 and binary nanocomposites increases the impact strength. All ternary nanocomposites give nearly the same impact strengths, which are higher than their corresponding binary nanocomposites. The reasons for the changes in impact strength with respect to organoclay and elastomer are discussed in sections 4.7.1.1 and 4.7.1.2.

Generally, GMA containing ternary nanocomposites have the highest impact strength, since interfacial adhesion is higher owing to two-side reaction possibility of GMA, and higher domain sizes in GMA containing nanocomposites.

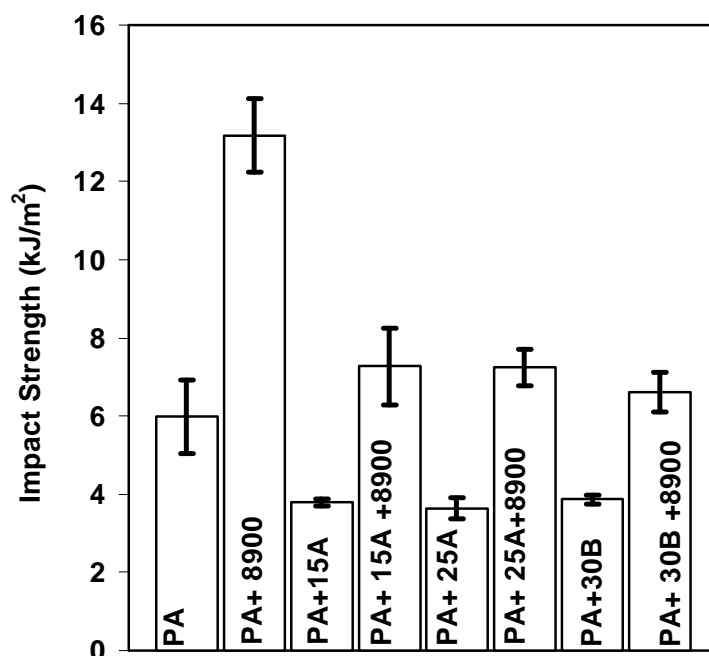


Figure 4.81 Effect of organoclay type on impact strength of E-MA-GMA elastomer toughened polyamide-6 nanocomposites

4.7.2 TOUGHNESS MEASUREMENTS

Toughness of the processed blends, nanocomposites and ternary systems is measured by calculating the area under tensile stress-strain curves. Due to the nature of testing methods, toughness and impact measurements are not correlated with each other. A polymer that has a yield point at a slow speed of testing may fracture in a brittle manner at high speeds. Also, many polymers which are ductile

under normal testing conditions may appear to be brittle if the test specimen contains a notch (Nielsen and Landel, 1994).

Figure 4.82 shows the effect of elastomer type on toughness of polyamide-6 blends with 5 wt % elastomer. E-BA-MAH is the most effective elastomer in terms of toughening, since it has butyl acrylate groups as the side chain. The decrease in toughness in polyamide-6/E-GMA and polyamide-6/E-MA-GMA blends can be attributed to the hindrance of free elastomer particles to cold drawing of the matrix, which may lead to an unstable flow that causes early rupture of the sample. Another reason may be the network effect induced by polyamide-6/elastomer copolymer, which acts as an interfacial agent between dispersed and continuous phases, and makes the system more or less interconnected and therefore less capable of flowing (Cimmino et al., 1986). Incorporation of organoclay increased polyamide-6 toughness. Nano scale dispersion and exfoliated nature of clay particles minimizes the stress concentration effects, and increase elongation at break and toughness by acting as crack stoppers. It is seen that toughness in binary nanocomposite systems is directly related with Young's modulus. Polyamide-6/Cloisite® 25A binary nanocomposite has higher tensile strength and Young's modulus than Polyamide-6/Cloisite® 15A and Polyamide-6/Cloisite® 30B nanocomposites, which are shown in Figures 4.88 and 4.89.

In ternary nanocomposites, as can be seen in Figure 4.84, polyamide-6/Cloisite® 15A/E-GMA, polyamide-6/Cloisite® 30B/E-GMA, polyamide-6/Cloisite® 15A/E-BA-MAH and polyamide-6/Cloisite® 25A/E-BA-MAH nanocomposites show equal or higher toughness values than pure polyamide-6. According to Figures 4.34-4.35 and 4.43-4.45, it can be seen that interparticle distance is generally smaller in these nanocomposites. E-BA-MAH elastomer is more effective in ternary nanocomposites, as it is also observed in binary blends.

These four materials combinations referred in the previous paragraph, are chosen to be promising, and different mixing orders which are explained in the experimental section are applied.

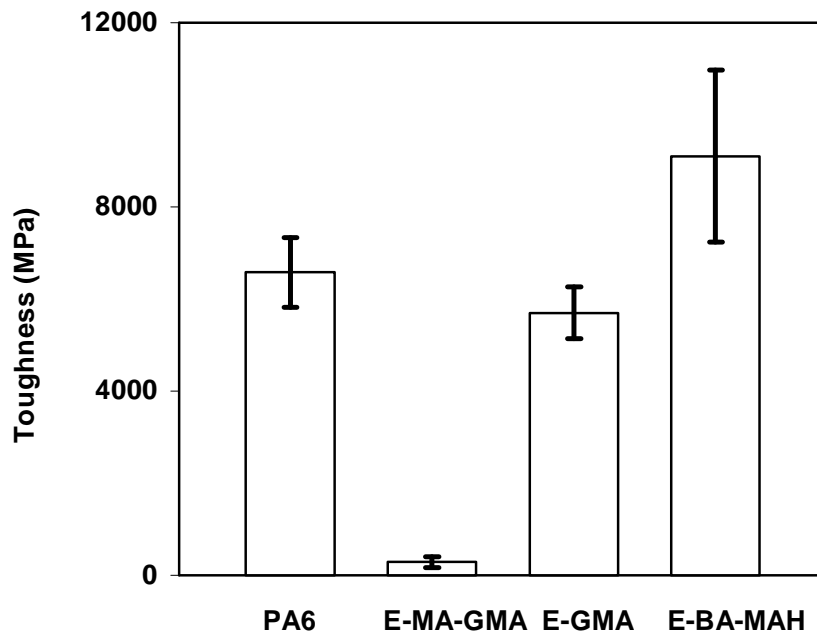


Figure 4.82 Effect of elastomer type on toughness of polyamide-6/elastomer blends

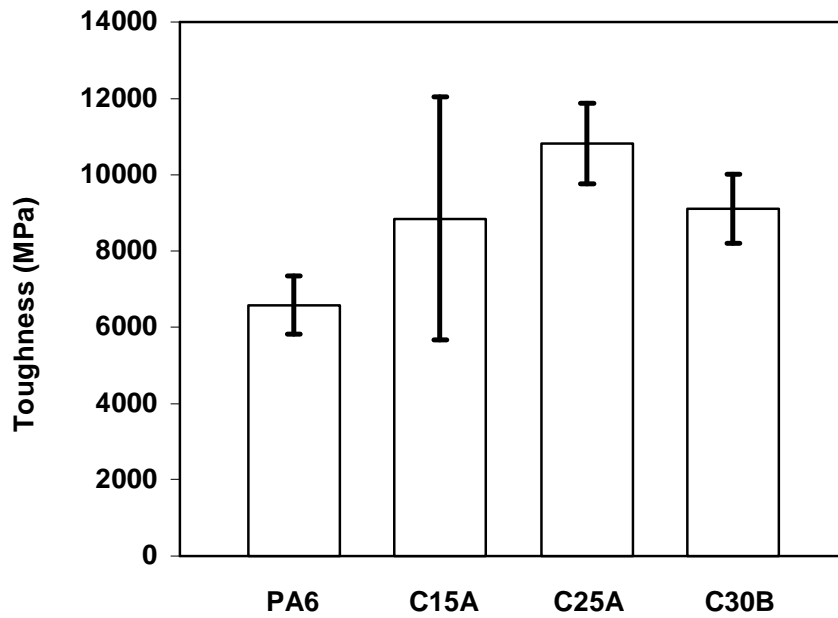


Figure 4.83 Effect of organoclay type on toughness of polyamide-6/organoclay nanocomposites

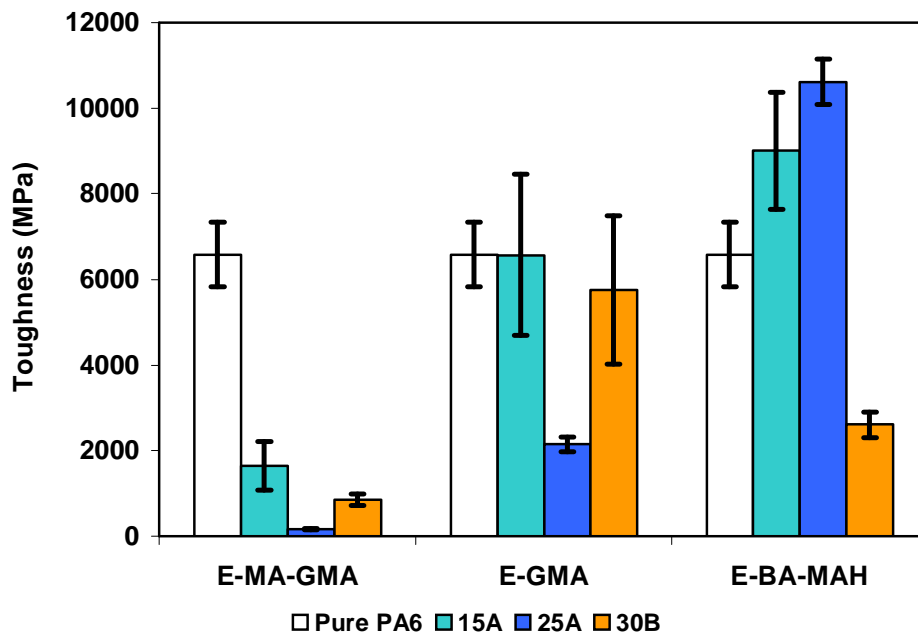


Figure 4.84 Toughness of polyamide-6/organoclay/elastomer ternary nanocomposites

4.7.3 TENSILE PROPERTIES

Mechanical characterization in terms of tensile properties is performed since these properties, especially elongation at break, are very sensitive to adhesion strength between components or partial miscibility at the interface of blend components in phase separated systems and are used to evaluate the degree of compatibilization in polymer blends and in nanocomposite systems (Nielsen and Landel, 1994).

In this study, tensile strength, Young's Modulus and percentage elongation at break values are determined by tensile test measurements.

4.7.3.1 Tensile Properties of Polyamide-6/Elastomer Blends

Figures 4.85-4.87 show the effects of E-BA-MAH elastomer on tensile properties. The tensile strength decreases as elastomer content increases, owing to the dilution effect, since the elastomer itself has a low tensile strength value of 12 MPa according to manufacturer's data. DSC analysis in Table 4.18 revealed that % crystallinity decreased with the increase in elastomer content. A decrease in crystallinity brings about decreases in tensile strength and in modulus, however, it increases elongation at break. Experimental results indicate that in the polyamide-6/E-BA-MAH blends, Young's Modulus remains unchanged in 5 wt % and 10 wt elastomer containing samples, owing to the low amount of elastomer balanced by chain extension/branching. For 15 wt % elastomer containing blend, modulus decreases. Except sample having 5 wt % E-BA-MAH, % elongation at break increases in the presence of elastomer. The decrease in elongation at break can be attributed to the hindrance of free elastomer particles to cold drawing of the matrix, which may lead to an unstable flow that causes early rupture of the sample. Another reason may be the network effect induced by polyamide-6/elastomer copolymer, which acts as an interfacial agent between dispersed and continuous phases, makes the system more or less interconnected and therefore less capable of flowing (Cimmino et al., 1986). Increase in elongation is assigned to the elastomeric character of rubber particles. The dispersed rubber particles act as stress concentrators during extension process. In this stress state, yielding or crazing occurs all around the particles, as a result, polymer absorbs high amount of energy and may elongate to a greater extent avoiding a highly localized strain process (Kim et al., 1998).

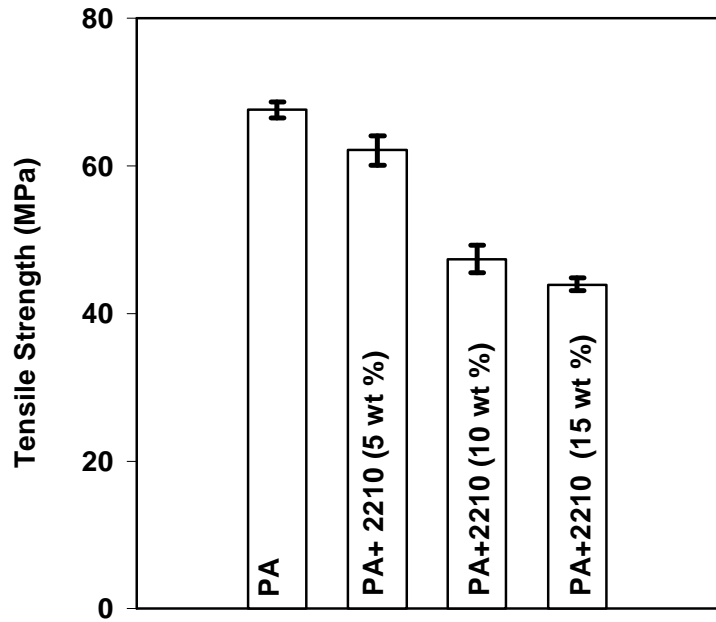


Figure 4.85 Effect of elastomer content on tensile strength of E-BA-MAH elastomer toughened polyamide-6 blends

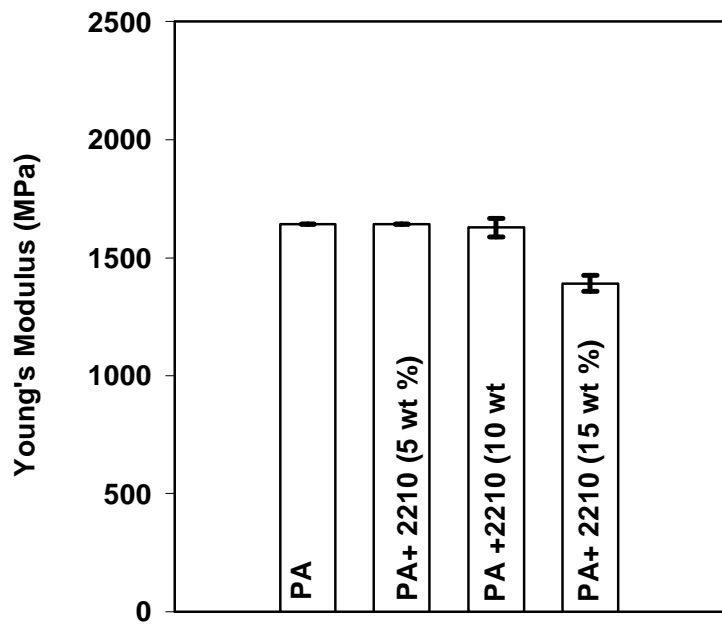


Figure 4.86 Effect of elastomer content on Young's Modulus of E-BA-MAH elastomer toughened polyamide-6 blends

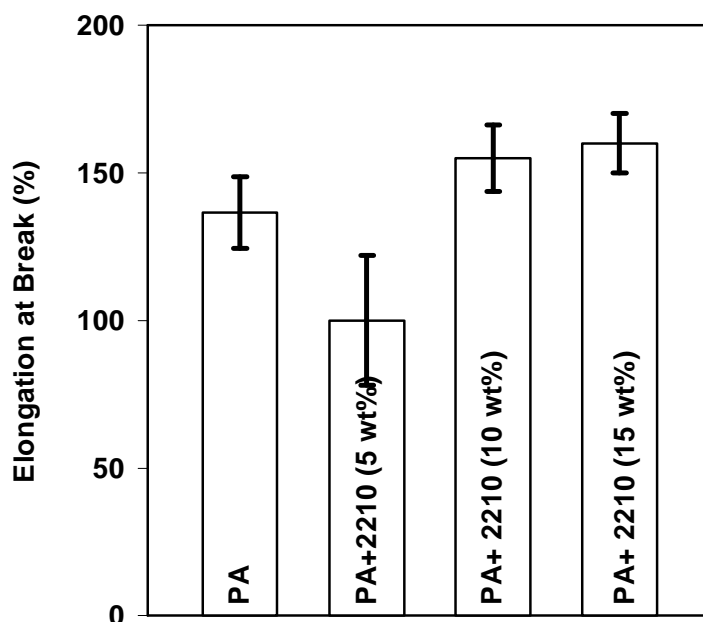


Figure 4.87 Effect of elastomer content on % elongation at break of E-BA-MAH elastomer toughened polyamide-6 blends

Figures 4.88 through 4.90 show the effect of elastomer content on tensile properties of E-GMA toughened polyamide-6 blends. Tensile strength shows a decreasing trend owing to the effect of elastomer. Addition of elastomer also decreases the crystallinity of the phases as shown in Table 4.20. Young's Modulus show no significant change upon E-GMA addition, owing to a decrease caused by the low modulus elastomer balanced by the possibility of obtaining high molecular weight copolymer due to chain extension/branching reactions, shown in Section 4.4.2. Tensile elongation at break data remain nearly the same, because of the reasons discussed above related with the Young's Modulus.

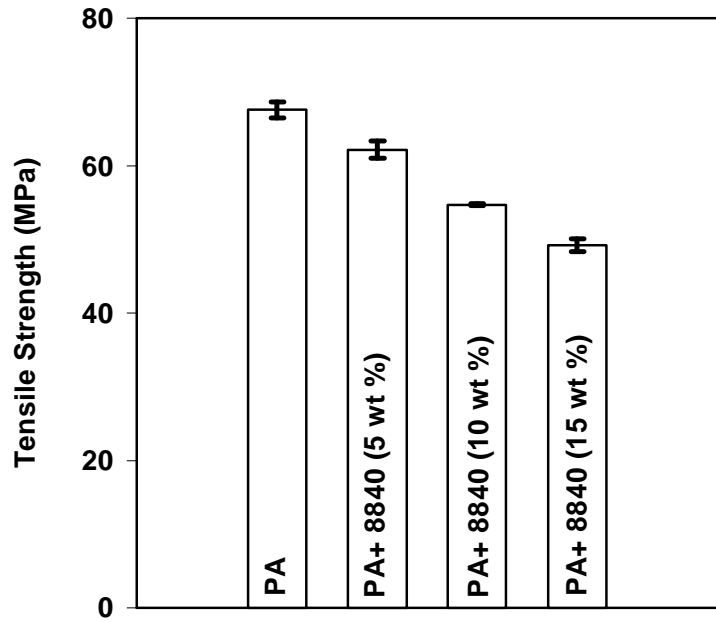


Figure 4.88 Effect of elastomer content on tensile strength of E-GMA elastomer toughened polyamide-6 blends

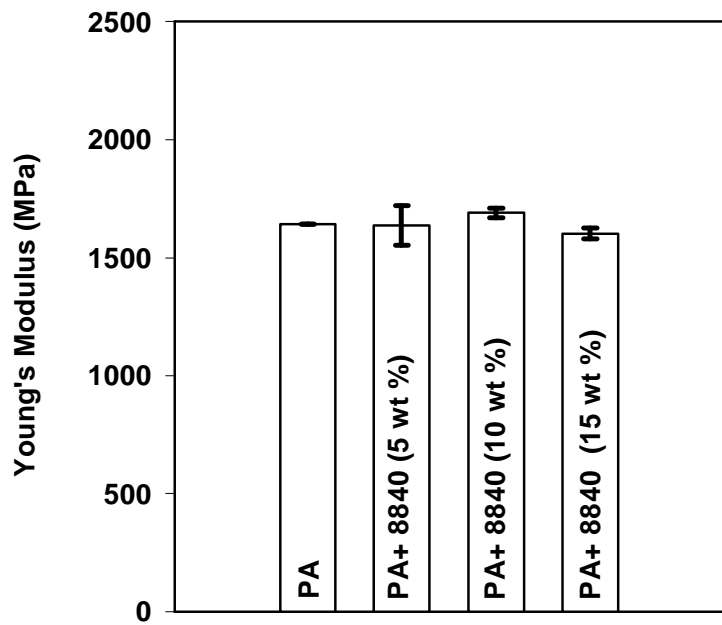


Figure 4.89 Effect of elastomer content on Young's Modulus of E-GMA elastomer toughened polyamide-6 blends

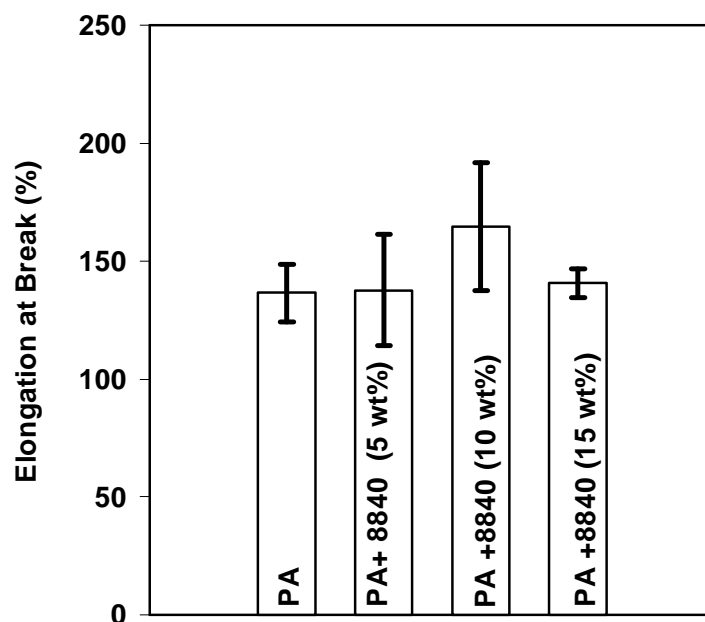


Figure 4.90 Effect of elastomer content on % elongation at break of E-GMA elastomer toughened polyamide-6 blends

Figures 4.91 through 4.93 show the effect of E-MA-GMA elastomer content on tensile properties of polyamide-6 based blends. Tensile strength decreases with increasing E-MA-GMA. The presence of elastomer does not cause significant variation in the tensile modulus. Elongation at break decreases in sample containing 5 wt % E-MA-GMA. Two main reasons can be invoked to explain the reduction of elongation at break for the blends. Hindrance effect of free elastomer particles to cold drawing and the copolymer network effect which makes the polymer matrix more or less interconnected therefore less capable of flowing. 15 wt % E-MA-GMA increases the tensile elongation at break.

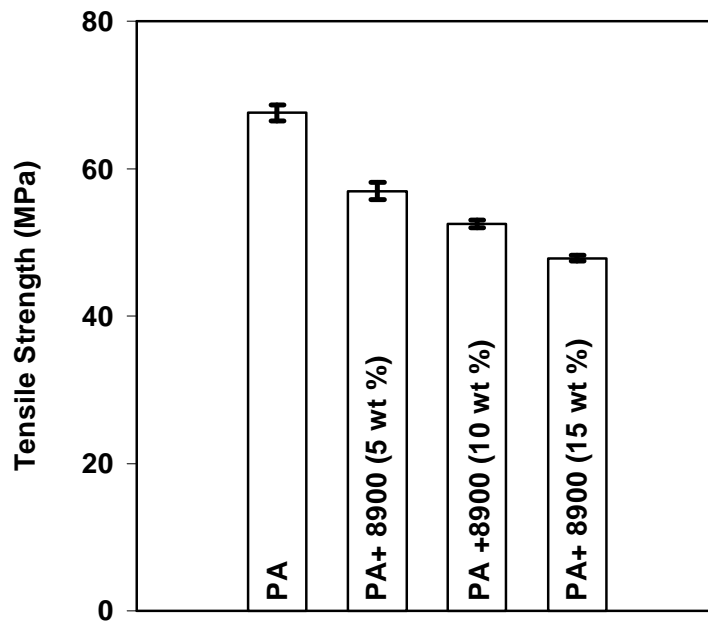


Figure 4.91 Effect of elastomer content on tensile strength of E-MA-GMA elastomer toughened polyamide-6 blends

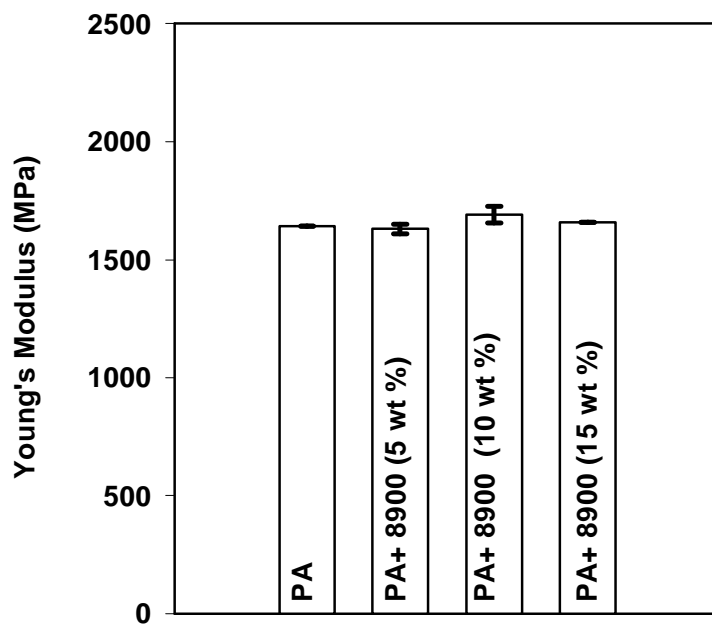


Figure 4.92 Effect of elastomer content on Young's Modulus of E-MA-GMA elastomer toughened polyamide-6 blends

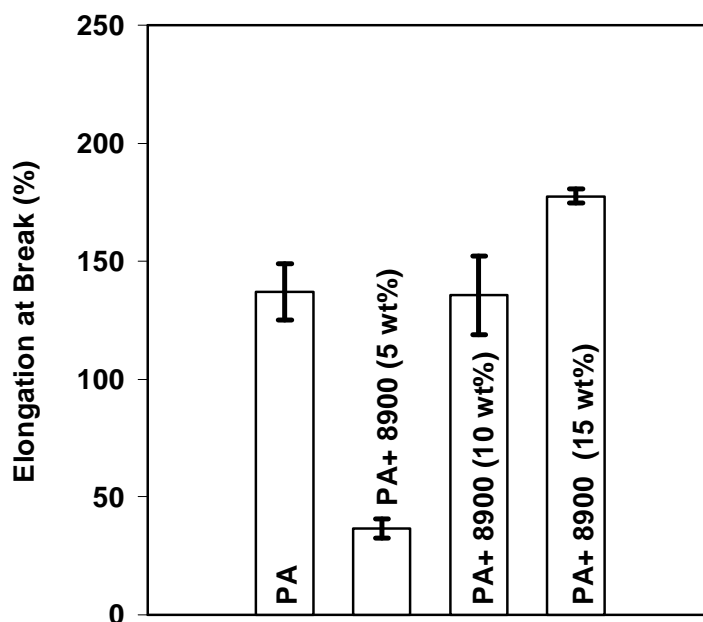


Figure 4.93 Effect of elastomer content on % elongation at break of E-MA-GMA elastomer toughened polyamide-6 blends

4.7.3.2 Tensile Properties of E-BA-MAH Elastomer Containing Nanocomposites

Figure 4.94 shows the variation in tensile strength with respect to both organoclay type and E-BA-MAH elastomer. As observed in this figure, in binary polyamide-6/organoclay nanocomposites, strength is increased with the addition of Cloisite® 25A and Cloisite® 30B organoclays with respect to unfilled polyamide-6. Clay organic modifier reduces the interlayer adhesion and promotes the compatibility with polyamide chains through strong polar interactions. For the organoclays 25A and 30B, XRD and TEM analysis results showed that d-spacing of organoclay is increased owing to the insertion of polyamide-6 matrix into clay galleries. This increase results in high contact surface area between the filler and the polymer matrix, so that polymer matrix-filler contact surface area increases. Cloisite® 15A

decreases the polyamide-6 tensile strength in binary nanocomposites. Surfactant of this organoclay has the most hydrophobic surface among the organoclays studied and with no polar groups on its modifier. It is known that polyamide-6 is a relatively polar polymer which has capability of making high degree of hydrogen bonding, and has a relatively good affinity for the polar surface of the montmorillonite. Furthermore, it can be seen from the Figure 4.1 that, d-spacing of pure Cloisite® 15A clay does not significantly change when it is melt blended with polyamide-6 and E-BA-MAH blended polyamide-6.

Tensile strength of polyamide-6/organoclay binary nanocomposite decreased when melt blended with elastomer E-BA-MAH. Thus, it can be concluded that, the effect of elastomer is more dominant than the effect of organoclay in terms of tensile strength. Polyamide-6/Cloisite® 15/E-BA-MAH nanocomposites have higher tensile strength than 25A and 30B containing ternary nanocomposites.

Young's Modulus of nanocomposites containing elastomer and various organoclays can be seen in Figure 4.95. For the binary nanocomposites, an increase in modulus is obtained with respect to neat polyamide-6. The increase in modulus with the addition of organoclay may again be attributed to the high aspect ratio of the organoclays providing high contact surface area between the filler and the polymer matrix. The increase in modulus with organoclay addition may also be attributed to the constraint of polymer chains by their interaction with clay surfaces. In ternary systems composed of polyamide-6, organoclay and E-BA-MAH, Young's modulus decreases when compared with nanocomposites with no elastomer. The reinforcement caused by the clay particles is partially opposed by the presence of elastomeric phase, which produces a slight decrease in Young's modulus. This phenomenon could be caused by the dilution effect by the low modulus elastomer, as well as the decrease in the crystallinity of polyamide-6 as discussed in Table 4.19. Observed reduced delamination of organoclay 25A and 30B particles in TEM analysis due to the presence of reactively formed copolymer may also be the reason for lower strength and modulus with respect to binary nanocomposites (Kelnar et al., 2006).

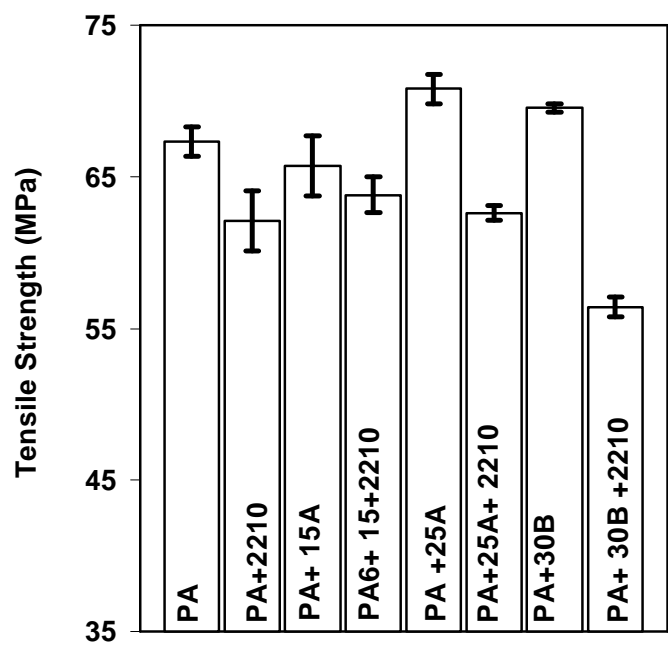


Figure 4.94 Effect of organoclay type on tensile strength of E-BA-MAH elastomer toughened polyamide-6 nanocomposites

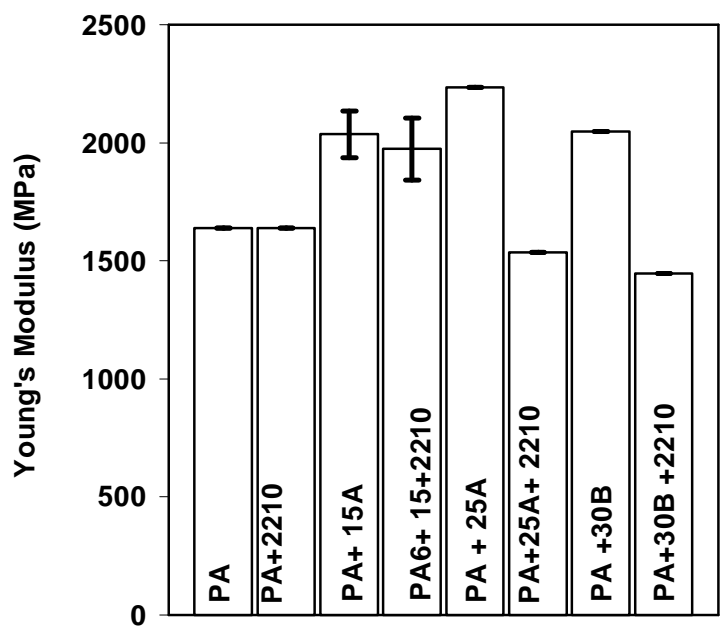


Figure 4.95 Effect of organoclay type on Young's Modulus of E-BA-MAH elastomer toughened polyamide-6 nanocomposites

It is interesting that in ternary nanocomposites, Cloisite® 15A gives the best result in both tensile strength and modulus. Hotta and Paul reported that the increase in modulus in polyethylene-maleic anhydride grafted polyethylene-organoclay nanocomposites is much higher for the organoclay with two alkyl tails, than in the one with one alkyl tail (Hotta and Paul, 2004). In another study, they have showed that the situation is exactly the opposite in polyamide-6; where one alkyl tail leads to much better dispersion of clay than two tails do (Fornes et al., 2002). They proposed that polyamide has relatively better affinity for the silicate surface than the alkyl part of organoclay; thus, minimizing the number of alkyl tails maximizes platelet dispersion in this polar polymer. But, polyethylene has much better affinity for the alkyl tails than the silicate surface; thus, maximizing alkyl tails should lead to better dispersion of clay in this non-polar matrix of polyethylene. The experimental data observed here lead to similar conclusions. Ternary nanocomposites prepared with Cloisite® 15A (with two alkyl tails) have higher tensile strength and modulus in comparison to the ternary nanocomposites prepared by Cloisite® 25A and Cloisite® 30B (with one alkyl tail in each). Cloisite® 15A is more compatible with the ethylene based backbone of E-BA-MAH, in comparison to Cloisite® 25A and Cloisite® 30B, owing to its hydrophobicity. On the other hand, Cloisite® 30B, being the most polar organoclay, would be the most compatible with the polyamide-6 phase, as supported by the XRD data. The tensile strength and modulus data indicate that the compatibility between the organoclay and the impact modifier is more effective in determining these mechanical properties than the compatibility between the organoclay and the polyamide-6 phase.

Figure 4.96 shows the variation in elongation at break with respect to both organoclay type and elastomer. Except for the materials polyamide-6/E-BA-MAH and polyamide-6/Cloisite® 30B/ E-BA-MAH, elongation at break values of all the processed samples are higher than that of unmodified polyamide-6. Generally, rigid inorganic particles decrease the elongation at break when their size is rather large. However, exfoliated nature and nano scale of clay particles minimizes the stress concentration effects, which may lead to a decrease in elongation. The organoclays used in this study increase the elongation at break by acting as crack stoppers. However, when E-BA-MAH is added to the binary polyamide-6/organoclay

nanocomposites, the elastomer E-BA-MAH decreases the elongation at break. The effect of clay is dominant than the organoclay effect, since elongation at break is lower for 5-wt % E-BA-MAH containing blends. Many factors affect the elongation at break of a polymer blend including impurities or defects and testing conditions, in addition to intrinsic structure and morphology.

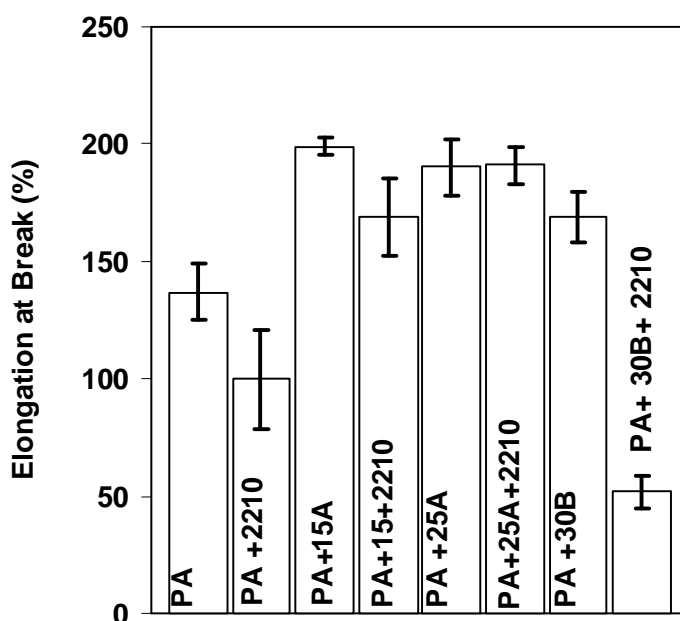


Figure 4.96 Effect of organoclay type on % elongation at break of E-BA-MAH elastomer toughened polyamide-6 nanocomposites

Effect of mixing order on tensile properties of E-BA-MAH toughened polyamide-6/Cloisite® 15A nanocomposites can be observed in Figures 4.97 through 4.99. It is seen that tensile strength of the composites decreases with the addition of elastomer. Among the other mixing orders, tensile strength, modulus and elongation at break is the highest in All-S sequence where all the components are simultaneously fed to the extruder. It is more favorable to mix all of the components

simultaneously since the same shear intensity is applied to all of them and the interactions that can take place between the components are maximized. Tensile strength is the lowest in IC-P sequence. In IC-P addition order, organoclay and polyamide-6 interactions are lower than the other addition orders, since clay and polyamide-6 are extruded together only once. Modulus increases for all mixing sequences with respect to unfilled polyamide-6, regardless of d-spacing. Young's Modulus and tensile elongation at break of the samples are lower in PI-C sequence, like the impact strength as observed in Figure 4.76. In this mixing procedure, organoclay is extruded with the polymer matrix once; hence, its dispersion may be limited. Strong interactions between elastomer and polyamide-6 via chemical reactions may hinder the distribution of organoclay in the polymer matrix in the second extrusion step.

Figure 4.100 shows the effect of mixing order on tensile strength of E-BA-MAH toughened polyamide-6/Cloisite® 25A nanocomposites. Tensile strength decreases with respect to pure polyamide-6 with the addition of elastomer as its observed in Figure 4.94. Nanocomposites processed by All-S sequence give higher tensile strength data than the nanocomposites produced by other mixing sequences. Similar result is obtained for the polyamide-6/Cloisite® 15A/E-BA-MAH nanocomposites. It is better to mix all of the components simultaneously in order to maximize the interactions that can take place between polyamide-6, elastomer and organoclay. Young's modulus of the nanocomposites containing Cloisite® 25A and E-BA-MAH processed by different addition orders can be observed in Figure 4.101. Young's Modulus data of the processed samples are nearly the same, regardless of the mixing procedure. Tensile elongation at break data in Figure 4.102 show similar behavior with impact strength shown in Figure 4.77. Lowest values are obtained in PI-C sequence. In this mixing sequence, since the organoclay is extruded only once, the organoclay agglomerates may have been dispersed to a lower extent .

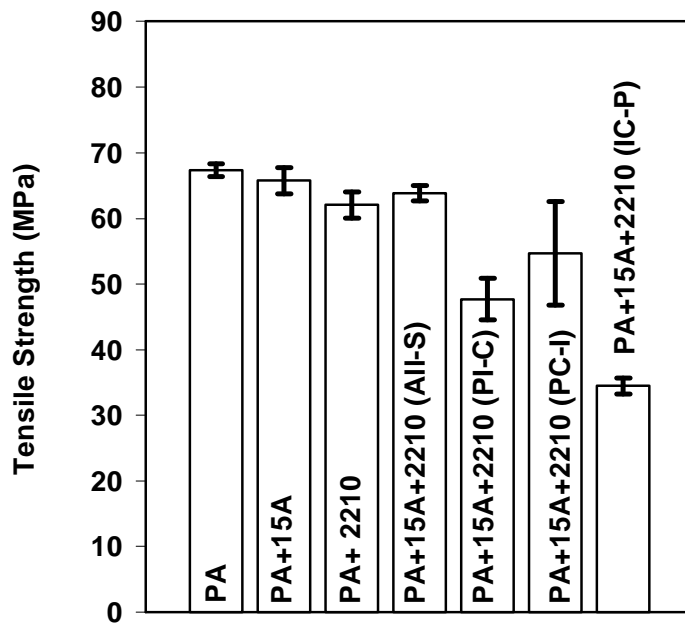


Figure 4.97 Effect of mixing order on tensile strength of E-BA-MAH elastomer toughened polyamide-6/Cloisite® 15A nanocomposites

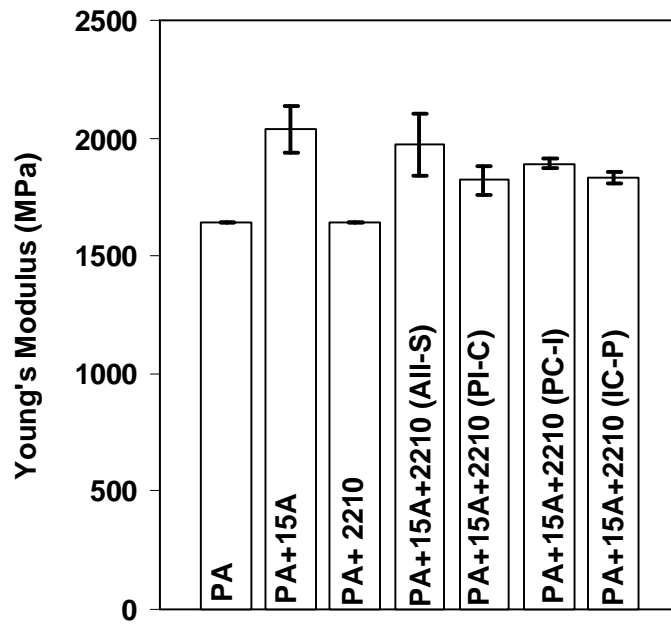


Figure 4.98 Effect of mixing order on Young's Modulus of E-BA-MAH elastomer toughened polyamide-6/Cloisite® 15A nanocomposites

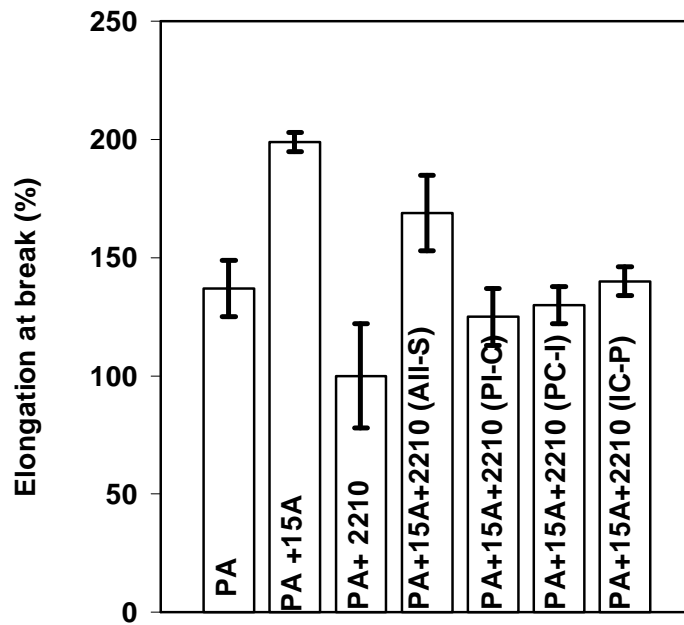


Figure 4.99 Effect of mixing order on % elongation at break of E-BA-MAH elastomer toughened polyamide-6/Cloisite® 15A nanocomposites

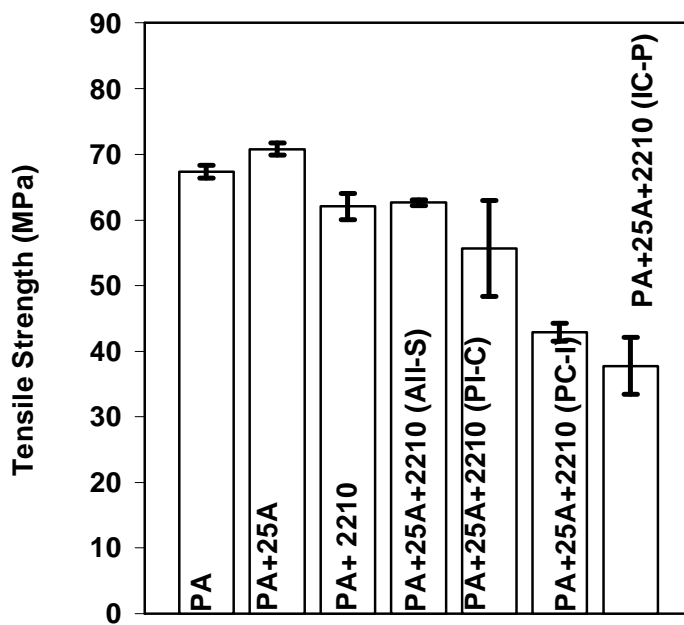


Figure 4.100 Effect of mixing order on tensile strength of E-BA-MAH elastomer toughened polyamide-6/Cloisite® 25A nanocomposites

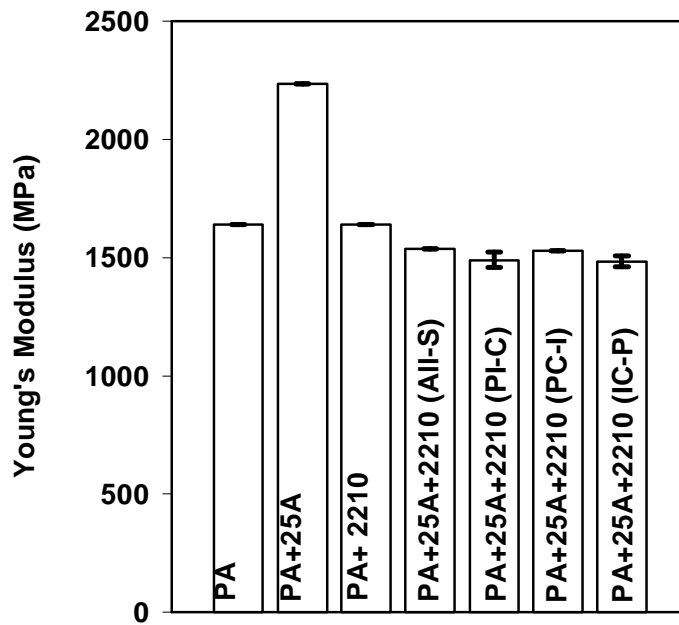


Figure 4.101 Effect of mixing order on Young's Modulus of E-BA-MAH elastomer toughened polyamide-6/Cloisite® 25A nanocomposites

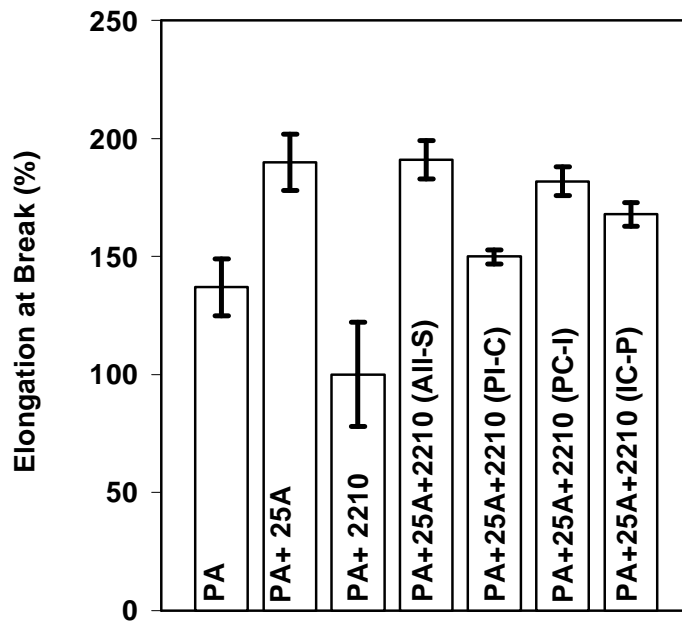


Figure 4.102 Effect of mixing order on % elongation at break of E-BA-MAH elastomer toughened polyamide-6/Cloisite® 25A nanocomposites

4.7.3.3 Tensile Properties of E-GMA Containing Nanocomposites

Figures 4.103 through 4.105 show the effect of organoclay type on tensile properties of E-GMA elastomer toughened polyamide-6 nanocomposites. The addition of rubbery phase to nanocomposites produces a reduction in tensile strength, which is more than that observed for unfilled polyamide-6: the addition of 5 wt % elastomer to the nanocomposite containing 2 wt % Cloisite® 25A and 30B reduces the tensile strength by 20 %, whereas for unfilled polyamide-6 a decrease of 7 % is observed. The decrease in tensile strength in Cloisite® 15A containing ternary nanocomposite is 10 % with respect to its binary nanocomposite. It can be concluded that elastomer effect is more dominant than the organoclay effect, since tensile strength is lower than neat polyamide-6 in elastomer containing nanocomposites. Polyamide-6/Cloisite® 15A/E-GMA gives higher strength, modulus and impact strength, since it has higher crystallinity than the other ternary systems. Interparticle distance, as well as rubber particle size, interfacial adhesion and modulus of the matrix/modulus of rubber ratio are very important in toughening mechanism. Modulus of elasticity influences the interparticle distance, a higher matrix modulus leading to smaller interparticle distance, i.e., closer rubber particles (Nielsen and Landel, 1994). Interparticle distance of domains seem to be closer in 15A and 25A organoclay containing nanocomposites than in 30B containing nanocomposite in SEM Figures 4.43 through 4.45. Improvements in the presence of organoclay 15A can be attributed to this reason. Young's modulus of polyamide-6 and blends increase with the addition of organoclay, whereas elastomer E-GMA decreases the modulus of polyamide-6/organoclay binary nanocomposites.

Organoclay particles increase the tensile elongation at break due to their nano scale and exfoliated nature. However, incorporating elastomer to binary polyamide-6/organoclay nanocomposites decreases elongation at break, since organoclay may reduce the compatibility of elastomer and polyamide-6, resulting a lack of adhesion between the phases. Elongation at break data are inaccordance with impact strength results in ternary nanocomposites.

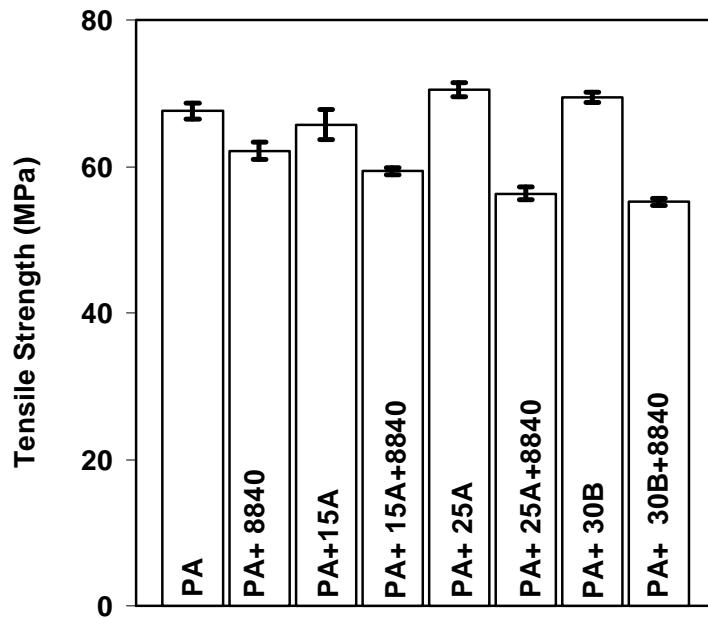


Figure 4.103 Effect of organoclay type on tensile strength of E-GMA elastomer toughened polyamide-6 nanocomposites

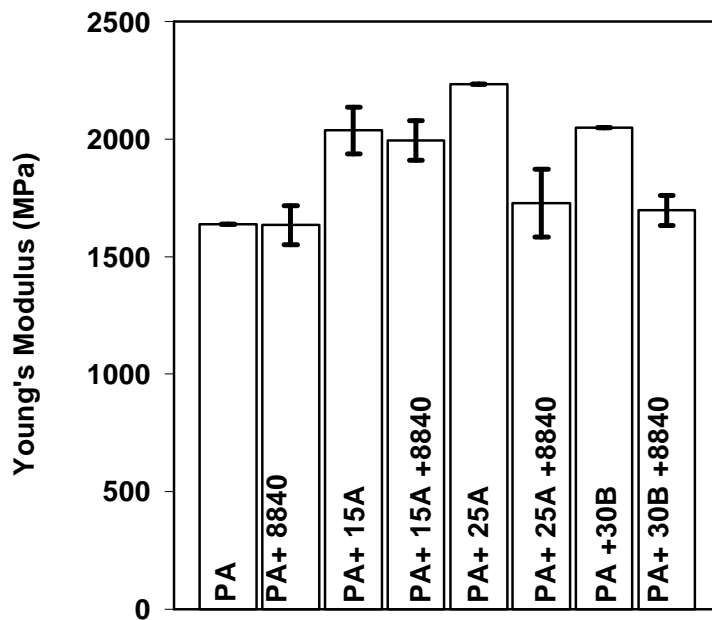


Figure 4.104 Effect of organoclay type on Young's Modulus of E-GMA elastomer toughened polyamide-6 nanocomposites

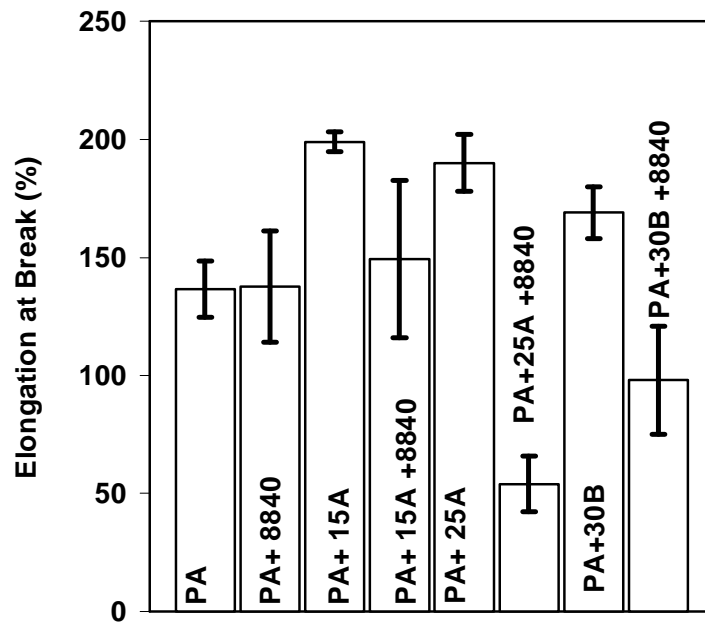


Figure 4.105 Effect of organoclay type on % elongation at break of E-GMA elastomer toughened polyamide-6 nanocomposites

Effect of mixing order on tensile properties of polyamide-6/Cloisite® 15A/E-GMA nanocomposites can be seen in Figures 4.106 through 4.108. Tensile strength is higher in All-S addition order. Young's Modulus of unfilled polyamide-6 increases in binary and ternary nanocomposites, since organoclay modulus is higher than the polymer matrix, and organoclay has high aspect ratio. In terms of Young's Modulus All-S seems to be best addition sequence. It is better to mix all the ingredients simultaneously, in order to have high level of interactions between all the components of the ternary nanocomposites. The elongation at break data have a relatively large standard deviation which makes it difficult to define clear trends. However, it may be accepted as unchanged in all mixing orders.

Effect of mixing order on tensile properties of polyamide-6/Cloisite® 30B/E-GMA nanocomposites can be seen in Figures 4.109 through 4.111. Nanocomposites prepared by All-S mixing sequence show the highest strength among all the

samples. Young's modulus is higher in PC-I sequence, as it is observed in impact strength. In PC-I sequence, clay and polyamide-6 are extruded prior to elastomer blending, thus, 30B/polyamide interactions can be maximized. The elongation at break data are relatively unchanged in all mixing orders.

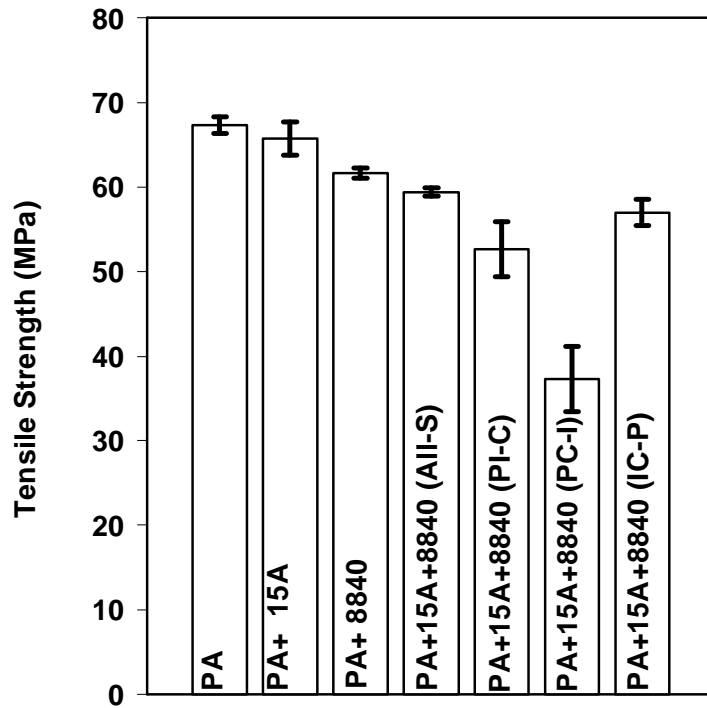


Figure 4.106 Effect of mixing order on tensile strength of E-GMA elastomer toughened polyamide-6/Cloisite® 15A nanocomposites

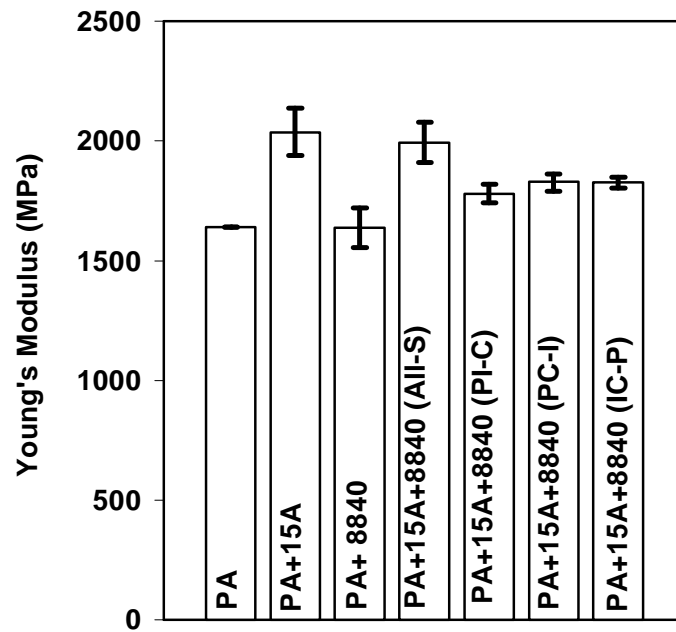


Figure 4.107 Effect of mixing order on Young's Modulus of E-GMA elastomer toughened polyamide-6/Cloisite® 15A nanocomposites

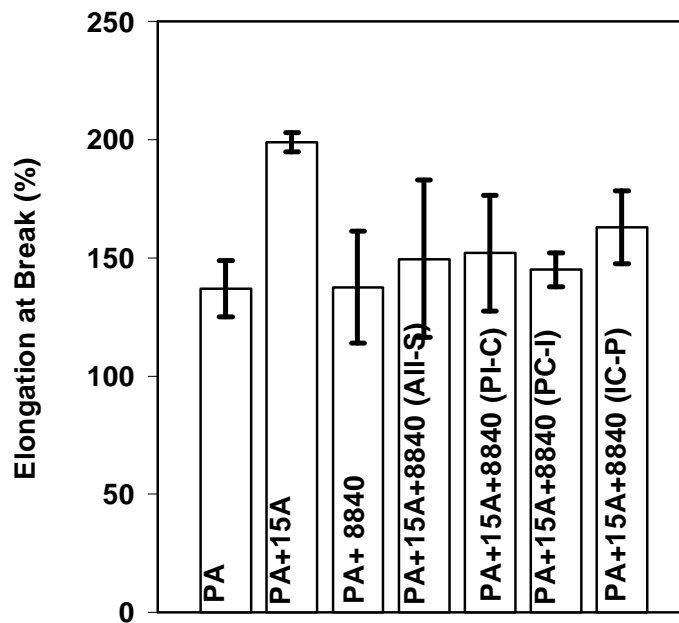


Figure 4.108 Effect of mixing order on % elongation at break of E-GMA elastomer toughened polyamide-6/Cloisite® 15A nanocomposites

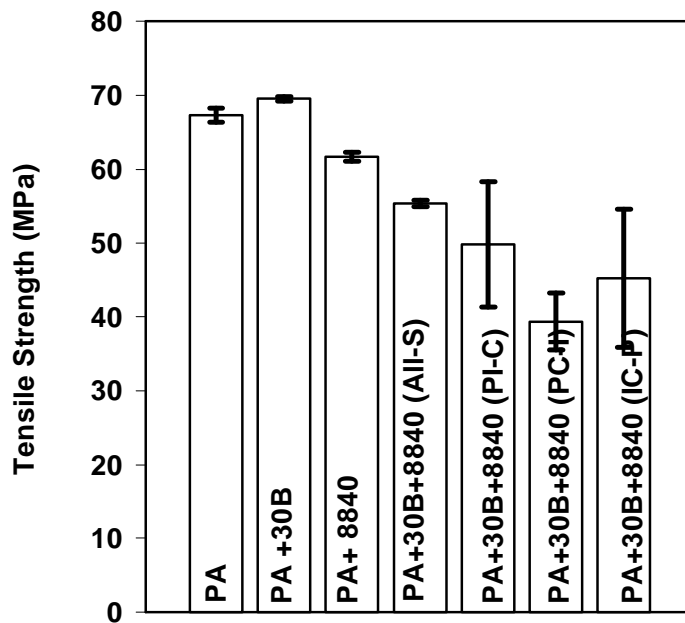


Figure 4.109 Effect of mixing order on tensile strength of E-GMA elastomer toughened polyamide-6/Cloisite® 30B nanocomposites

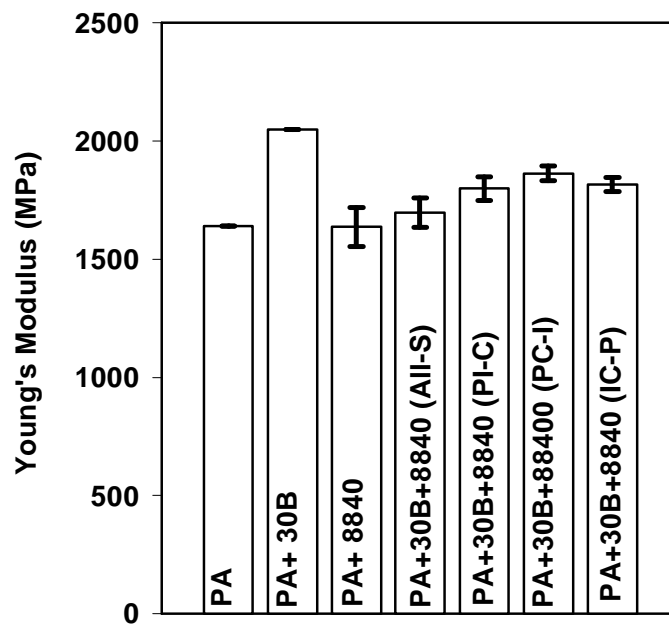


Figure 4.110 Effect of mixing order on Young's Modulus of E-GMA elastomer toughened polyamide-6/Cloisite® 30B nanocomposites

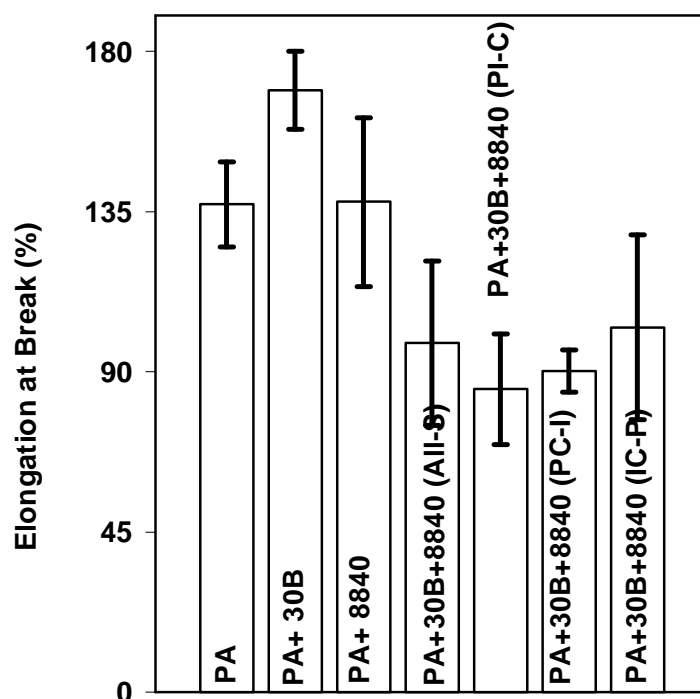


Figure 4.111 Effect of mixing order on % elongation at break of E-GMA elastomer toughened polyamide-6/Cloisite® 30B nanocomposites

4.7.3.4 Tensile Properties of E-MA-GMA Containing Nanocomposites

The tensile properties of polyamide-6/organoclay/E-MA-GMA nanocomposites can be seen in Figures 4.112-4.114. Tensile strengths in Cloisite® 15A and 25A containing ternary nanocomposites are nearly the same and they are higher than 30B containing nanocomposites. As for the effect of organoclay, polyamide-6/E-MA-GMA blends with clay have better Young's Modulus than the corresponding sample without organoclay. The modulus increases indicate a decrease in molecular mobility that could be the result of large interphase area/dispersed phase volume ratio, characteristic of intercalated/exfoliated nanocomposites. Polyamide-6/Cloisite®

30B/E-MA-GMA nanocomposites have the highest modulus among the other ternary nanocomposites, since there should be a great interaction between polyamide-6, E-MA-GMA and the –OH groups of clay surfactant. Methyl acrylate groups may increase the interaction between the polyamide-6 and elastomer since the same situation is not observed in polyamide-6/Cloisite® 30B/E-GMA nanocomposites. Elongation at break decreases with elastomer E-MA-GMA, because GMA can react with both amine and acidic end groups of polyamide-6, owing to these reactions and the presence of methyl acrylate groups, composites become less capable of extending, thus the strain at break decreases.

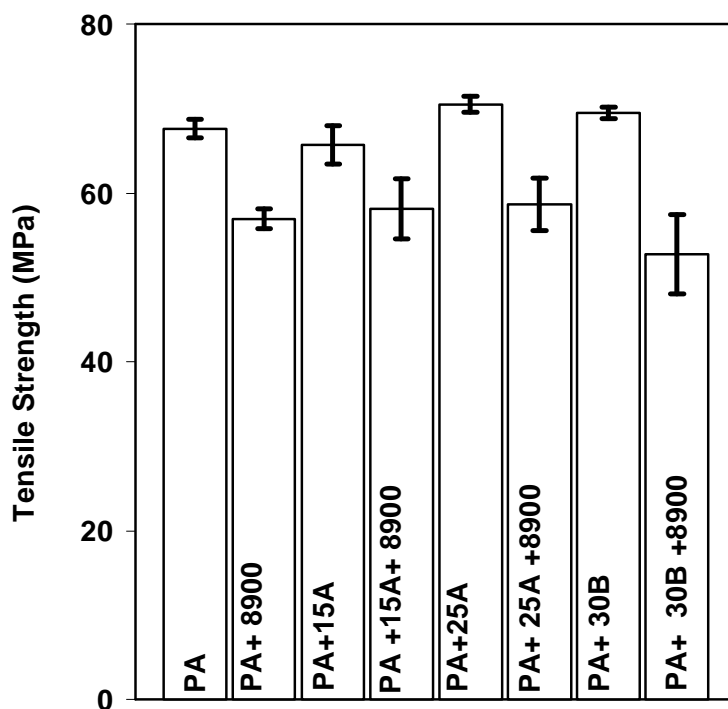


Figure 4.112 Effect of organoclay type on tensile strength of E-MA-GMA elastomer toughened polyamide-6 nanocomposites

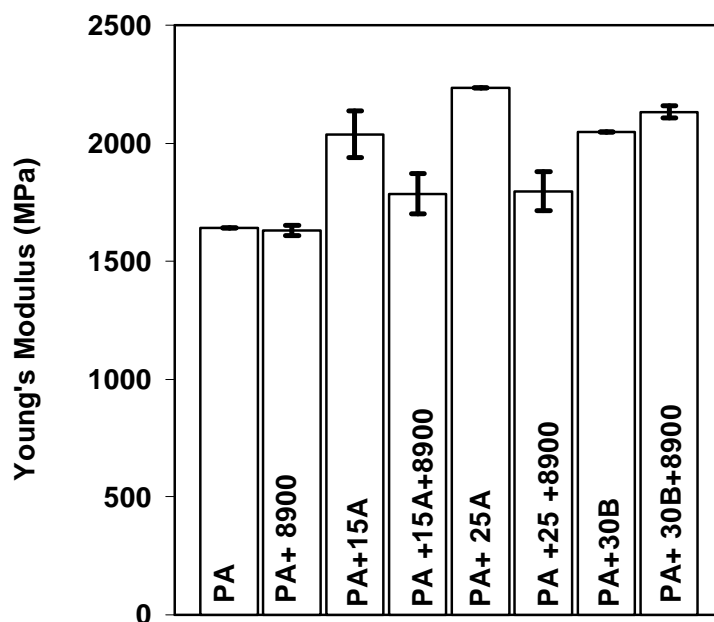


Figure 4.113 Effect of organoclay type on Young's Modulus of E-MA-GMA elastomer toughened polyamide-6 nanocomposites

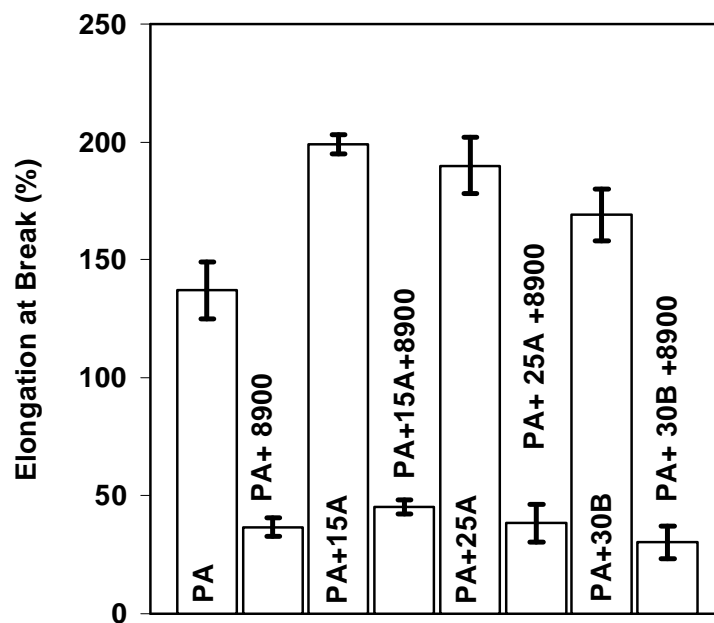


Figure 4.114 Effect of organoclay type on % elongation at break of E-MA-GMA elastomer toughened polyamide-6 nanocomposites

4.7.4 FLEXURAL PROPERTIES

Three point bending tests were performed to determine the flexural strength and modulus of the nanocomposites, since no fracture occurred in polyamide-6, polyamide-6/elastomer blends and nanocomposites. The tests were ended after maximum force was reached for the specimen fixed between two supports.

In general, all materials displayed a trend similar to that observed in tensile properties; however, flexural strength and modulus tend to be greater than tensile ones as the specimen is subjected to both compressive and tensile stresses in three point bending tests.

Mechanical properties of nanocomposites depend on the dispersion of organoclay particles, their orientation in the skin and core layers, and their exfoliation degree, as well as polymer matrix/clay interactions. Organoclay platelets, in the case of exfoliation, are aligned in the mold fill direction in TEM micrographs. This alignment may cause the observed increase in flexural strength. Kim stated that orientation in injection molding is parallel to the long axis of the layered silicates (Kim et al., 2001). Forced orientation of organoclay platelets during injection molding is a result of high shear rates during processing. In the central section of the injection molded specimens, the agglomerated clay particles should be oriented transverse to the mold fill direction like short fiber reinforced composites (Chow et al., 2004).

One of the reasons causing difference in flexural and tensile properties is the molding induced skin-core morphology. Clay, which is located in skin layers, is aligned in the mold fill direction. Skin layers are under tension/compression forces during the flexural tests and orientation of clay layers is favorable. On the contrary, in core, less intercalated clay particles are mostly present, which decrease the tensile properties (Chow et al., 2004).

4.7.4.1 Flexural Properties of Polyamide-6/Elastomer Blends

Flexural properties in terms of strength and modulus for E-BA-MAH toughened polyamide-6 blends are shown in Figures 4.115 and 4.116. Increases in elastomer content decreases the strength and modulus as observed in tensile tests. Similar results are obtained in E-GMA and E-MA-GMA containing blends seen in Figures 4.117-4.118 and 4.119-4.120.

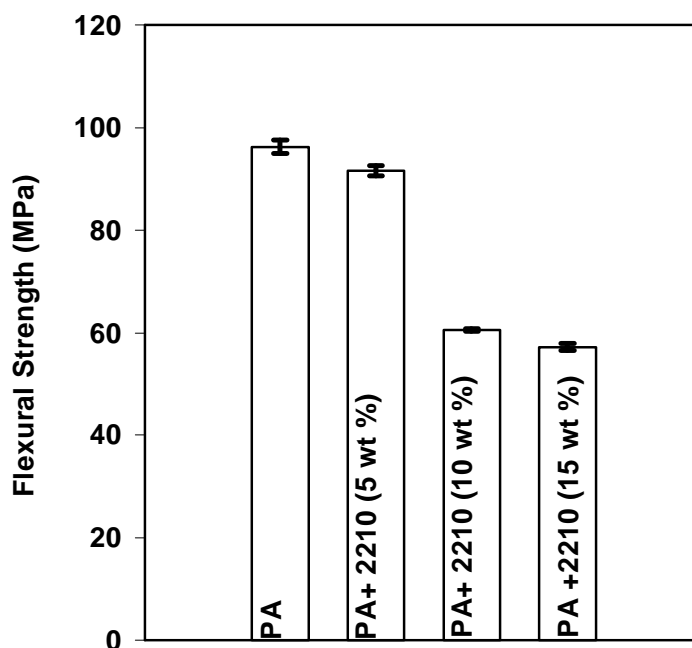


Figure 4.115 Effect of elastomer content on flexural strength of E-BA-MAH elastomer toughened polyamide-6 blends

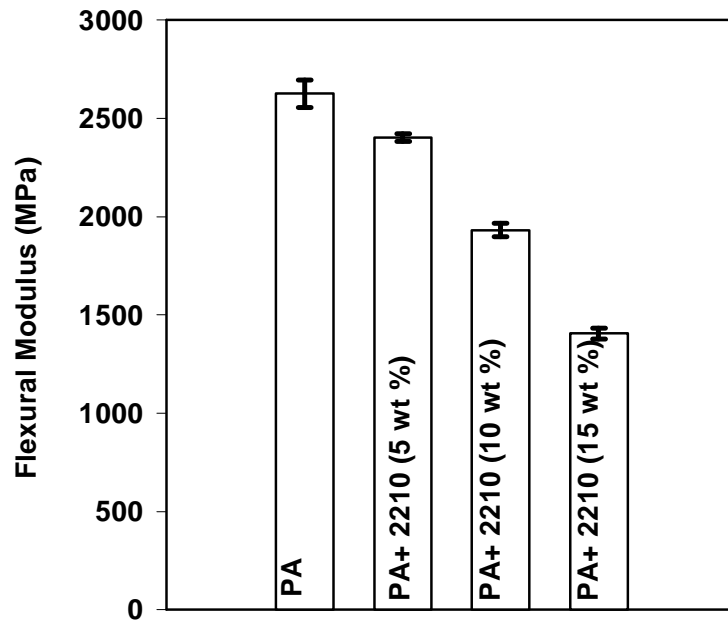


Figure 4.116 Effect of elastomer content on flexural modulus of E-BA-MAH elastomer toughened polyamide-6 blends

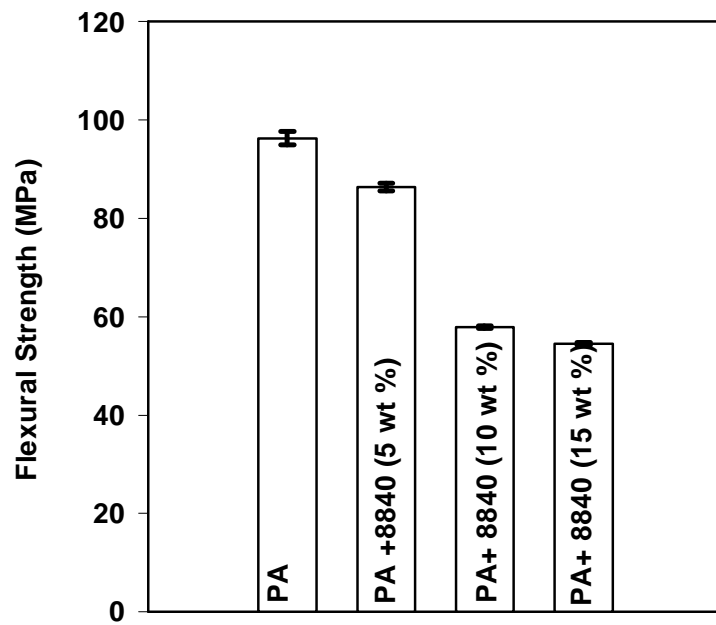


Figure 4.117 Effect of elastomer content on flexural strength of E-GMA elastomer toughened polyamide-6 blends

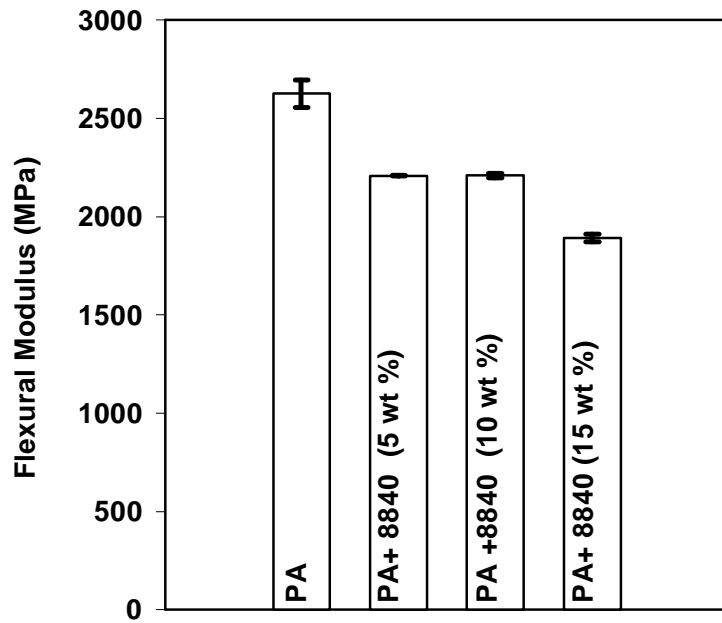


Figure 4.118 Effect of elastomer content on flexural modulus of E-GMA elastomer toughened polyamide-6 blends

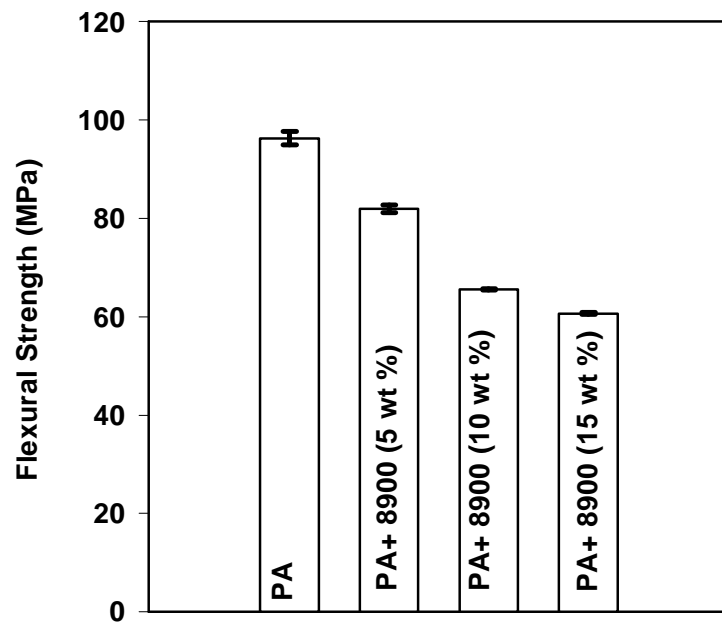


Figure 4.119 Effect of elastomer content on flexural strength of E-MA-GMA elastomer toughened polyamide-6 blends

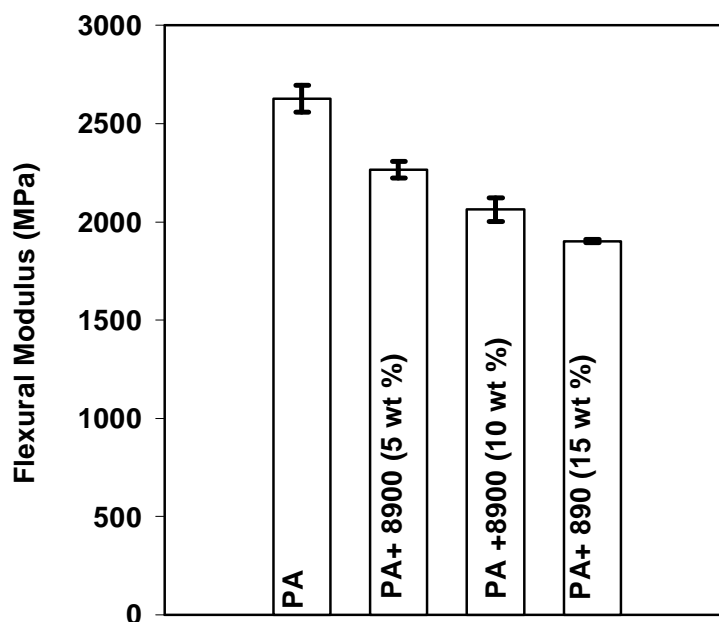


Figure 4.120 Effect of elastomer content on flexural modulus of E-MA-GMA elastomer toughened polyamide-6 blends

4.7.4.2 Flexural Properties of E-BA-MAH Elastomer Containing Nanocomposites

Effect of organoclay type on flexural strength and modulus of E-BA-MAH toughened polyamide-6 nanocomposites can be seen in Figures 4.121 and 4.122. Elastomer decreases strength and modulus both in blends and ternary nanocomposites. Except for polyamide-6/Cloisite 30B/E-BA-MAH, organoclay increases flexural strength and modulus. As discussed earlier, modulus and strength improvements are attributed to the high aspect ratio of organoclays, since polymer matrix-filler contact surface is increased. Modulus improvements are due to the constraint of polymer chains by their interaction with clay surfaces (Shelley et al., 2001). Higher organoclay modulus

leads to an increase in nanocomposite modulus. Cloisite® 15A and 25A containing ternary nanocomposites show higher strength and modulus than 30B as also observed in Figures 4.94 and 4.95 in tensile tests. Higher compatibility of organoclay with polyamide-6 matrix may decrease the polyamide-6/elastomer interactions, conducting to a reduction in interfacial adhesion, consequently, tensile strength and modulus.

Figures 4.123 and 4.124 show the effect of mixing order on flexural strength and modulus of E-BA-MAH elastomer toughened polyamide-6/Cloisite® 15A nanocomposites. Among the other mixing orders, flexural strength, like tensile strength of these samples, is the highest in All-S sequence where all the components are simultaneously fed to the extruder. Flexural strength is the lowest in IC-P sequence, this is also in accordance with tensile data. Mixing organoclay with elastomer prior to polyamide-6 may hinder the reactive groups of polymer pairs to come in contact; thus, the extent of reaction between polyamide-6 and elastomer is greatly reduced, decreasing flexural strength. Flexural modulus is nearly the same for all mixing orders, except for the All-S sequence. All-S sequence gives the lowest flexural modulus data. However, according to tensile measurements All-S sequence resulted in the highest modulus.

Figures 4.125 and 4.126 show the effect of mixing order on flexural properties of polyamide-6/Cloisite® 25A/E-BA-MAH nanocomposites. Flexural strength results are similar to tensile strength results, since All-S sequence gives the best result in two tests. Flexural modulus results are not in accordance with tensile test results, as it is observed in Figure 4.124. Young's Modulus is improved by 28% with respect to pure polyamide-6 in PI-C sequence. The difference between tensile and flexural properties in Young's Modulus data may be attributed to the orientation of clay in the polymer matrix.

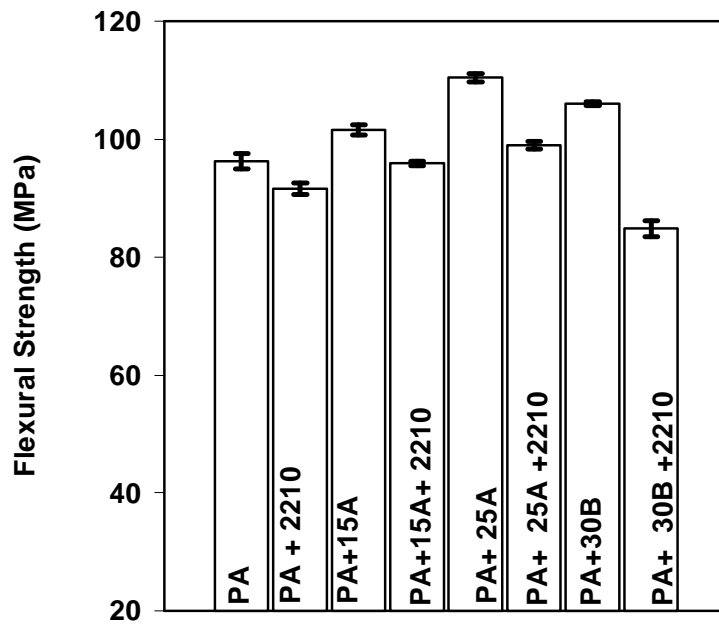


Figure 4.121 Effect of organoclay type on flexural strength of E-BA-MAH elastomer toughened polyamide-6 nanocomposites

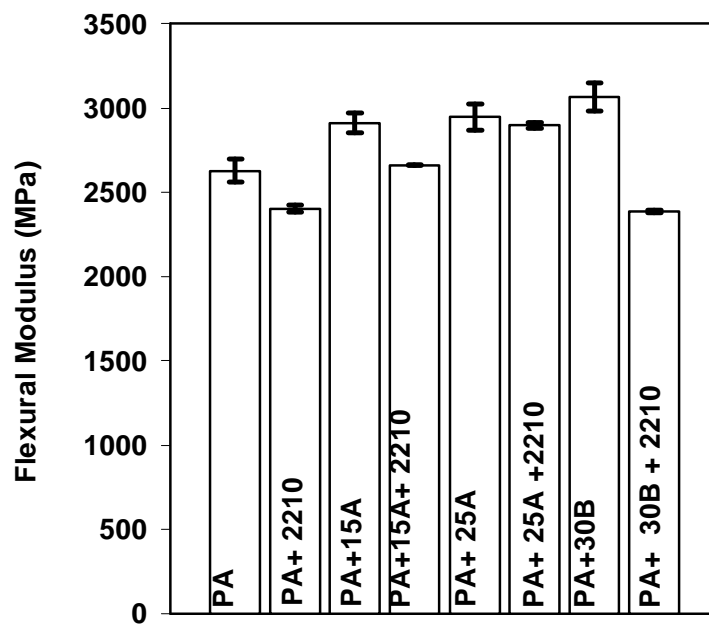


Figure 4.122 Effect of organoclay type on flexural modulus of E-BA-MAH elastomer toughened polyamide-6 nanocomposites

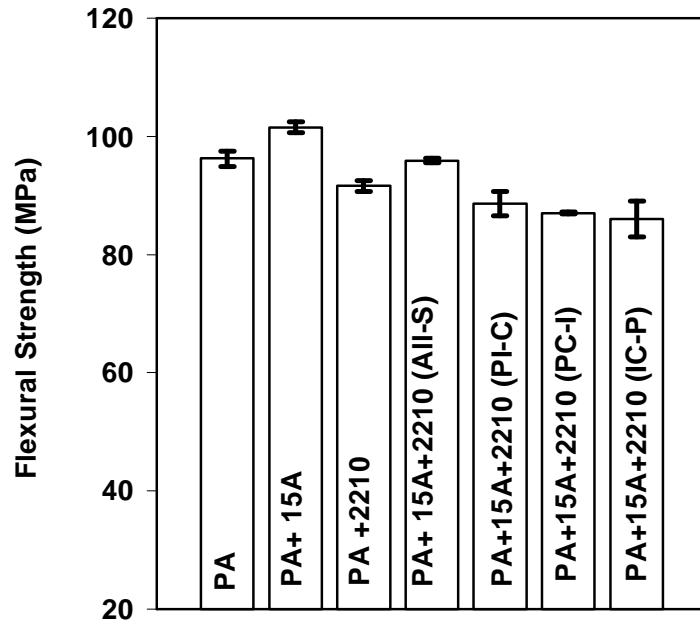


Figure 4.123 Effect of mixing order on flexural strength of E-BA-MAH elastomer toughened polyamide-6/Cloisite® 15A nanocomposites

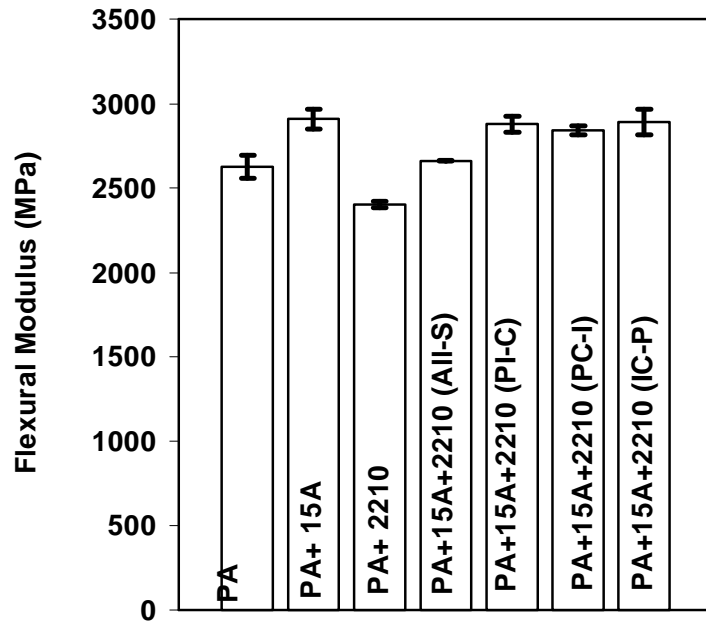


Figure 4.124 Effect of mixing order on flexural strength of E-BA-MAH elastomer toughened polyamide-6/Cloisite® 15A nanocomposites

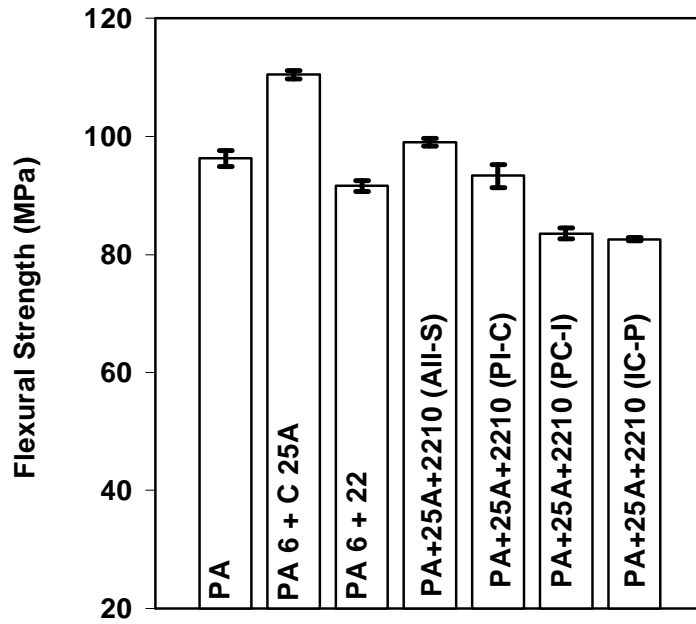


Figure 4.125 Effect of mixing order on flexural strength of E-BA-MAH elastomer toughened polyamide-6/Cloisite® 25A nanocomposites

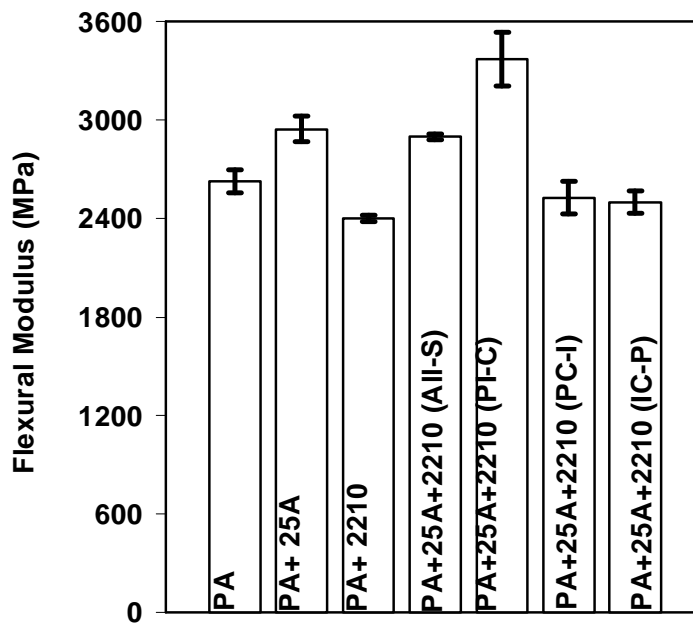


Figure 4.126 Effect of mixing order on flexural modulus of E-BA-MAH elastomer toughened polyamide-6/Cloisite® 25A nanocomposites

4.7.4.3 Flexural Properties of E-GMA Elastomer Containing Nanocomposites

Effect of organoclay type on flexural strength and modulus of E-GMA toughened polyamide-6 nanocomposites can be seen in Figures 4.127 and 4.128, respectively. The effect of organoclay and elastomer on flexural and tensile properties are similar, since, Figures 4.103 and 4.104 resemble Figures 4.127 and 4.128.

Effects of mixing order on the flexural properties of polyamide-6/Cloisite® 15A/E-GMA nanocomposites are shown in Figures 4.129 and 4.130. Flexural strength is higher in All-S and PC-I sequences. PI-C sequence gives the lowest strength, since strong elastomer/polyamide-6 interactions via chemical reactions prevent organoclay/polymer matrix interrelations. Organoclay dispersion may be partially prevented since clay is extruded once in this mixing sequence. PC-I sequence, in which polyamide-6 is mixed with organoclay first, gives the highest flexural modulus, since organoclay/polyamide-6 interactions are maximized.

Figures 4.131 and 4.132 show the effect of mixing order on flexural properties of polyamide-6/Cloisite® 30B/E-GMA nanocomposites. All-S sequence gives the highest strength as observed in tensile strength of these samples observed in Figure 4.109. Flexural modulus, like Young's Modulus and impact strength, is the highest in PC-I sequence.

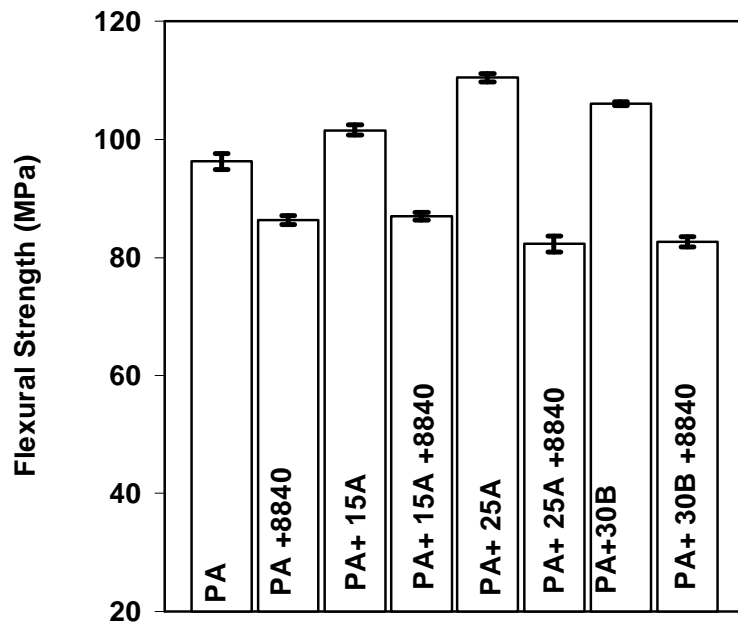


Figure 4.127 Effect of organoclay type on on flexural strength of E-GMA elastomer toughened polyamide-6 nanocomposites

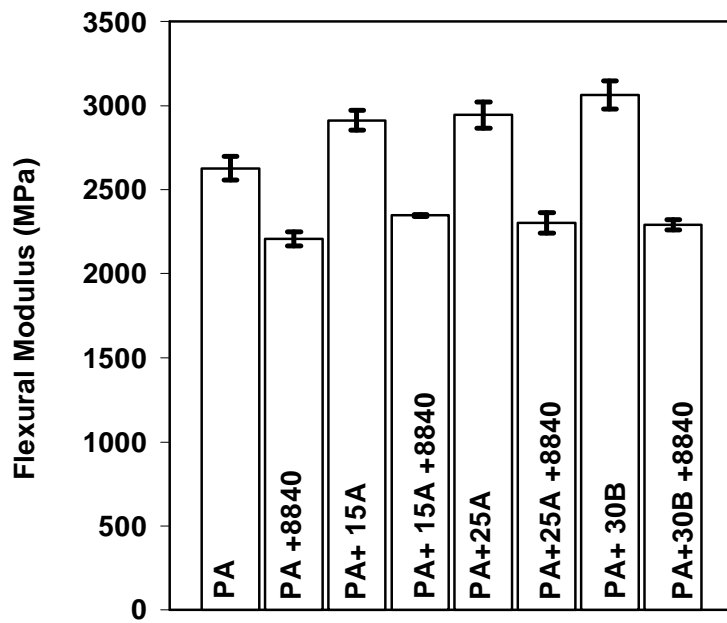


Figure 4.128 Effect of organoclay type on flexural modulus of E-GMA elastomer toughened polyamide-6 nanocomposites

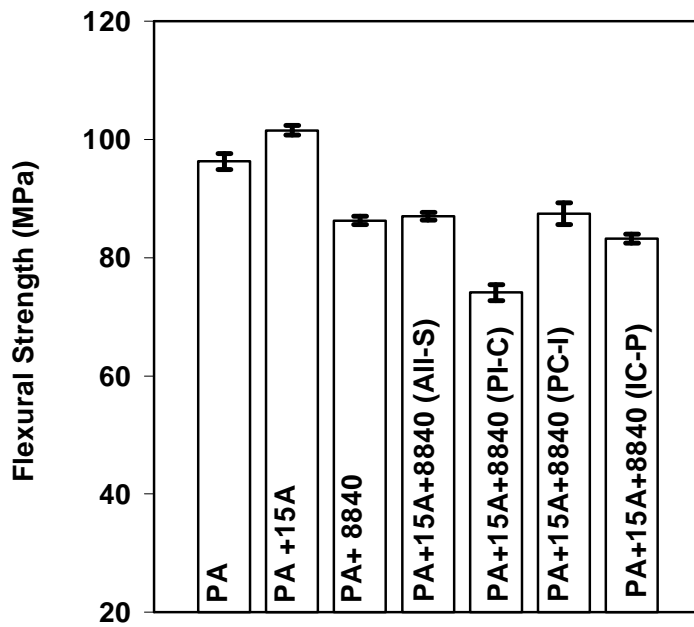


Figure 4.129 Effect of mixing order on flexural strength of E-GMA elastomer toughened polyamide-6/Cloisite® 15A nanocomposites

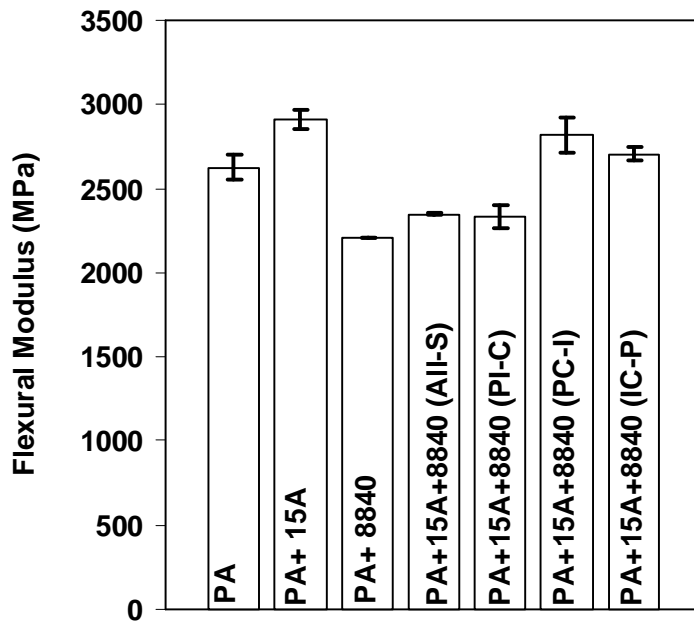


Figure 4.130 Effect of mixing order on flexural modulus of E-GMA elastomer toughened polyamide-6/Cloisite® 15A nanocomposites

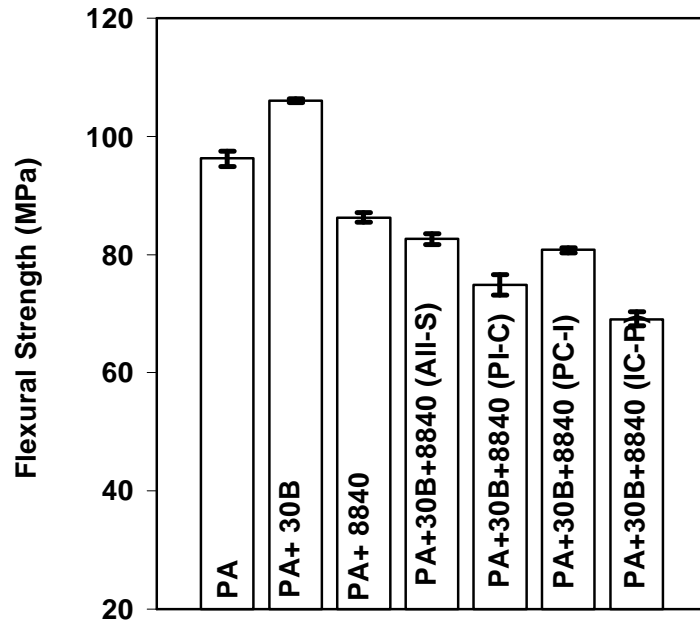


Figure 4.131 Effect of mixing order on flexural strength of E-GMA elastomer toughened polyamide-6/Cloisite® 30B nanocomposites

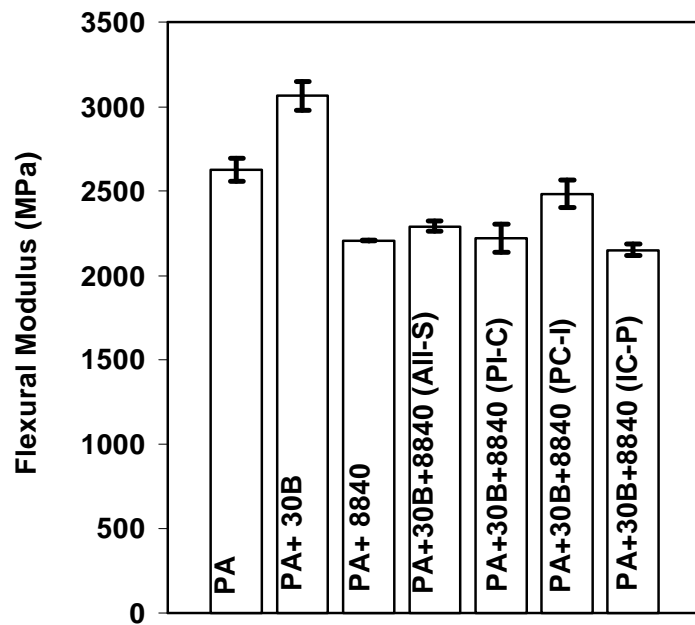


Figure 4.132 Effect of mixing order on flexural modulus of E-GMA elastomer toughened polyamide-6/Cloisite® 30B nanocomposites

4.7.4.4 Flexural Properties of E-MA-GMA Elastomer Containing Nanocomposites

Flexural properties of polyamide-6/organoclay/E-MA-GMA nanocomposites are shown in Figures 4.133 and 4.134. Flexural strength and modulus in ternary nanocomposites having 15A and 25A are nearly the same, whereas 30B introduced higher mechanical properties than other organoclays.

Flexural and tensile behaviors in terms of strength data are not consistent for this system. This is probably due to the nature of these two tests and alignment of organoclay platelets in the testing sample.

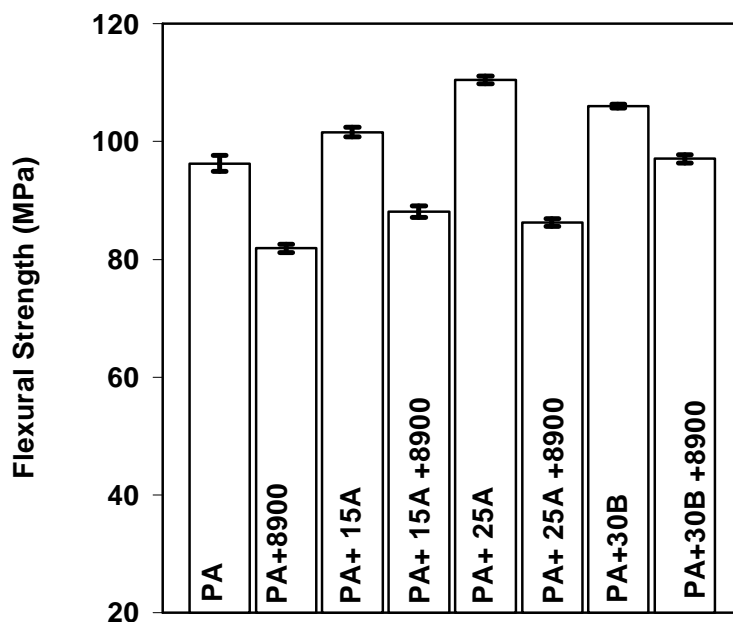


Figure 4.133 Effect of organoclay type on flexural strength of E-MA-GMA elastomer toughened polyamide-6 nanocomposites

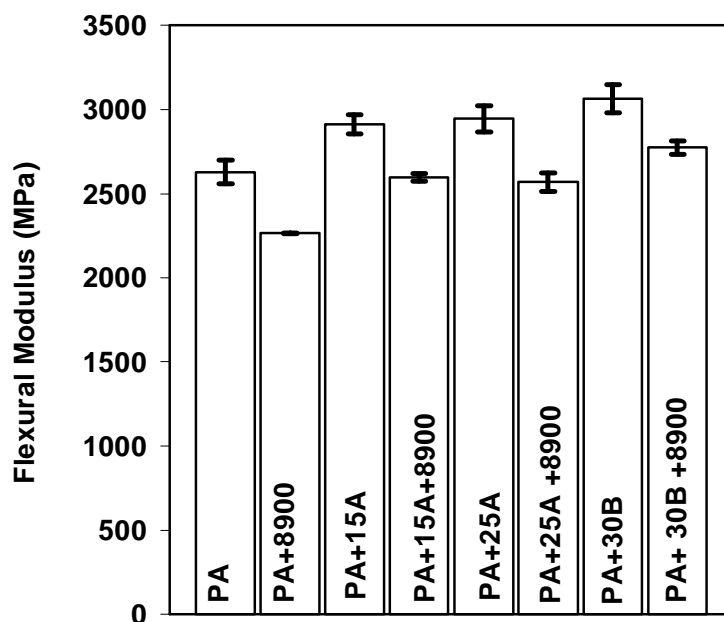


Figure 4.134 Effect of organoclay type on flexural modulus of E-MA-GMA elastomer toughened polyamide-6 nanocomposites

4.7.5 DYNAMIC MECHANICAL ANALYSIS

Viscoelastic measurements are highly sensitive to the nanoscale structure of the composites and used to investigate the structure of these materials. Dynamic mechanical analysis is carried out to understand the viscoelastic properties as a function of temperature.

Dynamic mechanical properties of pure elastomeric materials are shown in Figures 4.135-4.137. It is seen that E-MA-GMA elastomer has the lowest storage modulus relative to other elastomers, thus, it can be more attractive for toughening polyamide-6. Impact strength results showed that polyblends having E-MA-GMA have higher impact strength than the other polyblends prepared with E-BA-MAH and E-GMA, as seen in Figures 4.72, 4.73 and 4.74. Compatibility with polymer matrix and lower

glass transitions of the elastomers also make them good impact modifiers, since they decrease ductile-brittle transition temperature of polyamide-6.

The dynamic storage and loss modulus, as well as loss tangent versus temperature traces for the polyamide-6/organoclay systems are shown in Figures 4.138-4.140. It is seen that modulus enhancements of polyamide-6 matrix is greater above the glass transition temperature, T_g . This is a typical behavior of reinforced semi-crystalline polyamides, since reinforcements constrain the mobility of chain segments in amorphous phase (Wilkinson et al., 2006). Another reason is the larger difference between filler and the matrix in terms of mechanical properties. Polymer matrix goes from glassy to rubbery region, on the other hand, filler remains rigid throughout the entire temperature range.

At lower temperatures, nanocomposites with Cloisite® 30B exhibit higher storage and loss modulus than the other nanocomposites prepared by Cloisite® 25A and 15A, and pure polyamide-6. In the rubbery region, reinforcing effect of organoclay increases with decreasing surface hydrophobicity, i.e. polymer/organoclay compatibility. As it is mentioned earlier, Cloisite® 30B has the least hydrophobic surface modifier among the three, thus, its compatibility is higher with polyamide-6 matrix than 15A and 25A organoclays. XRD and TEM analysis also reveal this phenomena.

Figure 4.140 shows $\tan \delta$ of polyamide-6/organoclay nanocomposite systems. For pure polyamide-6, two dynamic relaxation peaks are observed around 65 °C and -58 °C, which are referred to as α and β relaxation peaks of polyamide-6, respectively (Liu et al., 2001). α relaxation peak is assigned to the glass transition temperature (T_g) of polyamide-6. According to Mohd-Ishak and Berry, 1994, this peak is believed to be related to the breakage of hydrogen bonding between polymer chains which actuates long range segmental chain movement in the amorphous area. The β relaxation peak is related to the segmental amide group which is unattached to the other amide group by hydrogen bonding in the amorphous area. According to α relaxation peak in loss tangent curves, glass-transition temperature of unfilled polyamide-6 (65 °C) is slightly shifted to lower temperatures in Cloisite® 15A (60 °C),

25A (62 °C) and 30B (60 °C) nanocomposites (Table 4.22). Clay particles should lead to a decrease in polymer chain mobility; leading to an increase in glass transition temperature. The degradation of any of the components may decrease T_g , but according to TGA analysis which can be seen in Figures B.35 through B.40 in Appendix B, no degradation is expected under the processing conditions used in this study. Excess surfactant groups, which are not ionically bound to the clay surface, may decrease T_g , because of their plasticization effect (Morgan and Harris, 2003). The decrease in T_g can also be attributed to the formation of intercalated/exfoliated structure and polymer layer formed around the layers (Chow et al., 2003).

The intensity value of loss tangent peak at T_g is related to the volume of constrained polymer within the nanocomposite, in other words, the volume fraction of chain segments whose mobility is constrained due to either incorporation into crystallites or polymer-clay interactions. Thus, the value of $\tan \delta$ at T_g is an indicator of the volume fraction of unconstrained, amorphous chain segments within the material (Wilkinson et al., 2006). DMA analysis showed that the intensity of loss tangent peak increased in nanocomposites with respect to unfilled polyamide-6 in this study. These increments are consistent with the results obtained in DSC results, since % crystallinity of polyamide-6 phase decreases with the organoclay loading. Nucleation effect of organoclays may be counteracted by the clay particles since crystal growth can be terminated by clay particles (Fornes and Paul, 2003). Excess damping in the polymer near the interface takes place because of induced thermal stresses or changes in polymer conformation or morphology.

Table 4.22 Effect of organoclay type on glass transition temperature of binary nanocomposites

	T_g (°C)
Polyamide-6	64.5
Polyamide-6 / Cloisite® 15A Nanocomposite	60.4
Polyamide-6 / Cloisite® 25A Nanocomposite	62.8
Polyamide-6 / Cloisite® 30B Nanocomposite	60.0

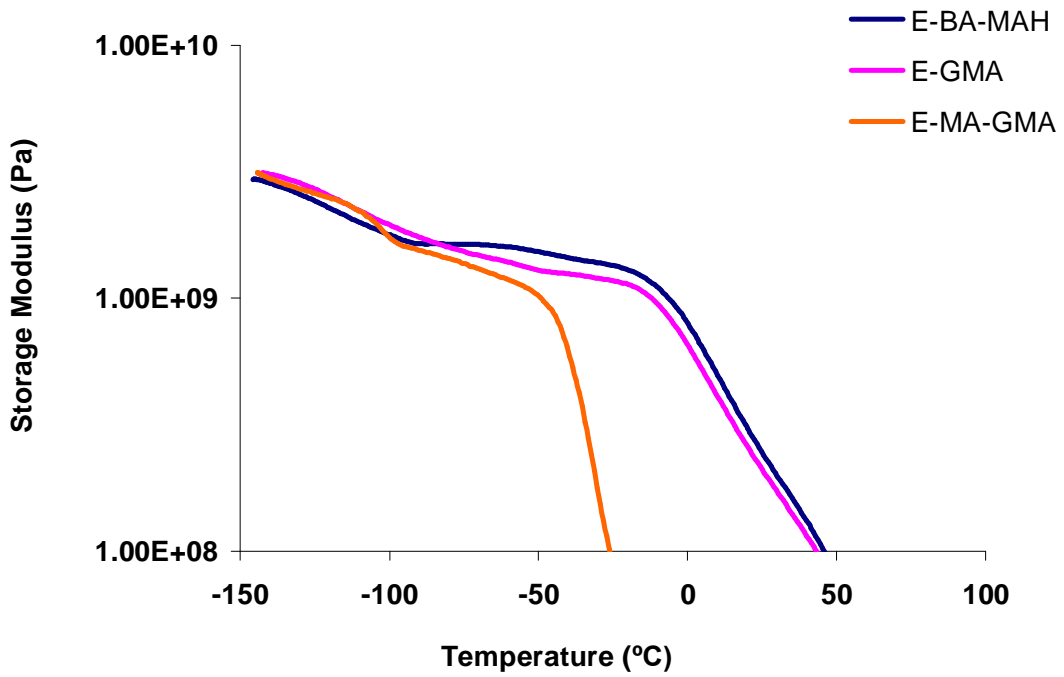


Figure 4.135 Storage Modulus versus temperature data for pure elastomeric materials

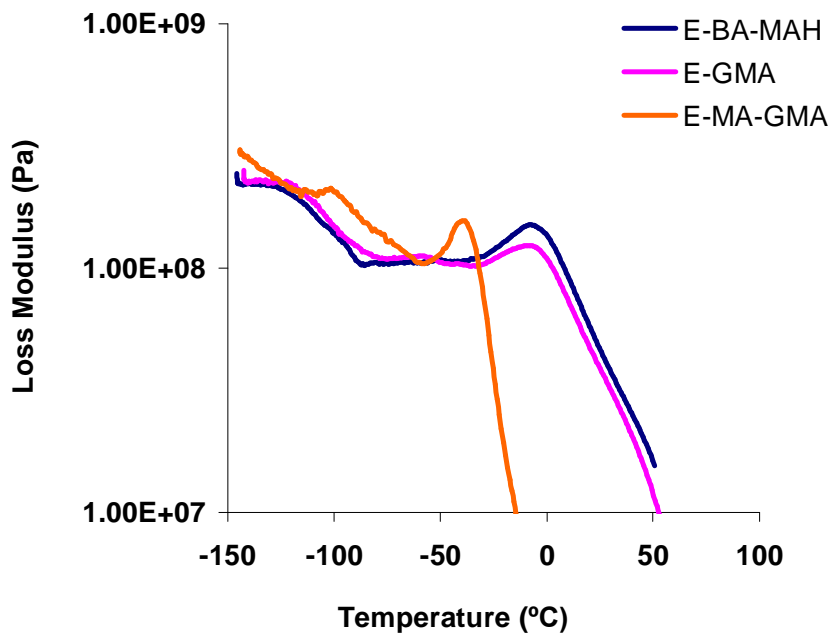


Figure 4.136 Loss Modulus versus temperature data for pure elastomeric materials

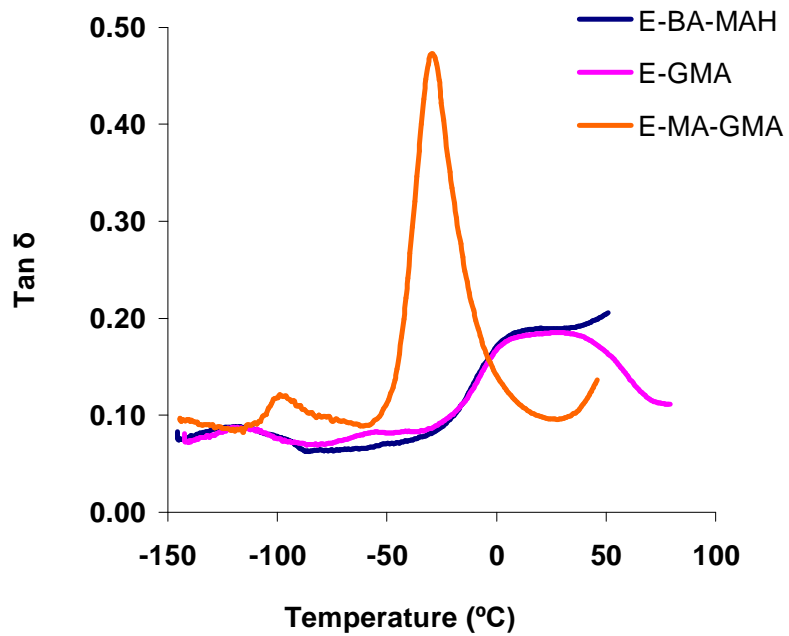


Figure 4.137 Loss tangent ($\tan \delta$) versus temperature data for pure elastomeric materials

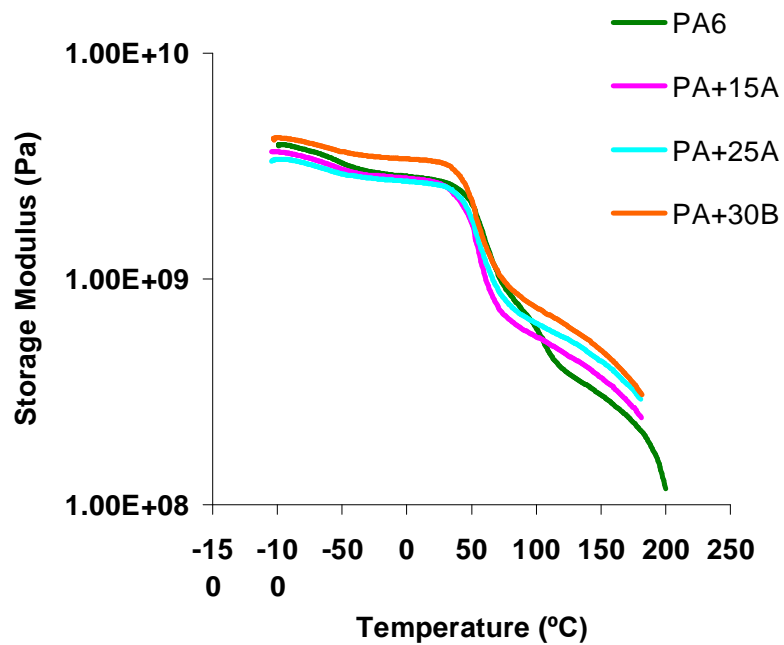


Figure 4.138 Effect of organoclay type on Storage Modulus versus temperature

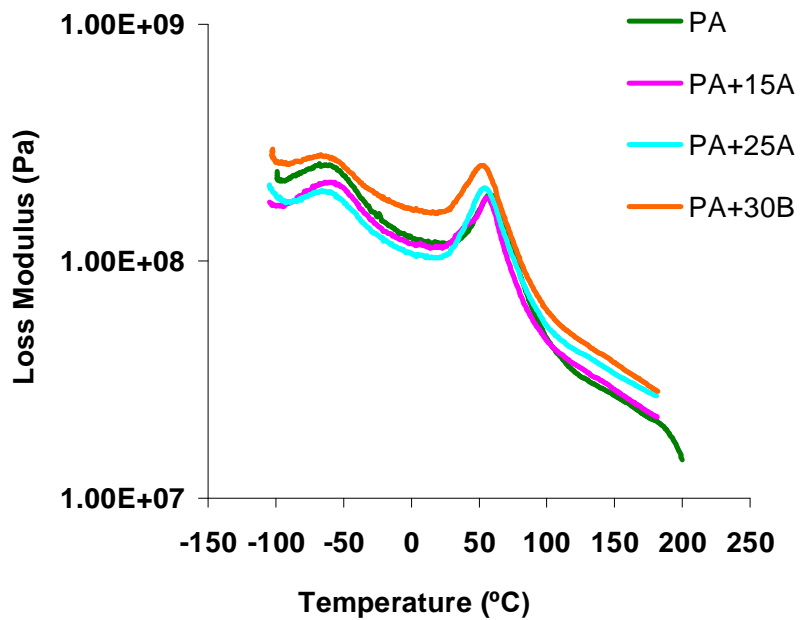


Figure 4.139 Effect of organoclay type on Loss Modulus versus temperature

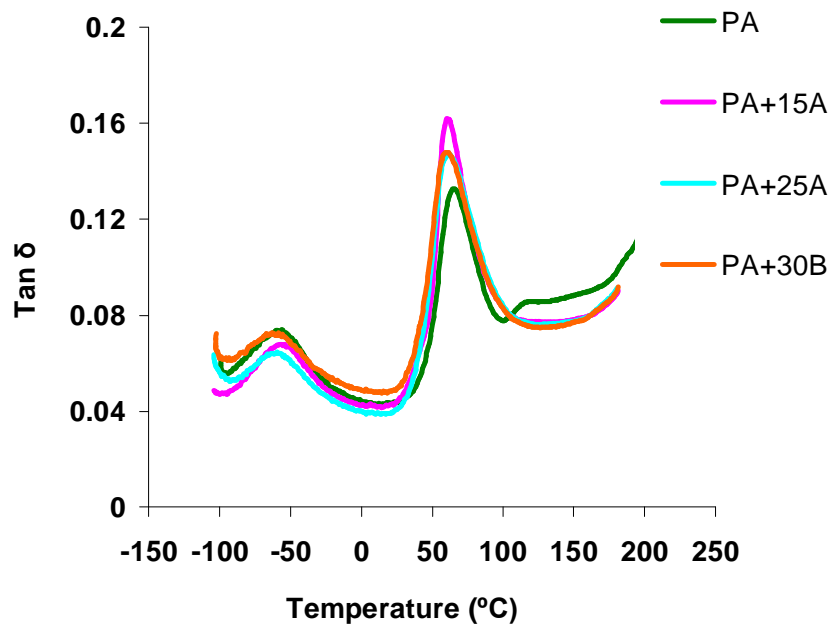


Figure 4.140 Effect of organoclay type on Loss tangent (tan δ) versus temperature

4.7.5.1 Dynamic Mechanical Analysis Results of E-BA-MAH Elastomer Containing Nanocomposites

Dynamic mechanical spectra of nanocomposites composed of E-BA-MAH elastomer and polyamide-6/Cloisite® 15A, polyamide-6/Cloisite® 25A, polyamide-6/Cloisite® 30B can be observed through Figures 4.141-4.143, 4.144-4.146, and 4.147-4.149, respectively.

The viscoelastic behaviors of the nanocomposites with respect to temperature are the same, regardless of the organoclay type. Storage modulus of polyamide-6/E-BA-MAH blends is lower than pure polyamide-6, binary and ternary nanocomposites, indicating lower stiffness of these samples. Especially at temperatures lower than the glass transition temperature, synergistic effects of organoclay and E-BA-MAH can be observed in Figures 4.141, 4.144 and 4.147. Although, they exhibit lower storage modulus values than polyamide-6 individually, ternary nanocomposites show the highest storage modulus among the nanocomposite systems. In rubbery region, all nanocomposites show higher storage modulus than polyamide-6 and polyamide-6/E-BA-MAH blends. Fillers have a larger effect in raising the modulus above T_g than below it. The main reason for this is the larger modulus ratio of the components when the polymer is in the rubbery state compared to the rigid glassy state (Nielsen and Landel, 1994).

Loss modulus and loss tangent curves in Figures 4.142-4.143, 4.145-4.146, and 4.148-4.149 showed that as rubber is introduced to pure polyamide-6 and binary nanocomposites, an increase in β transition temperature is observed; because of higher polyamide-6 main chain mobility due to the presence of rubbery domains. On the other hand, grafting reduces the intensity of this peak, as seen in $\tan \delta$ figures due to the reduction of chain mobility (Takeda et al., 1992).

There is often a good correlation between impact strength and dynamic mechanical properties of blends. Impact strength is observed to increase as the size of the damping peak due to the rubber phase increases. Rubber phase morphology,

specimen preparation, and adhesion affect the correlation to some extent (Nielsen and Landel, 1994). This correlation is observed in polyamide-6/organoclay/E-BA-MAH ternary nanocomposites. Loss tangent curve of polyamide-6/Cloisite® 15A/E-BA-MAH nanocomposite in Figure 4.143 exhibit a relatively intense damping peak ($\tan \delta = 0.154$) at T_g in comparison to polyamide-6/Cloisite® 25A/E-BA-MAH nanocomposite in Figure 4.146 ($\tan \delta = 0.116$) and polyamide-6/Cloisite® 30B/E-BA-MAH sample in Figure 4.149 ($\tan \delta = 0.137$). These results are in accordance with impact strength results in Figure 4.75, since Cloisite® 15A/E-BA-MAH nanocomposite has the highest impact strength value.

Figures 4.150 through 4.152 show the dependence of dynamic mechanical properties on mixing order in polyamide-6/Cloisite® 25A/E-BA-MAH nanocomposites. Storage and loss moduli are lowest in PC-I sequence both in rubbery and glassy regions. Storage modulus for All-S sequence is the highest especially at temperatures below T_g , however in glassy region, IC-P sequence turns out to be the highest. Young's Modulus results of the samples in Figure 4.101 are nearly the same, regardless of the mixing procedure. Flexural modulus in PI-C sequence is higher than the flexural modulus of the other ternary nanocomposites as seen in Figure 4.126. This discrepancy between the dynamic mechanical, tensile and flexural property results arises from the strong sensitivity of the polyethylene based elastomer modulus to differences in loading configurations and testing rates, because of their viscoelastic nature employed by these methods; on the contrary, polyamide-6 modulus is relatively independent of these differences (Kudva et al., 1999).

The effects of organoclay type and elastomer E-BA-MAH on glass transition temperature of polyamide-6 can be observed in Table 4.23. T_g decreases in the presence organoclay and remain nearly unchanged when melt blended with E-BA-MAH elastomer. The effect of organoclay on glass transition temperature can be attributed to the formation of free chain ends around the silicate layers and to the intercalated/exfoliated structure.

Table 4.23 Glass transition temperature of polyamide-6/organoclay/E-BA-MAH nanocomposites

	T_g (°C)
Polyamide-6	65.2
Polyamide-6 + Cloisite® 15A	60.4
Polyamide-6 + Cloisite® 25A	62.8
Polyamide-6 + Cloisite® 30B	60.0
Polyamide-6 / 5 weight % E-BA-MAH	64.6
Polyamide-6 + Cloisite® 15A+ E-BA-MAH (All-S)	59.8
Polyamide-6 + Cloisite® 25A+ E-BA-MAH (All-S)	61.9
Polyamide-6 + Cloisite® 25A+ E-BA-MAH (PI-C)	61.3
Polyamide-6 + Cloisite® 25A+ E-BA-MAH (PC-I)	60.5
Polyamide-6 + Cloisite® 25A+ E-BA-MAH (IC-P)	59.6
Polyamide-6 + Cloisite® 30B+ E-BA-MAH (All-S)	58.5

Table 4.23 also shows the effect of mixing orders on glass transition temperature of polyamide-6/Cloisite® 25A/E-BA-MAH nanocomposites. Glass transition temperatures are generally the same for all mixing sequences similar to their % crystallinities and melting temperatures as observed in Figure 4.19.

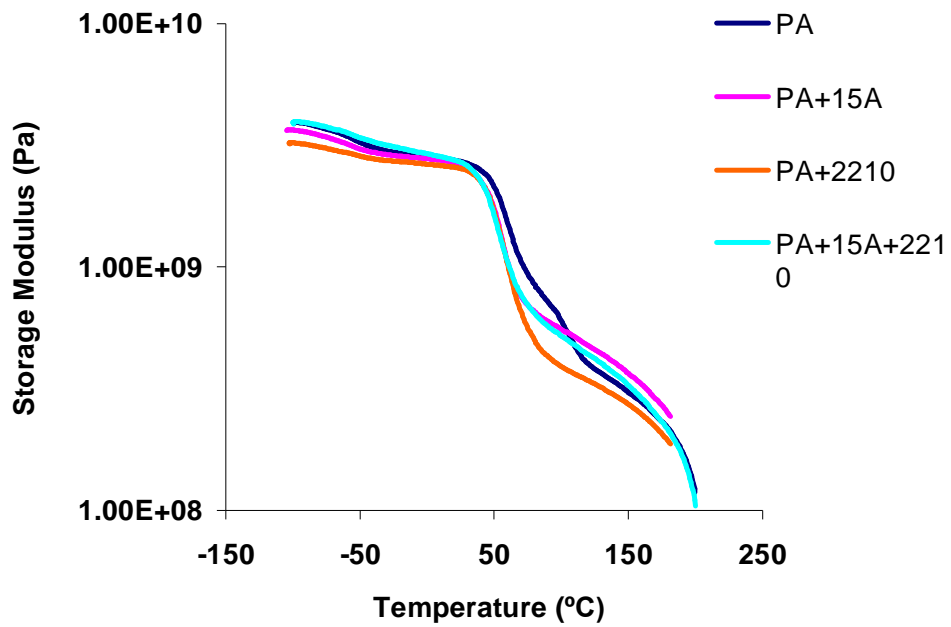


Figure 4.141 Storage Modulus versus temperature data for polyamide-6/Cloisite® 15A/E-BA-MAH nanocomposite

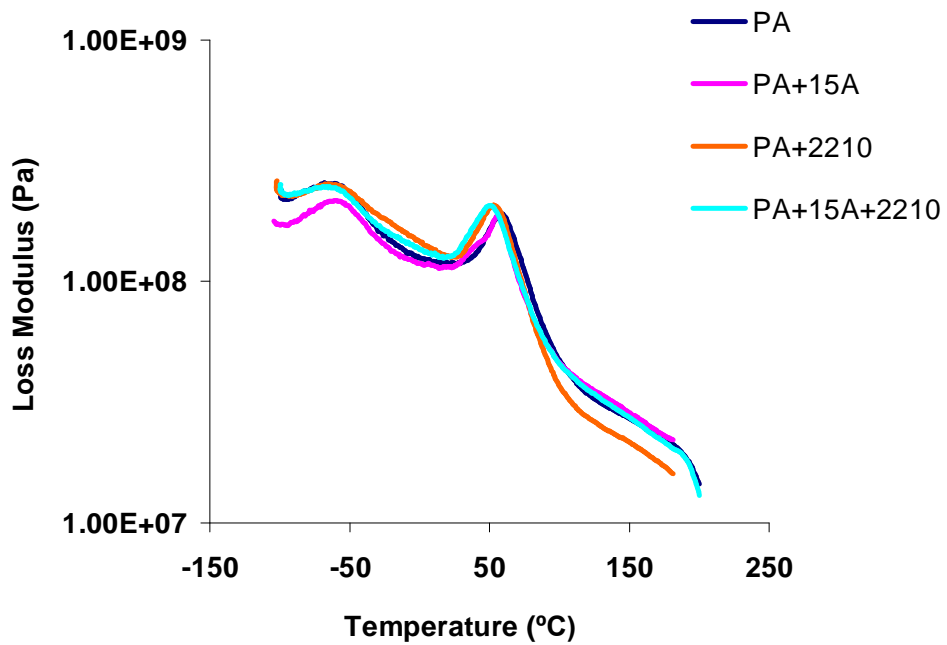


Figure 4.142 Loss Modulus versus temperature data for polyamide-6/Cloisite® 15A/E-BA-MAH nanocomposite

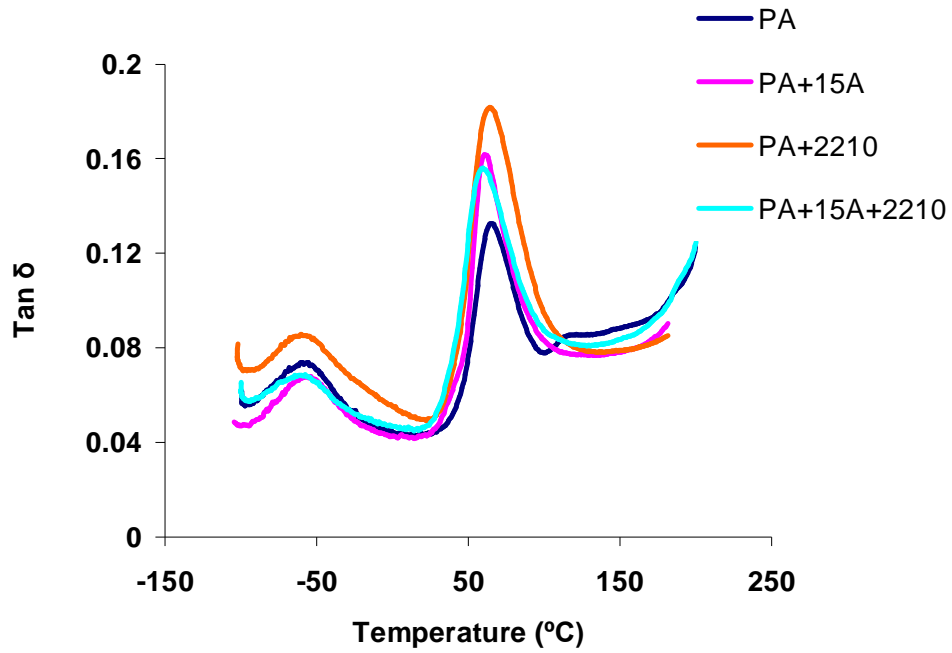


Figure 4.143 Loss tangent ($\tan \delta$) versus temperature data for polyamide-6/Cloisite® 15A/E-BA-MAH nanocomposite

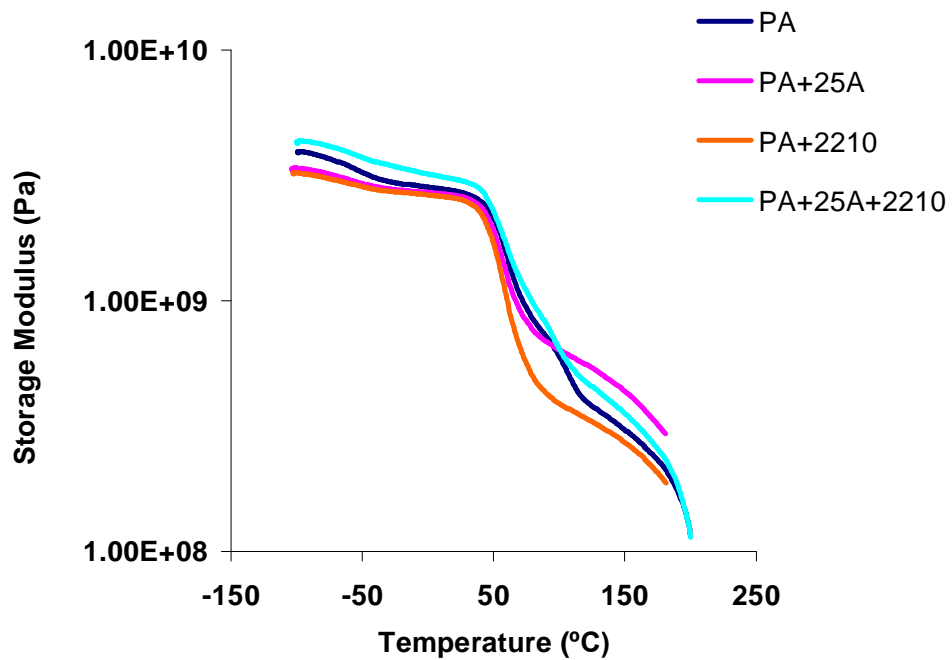


Figure 4.144 Storage Modulus versus temperature data for polyamide-6/Cloisite® 25A/E-BA-MAH nanocomposite

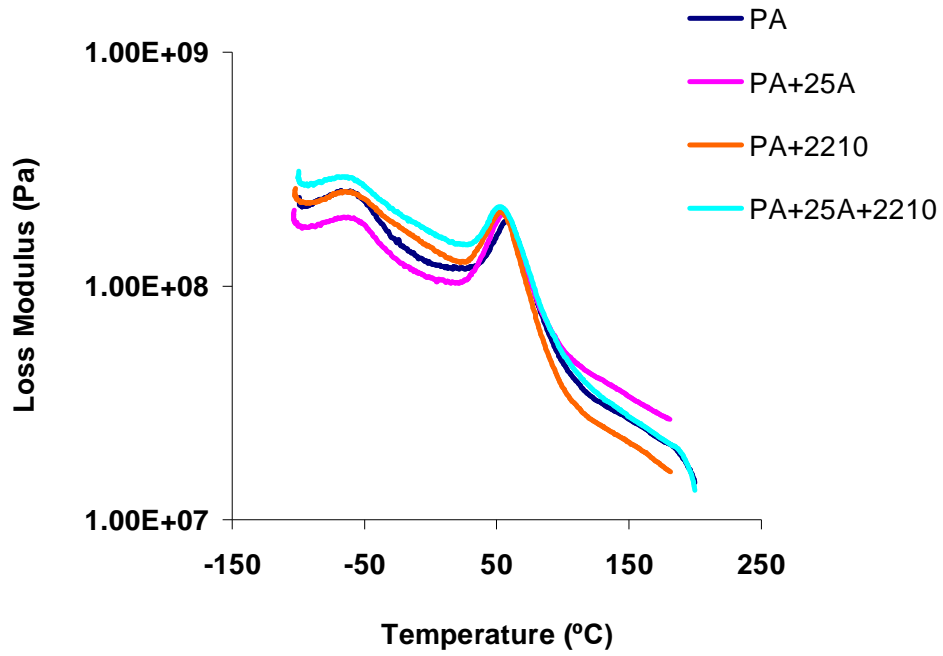


Figure 4.145 Loss Modulus versus temperature data for polyamide-6/Cloisite® 25A/E-BA-MAH nanocomposite

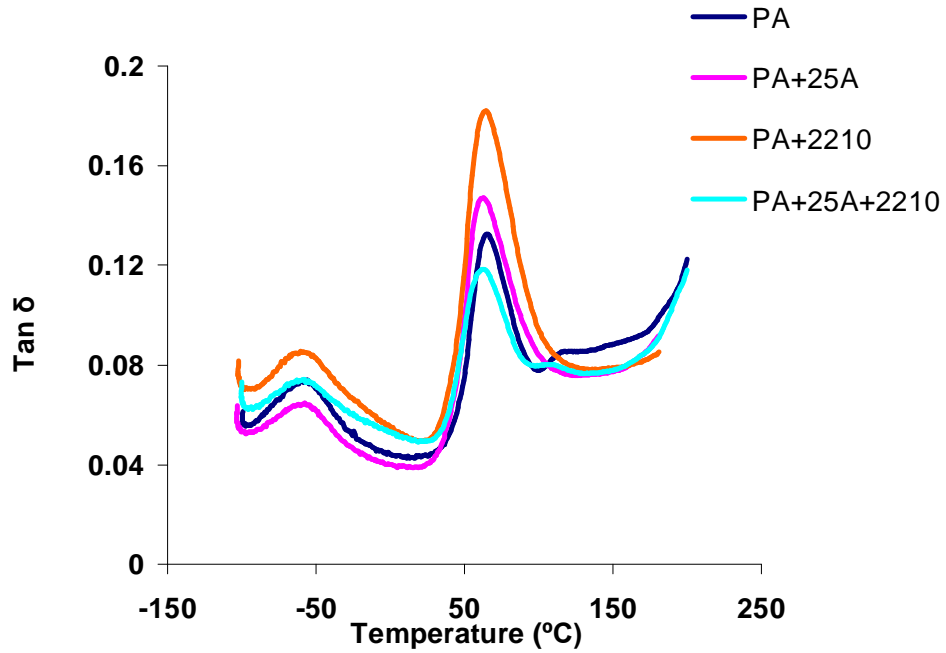


Figure 4.146 Loss tangent ($\tan \delta$) versus temperature data for polyamide-6/Cloisite® 25A/E-BA-MAH nanocomposite

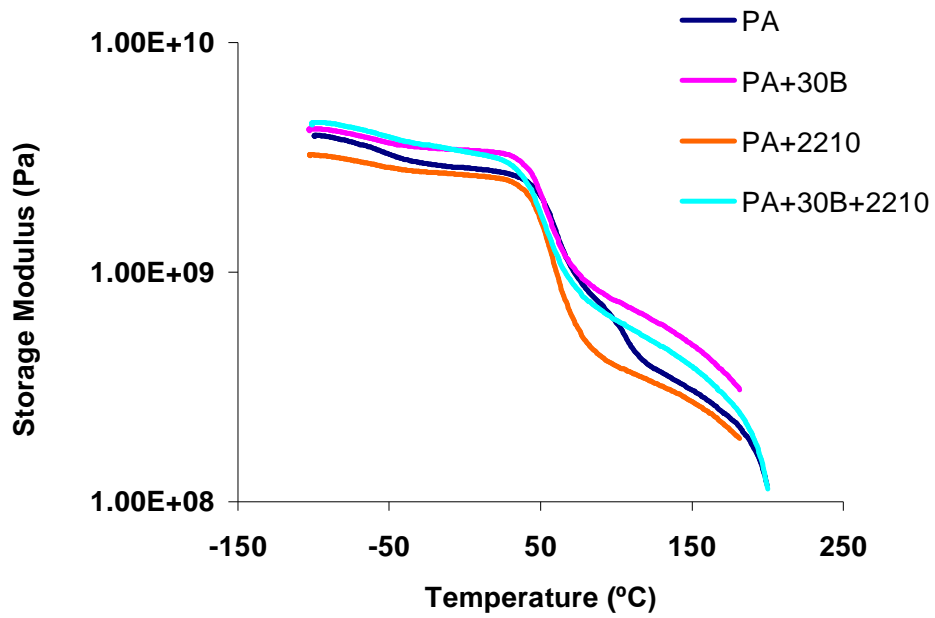


Figure 4.147 Storage Modulus versus temperature data for polyamide-6/Cloisite® 30B/E-BA-MAH nanocomposite

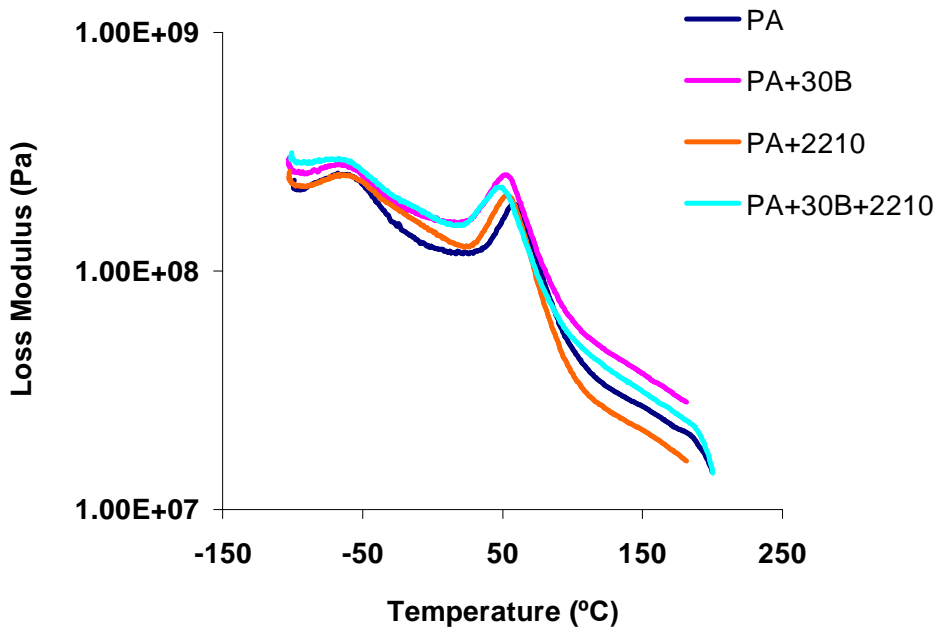


Figure 4.148 Loss Modulus versus temperature data for polyamide-6/Cloisite® 30B/E-BA-MAH nanocomposite

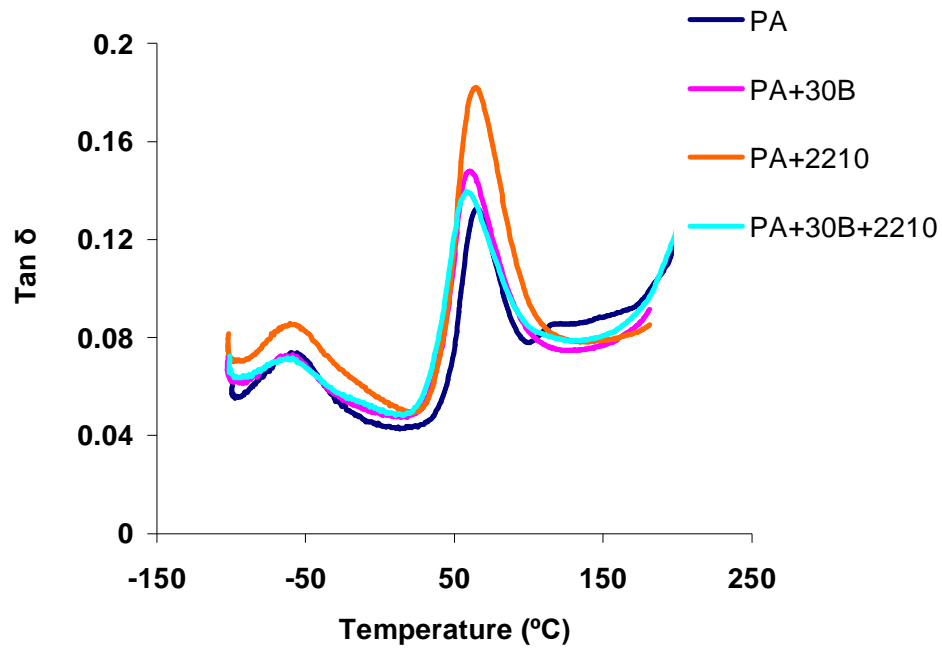


Figure 4.149 Loss tangent ($\tan \delta$) versus temperature data for polyamide-6/Cloisite® 30B/E-BA-MAH nanocomposite

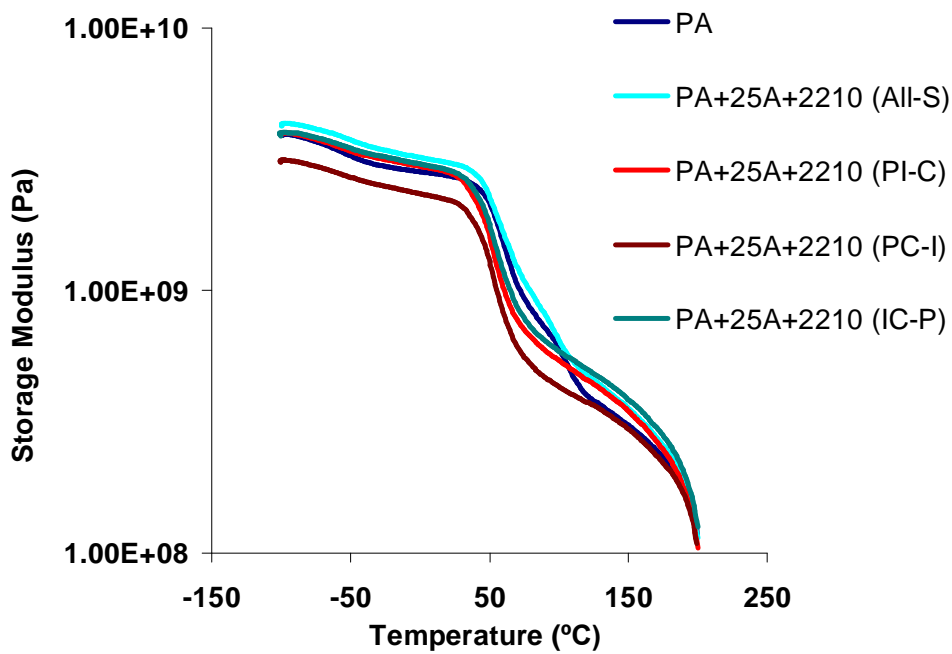


Figure 4.150 Effect of mixing order on storage modulus of polyamide-6/Cloisite® 25A/ E-BA-MAH ternary nanocomposites

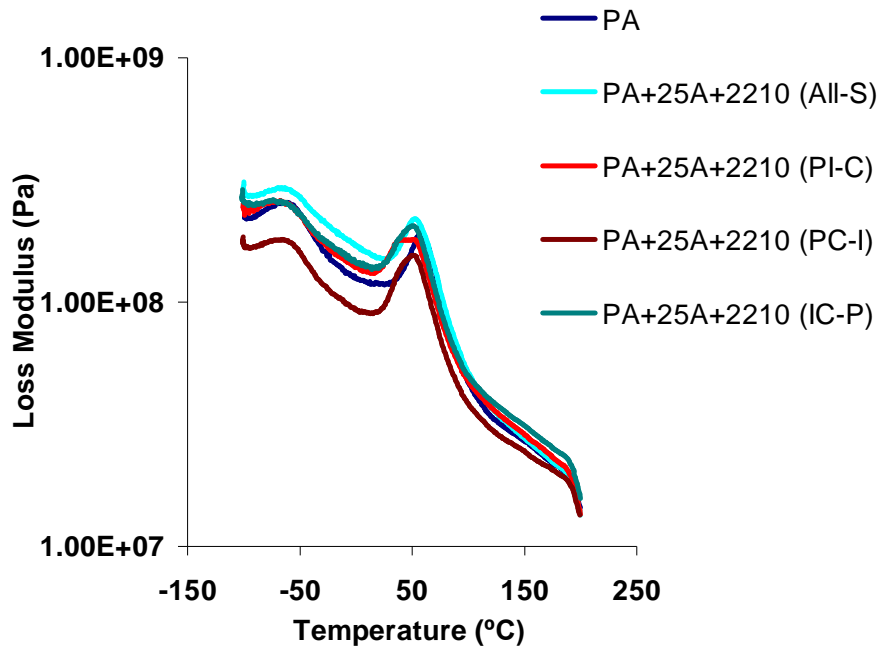


Figure 4.151 Effect of mixing order on loss modulus of polyamide-6/Cloisite® 25A/ E-BA-MAH ternary nanocomposites

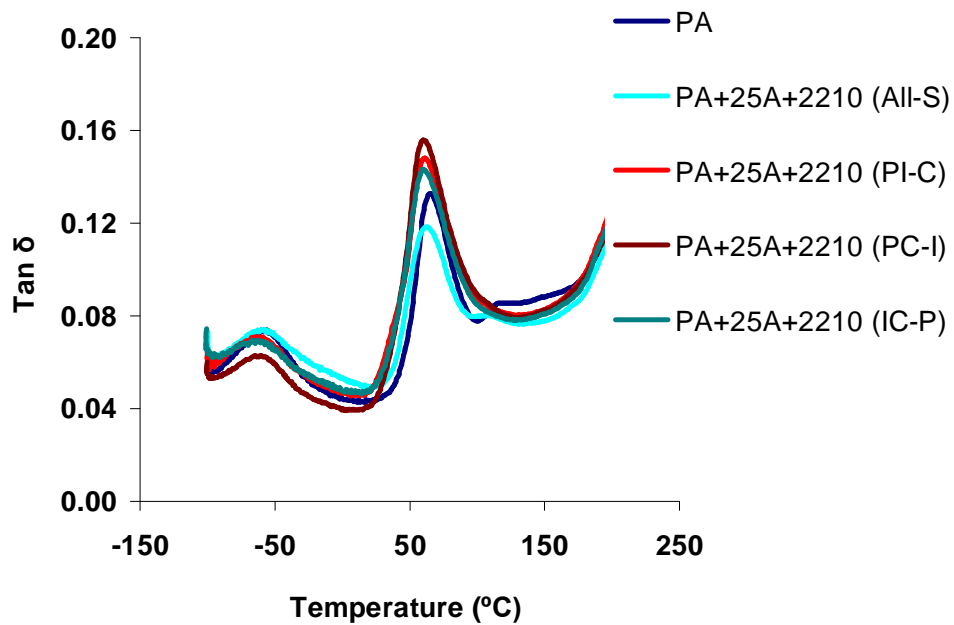


Figure 4.152 Effect of mixing order on loss tangent (tan δ) of polyamide-6/Cloisite® 25A/ E-BA-MAH ternary nanocomposites

4.7.5.2 Dynamic Mechanical Analysis Results of E-GMA Elastomer Containing Nanocomposites

Dynamic mechanical spectra of nanocomposites composed of E-GMA elastomer and polyamide-6/Cloisite® 15A, polyamide-6/Cloisite® 25A, polyamide-6/Cloisite® 30B can be observed through Figures 4.153-4.155, 4.156-4.158, 4.159-4.161, respectively.

Synergistic effects of organoclay and elastomer can be observed in increasing storage modulus, especially in glassy region. In rubbery region binary nanocomposites show higher storage modulus than pure polyamide-6, resulting in a remarkable increase of stiffness, as seen in Figures 4.153, 4.156 and 4.159.

Effects of mixing order on dynamic mechanical properties of polyamide-6/Cloisite® 15A/E-GMA nanocomposites are shown in Figures 4.162-4.164. Above glass transition temperature, PC-I gives the highest storage modulus, like flexural modulus in Figure 4.130. Loss tangent curves show that T_g is shifted to lower temperatures especially in PI-C, PC-I and IC-P mixing sequences.

Dynamic mechanical properties of polyamide-6/Cloisite® 30B/E-GMA nanocomposites, processed by different addition orders can be seen in Figures 4.165-4.167. Storage modulus behavior is different in glassy and rubbery regions for polyamide-6/Cloisite® 30B/E-GMA nanocomposites processed by various addition orders. In glassy region, IC-P and PI-C produce higher storage modulus than the other mixing sequences, whereas in rubbery region modulus is nearly the same. PC-I mixing protocol produces a moderate increase. The results obtained in the rubbery region are consistent with impact strength (Figure 4.80), Young's modulus (Figure 4.110) and flexural modulus (Figure 4.132) data. $\tan \delta$ curves show that glass transition temperature for pure polyamide-6 decreases in the ternary nanocomposites, owing to increases in chain mobility.

Table 4.24 Glass transition temperatures of polyamide-6/organoclay/E-GMA nanocomposites

	T_g (°C)
Polyamide-6	65.2
Polyamide-6 + Cloisite® 15A	60.4
Polyamide-6 + Cloisite® 25A	62.8
Polyamide-6 + Cloisite® 30B	60.0
Polyamide-6 / 5 weight % E-GMA	65.8
Polyamide-6 + Cloisite® 15A+ E-GMA (All-S)	61.4
Polyamide-6 + Cloisite® 15A+ E-GMA (PI-C)	55.7
Polyamide-6 + Cloisite® 15A+ E-GMA (PC-I)	57.1
Polyamide-6 + Cloisite® 15A+ E-GMA (IC-P)	56.9
Polyamide-6 + Cloisite® 25A+ E-GMA (All-S)	59.6
Polyamide-6 + Cloisite® 30B+ E-GMA (All-S)	60.8
Polyamide-6 + Cloisite® 30B+ E-GMA (PI-C)	55.6
Polyamide-6 + Cloisite® 30B+ E-GMA (PC-I)	57.3
Polyamide-6 + Cloisite® 30B+ E-GMA (IC-P)	57.1

Glass transition temperatures of polyamide-6/organoclay/E-GMA nanocomposites in all mixing sequences can be observed in Table 4.24. T_g of binary nanocomposites are generally decreased in the presence of elastomer due to increased chain mobility at the polyamide-elastomer interface.

Table 4.24 also shows the effect of mixing orders on glass transition temperatures of polyamide-6/Cloisite® 15A/E-GMA and polyamide-6/Cloisite® 30B/E-GMA nanocomposites. It is seen that PI-C mixing sequence in polyamide-6/Cloisite® 15A/E-GMA and polyamide-6/Cloisite® 30B/E-GMA nanocomposite gives the lowest T_g among the other mixing sequences. In PI-C mixing order, the organoclay is extruded only once, thus organoclay agglomerates may have been dispersed to a lower extent, resulting a decrease in T_g .

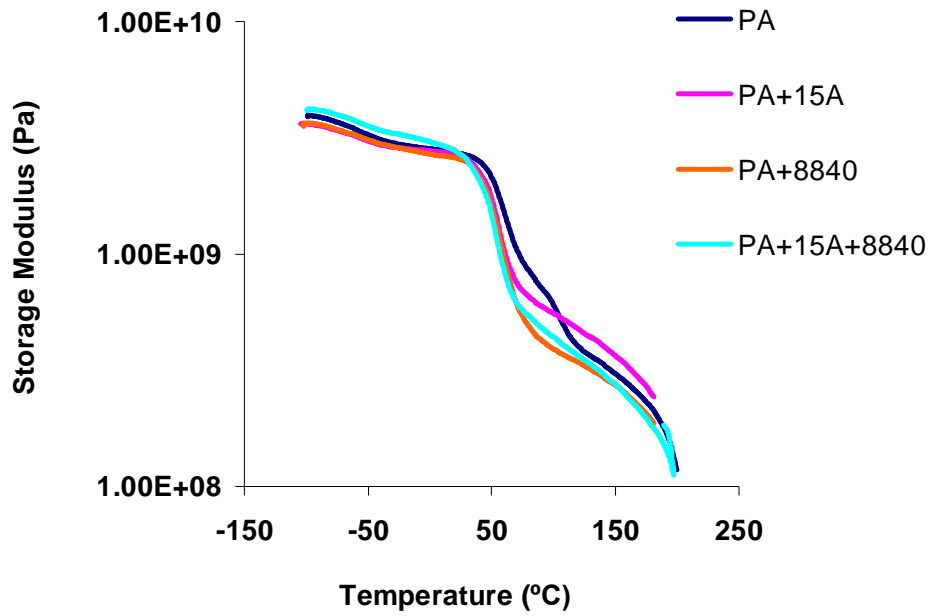


Figure 4.153 Storage Modulus versus temperature data for polyamide-6/Cloisite® 15A/E-GMA nanocomposite

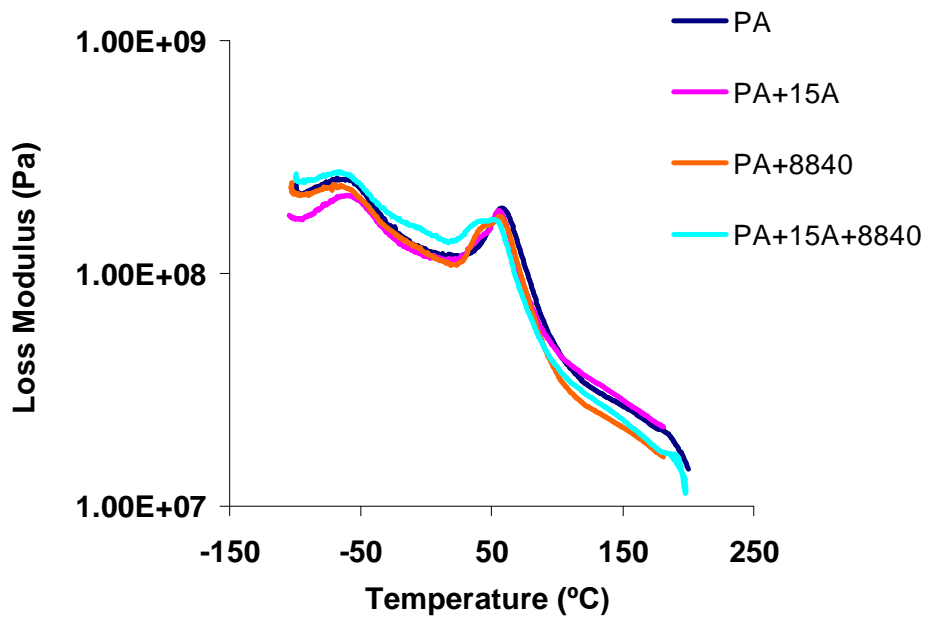


Figure 4.154 Loss Modulus versus temperature data for polyamide-6/Cloisite® 15A/E-GMA nanocomposite

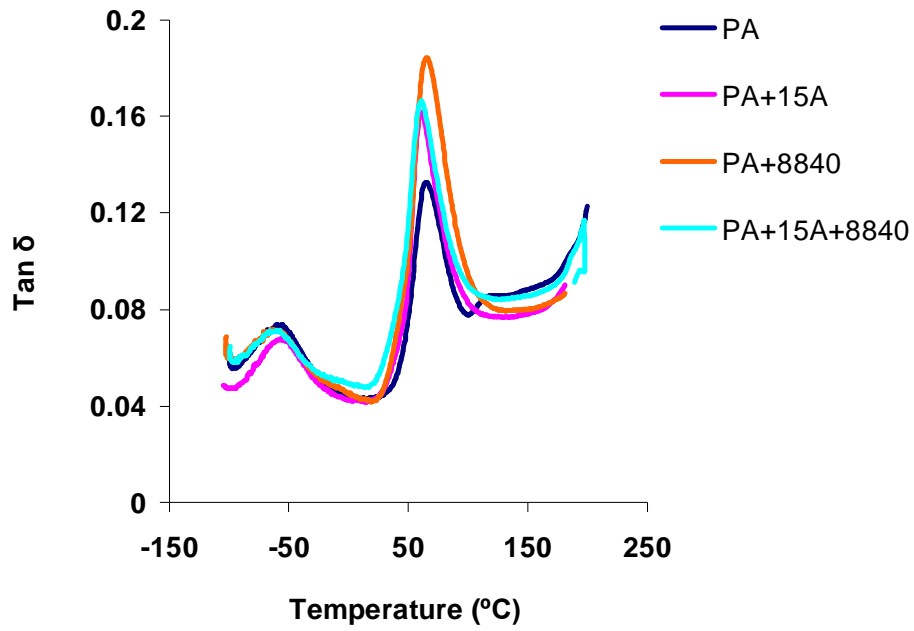


Figure 4.155 Loss tangent ($\tan \delta$) versus temperature data for polyamide-6/Cloisite® 15A/E-GMA nanocomposite

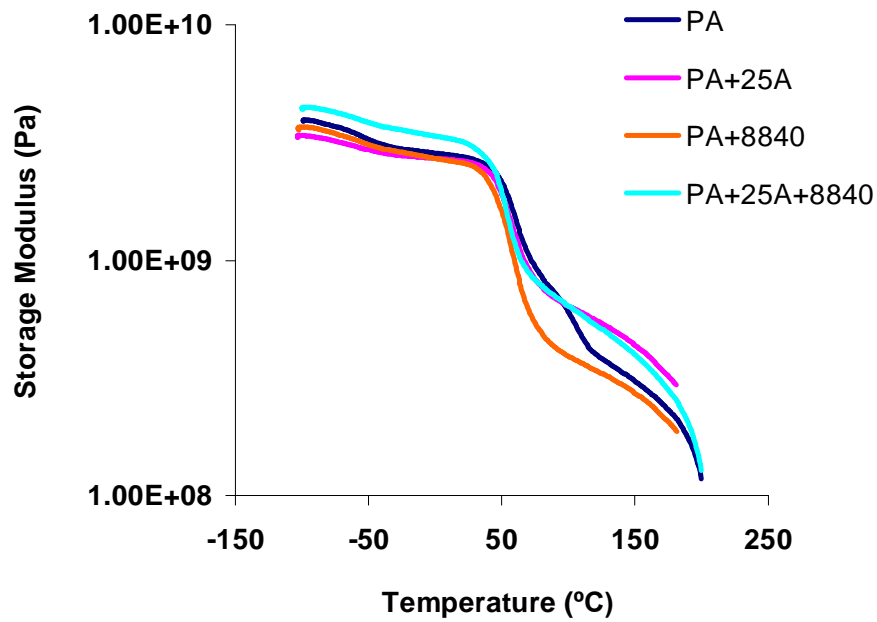


Figure 4.156 Storage Modulus versus temperature data for polyamide-6/Cloisite® 25A/E-GMA nanocomposite

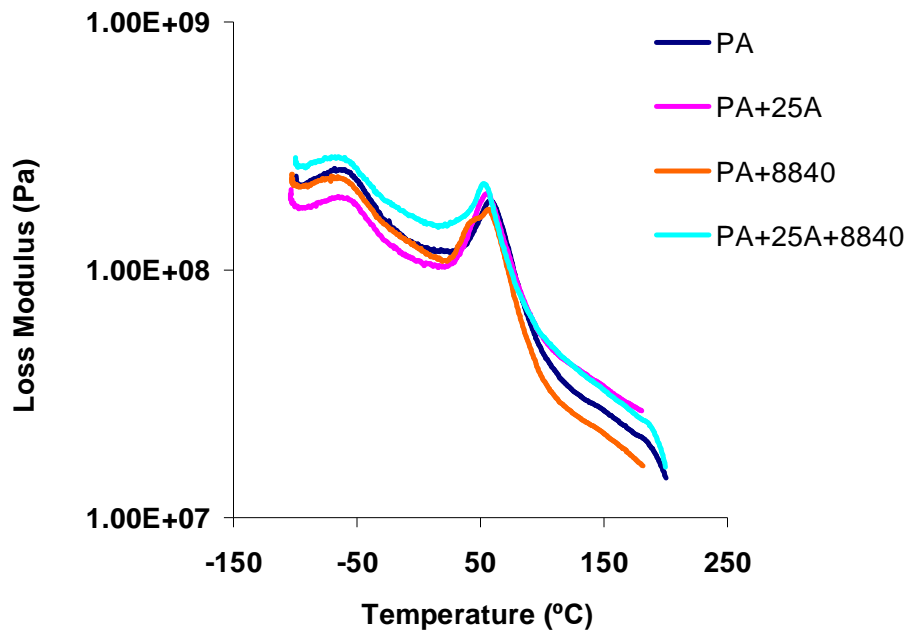


Figure 4.157 Loss Modulus versus temperature data for polyamide-6/Cloisite® 25A/E-GMA nanocomposite

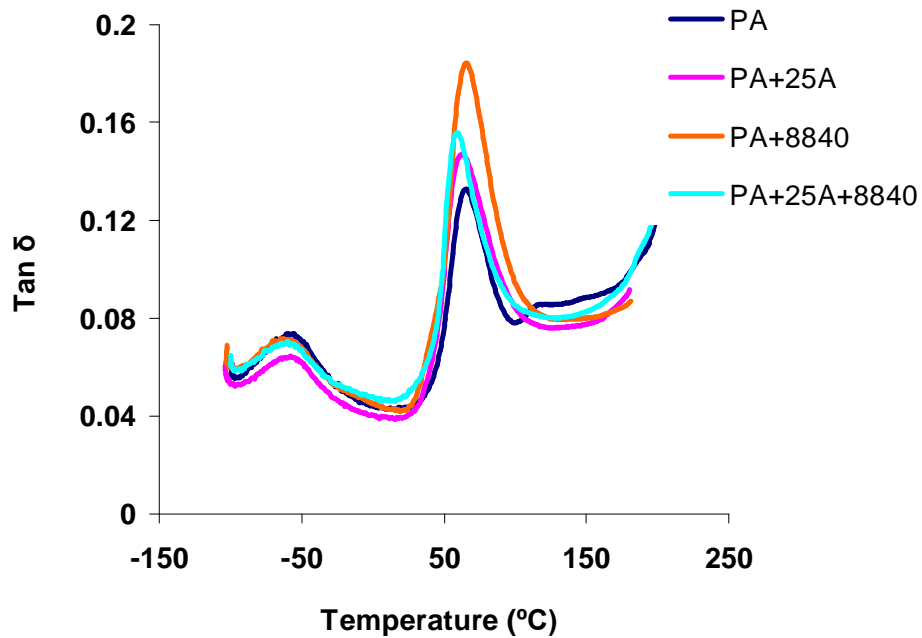


Figure 4.158 Loss tangent (tan δ) versus temperature data for polyamide-6/Cloisite® 25A/E-GMA nanocomposite

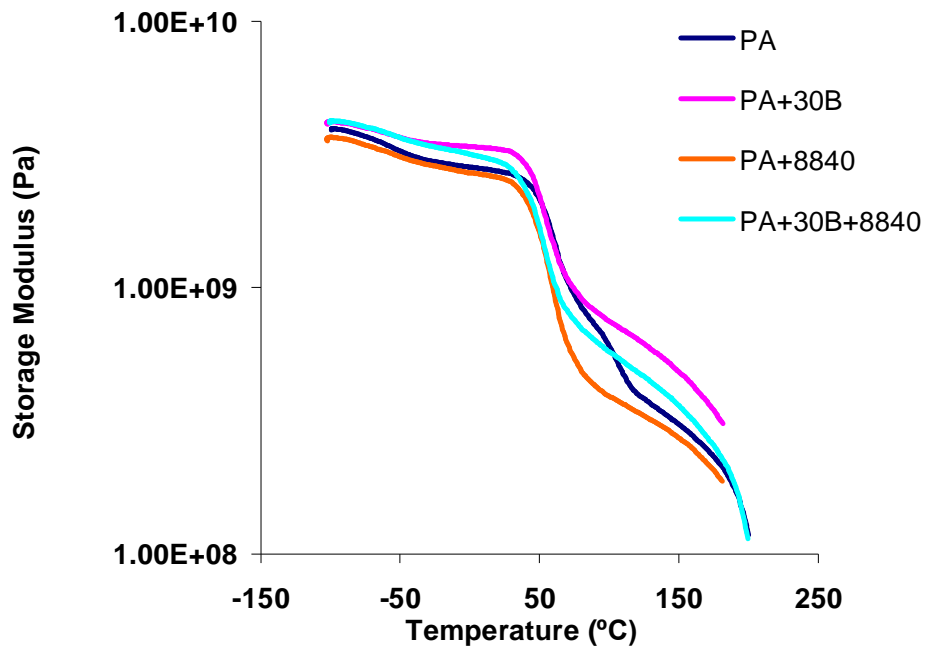


Figure 4.159 Storage Modulus versus temperature data for polyamide-6/Cloisite® 30B/E-GMA nanocomposite

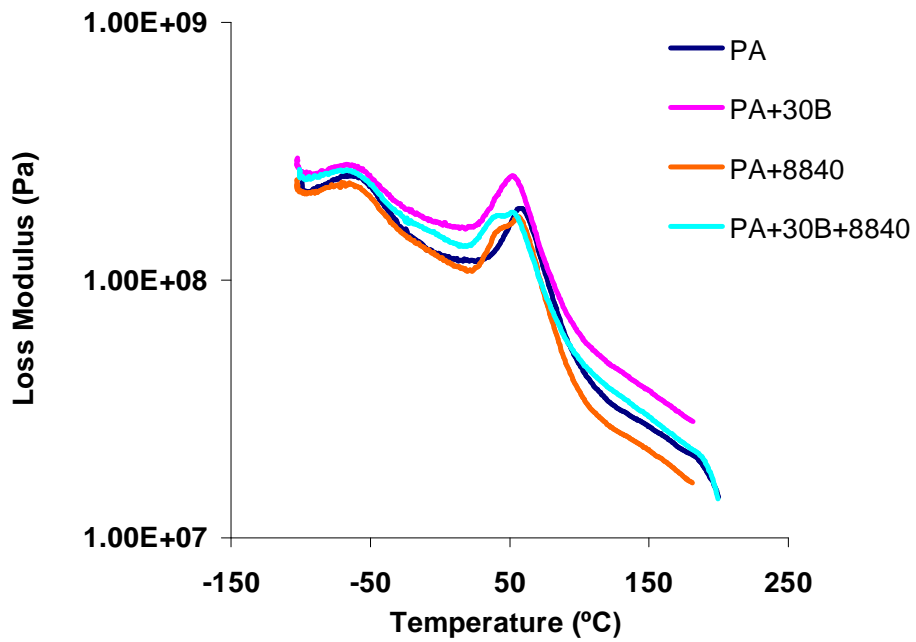


Figure 4.160 Loss Modulus versus temperature data for polyamide-6/Cloisite® 30B/E-GMA nanocomposite

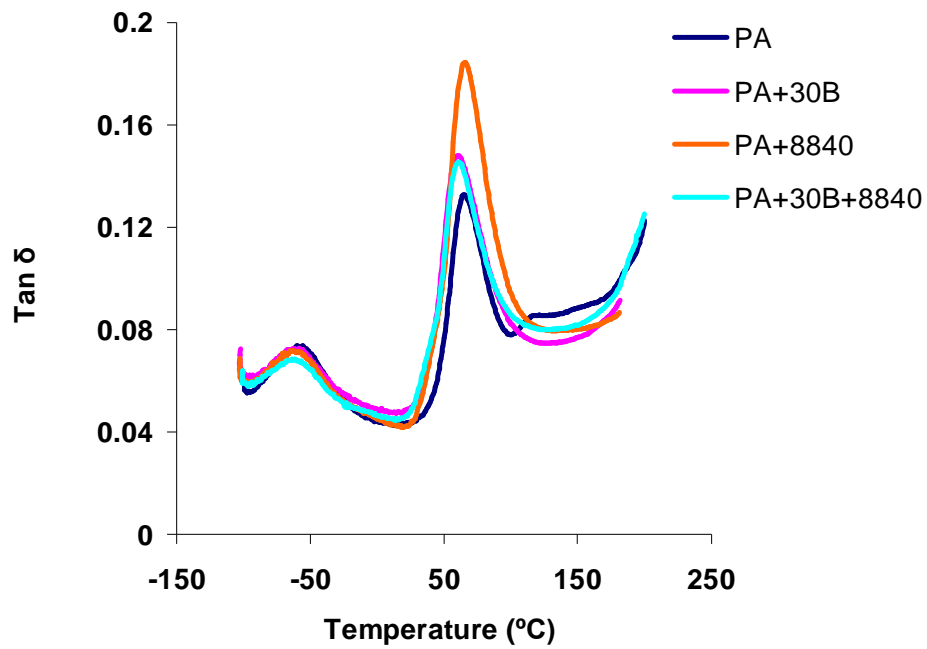


Figure 4.161 Loss tangent ($\tan \delta$) versus temperature data for polyamide-6/Cloisite® 30B/E-GMA nanocomposite

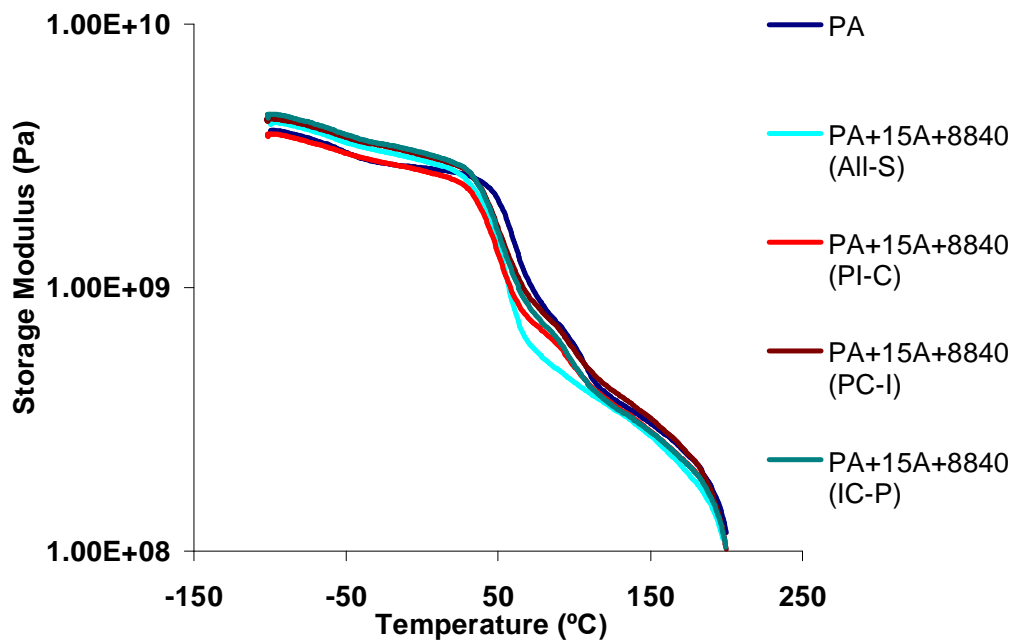


Figure 4.162 Effect of mixing order on storage modulus of polyamide-6/Cloisite® 15A/ E-GMA ternary nanocomposites

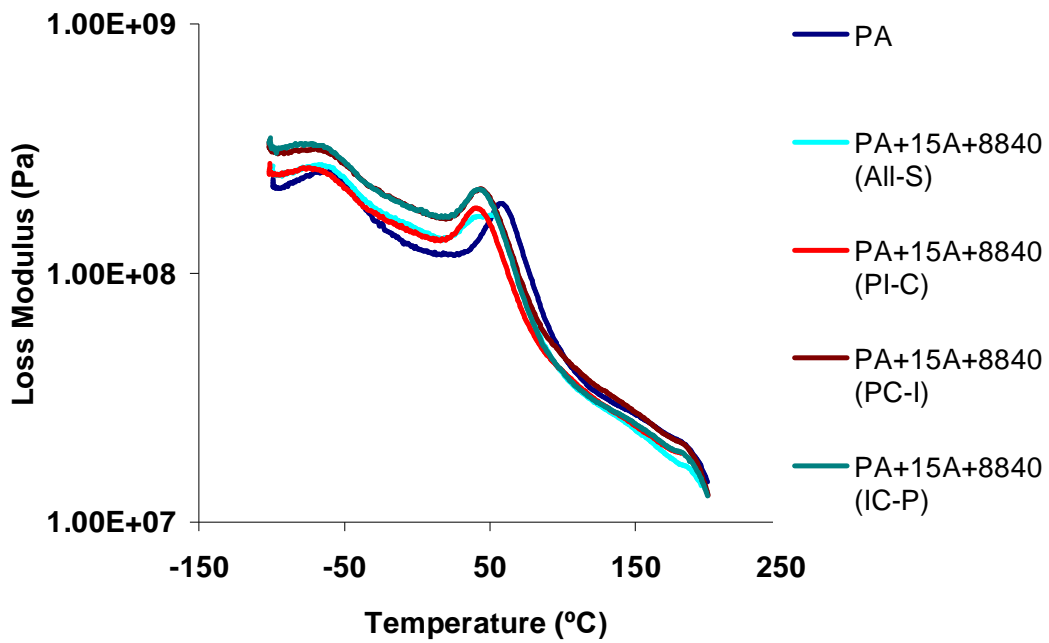


Figure 4.163 Effect of mixing order on loss modulus of polyamide-6/Cloisite® 15A/ E-GMA ternary nanocomposites

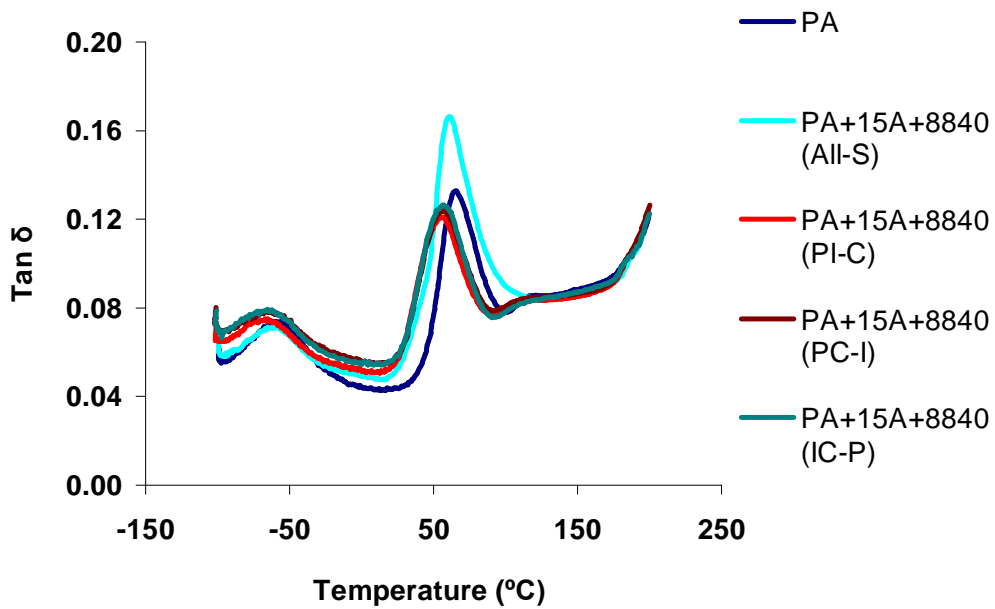


Figure 4.164 Effect of mixing order on loss tangent ($\tan \delta$) of polyamide-6/Cloisite® 15A/ E-GMA ternary nanocomposites

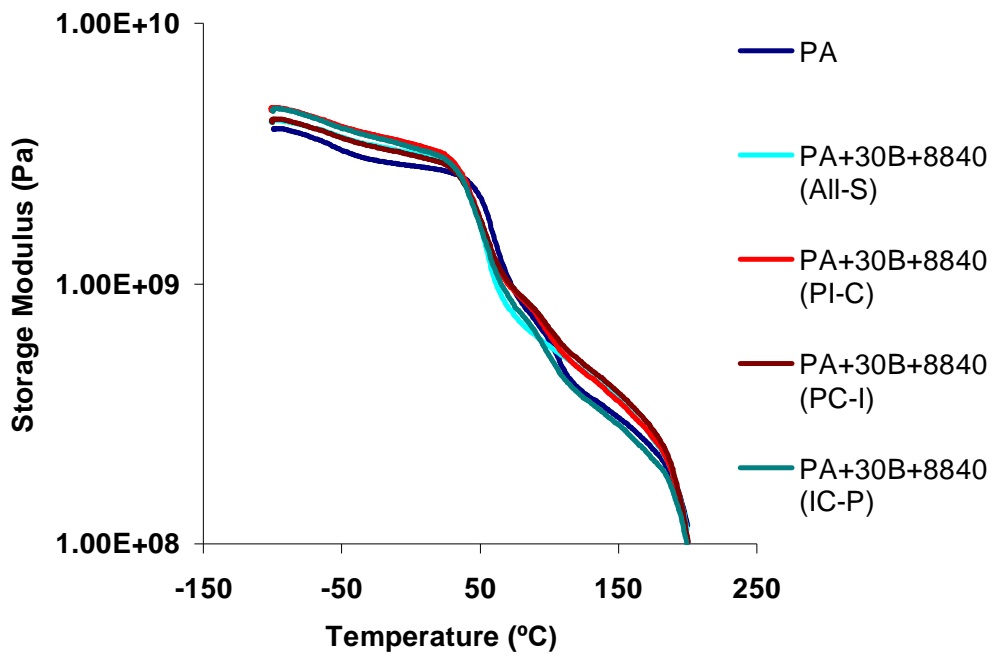


Figure 4.165 Effect of mixing order on storage modulus of polyamide-6/Cloisite® 30B/ E-GMA ternary nanocomposites

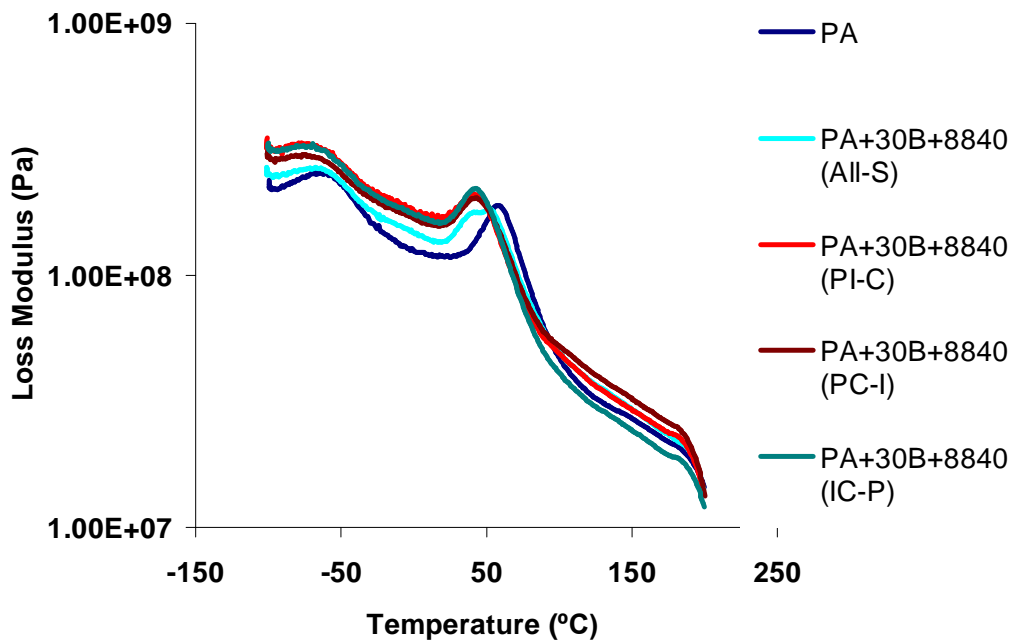


Figure 4.166 Effect of mixing order on loss modulus of polyamide-6/Cloisite® 30B/E-GMA ternary nanocomposites

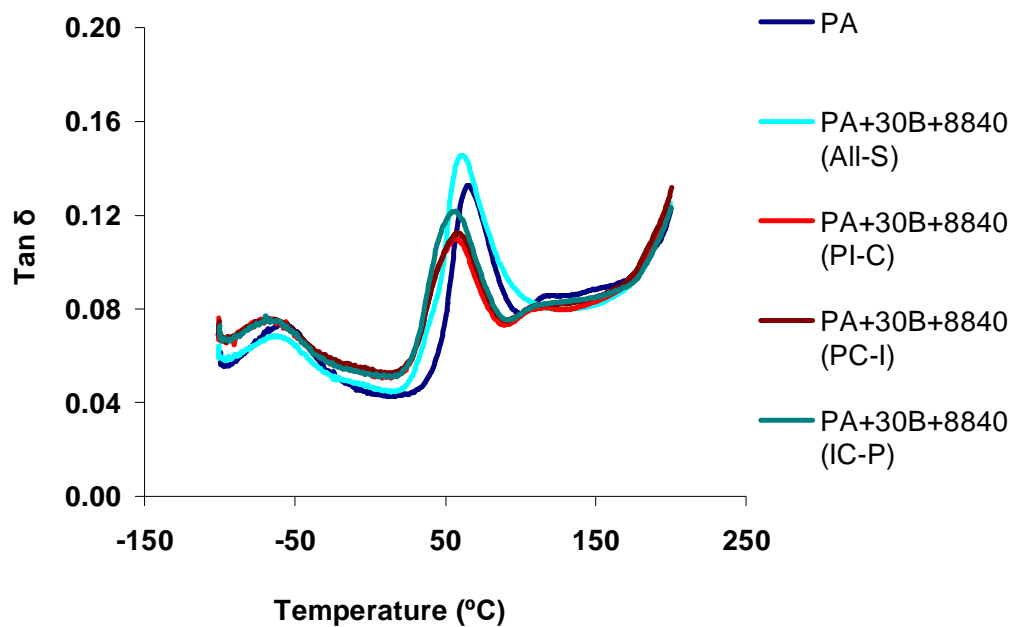


Figure 4.167 Effect of mixing order on loss tangent ($\tan \delta$) of polyamide-6/Cloisite® 30B/ E-GMA ternary nanocomposites

4.7.5.3 Dynamic Mechanical Analysis Results of Nanocomposites Containing E-MA-GMA Elastomer

Figures 4.168-4.170, 4.171-4.173, and 4.174-176 show the dynamic mechanical spectra of nanocomposites composed of polyamide-6/ Cloisite® 15A/E-GMA, polyamide-6/ Cloisite® 25A/E-GMA and polyamide-6/ Cloisite® 30B/E-GMA.

Storage modulus of polyamide-6/Cloisite® 15A/E-MA-GMA nanocomposite is lower than polyamide-6 both in glassy and rubbery regions as observed in Figure 4.168, on the other hand, in 25A containing ternary nanocomposites, synergistic effects of elastomer and organoclay can be observed in Figure 4.171. According to Figure 4.174, polyamide-6/Cloisite 30B binary nanocomposites gives the highest storage modulus data due to the high compatibility of this organoclay with polyamide-6. Loss

modulus curves which can be seen in Figures 4.169, 4.172 and 4. 175 follow the same trend with storage modulus curves.

Table 4.25 Glass transition temperatures of polyamide-6/organoclay/E-MA-GMA nanocomposites

	T_g (°C)
Polyamide-6	65.2
Polyamide-6 + Cloisite® 15A	60.4
Polyamide-6 + Cloisite® 25A	62.8
Polyamide-6 + Cloisite® 30B	60.0
Polyamide-6 / 5 weight % E-MA-GMA	63.2
Polyamide-6 + Cloisite® 15A + E-MA-GMA (All-S)	59.9
Polyamide-6 + Cloisite® 25A + E-MA-GMA (All-S)	62.0
Polyamide-6 + Cloisite® 30B + E-MA-GMA (All-S)	59.4

Glass transition temperatures of polyamide-6/organoclay/E-MA-GMA nanocomposites in All-S sequence are demonstrated in Table 4.25. It can be seen that in the presence of elastomer, glass transition temperatures of polyamide-6/organoclay/E-MA-GMA nanocomposites remain relatively unchanged when compared with the glass transition temperature of binary polyamide-6/organoclay nanocomposites.

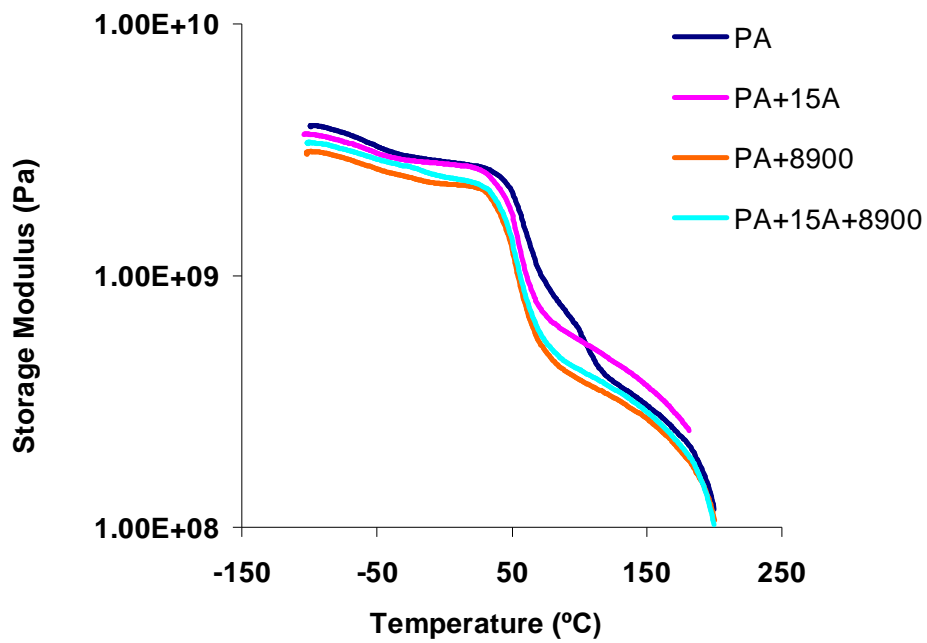


Figure 4.168 Storage Modulus versus temperature data for polyamide-6/Cloisite® 15A/E-MA-GMA nanocomposite

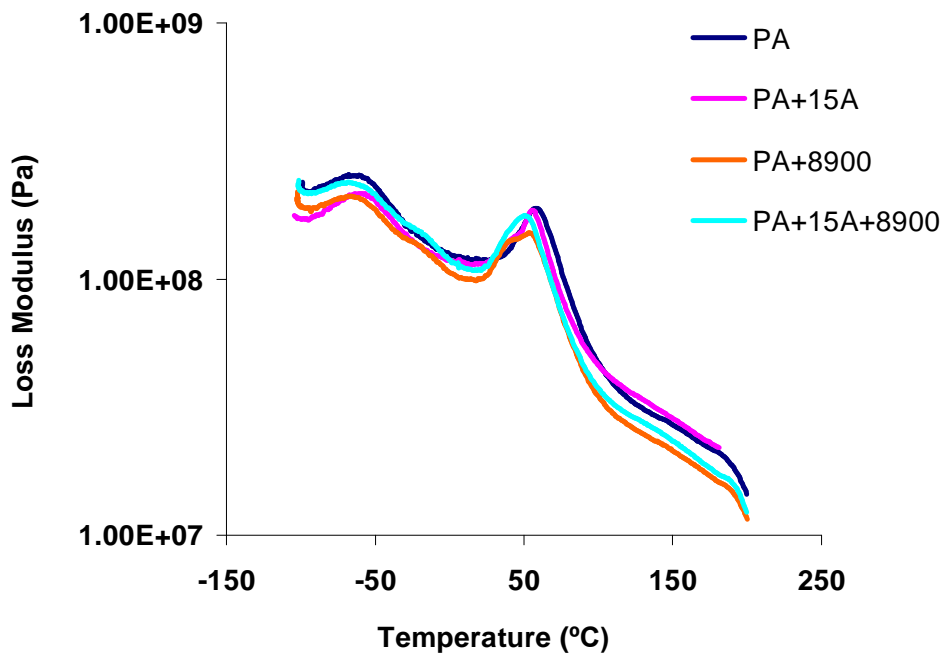


Figure 4.169 Loss Modulus versus temperature data for polyamide-6/Cloisite® 15A/E-MA-GMA nanocomposite

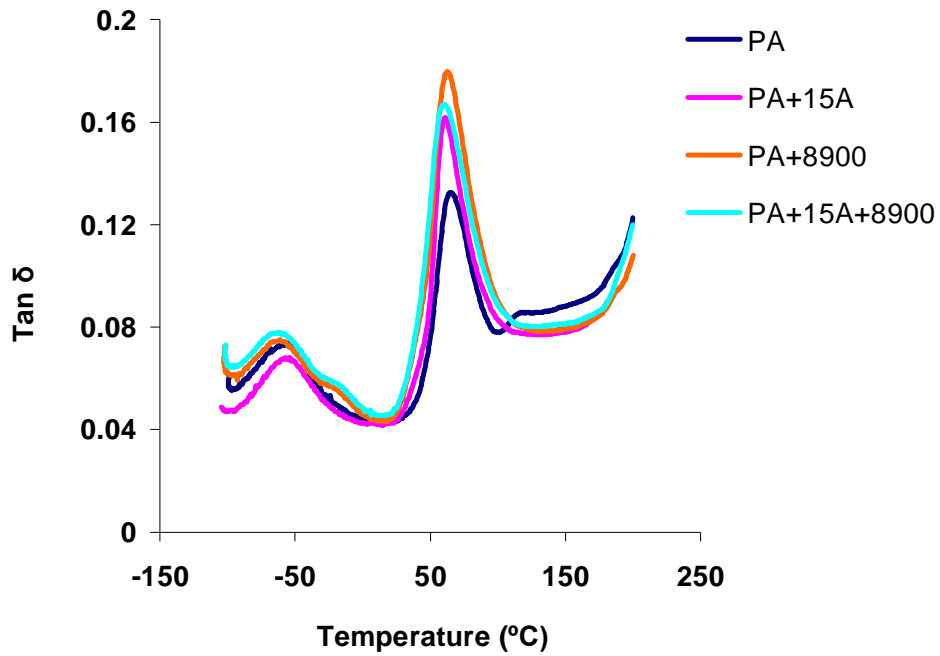


Figure 4.170 Loss tangent ($\tan \delta$) versus temperature data for polyamide-6/Cloisite® 15A/E-MA-GMA nanocomposite

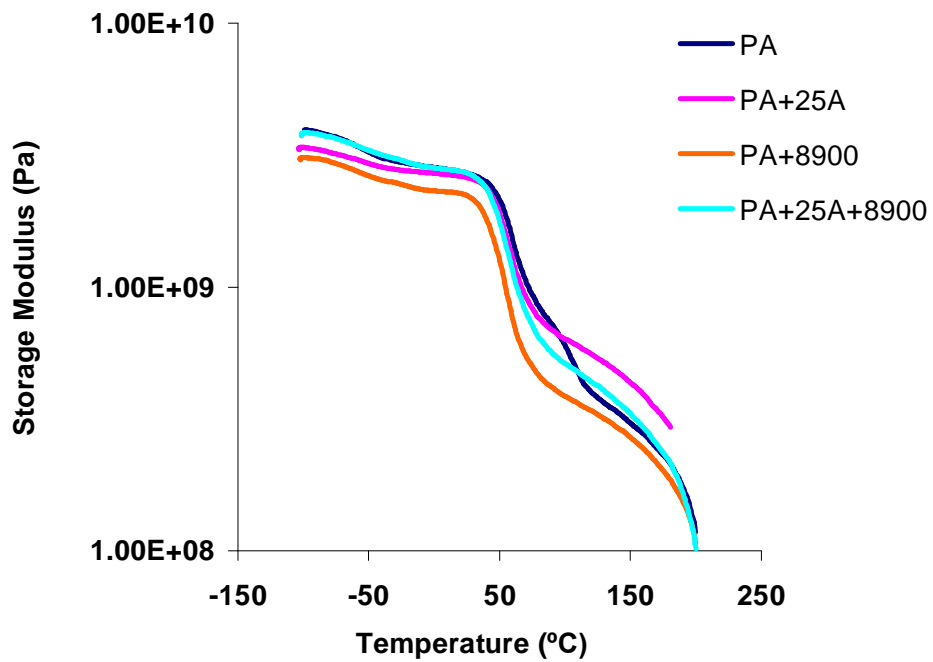


Figure 4.171 Storage Modulus versus temperature data for polyamide-6/Cloisite® 25A/E-MA-GMA nanocomposite

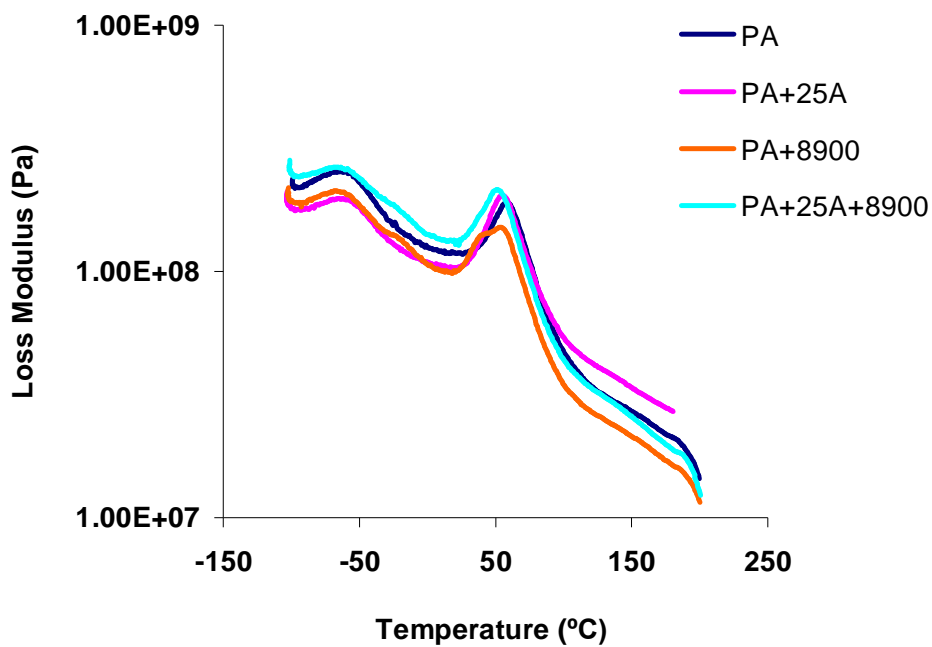


Figure 4.172 Loss modulus versus temperature data for polyamide-6/Cloisite® 25A/E-MA-GMA nanocomposite

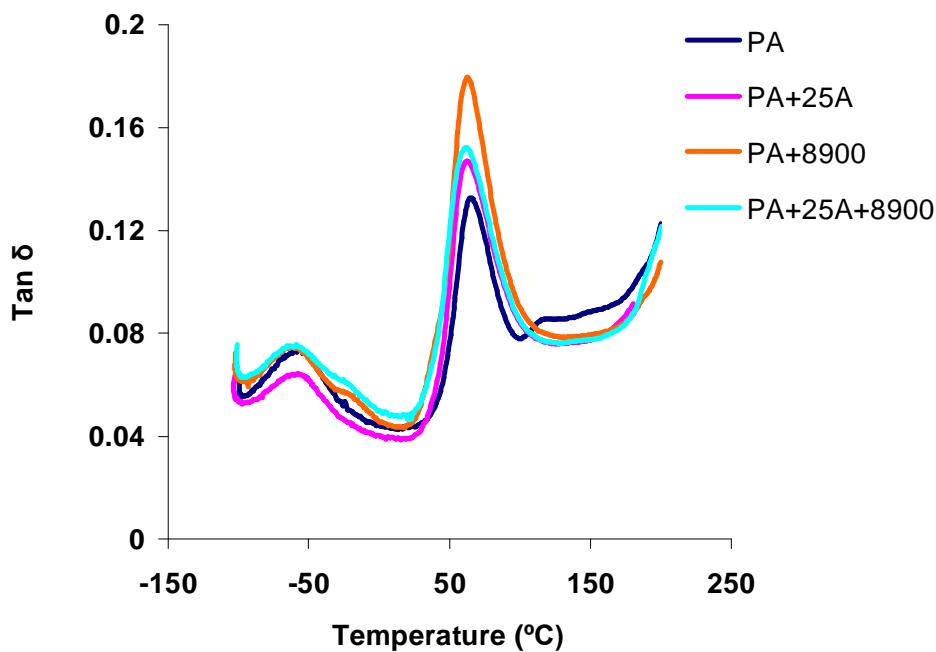


Figure 4.173 Loss tangent ($\tan \delta$) versus temperature data for polyamide-6/Cloisite® 25A/E-MA-GMA nanocomposite

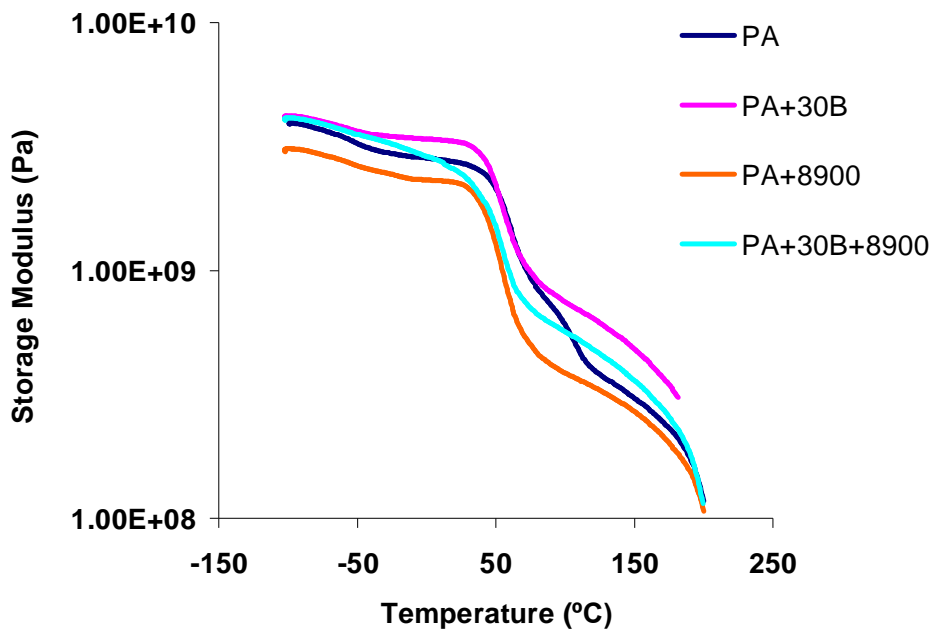


Figure 4.174 Storage modulus versus temperature data for polyamide-6/Cloisite® 30B/E-MA-GMA nanocomposite

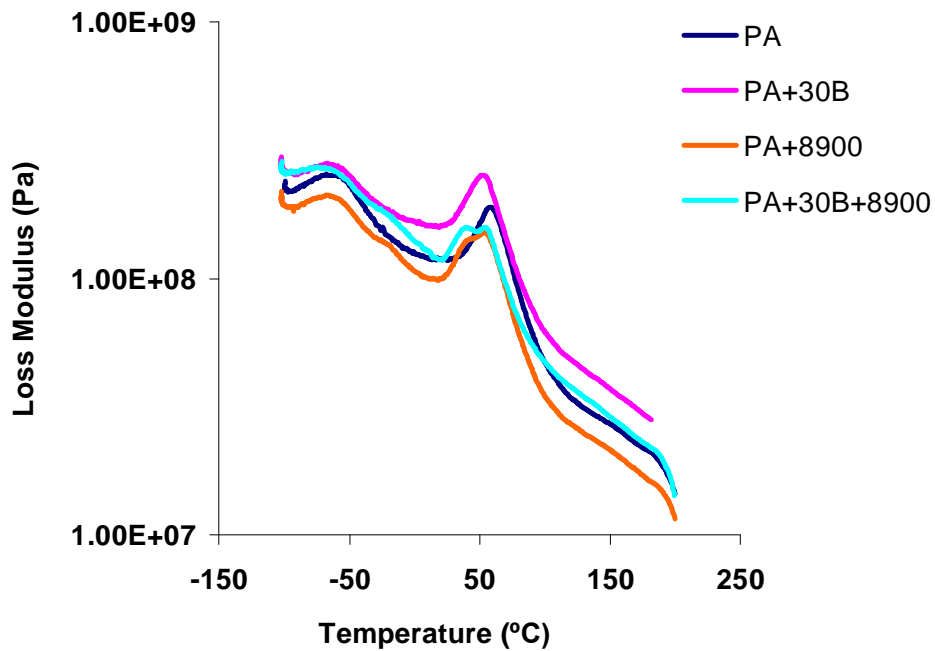


Figure 4.175 Loss modulus versus temperature data for polyamide-6/Cloisite® 30B/E-MA-GMA nanocomposite

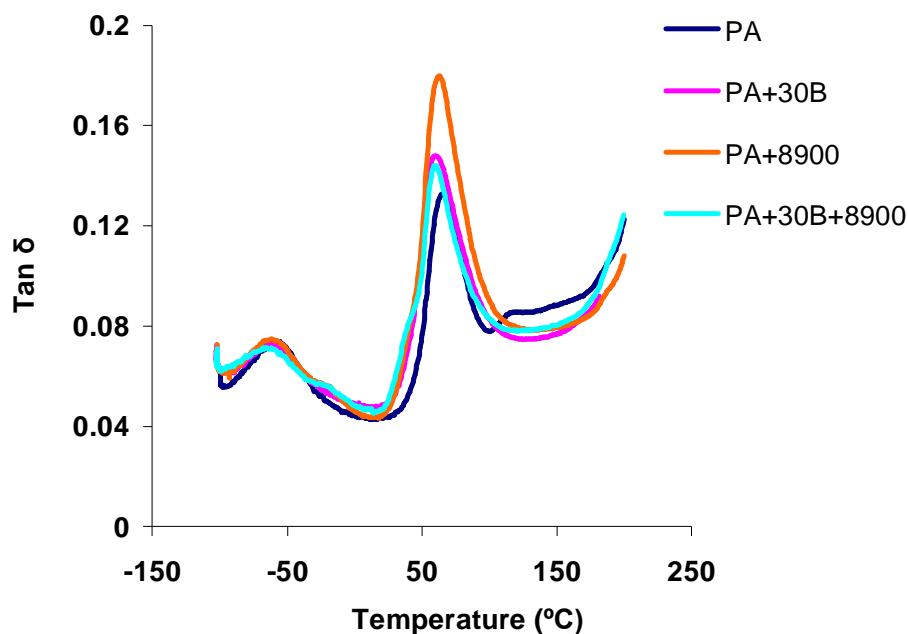


Figure 4.176 Loss tangent ($\tan \delta$) versus temperature data for polyamide-6/Cloisite® 30B/E-MA-GMA nanocomposite

4.8 VISCOELASTIC PROPERTIES IN THE MELT STATE

In order to understand the effects of various shear environments on polymer nanocomposite systems, rheological behavior of nanocomposites are studied (Cho and Paul, 2001; Krishnamoorti et al., 1996; Krishnamoorti and Giannelis, 1997).

Viscoelastic characteristics of polyamide-6/organoclay/E-MA-GMA nanocomposites over a wide range of frequencies are investigated in this study. Storage modulus, loss modulus and complex viscosity are determined. Storage modulus represents the strain energy reversibly stored in the substance; whereas loss modulus represents the amount of energy irreversibly given off by the substance to its environment (Hyun et al., 2001).

Figures 4.177-4.179 show logarithmic plots of storage modulus, loss modulus and complex viscosity versus strain amplitude for polyamide-6/Cloisite® 25A/E-MA-GMA nanocomposite, at 240 °C and 5 rad/s angular frequency, obtained using parallel plate oscillating rheometer. Storage and loss moduli, also complex viscosity remain constant in 1-20 % strain amplitude range. Thus, in the analysis 5% strain amplitude is selected to ensure that experiments are performed in linear viscoelastic region.

The storage and loss modulus moduli and complex viscosity resulting from dynamic frequency scans for polyamide-6/organoclay/E-MA-GMA nanocomposites are shown in Figures 4.180-4.182.

More detailed data are given in Appendix D in Figures D.1-D.3, D.4-D.6, and D.7-D.9 for polyamide-6/Cloisite® 15A/E-MA-GMA, polyamide-6/Cloisite® 25A/E-MA-GMA and polyamide-6/Cloisite® 30B/E-MA-GMA nanocomposites, respectively.

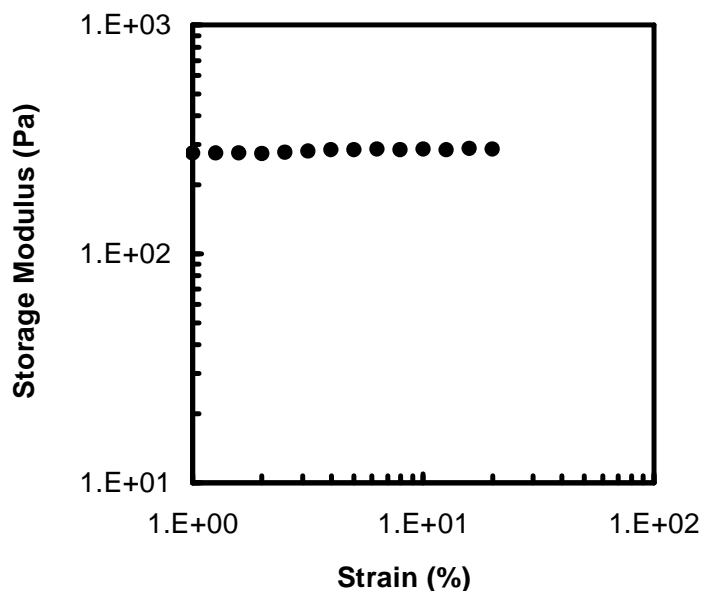


Figure 4.177 Influence of strain amplitude on storage modulus for polyamide-6/Cloisite® 25A/E-MA-GMA nanocomposite

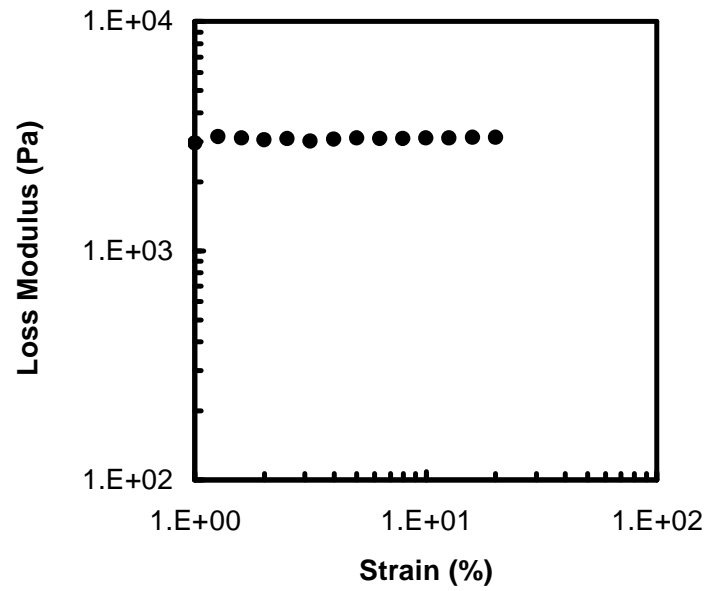


Figure 4.178 Influence of strain amplitude on loss modulus for polyamide-6/Cloisite® 25A/E-MA-GMA nanocomposite

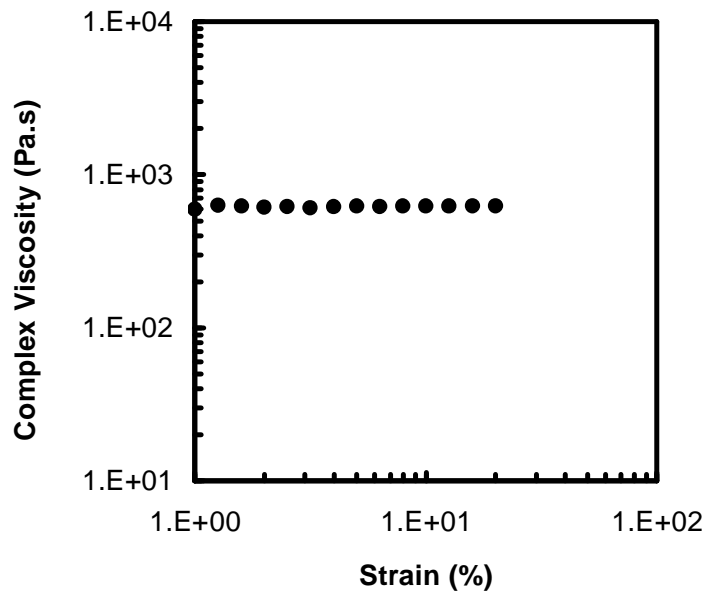


Figure 4.179 Influence of strain amplitude on complex viscosity for polyamide-6/Cloisite® 25A/E-MA-GMA nanocomposite

As observed in Figures 4.180-4.182, both storage and loss moduli and complex viscosity of unfilled polyamide-6 increases with the addition of organoclay in the frequency range studied. This reflects the strong effect of intercalated/exfoliated clay layers on the viscosity of unfilled polyamide-6. Increase in storage modulus, loss modulus and complex viscosity are higher in binary polyamide-6/Cloisite® 15A nanocomposites than in polyamide-6/Cloisite® 25A and polyamide-6/Cloisite® 30B nanocomposites. When an organoclay-polymer mixture is subjected to cyclic deformation, three types of interactions may take place: polymer chain-polymer chain, polymer chain-organoclay surface and organoclay surface-surface. Interactions between the polymer chains are assumed to be constant in the materials considered in Figures 4.180-4.182, whereas polymer chain-organoclay surface interaction depends on molecular attraction between the two, and the surface area of organoclay. Organoclay surface-surface interactions are higher if d-spacing is smaller. According to XRD Figures 4.5, 4.9 and 4.13, it is seen that the % expansion of the organoclay upon melt mixing with polyamide-6 is the highest for Cloisite® 30BA, followed by Cloisite® 25A and Cloisite® 15A. The amount of polymer chains that have entered the interlayer galleries follow the same order. Owing to high organoclay surface-surface interactions polyamide-6/Cloisite® 15A nanocomposite has the highest storage and loss modulus and complex viscosity, followed by Cloisite® 25A and Cloisite® 30B.

Figure 4.183 shows the relationship between loss and storage modulus in polyamide-6/organoclay binary nanocomposites. The dashed line in the Figure represents $G''=G'$. It is seen that polyamide-6 is the least elastic, since it is on the very left side of the equi-moduli line. Liquid-like behavior of polyamide-6 turns to pseudo solid-like as it is compounded with the organoclays. It is seen that polyamide-6/Cloisite® 15A nanocomposite is more elastic than polyamide-6/Cloisite® 25A and polyamide-6/Cloisite® 30B nanocomposites, since it is near the right side of the equi-moduli line, owing to the high organoclay surface-surface interactions explained earlier.

Figures 4.184 and 4.185 show the storage and loss modulus of polyamide-6/organoclay/E-MA-GMA nanocomposites. It is seen that storage and loss modulus of polyamide-6/Cloisite® 30B/E-MA-GMA nanocomposite is the highest among the ternary nanocomposites. Polymer chain-surface interactions are dominant in this system since there should be a great interaction between organoclay hydroxyethyl groups and E-MA-GMA. In ternary systems, since the d-spacings are higher in comparison to the d-spacings of binary nanocomposites, organoclay surface-surface interactions could be less effective than polymer chain-organoclay surface interactions. The data regarding polyamide-6/Cloisite® 15A/E-MA-GMA are in between polyamide-6/ Cloisite® 30B/E-MA-GMA and polyamide-6/Cloisite® 25A/E-MA-GMA, since in this system organoclay surface-surface interactions could still be important.

Figure 4.186 shows that elastomer E-MA-GMA exhibits solid-like non-Newtonian behavior, complex viscosity gradually increases with decreasing frequency. In contrast, polyamide-6 based blends and nanocomposites display Newtonian-like behavior, since complex viscosity is not changed significantly with frequency at low frequencies. Incorporation of E-MA-GMA elastomer enhances the complex viscosity of unfilled polyamide-6 for the studied viscoelastic range. This is due to the high viscosity of elastomer E-MA-GMA and the reactions occurring between polyamide-6 and E-MA-GMA which leads to the formation of graft copolymers. Complex viscosities in polyamide-6/organoclay/E-MA-GMA ternary nanocomposites are generally higher than polyamide-6/E-MA-GMA blends because of the flow hindrance by organoclay particles and interactions between organoclay and polyamide-6 (Chow et al., 2005). Complex viscosity in polyamide-6/Cloisite® 30B/E-MA-GMA nanocomposite is the highest among the ternary nanocomposites. The interactions between organoclay –OH groups in 30B and GMA may have lead to an increase in viscosity.

Table 4.26 shows that the viscoelastic behavior of liquid-like unfilled polyamide-6 changes to pseudo solid-like for nanocomposites with the addition of organoclay, since for liquid-like polymers G' is proportional to ω^2 and G'' is proportional to ω^1 and for solid-like G' and G'' is proportional to ω^0 . This change is attributed to the

formation of a percolated network superstructure of the exfoliated layers or stacks of intercalated layers (Krishnamoorti and Yurekli, 2001). Storage and loss modulus slope changes in the viscoelastic range gives information about clay dispersion and the higher the slope, the worse is the clay dispersion (Li et al., 2003). The differences in slopes may be attributed to the differences in the extent of organoclay exfoliation. A larger extent of exfoliation will lead to more solid-like (or pseudo-solid like) behavior due to the increased number of particle-polymer interactions (Fornes et al., 2001). According to Hoffman et al. (2000), the higher the storage moduli, and the smaller the slope of storage modulus vs. frequency data, especially at lower frequency, the higher is the interaction between the silicate platelets and polymer and their tendency to form a three-dimensional superstructure. In order to minimize the matrix molecular weight differences, the comparisons should be made between the ternary nanocomposites. According to Table 4.26, which shows storage and loss modulus slopes as a function of frequency in double logarithmic scale, polyamide-6/Cloisite® 30B/E-MA-GMA nanocomposite has the lowest slope among the ternary nanocomposites. Storage modulus with respect to frequency in polyamide-6/Cloisite® 30B/E-MA-GMA nanocomposite is the highest among the ternary nanocomposites, as it is also observed in Young's Modulus (Figure 4.113), flexural strength (Figure 4.133) and flexural modulus (Figure 4.134).

Figure 4.187 shows the relationship between loss and storage modulus. The dashed line in the Figure represents $G''=G'$. It is seen that elastomer E-MA-GMA is more elastic than polyamide-6 and nanocomposites, since it is near the right side of the equi-moduli line. Loss moduli of polyamide-6 based nanocomposites are greater than storage moduli throughout the frequency range. Polyamide-6 is the least elastic, since it is on the very left side of the equi-moduli line. Liquid-like behavior of polyamide-6 turns to pseudo solid-like as it is blended with E-MA-GMA or as it is compounded with the organoclays. Polyamide-6/Cloisite® 30B/E-MA-GMA is the most elastic material among the ternary nanocomposites.

Table 4.26 Storage and Loss Modulus slopes as a function of frequency in double logarithmic scale

Slopes		
	Storage Modulus (G')	Loss Modulus (G'')
Polyamide-6	1.38	0.98
Polyamide-6 + E-MA-GMA	1.24	0.91
Polyamide-6 + Cloisite® 15A	1.14	0.90
Polyamide-6 + Cloisite® 15A + E-MA-GMA	1.35	0.93
Polyamide-6 + Cloisite® 25A	1.10	0.92
Polyamide-6 + Cloisite® 25A + E-MA-GMA	1.35	0.93
Polyamide-6 + Cloisite® 30B	1.20	0.93
Polyamide-6 + Cloisite® 30B + E-MA-GMA	1.16	0.88

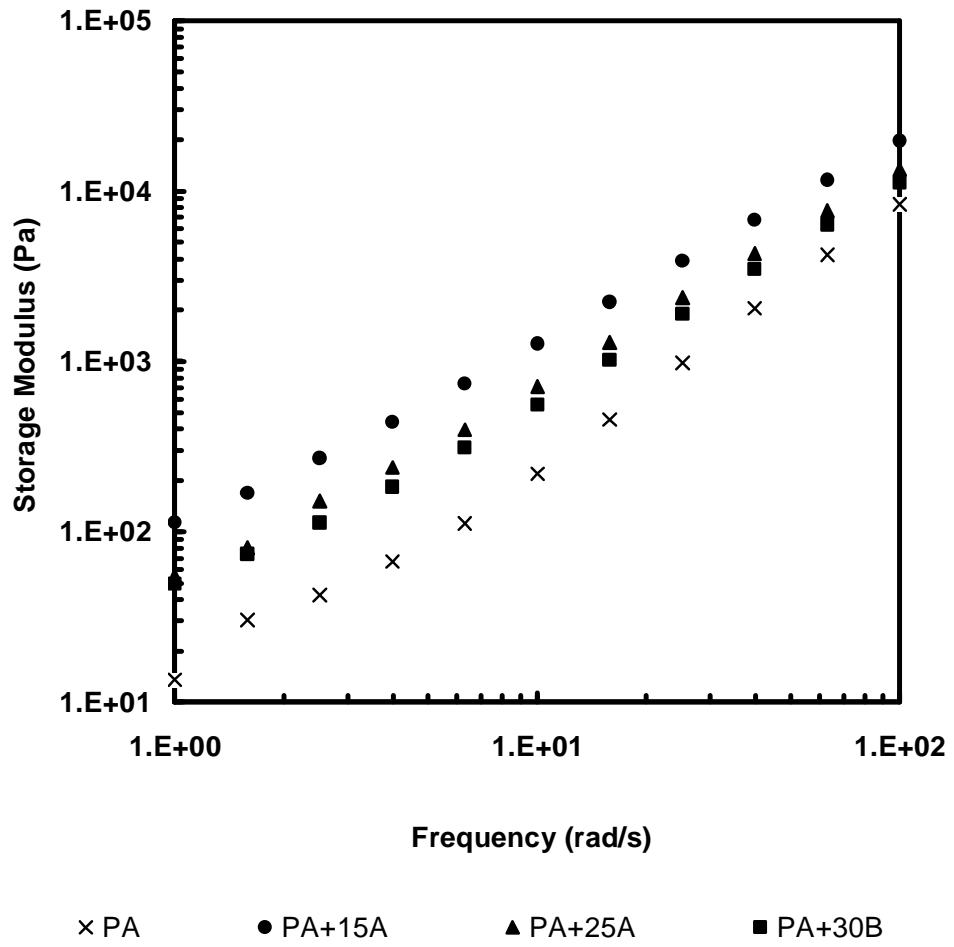


Figure 4.180 Influence of frequency on storage modulus for polyamide-6/organoclay nanocomposites

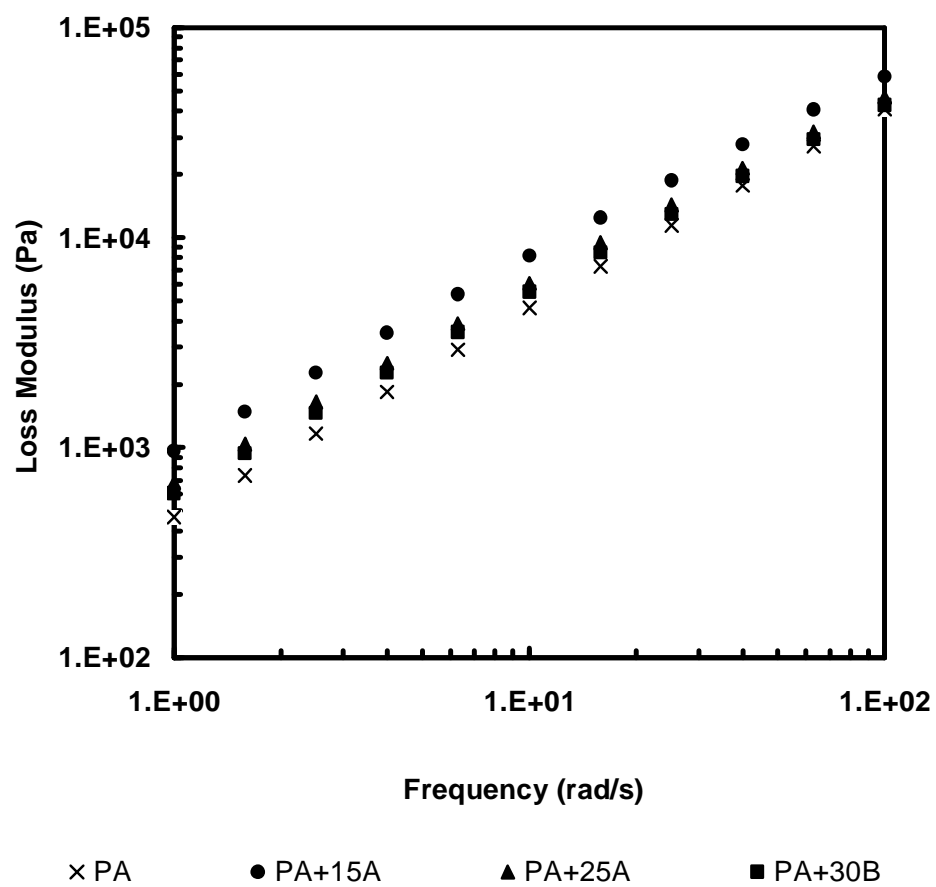


Figure 4.181 Influence of frequency on loss modulus for polyamide-6/organoclay nanocomposites

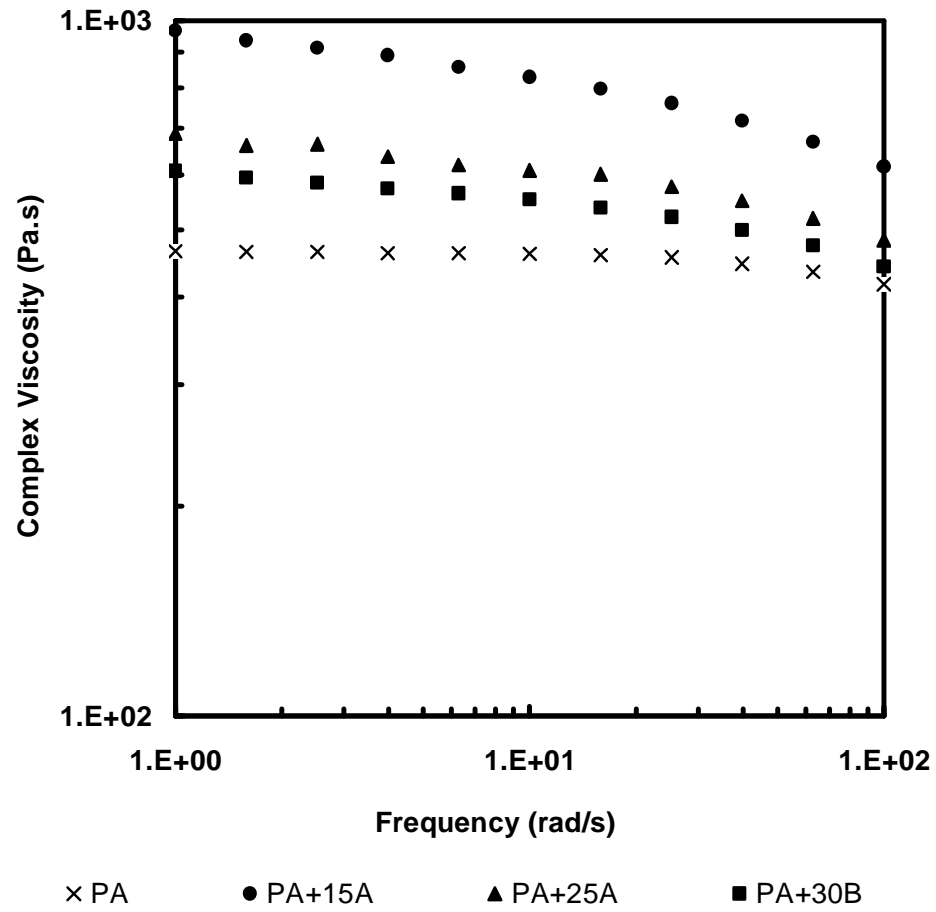


Figure 4.182 Influence of frequency on complex viscosity for polyamide-6/organoclay nanocomposites

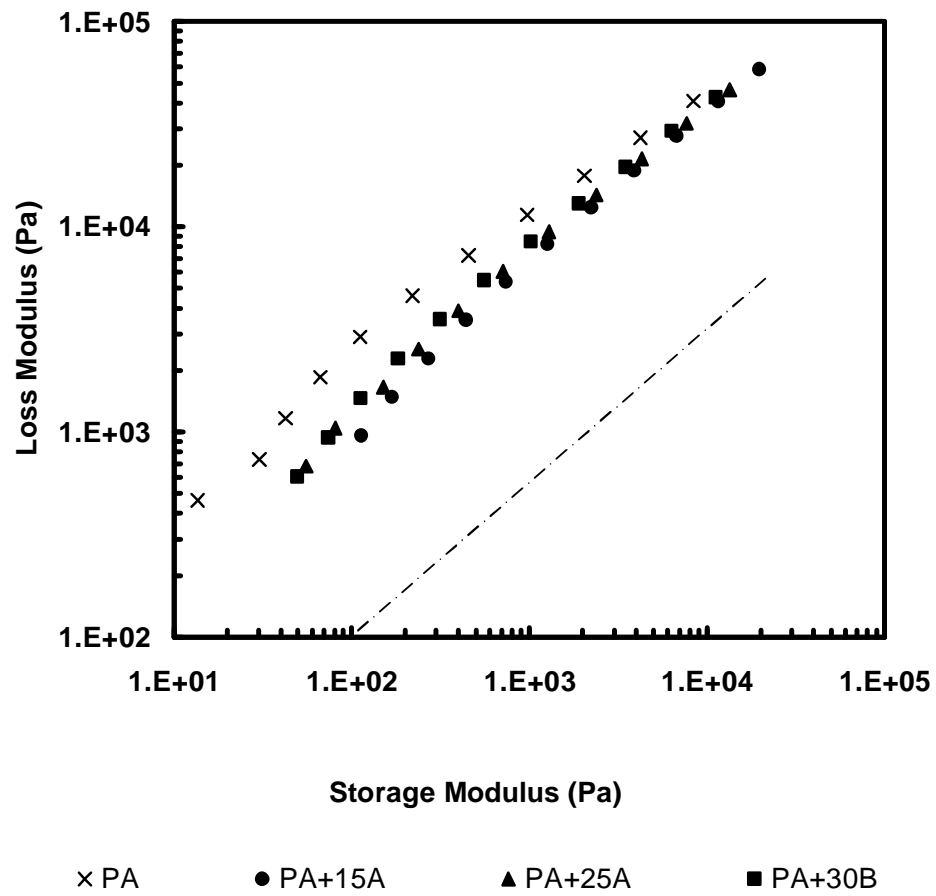


Figure 4.183 Loss modulus as a function of storage modulus for polyamide-6/organoclay nanocomposites

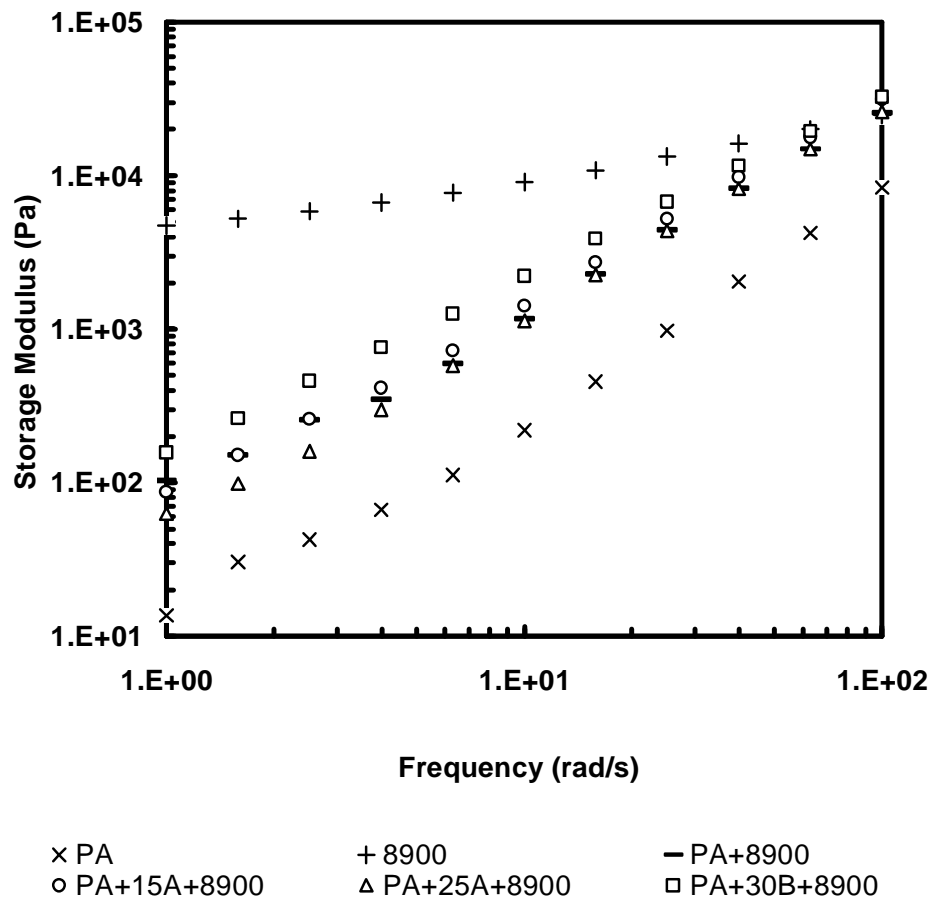


Figure 4.184 Influence of frequency on storage modulus for polyamide-6/organoclay/E-MA-GMA nanocomposites

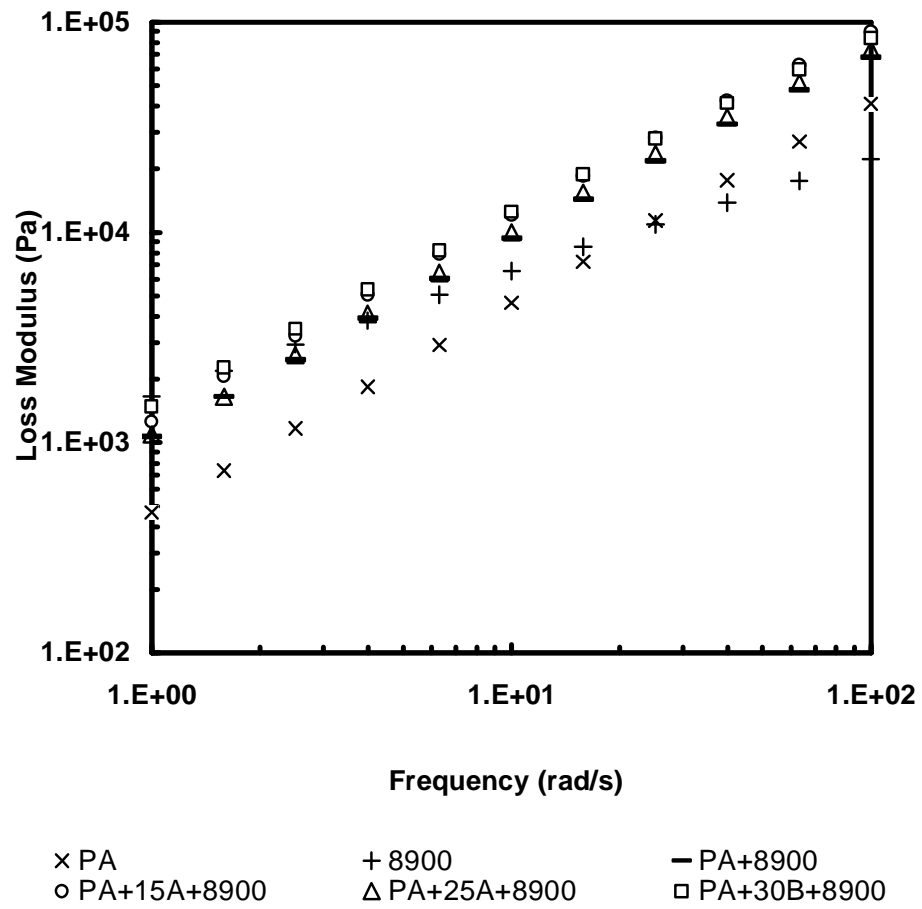


Figure 4.185 Influence of frequency on loss modulus for polyamide-6/organoclay/E-MA-GMA nanocomposites

CHAPTER 5

CONCLUSIONS

Polyamide-6/Elastomer Blends

All the elastomers have the reaction capability with polyamide-6. After compounding, the FTIR-ATR spectra of polyamide-6/E-BA-MAH blend show typical bands of imide group at 1770 cm^{-1} , corresponding to imide carbonyl asymmetric stretching. FTIR spectra of polyamide-6/E-GMA and polyamide-6/E-MA-GMA blends show that absorption band for ring vibration of oxirane group at 910 cm^{-1} disappears after melt mixing.

SEM micrographs of the binary blends show two-phase, particle-in-matrix morphology. As the elastomer amount increases, elastomeric domain size decreases in polyamide-6/E-BA-MAH blends, since reaction between MAH and amine end groups through imidization reduces interfacial tension and retards particle coalescence. However, elastomeric domain sizes in polyamide-6/E-GMA and polyamide-6/E-MA-GMA binary blends increase, as the elastomer amount increases. GMA can react with both amine and acid ends of polyamide-6, which may lead to some crosslinking and inhibit elastomeric domain breakdown during compounding. MAH based elastomer domains are around 50-60 nm and much smaller than the GMA based elastomer domains.

The MFI results show that for the binary polyamide-6/elastomer blends, MFI of polyamide-6 decreases (viscosity increases) upon addition of elastomer and as the amount of elastomer increases, MFI of blends decrease.

The crystallinity of the polyamide-6 decreases slightly in the presence of elastomers, owing to the difficulties in polymer chain arrangement and restricted movement by the branched chains which are formed by the reactions between the functional groups of the elastomers and polyamide-6.

In blends and ternary nanocomposites, E-BA-MAH is the most effective elastomer in terms of toughening, since it has butyl acrylate and maleic anhydride groups. On the other hand, polyamide-6/E-BA-MAH blends have lower impact strength than E-GMA and E-MA-GMA containing blends, since the size of elastomeric domains is too small in polyamide-6/E-BA-MAH blends.

In polyamide-6/elastomer blends, tensile and flexural strength decrease as the elastomer content increases, due to the dilution effect. Young's Modulus show no significant change upon addition of E-GMA and E-MA-GMA, since the decrease caused by the low modulus elastomer may be balanced by the chain extension/branching reactions that would result in high molecular weight copolymer. Flexural modulus decreases in the presence of all elastomers. DMA analyses show that, storage moduli of polyamide-6/elastomer blends are lower than pure polyamide-6, and binary and ternary nanocomposites, owing to the low stiffness of the elastomers.

In the melt state, polyamide-6 based blends and nanocomposites reveal Newtonian behavior. Incorporation of E-MA-GMA elastomer increase the complex viscosity of unfilled polyamide-6 and binary nanocomposites, owing to the reactions mentioned.

Polyamide-6/Organoclay Binary Nanocomposites

Original d_{001} d-spacing of organoclay Cloisite® 15A is not significantly changed in binary as well as ternary nanocomposite systems, whereas d_{002} peak is shifted to lower angles when organoclay 15A is mixed with polymers indicating a few polymer chains are intercalated between the clay layers. TEM analysis show that nanocomposites with Cloisite® 15A contain small fraction of dispersed features

involving one or two layered silicate layers, as well as a large fraction of intercalated multi-layered clay platelet stacks. TEM figures indicate the presence of both intercalated structures and delaminated platelets, while XRD results suggest only a low degree of intercalation.

Among the organoclays used, Cloisite® 30B is the most compatible organoclay with polyamide-6. XRD and TEM analysis reveal this phenomenon, since the % increase in d-spacing is highest in the nanocomposites containing organoclay 30B, and clay layers are uniformly dispersed and exfoliated in the polyamide-6 matrix. High degree of dispersion of Cloisite® 30B in nanocomposites can be attributed to the existence of reaction between the hydroxyl group of Cloisite 30B and the carboxyl group of polyamide-6, as well as to hydrogen bonding between the surfaces of the two.

Addition of Cloisite® 15A to polyamide-6 decreases the MFI of binary nanocomposites due to large clusters formed by the organoclay, whereas the addition of Cloisite® 25A or 30B increases the MFI of binary nanocomposites due to the higher clay platelet alignment and small particle sizes.

DSC analysis show that crystallinity decreases slightly in the presence of Cloisite® 25A and Cloisite® 30B organoclays. According to DMA analysis the intensity of loss tangent peak increases in nanocomposites in comparison to unfilled polyamide-6. Nucleation effect of organoclays may be counteracted by the clay particles, since crystal growth can be terminated by clay particles.

Tensile strength increases in binary polyamide-6/organoclay nanocomposites with the addition of Cloisite® 25A and Cloisite® 30B. The increase in d-spacing of these organoclays results in high contact surface area between the organoclay and the polymer matrix. Thus, Young's and flexural modulus and toughness of these binary nanocomposites increase with respect to unfilled polyamide-6. All the organoclays increase the elongation at break and toughness of polyamide-6 by acting as crack stoppers.

In DMA analysis, especially at lower temperatures, nanocomposites with Cloisite® 30B exhibit higher storage and loss modulus than the other

nanocomposites and pure polyamide-6. In the rubbery region, reinforcing effect of organoclay increases with decreasing surface hydrophobicity, i.e. polymer/organoclay compatibility.

In the melt state, the increase in storage modulus, loss modulus, and complex viscosity are higher in binary polyamide-6/Cloisite® 15A nanocomposites than in polyamide-6/Cloisite® 25A and polyamide-6/Cloisite® 30B nanocomposites, owing to high organoclay surface-surface interactions.

Polyamide-6/Organoclay/Elastomer Ternary Nanocomposites

TEM micrographs and XRD data show that the addition of elastomeric material hardly alters the organoclay dispersibility in the nanocomposites. Since the interfacial tension between the matrix and the dispersed phase might be changed in the presence of organoclay, elastomer domain sizes are larger in nanocomposites than their corresponding polyamide-6/elastomer blends. SEM analysis show that interparticle distance of elastomeric domains seems to be closer in 15A and 25A containing nanocomposites than in 30B containing nanocomposite.

Generally, tensile and flexural strength, Young's and flexural modulus and elongation at break decrease when polyamide-6/organoclay binary nanocomposites are melt blended with the elastomer to form polyamide-6/organoclay/elastomer ternary nanocomposites. Organoclay may reduce the compatibility of elastomer and polyamide-6, resulting in lack of adhesion between the phases. Generally, polyamide-6/Cloisite® 15/elastomer nanocomposites have higher tensile, flexural and impact strength and Young's and flexural modulus than 25A and 30B containing ternary nanocomposites.

Polyamide-6/Cloisite® 30B/E-MA-GMA nanocomposite has the highest Young's and flexural modulus, flexural strength, complex viscosity and storage modulus in the melt state among the ternary nanocomposites, since there is high interaction between polyamide-6, E-MA-GMA and the –OH groups of clay surfactant. Methyl

acrylate groups also increase the interaction between polyamide-6 and elastomer since the same situation is not observed in polyamide-6/Cloisite® 30B/E-GMA nanocomposites which do not contain methyl acrylate.

In ternary nanocomposites, polyamide-6/Cloisite® 15A/E-GMA, polyamide-6/Cloisite® 30B/E-GMA, polyamide-6/Cloisite® 15A/E-BA-MAH and polyamide-6/Cloisite® 25A/E-BA-MAH nanocomposites show equal or higher toughness values than pure polyamide-6. Thus, different addition orders of the components are studied for these nanocomposites.

Generally, All-S mixing sequence gives the highest tensile and flexural strength, Young's modulus and elongation at break. Variations in mixing sequence do not result in significant changes in crystallinity. The crystallinity in polyamide-6/Cloisite® 30B/E-GMA nanocomposites is lower than the crystallinity of polyamide-6/Cloisite® 15A/E-GMA nanocomposites, due to the complications in polymer chain arrangement that result from the interactions between hydroxyl groups on Cloisite® 30B surface and GMA functional group.

REFERENCES

Ahn Y.C. and Paul D.R., 2006. Rubber toughening of nylon 6 nanocomposites, *Polymer*, 47, 2830-2838.

Akkapeddi M. K., 2001. *Reactive Polymer Blending*, Edited by: Baker W., Scott C. and Hu G. H., Hanser Gardner Publications, Inc., USA.

Alexandre M. and Dubois P., 2000. Polymer-layered silicate nanocomposites: Preparation, properties and uses of a new class of materials, *Materials Science and Engineering*, 28, 1-63.

Araújo E. M., Hage E. Jr. and Carvalho A. J. F., 2003. Effect of Compatibilizer in Acrylonitrile-Butadiene-Styrene toughened Nylon 6 blends: Ductile–Brittle Transition Temperature, *Journal of Applied Polymer Science*, 90, 2643–2647.

ASTM D638-03, 2004. *Standart Test Methods for Tensile Properties of Plastics*, Annual Book of ASTM Standards, 08.01, Philadelphia, PA.

ASTM D790-03, 2003. *Standart Test Methods for Flexural Properties of Unreinforced and Reinforced Plastics and Electrical Insulating Materials*, Annual Book of ASTM Standards, 08.01, Philadelphia, PA.

ASTM D1238-04c, 2004. *Standard Test Method for Melt Flow Rates of Thermoplastics by Extrusion Plastometer*, Annual Book of ASTM Standards, 08.01, Philadelphia, PA.

Balazs A.C., Singh C. and Zhulina E., 1998. Modeling the interactions between polymers and clay surfaces through self-consistent field theory, *Macromolecules*, 31, 8370-8381.

Baldi F., Bignotti F., Tieghi G., and Ricco T., 2006. Rubber toughening of polyamide-6 /organoclay nanocomposites obtained by melt blending, *Journal of Applied Polymer Science*, 99, 3406-3416.

Barnes H. A., Hutton J. F. and Walters K., 1989. An Introduction to Rheology, Elsevier Science B. V., Netherlands.

Bhattacharyya A. R. and Pötschke P., 2006. Mechanical properties and morphology of melt-mixed PA6/SWNT composites: effect of reactive coupling, *Macromolecular Symposia*, 233, 161-169.

Billmeyer W. F., 1984. *Textbook of Polymer Science*, John-Wiley & Sons, Toronto

Borggreve R. J. M., Gaymans R. J. and Eichenwald H. M., 1989. Impact behaviour of nylon-rubber blends: 6. Influence of structure on voiding processes; toughening mechanism, *Polymer*, 30, 78-83.

Borggreve R. J. M., Gaymans R. J., Schuijjer J. and Ingen Housz J. F., 1987. Brittle-tough transition in nylon-rubber blends: effect of rubber concentration and particle size, *Polymer*, 28, 1489-1496.

Bureau M. N., Denault J., Cole K. C. and Enright G. D., 2002. The Role of Crystallinity and Reinforcement in the Mechanical Behavior of Polyamide-6/Clay Nanocomposites, *Polymer Engineering and Science*, 42, 1897-1906.

Bucknall C. B., Heather P.S. and Lazzeri A. J., 1989. Rubber toughening of plastics Part 12 Deformation mechanisms in toughened nylon 6,6, *Journal of Material Science*, 16, 2255-2261.

Callister W., 1997. *Materials Science and Engineering, An Introduction*, Fourth Edition, John-Wiley & Sons, USA.

Campbell J. R., Hobbs S. Y., Shea T. J. and Watkins V. H., 1990. Poly(Phenylene oxide)/polyamide blends via reactive extrusion, *Polymer Engineering and Science*, 30, 1056-1062.

Campbell D., Pethrick R. A. and White J. R., 2000. *Polymer Characterization, Physical Techniques*, Second Edition, Stanley Thornes (Publishers) Ltd., United Kingdom.

Carone Jr E., Kopcak U., Gonçalves M.C., Nunes S.P., 2000. In situ compatibilization of polyamide 6/natural rubber blends with maleic anhydride, *Polymer*, 41, 5929-5935.

Cecere A., Greco R., Ragosta G., Scarinzi G. and Tagliatela A., 1990. Rubber toughened polybutylene terephthalate: influence of processing on morphology and impact properties, *Polymer*, 31, 1239-1244.

Chavarria F. and Paul D. R., 2004. Comparison of nanocomposites based on nylon 6 and nylon 66, *Polymer*, 45, 8501-8515.

Chiono V., Filippi S., Yordanov H., Minkova L. and Magagnini P., 2003. Reactive compatibilizer precursors for LDPE/PA6 blends. III: ethylene-glycidylmethacrylate copolymer, *Polymer*, 44, 2423-2432.

Chiu F.C., Lai S. M., Chen Y. L., and Lee T. H., 2005. Investigation on the polyamide 6/organoclay nanocomposites with or without a maleated polyolefin elastomer as a toughener, *Polymer*, 46, 11600-11609.

Cho J.W. and Paul D.R., 2001. Nylon 6 nanocomposites by melt compounding, *Polymer*, 42, 1083–1094.

Chow W. S., Mohd Ishak Z. A., Ishiaku U. S., Karger-Kocsis J. and Apostolov A. A., 2004. The effect of organoclay on the mechanical properties and morphology of injection-molded polyamide 6/polypropylene nanocomposites, *Journal of Applied Polymer Science*, 91, 175-189.

Chow W. S., Mohd Ishak Z. A., Karger-Kocsis J., Apostolov A. A. and Ishiaku U. S., 2003. Compatibilizing effect of maleated polypropylene on the mechanical properties and morphology of injection molded polyamide 6/polypropylene/organoclay nanocomposites, *Polymer*, 44, 7427-7440.

Chow W.S., Mohd Ishak Z. A. and Karger-Kocsis J., 2005. Morphological and Rheological Properties of Polyamide 6/Poly(propylene)/Organoclay Nanocomposites, *Macromolecular Materials and Engineering*, 290, 122-127.

Cimmino S., Coppola F., D'Orazio L., Greco R., Maglio G., Malinconico M., Mancarella C., Martuscelli E. and Ragosta G., 1986. Ternary nylon-6/rubber/modified rubber blends: Effect of the mixing procedure on morphology, mechanical and impact properties, *Polymer*, 27, 1874-1884.

Contreras V., Cafiero M, Da Silva S., Rosales C., Perera R. and Matos M., 2006. Characterization and tensile properties of ternary blends with PA-6 nanocomposites, *Polymer Engineering and Science*, 46, 1111-1120.

Daniel I. and Ishai O., 1994. *Engineering Mechanics of Composite Materials*, Oxford University Press Inc., USA.

Davis R. D., Gilman J. W. and VanderHart D. L., 2003. Processing degradation of polyamide 6/montmorillonite clay nanocomposites and clay organic modifier, *Polymer Degradation and Stability*, 79, 111-121.

Dennis H. R., Hunter D. L., Chang D., Kim S., White J. L., Cho J. W. and Paul D. R., 2001. Effect of melt processing conditions on the extent of exfoliation in organoclay-based nanocomposites, *Polymer*, 42, 9513-9522.

Devaux E., Bourbigot S. and El Achari A., 2002. Crystallization behavior of PA-6 clay nanocomposite hybrid, *Journal of Applied Polymer Science*, 86, 2416-2423.

Dong W., Zhang X., Liu Y., Gui H., Wang Q., Gao J., Song Z., Lai J., Huang F. and Qiao J., 2006. Effect of rubber on properties of nylon-6/unmodified clay/rubber blends, *European Polymer Journal*, 42, 2515-2522.

Duffy J. V., Hui E. and Hartmann B., 1987. Reaction kinetics for hindered amine/epoxides by DSC, *Journal of Applied Polymer Science*, 33, 2959-2964.

Fornes T. D. and Paul D. R., 2003. Crystallization behavior of nylon 6 nanocomposites, *Polymer*, 44, 3945-3961.

Finnigan B., Martin D., Halley P., Truss R., and Campell K., 2005. Morphology and Properties of Thermoplastic Polyurethane Nanocomposites Incorporating Hydrophobic Layered Silicates, *Journal of Applied Polymer Science*, 97, 300-309.

Fornes T.D., Yoon P.J., Hunter D.L., Keskkula H. and Paul D.R., 2002. Effect of organoclay structure on nylon 6 nanocomposite morphology and properties, *Polymer*, 43, 5915–5933.

Fornes T.D., Yoon P.J., Keskkula H. and Paul D.R., 2001. Nylon 6 Nanocomposites: the effect of matrix molecular weight, *Polymer*, 42, 9929-9940.

Giannelis E.P., 1996. Polymer Layered Silicate Nanocomposites, Review, *Advanced Materials*, 8, 29-35.

Glover D. J., Duffy J. V. and Hartmann B., 1988. Steric hindrance in the amine-epoxide reaction, *Journal of Polymer Science Part A: Polymer Chemistry*, 26, 79-87.

González I, Eguiazábal J.I. and Nazábal J., 2006. Rubber-toughened polyamide 6/clay nanocomposites, *Composites Science and Technology*, 66, 1833-1843.

González I, Eguiazábal J.I. and Nazábal J., 2006. Nanocomposites based on a polyamide 6/maleated styrene-butylene-co-ethylene-styrene blend: Effects of clay loading on morphology and mechanical properties, *European Polymer Journal*, 42, 2905-2913.

González-Montiel A., Keskkula H. and Paul D. R., 1995. Impact-modified nylon 6/polypropylene blends: 1. Morphology-property relationships, *Polymer*, 36, 4587-4603.

Greco R., Malinconico M., Martuscelli E., Ragosta E. and Scarinzi G., 1987. Role of degree of grafting of functionalized ethylene-propylene rubber on the properties of rubber-modified polyamide-6, *Polymer*, 28, 1185-1189.

Grim R. E., 1968. *Clay Mineralogy*, Second Edition, McGraw-Hill Inc., USA

Homminga D., Goderis B., Hoffman S., Reynaers H. and Groeninckx G., 2005. Influence of shear flow on the preparation of polymer layered silicate nanocomposites, *Polymer*, 46, 9941-9954.

Homminga D., Goderis B., Mathot V., and Groeninckx G., 2006. Crystallization behavior of polymer/montmorillonite nanocomposites. Part III. Polyamide-6/montmorillonite nanocomposites, influence of matrix molecular weight, and of montmorillonite type and concentration, *Polymer*, 47, 1630-1639.

Hoffmann U., Endell K., Wilm D., 1933. Kristallstruktur und Quellung von Montmorillonite, *Zeitschrift Fuer Kristallographie*, 86, 340-348.

Hoffmann B., Kressler J., Stöppelmann G., Friedrich C. and Kim G. M., 2000. Rheology of nanocomposites based on layered silicates and polyamide-12, *Colloid and Polymer Science*, 278, 629-636.

Hotta S. and Paul D. R., 2004. Nanocomposites formed from linear low density polyethylene and organoclays, *Polymer*, 45, 7639-7654.

Huang X., Lewis S., Brittain W. J. and Vaia R. A., 2000. Synthesis of Polycarbonate-Layered Silicate Nanocomposites via Cyclic Oligomers, *Macromolecules*, 33, 2000-2004.

Hyun Y. H., Lim S. T., Choi H. J. and Jhon M. S., 2001. Rheology of Poly (ethylene oxide)/Organoclay Nanocomposites, *Macromolecules*, 34, 8084-8093.

Inoue M, 1963. Studies on crystallization of high polymers by differential thermal analysis, *Journal of Polymer Science Part A: General Papers*, 1, 2697-2709.

Isik I., Yilmazer U. and Bayram G., 2003. Impact modified epoxy/montmorillonite nanocomposites: synthesis and characterization, *Polymer*, 44, 6371-6377.

ISO 179-2:1997. Plastics-Determination of Charpy impact properties-Part 2: Instrumented impact test, International Organization for Standardization

Jiang W., Liu C. H., Wang Z. G., An L. J., Liang H. J., Jiang B.Z., Wang X. H. and Zhang H. X., 1998. Brittle-tough transition in PP/EPDM blends: effects of interparticle distance and temperature, *Polymer*, 39, 3285-3288.

Kalal J., Svec F. and Marousek V., 1974. Reaction of epoxide groups of glycidyl methacrylate copolymers, *Journal of Polymer Science Part C: Polymer Symposia*, 47, 155-166.

Karayannidis G.P., Bikiaris D.N., Papageorgiou G.Z. and Bakirtzis V., 2002. Rubber toughening of glass fiber reinforced nylon-6,6 with functionalized block copolymer SEBS-g-MA, *Advances in Polymer Technology*, 21, 153-163.

Kayano Y., Keskkula H. and Paul D. R., 1997. Evaluation of the fracture behaviour of nylon 6/SEBS-g-MA blends, *Polymer*, 38, 1885-1902.

Kelnar I., Kotek J., Kaprálková L., Hromádková J. and Kratochvíl J., 2006. Effect of elastomer type and functionality on the behavior of toughened polyamide nanocomposites, *Journal of Applied Polymer Science*, 100, 1571-1576.

Kelnar I., Kotek J., Kaprálková L., Hromádková J. and Munteanu B. S., 2005. Polyamide Nanocomposites with Improved Toughness, *Journal of Applied Polymer Science*, 96, 288-293.

Khatua B.B., Lee D.J., Kim H.Y. and Kim J.K., 2004. Effect of organoclay platelets on morphology of nylon-6 and poly(ethylene-ran-propylene) rubber blends, *Macromolecules*, 37, 2454-2459.

Kim G. M., Lee D. H., Hoffmann B., Kressler J. and Stöppelmann G., 2001. Influence of nanofillers on the deformation process in layered silicate/polyamide-12 nanocomposites, *Polymer*, 42, 1095-1100.

Kim G.M., Michler G. H., Rösch J. and Mülhaupt R., 1998. Micromechanical deformation processes in toughened PP/PA/SEBS-g-MA blends prepared by reactive processing, *Acta Polymerica*, 49, 88-95.

Kirk-Othmer Encyclopedia of Chemical Technology, 2001, Fifth Edition, John Wiley & Sons, Inc., USA.

Kojima Y., Usuki A., Kawasumi M., Okada A., Kurauchi T., and Kamigaito O., 1993. Synthesis of nylon 6-clay hybrid by montmorillonite intercalated with ϵ -caprolactam, *Journal of Polymer Science Part A: Polymer Chemistry*, 31, 983-986.

Kojima Y., Usuki A., Kawasumi M., Okada A., Kurauchi T., Kamigaito O. and Kaji K., 1994. Fine structure of nylon-6-clay hybrid, *Journal of Polymer Science Part B: Polymer Physics*, 32, 625-630.

Koulouri E.G. Georgaki A. X. and Kallitsis J. K., 1997. Reactive compatibilization of aliphatic polyamides with functionalized polyethylenes, *Polymer*, 38, 4185-4192.

Kornmann, X., 2001. PhD Thesis, Synthesis and characterization of thermoset-clay nanocomposites, Division of Polymer Engineering, Luleå University of Technology: Luleå, Sweden

Krishnamoorti R. and Giannelis E. P., 1997. Rheology of End-Tethered Polymer Layered Silicate Nanocomposites, *Macromolecules*, 30, 4097-4102.

Krishnamoorti R., Vaia R. and Giannelis E. P., 1996. Structure and Dynamics of Polymer-Layered Silicate Nanocomposites, *Chemistry of Materials*, 8, 1728-1734.

Krishnamoorti R. and Yurekli K., 2001. Rheology of polymer layered silicate nanocomposites, *Current Opinion in Colloid and Interface Science*, 6, 464-470.

Kudva R. A., Keskkula H. and Paul D.R., 1998, Compatibilization of nylon 6/ABS blends using glycidyl methacrylate/methyl methacrylate copolymers, *Polymer*, 39, 2447-2460.

Kudva R. A., Keskkula H., Paul D. R., 1999. Morphology and mechanical properties of compatibilized nylon 6/polyethylene blends, *Polymer* 40, 6003–6021.

Lan T., Kaviratna P. D. and Pinnavaia T. J., 1995. Mechanism of Clay Tactoid Exfoliation in Epoxy-Clay Nanocomposites, *Chemistry of Materials*, 7, 2144-2150.

Lee M.H., Dan C.H., Kim J.H., Cha J., Kim S., Hwang Y. and Lee C.H., 2005. Effect of clay on the morphology and properties of PMMA/poly(styrene-co-acrylonitrile)/clay nanocomposites prepared by melt mixing, *Polymer*, 47, 4359-4369.

Lee K. M. and Han C. D., 2003. Rheology of Organoclay Nanocomposites: Effects of Polymer Matrix/Organoclay Compatibility and the Gallery Distance of Organoclay, *Macromolecules*, 36, 7165-7178.

Li J., Zhou C., Wang G., Yu W., Tao Y. and Liu Q., 2003. Preparation and linear rheological behavior of polypropylene/MMT nanocomposites, *Polymer Composites*, 24, 323-331.

Liu L., Qi Z. and Zhu X., 1999. Studies on Nylon 6/Clay Nanocomposites by Melt-Intercalation Process, *Journal of Applied Polymer Science*, 71, 1133–1138.

Liu X., Wu Q., Berglund L.A., Fan J. and Qi Z., 2001. Polyamide 6-clay nanocomposites/polypropylene-grafted-maleic anhydride alloys, *Polymer*, 42, 8235-8239.

Liu Z., Zhu X., Wu L., Li Y., Qi Z., Choy C. and Wang F., 2001. Effects of interfacial adhesion on the rubber toughening of poly(vinyl chloride) Part 1. Impact Tests, *Polymer*, 42, 737-746.

Loyens W. and Groeninckx G., 2002. Phase morphology development in reactively compatibilised polyethylene terephthalate/elastomer blends, *Macromolecular Chemistry and Physics*, 203, 1702-1714.

MacKnight W. J., Lenz R. W., Musto P.V. and Somani R.J., 1985. Binary alloys of Nylon 6 and ethylene-methacrylic acid copolymers: Morphological, Thermal and Mechanical analysis, *Polymer Engineering and Science*, 25, 1124-1134.

Majumdar B., Paul D.R. and Oshinski A.J., 1997. Evolution of morphology in compatibilized vs uncompatibilized polyamide blends, *Polymer*, 38, 1787-1808.

Majumdar B, Keskkula H. and Paul D. R., 1994. Deformation mechanisms in nylon 6/ABS blends, *Journal of Polymer Science Part B: Polymer Physics*, 32, 2127-2133.

Mark H. F. (Ed), 2003. *Encyclopedia of Polymer Science and Technology*, Third Edition, John Wiley & Sons, Inc., USA.

Martuscelli E., Riva F., Sellitti C. and Silvestre C., 1985. Crystallization, morphology, structure and thermal behaviour of nylon-6/rubber blends, *Polymer*, 26, 270-282.

Matthews L. F. and Rawlings D. R., 1996. *Composite Materials: Engineering and Science*, First Edition, Chapman & Hall Inc., Oxford.

Mehrabzadeh M., and Kamal M., 2004. Melt Processing of PA-66/Clay HDPE/Clay and HDPE/PA66/Clay, *Polymer Engineering and Science*, 44, 1151-1161.

Minkova L., Yordanov H., and Filippi S., 2002. Characterization of blends of LDPE and PA6 with functionalized polyethylenes, *Polymer*, 43, 6195-6204.

Mohd Ishak Z. A. and Berry J, P., 1994. Hygrothermal aging studies of short carbon fiber reinforced nylon 6.6, *Journal of Applied Polymer Science*, 51, 2145-2155.

Morgan A. B. and Harris J. D., 2003. Effects of organoclay Soxhlet extraction on mechanical properties, flammability properties and organoclay dispersion of polypropylene nanocomposites, *Polymer*, 44, 2313-2320.

Nielsen L. E. and Landel R. F., 1994. *Mechanical Properties of Polymers and Composites*, 2nd Ed., Marcel Dekker Inc., USA

Ogata N., Kawakage S. and Ogihara T., 1997. Structure and thermal/mechanical properties of poly(ethylene oxide)-clay mineral blends, *Polymer*, 38, 5115-5118.

Oshinski A. J., Keskkula H., and Paul D. R., 1992. Rubber toughening of polyamides with functionalized block copolymers: 1. Nylon-6, *Polymer*, 33, 268-283.

Oshinski A. J., Keskkula H., and Paul D. R., 1996. The role of matrix molecular weight in rubber toughened nylon 6 blends: 1. Morphology, *Polymer*, 37, 4891-4907.

Oshinski A. J., Keskkula H., and Paul D. R., 1996. The role of matrix molecular weight in rubber toughened nylon 6 blends: 2. Room temperature Izod impact toughness, *Polymer*, 37, 4909-4918.

Ramsteiner F. and Heckmann W., 1985. Mode of deformation in rubber-modified polyamide, *Polymer Communications*, 26, 199-200.

Raval H., Devi S., Singh Y.P. and Mehta M. H., 1991. Relationship between morphology and properties of polyamide-6 low-density polyethylene blends: effect of the addition of functionalized low-density polyethylene, *Polymer*, 32, 493-500.

Ray S. S., and Okamoto M., 2003. Polymer/layered silicate nanocomposites: a review from preparation to processing, *Progress in Polymer Science*, 28, 1539-1641

Rosen S., 1982. *Fundamental Principles of Polymeric Materials*, Second Edition, John-Wiley & Sons, USA

Sathe S. N., Rao G. S. S., Rao K. V. and Devi S., 1996. The effect of composition on morphological, thermal, and mechanical properties of polypropylene/nylon-6/polypropylene-g-butyl acrylate blends, *Polymer Engineering and Science*, 36, 2443-2450.

Shah V., 1998. *Handbook of Plastics Testing Technology*, John Wiley & Sons, USA

Shechter L. and Wynstra J., 1956. Glycidyl ether reactions with alcohols, phenols, carboxylic acids, and acid anhydrides, *Industrial Engineering Chemistry*, 48, 86-93.

Shelley J. S., Mather P. T. and DeVries K. L., 2001. Reinforcement and environmental degradation of nylon-6/clay nanocomposites, *Polymer*, 42, 5849-5858.

Simon G. P., 2003. *Polymer Characterization Techniques and Their Application to Blends*, Oxford University Press Inc., New York, USA

Sundararaj U. and Macosko C. W., 1995. Drop Breakup and Coalescence in Polymer Blends, *Macromolecules*, 28, 2647-2657.

Takeda Y., Keskkula H. and Paul D.R., 1992. Effect of polyamide functionality on the morphology and toughness of blends with a functionalized block copolymer, *Polymer*, 33, 3173-3181.

Takeda Y., Keskkula H. and Paul D. R., 1992. Toughening of phase-homogenized mixtures of nylon-6 and poly(m-xylene adipamide) with a functionalized block copolymer, *Polymer*, 33, 3394-3407.

Tedesco A., Krey P. F., Barbosa R. V. and Mauler R. S., 2001. Effect of the type of nylon chain-end on the compatibilization of PP/PP-GMA/nylon 6 blends, *Polymer International*, 51, 105-110.

Thomas S. and Groeninckx G., 1999. Reactive compatibilisation of heterogeneous ethylene propylene rubber (EPM)/nylon 6 blends by the addition of compatibiliser precursor EPM-g-MA, *Polymer*, 40, 5799-5819.

Tjong S. C. and Bao S. P., 2005. Impact fracture toughness of polyamide-6/montmorillonite nanocomposites toughened with a maleated styrene/ethylene butylene/styrene elastomer, *Journal of Polymer Science: Part B: Polymer Physics*, 43, 585-595.

Triacca V. J., Ziaee S., Barlow J. W., Keskkula H. and Paul D. R., 1991. Reactive compatibilization of blends of nylon 6 and ABS materials, *Polymer*, 32, 1401-1413.

Usuki A., Koiwai A., Kojima Y., Kawasumi M., Okada A., Kurauchi T., and Kamigaito O., 1995. Interaction of nylon 6-clay surface and mechanical properties of nylon 6-clay hybrid, *Journal of Applied Polymer Science*, 55, 119-123

Usuki U., Tukigase A. and Kato M., 2002. Preparation and properties of EPDM-clay hybrids, *Polymer*, 43, 2185-2189.

Utracki L. A., 2004. *Clay-Containing Polymeric Nanocomposites*, Volume 1, Rapra Technology Limited, UK

Wang L. Z., 2001. Characterization of Nanophase Materials, Wiley-VCH, Germany.

Wilkinson A. N., Man Z., Stanford J. L., Matikainen P., Clemens M. L., Lees G. C. and Liauw C. M., 2006. Structure and dynamic mechanical properties of melt intercalated polyamide 6-montmorillonite nanocomposites, *Macromolecular Materials and Engineering*, 291, 917-928.

Wu S., 1985. Phase structure and adhesion in polymer blends: A criterion for rubber toughening, *Polymer*, 26, 1855-1863.

Wu S., 1988. Generalized Criterion For Rubber Toughening: The Critical Matrix Ligament Thickness, *Journal of Applied Polymer Science*, 35, 549-561.

www.lotader.com (Arkema Chemicals), fast accessed; May 2007.

www.nanoclay.com (Southern Clay Products), fast accessed; May 2007.

Xanthos M., 2005. Functional Fillers for Plastics, Wiley-VCH, Weinheim, Germany.

Vaia R.A and Giannelis E.P., 1997. Lattice model of polymer melt intercalation in organically-modified layered silicates, *Macromolecules*, 30, 7990-7999.

Vaia R. A., Ishii H. and Giannelis E. P., 1993. Synthesis and properties of two-dimensional nanostructures by direct intercalation of polymer melts in layered silicates *Chemistry of Materials*, 5, 1694-1696.

Vaia R.A., Jandt K.D., Kramer E.J. and Giannelis E.P., 1995. Kinetics of polymer melt intercalation, *Macromolecules*, 28, 8080-8085.

van der Wal A., Nijhof R. and Gaymans R., 1990. Polypropylene–rubber blends: 2. the effect of the rubber content on the deformation and impact behaviour, *Polymer*, 40, 6031-6044.

Velde B., 1992. Introduction to Clay Minerals, Chemistry, Origins, Uses, and Environmental Significance, First Edition, Chapman & Hall Inc., Great Britain

Zanetti M., Lomakin S. and Camino G., 2000. Polymer-layered Silicate nanocomposites, *Macromolecular Materials and Engineering*, 279, 1-9.

APPENDIX A

DSC ANALYSIS

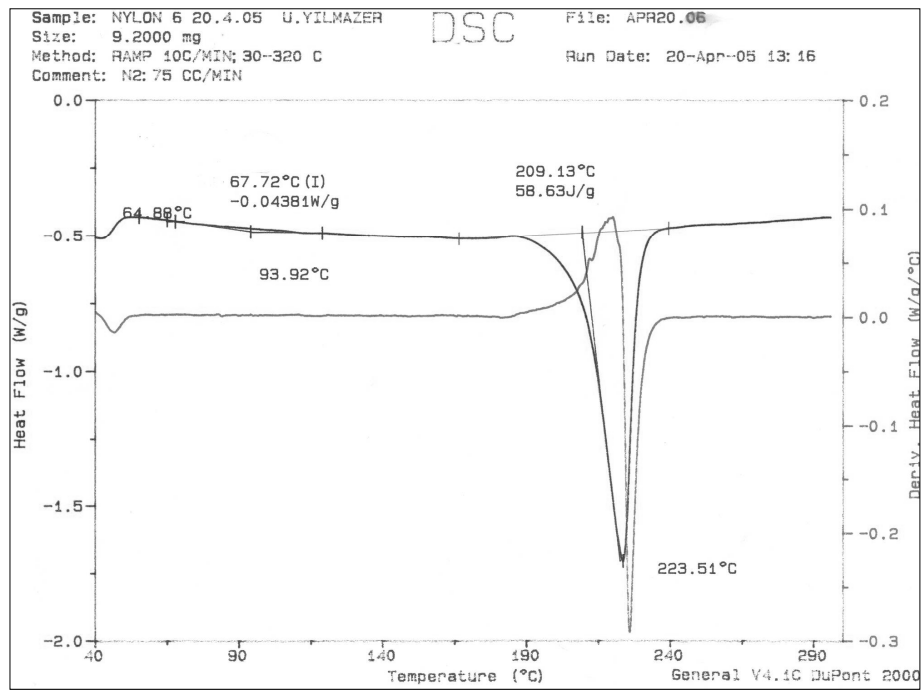


Figure A.1 DSC thermogram of polyamide-6

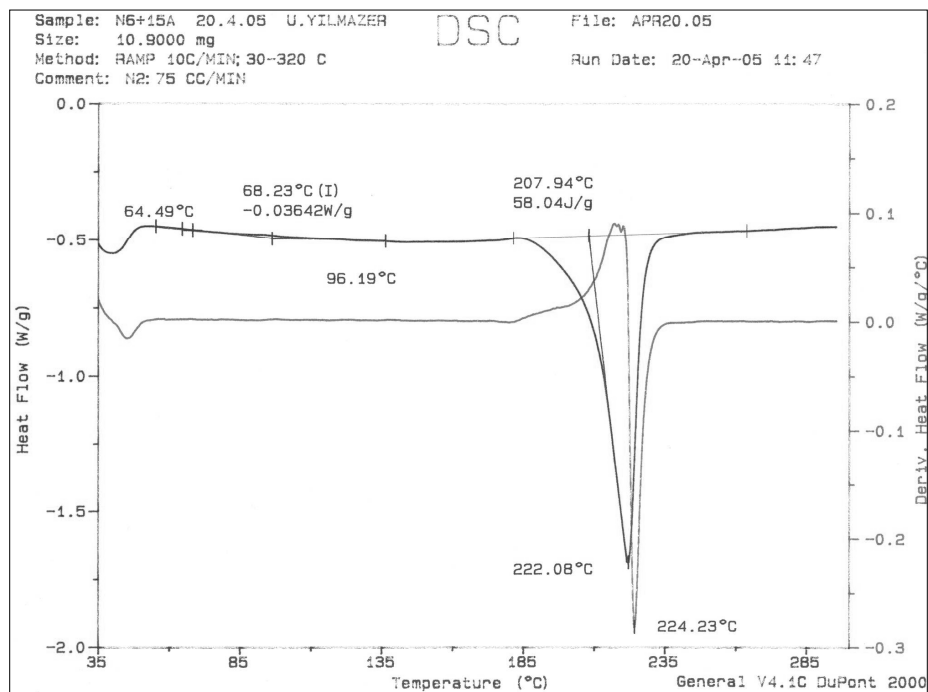


Figure A.2 DSC thermogram of polyamide-6/Cloisite® 15A nanocomposite

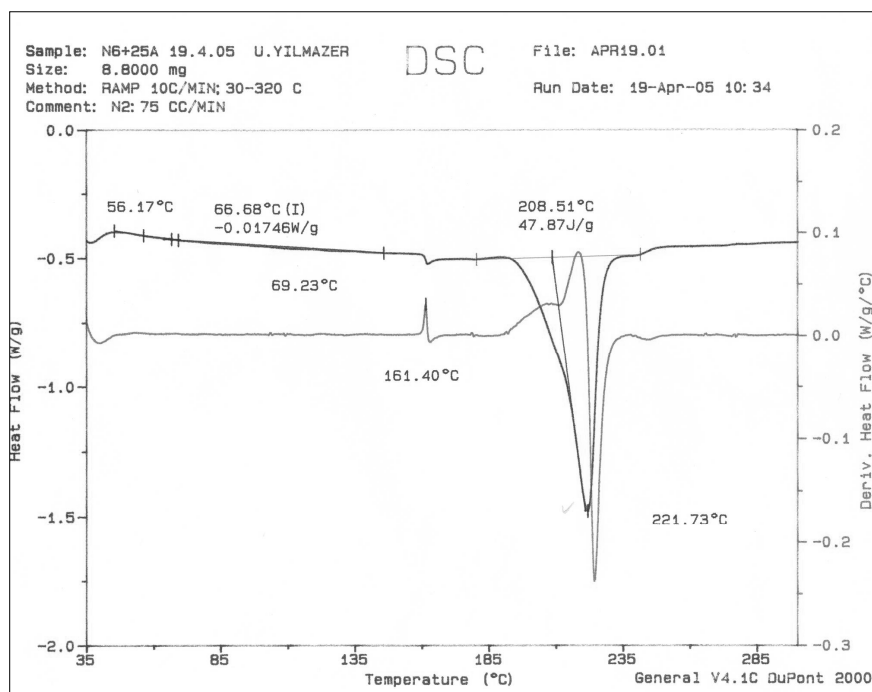


Figure A.3 DSC thermogram of polyamide-6/Cloisite® 25A nanocomposite

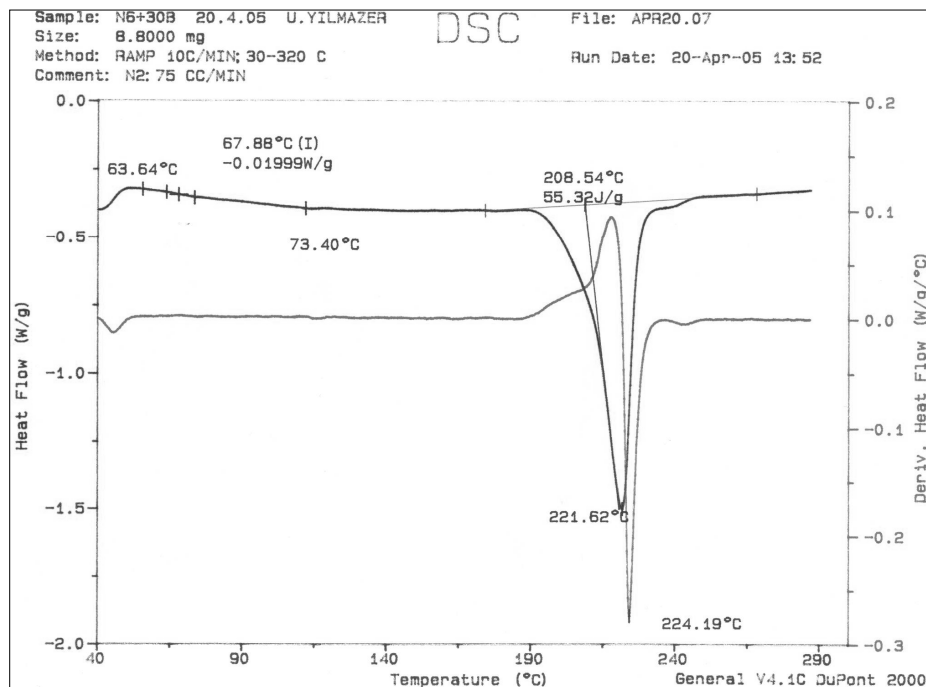


Figure A.4 DSC thermogram of polyamide-6/Cloisite® 30B nanocomposite

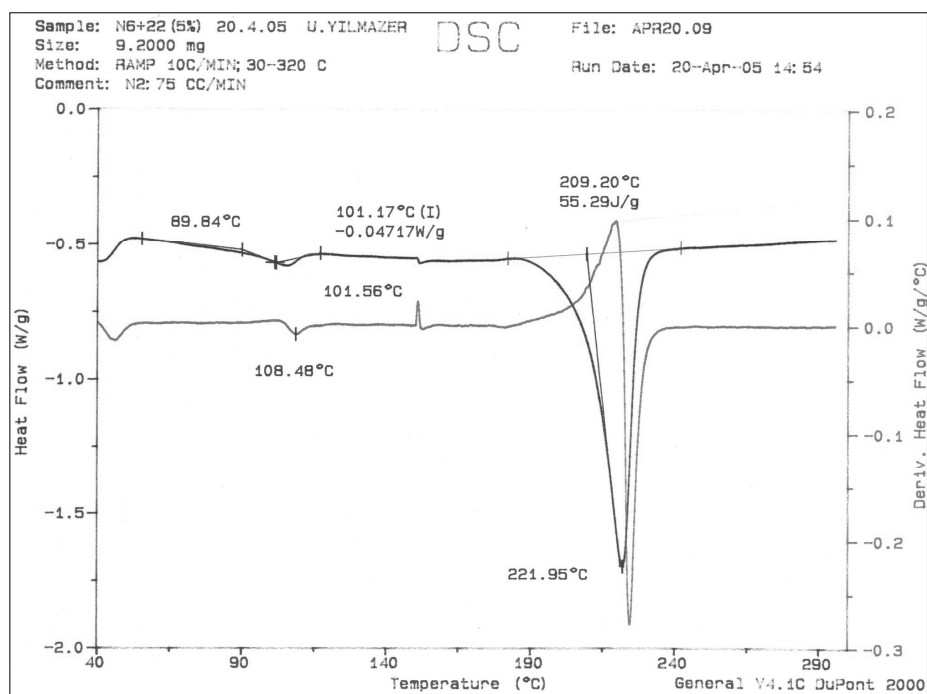


Figure A.5 DSC thermogram of polyamide-6/E-BA-MAH (5 wt %) blend

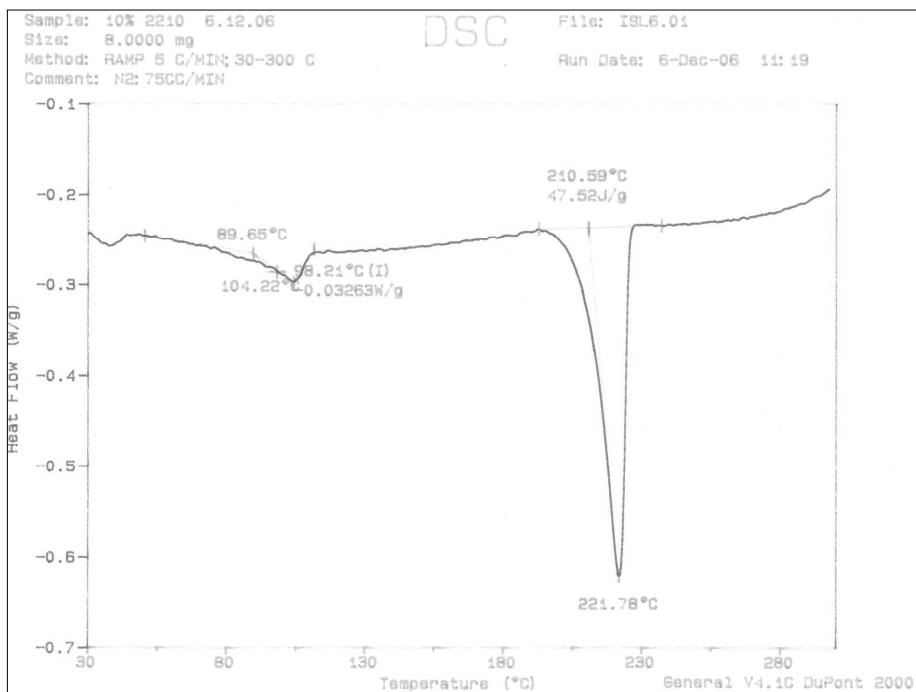


Figure A.6 DSC thermogram of polyamide-6/E-BA-MAH (10 wt %) blend

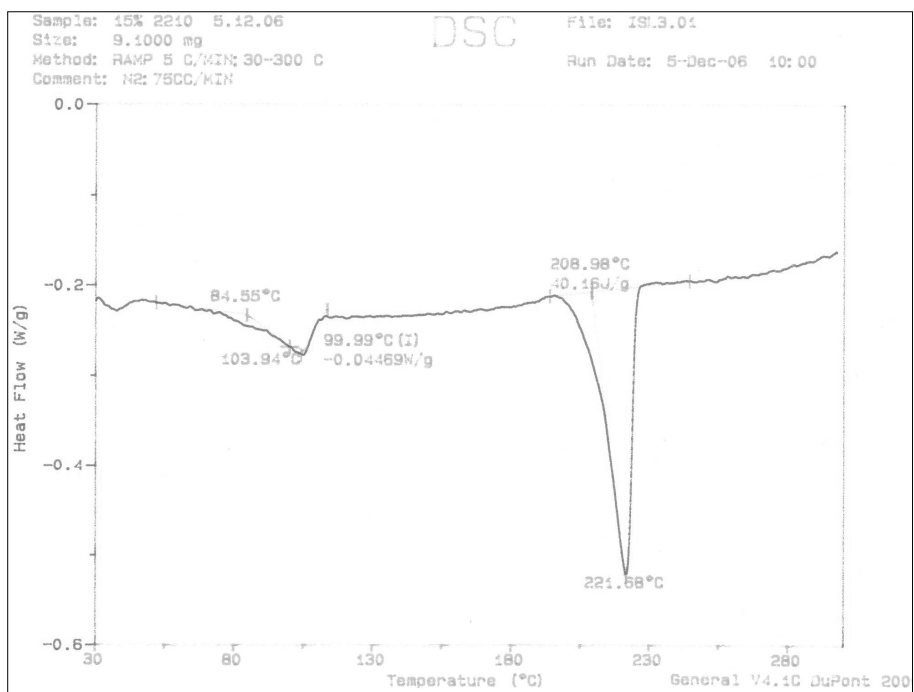


Figure A.7 DSC thermogram of polyamide-6/E-BA-MAH (15 wt %) blend

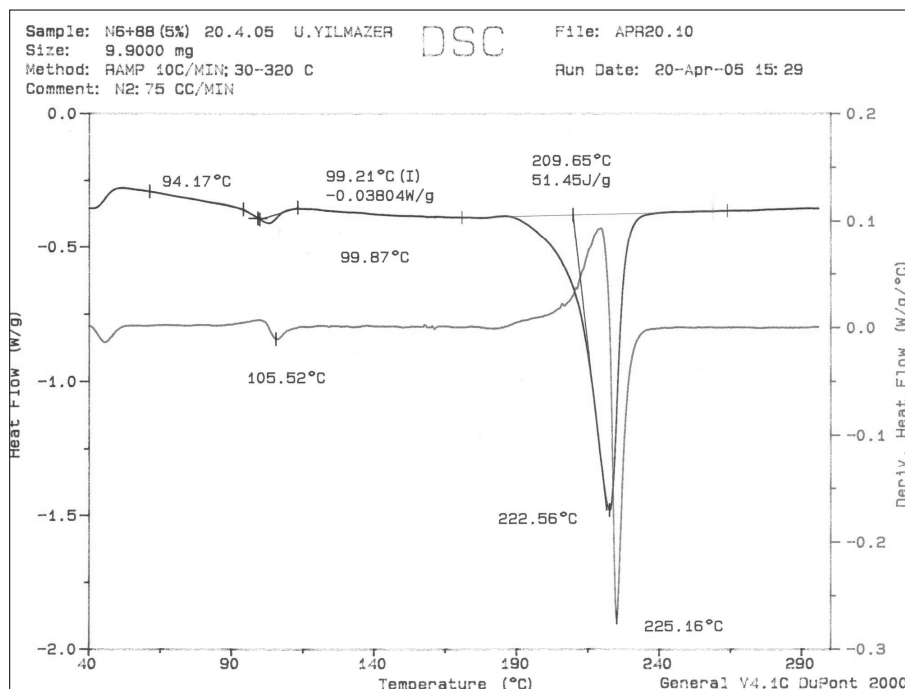


Figure A.8 DSC thermogram of polyamide-6/E-GMA (5 wt %) blend

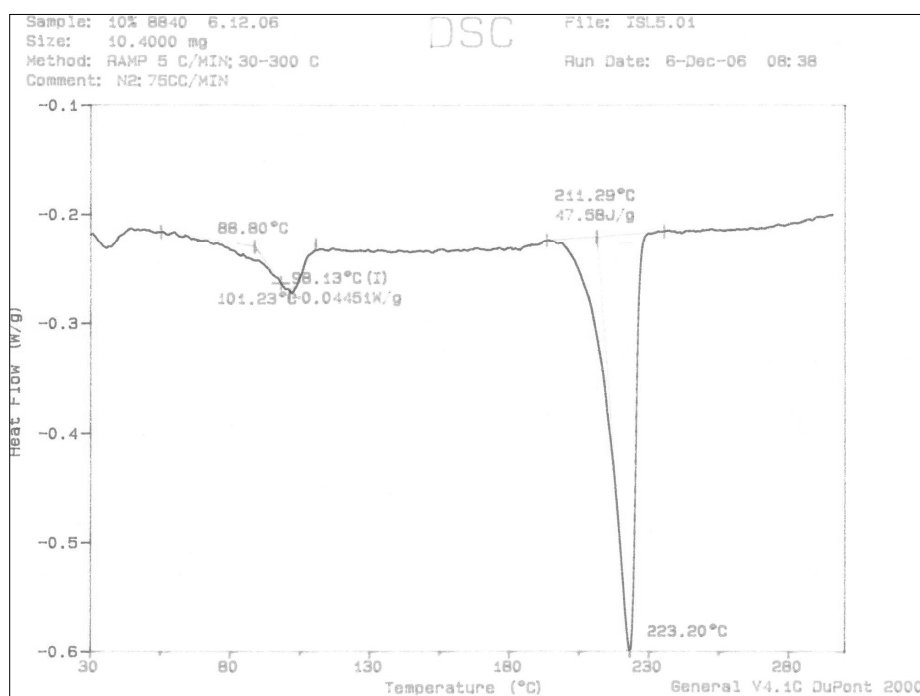


Figure A.9 DSC thermogram of polyamide-6/E-GMA (10 wt %) blend

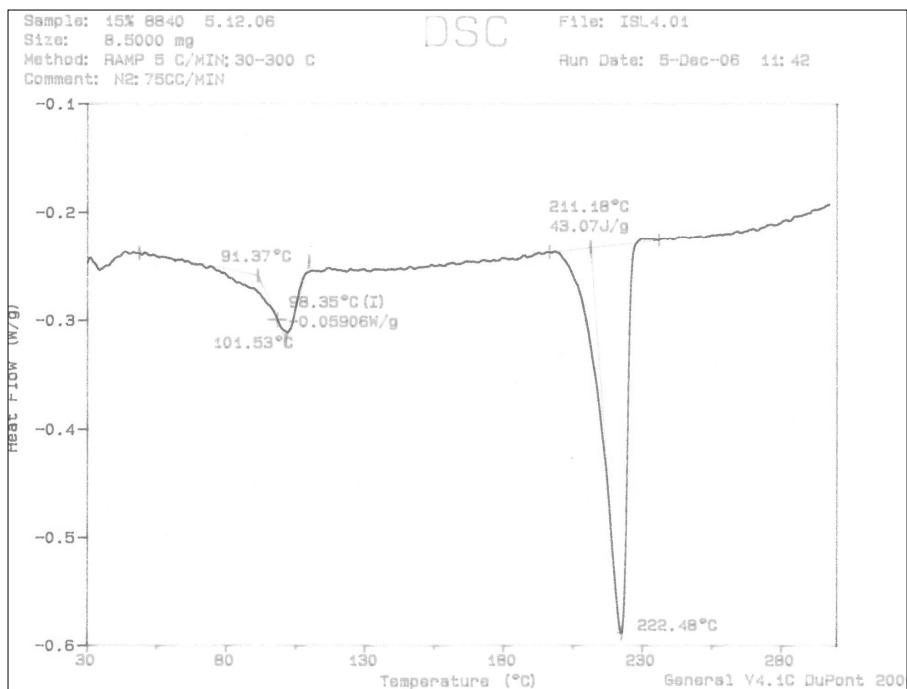


Figure A.10 DSC thermogram of polyamide-6/E-GMA (15 wt %) blend

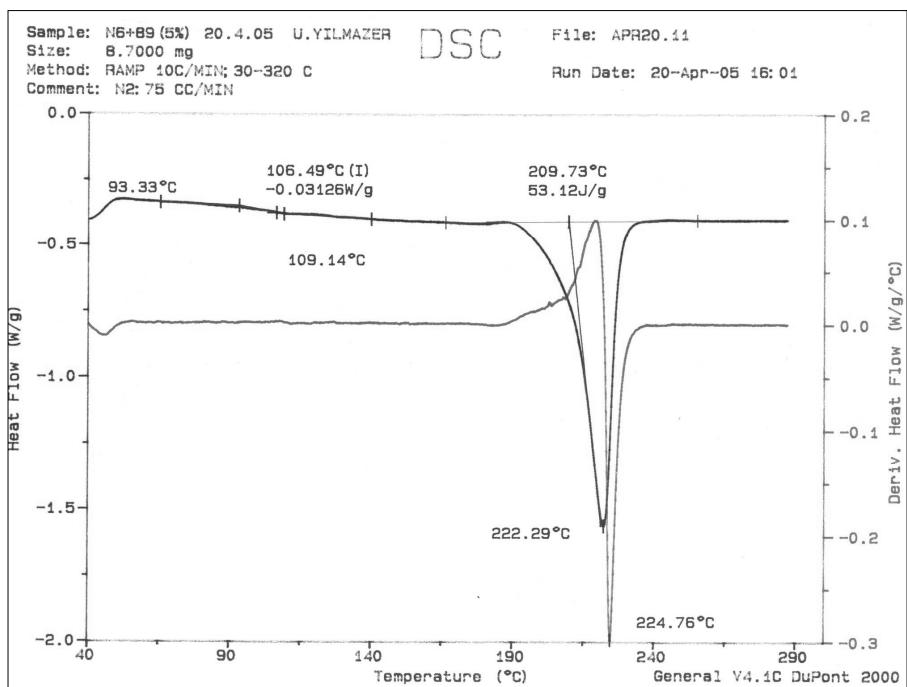


Figure A.11 DSC thermogram of polyamide-6/E-MA-GMA (5 wt %) blend

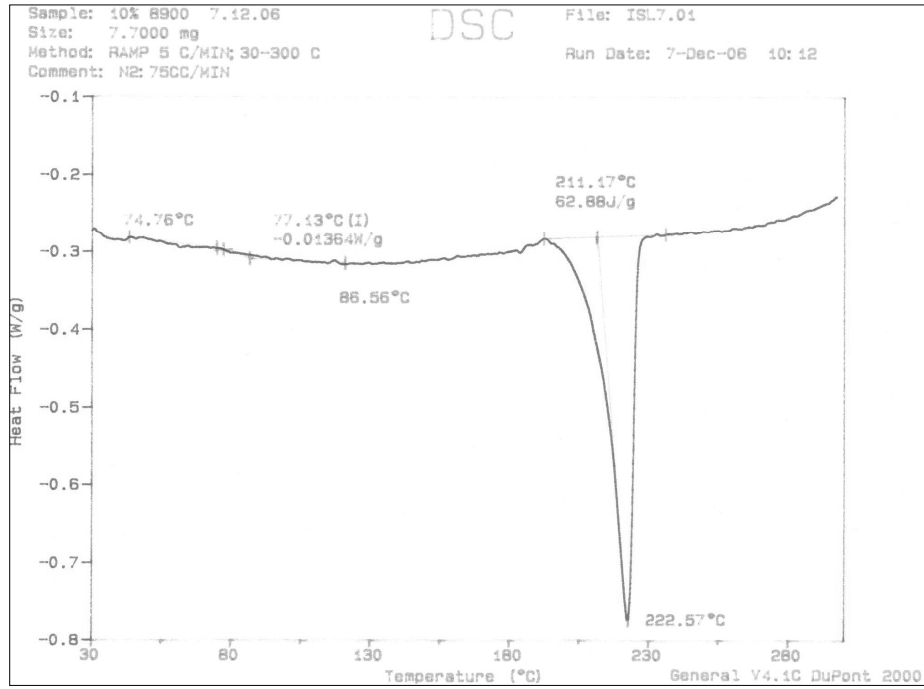


Figure A.12 DSC thermogram of polyamide-6/E-MA-GMA (10 wt %) blend

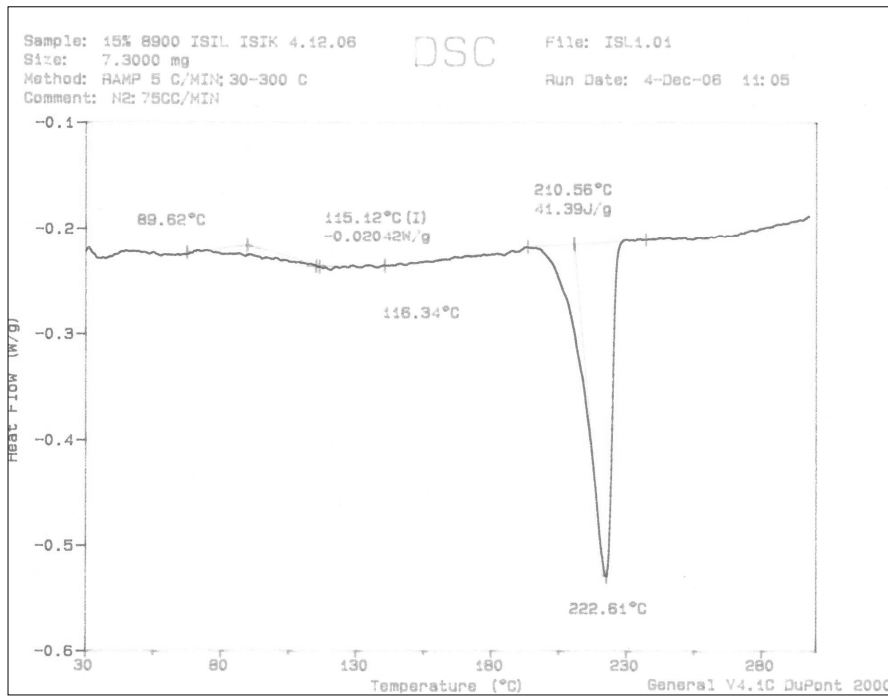


Figure A.13 DSC thermogram of polyamide-6/E-MA-GMA (15 wt %) blend

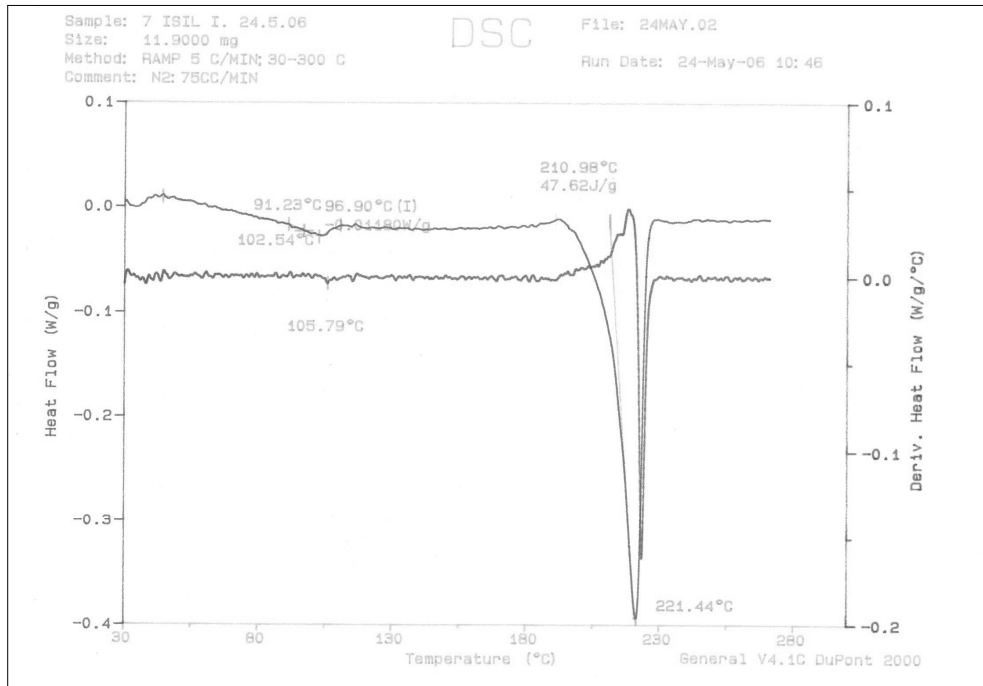


Figure A.14 DSC thermogram of polyamide-6/Cloisite® 15A/E-BA-MAH (All-S) nanocomposite

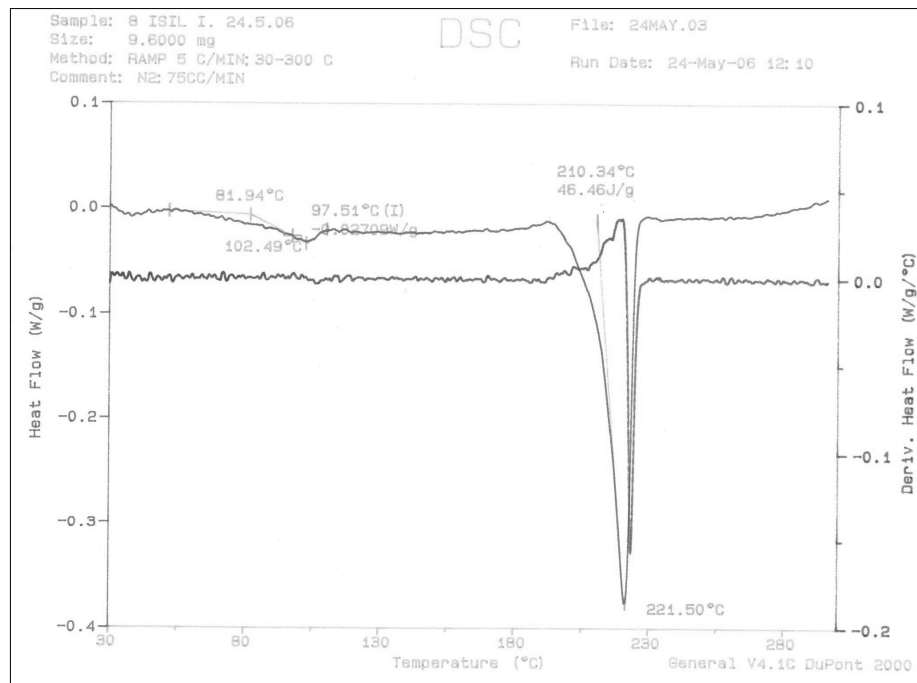


Figure A.15 DSC thermogram of polyamide-6/Cloisite® 15A/E-BA-MAH (PI-C) nanocomposite

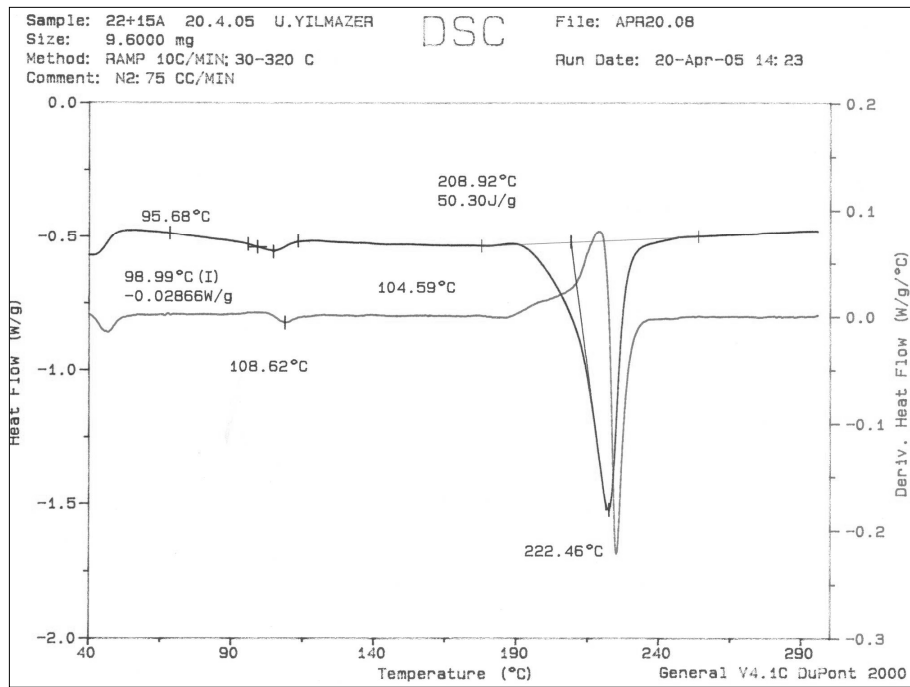


Figure A.16 DSC thermogram of polyamide-6/Cloisite® 15A/E-BA-MAH (PC-I) nanocomposite

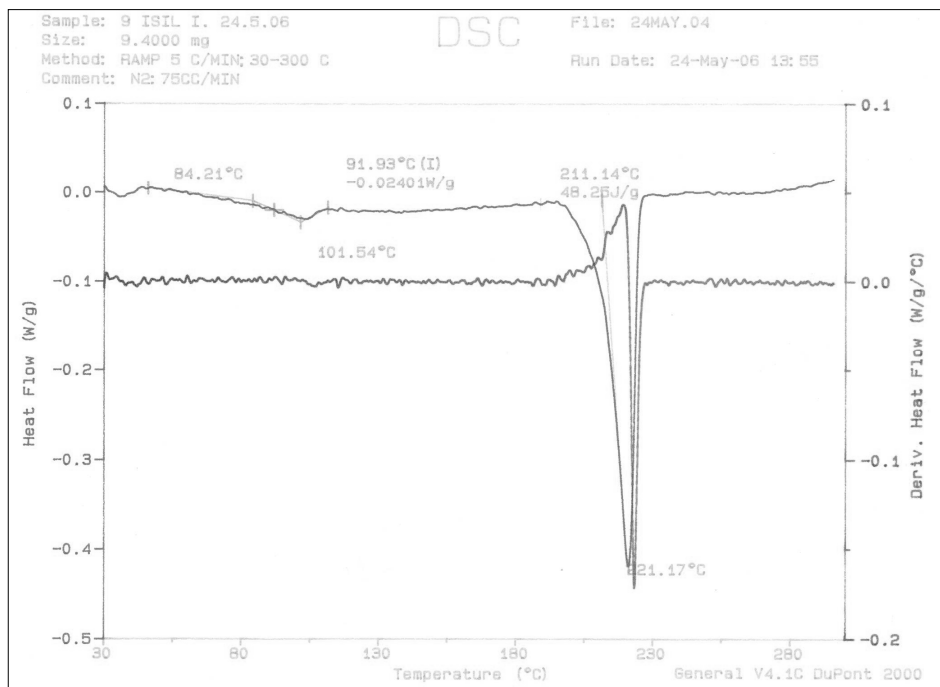


Figure A.17 DSC thermogram of polyamide-6/Cloisite® 15A/E-BA-MAH (IC-P) nanocomposite

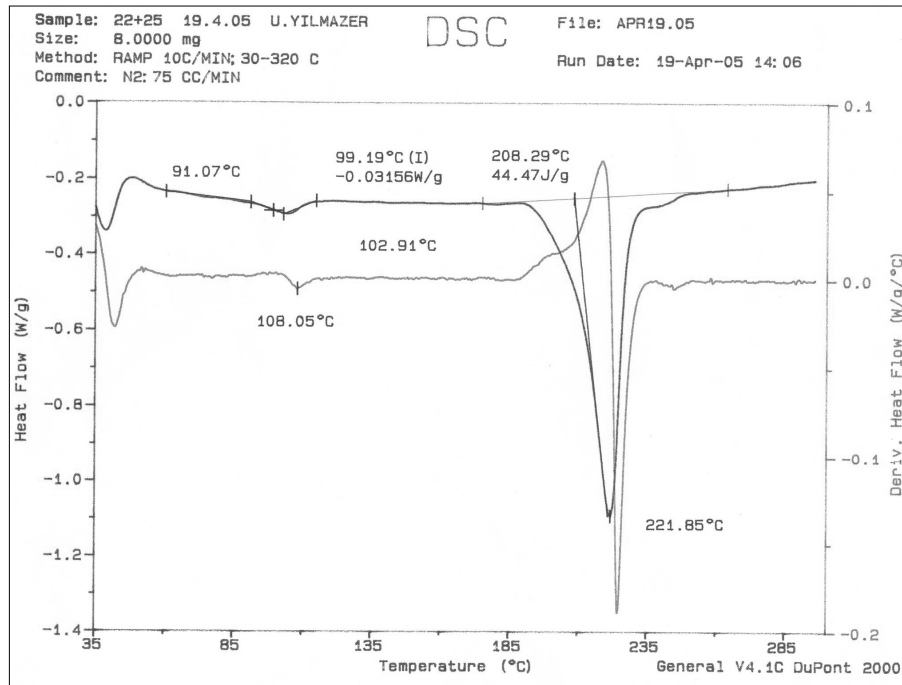


Figure A.18 DSC thermogram of polyamide-6/Cloisite® 25A/E-BA-MAH (All-S) nanocomposite

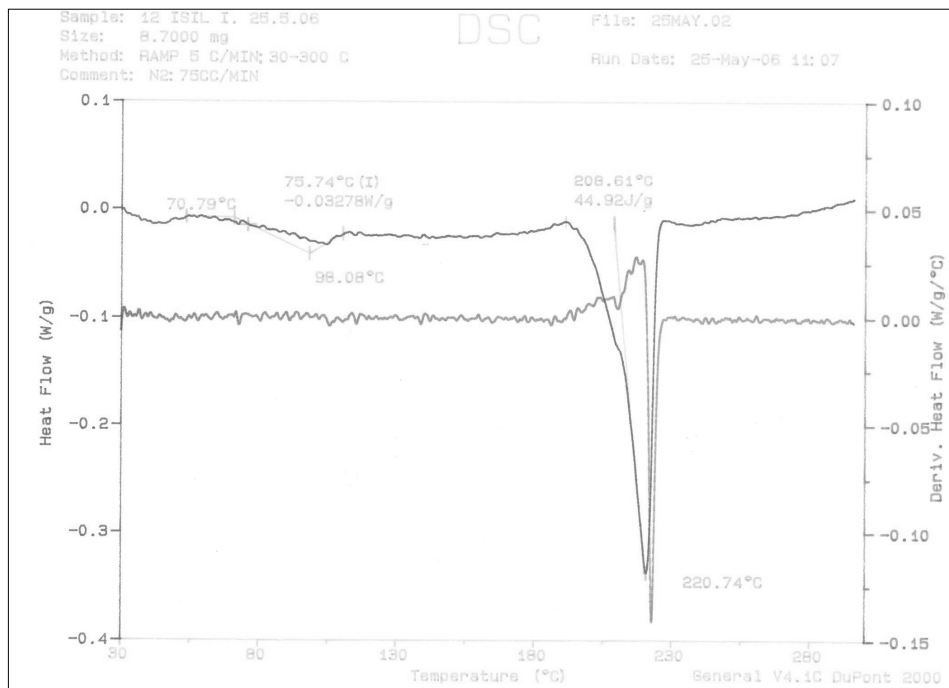


Figure A.19 DSC thermogram of polyamide-6/Cloisite® 25A/E-BA-MAH (PI-C) nanocomposite

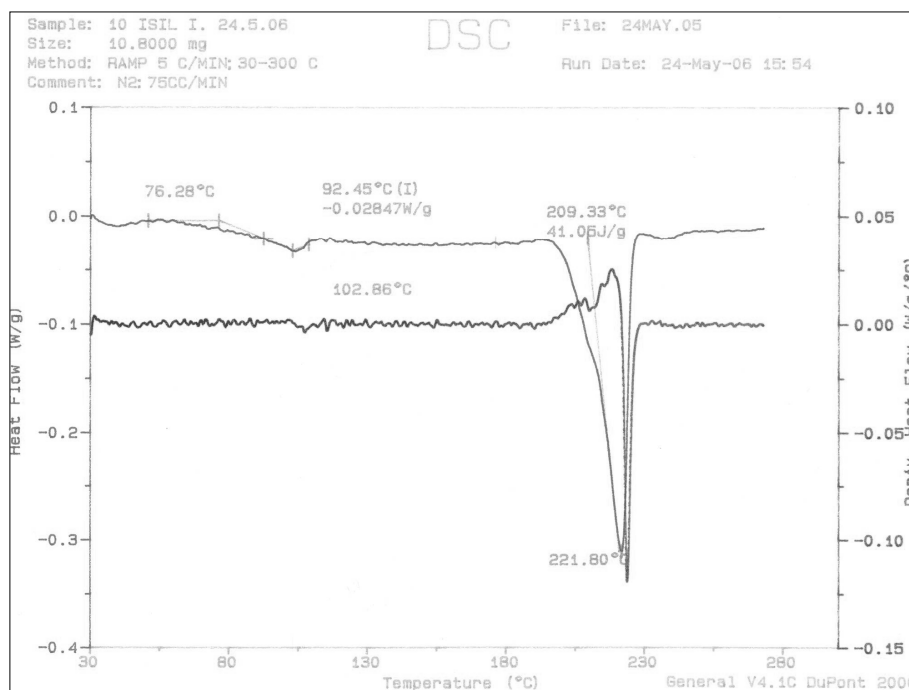


Figure A.20 DSC thermogram of polyamide-6/Cloisite® 25A/E-BA-MAH (PC-I) nanocomposite

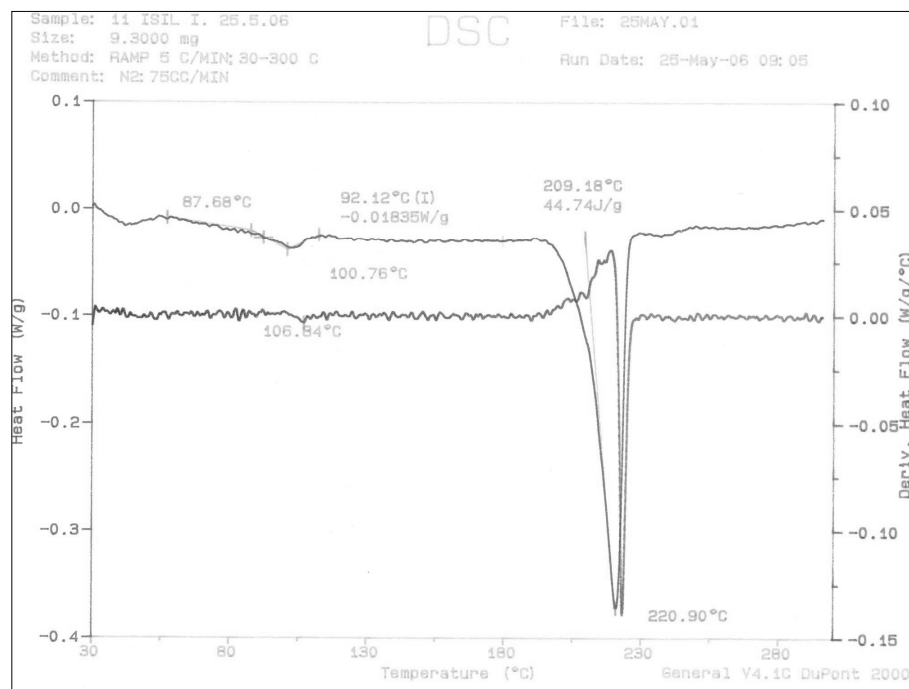


Figure A.21 DSC thermogram of polyamide-6/Cloisite® 25A/E-BA-MAH (IC-P) nanocomposite

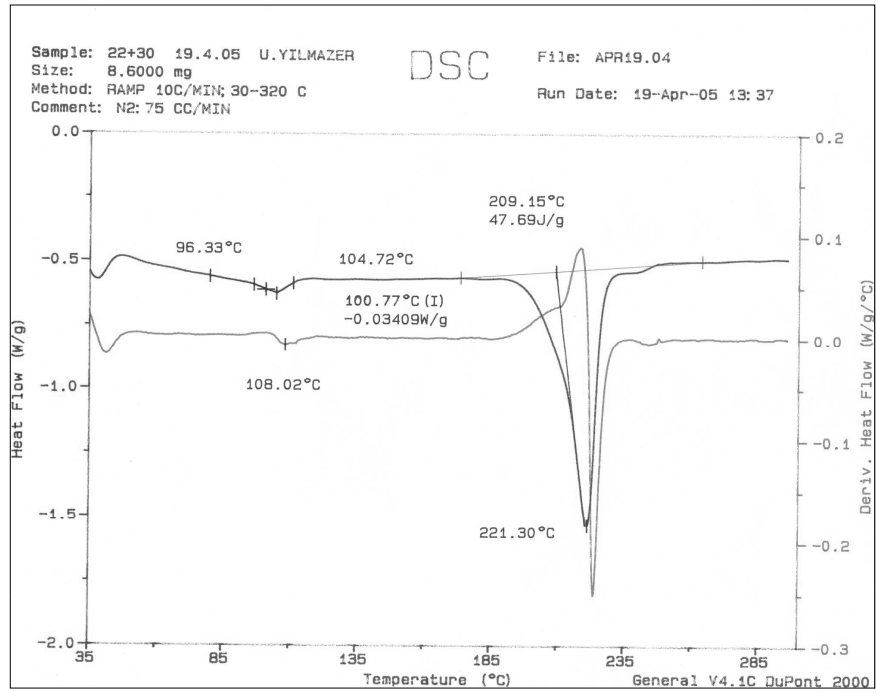


Figure A.22 DSC thermogram of polyamide-6/Cloisite® 30B/E-BA-MAH (All-S) nanocomposite

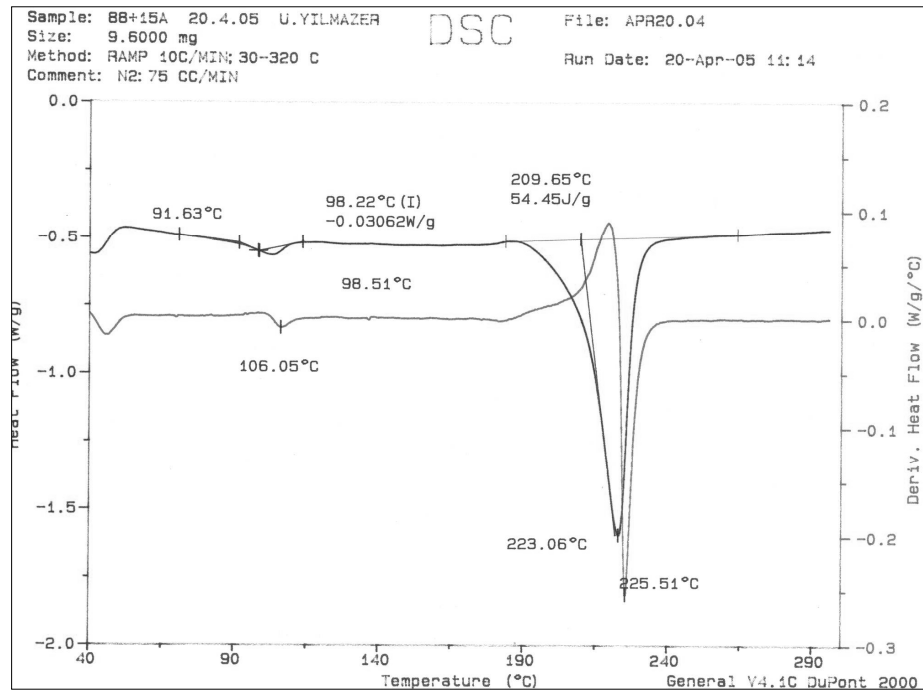


Figure A.23 DSC thermogram of polyamide-6/Cloisite® 15A/E-GMA (All-S) nanocomposite

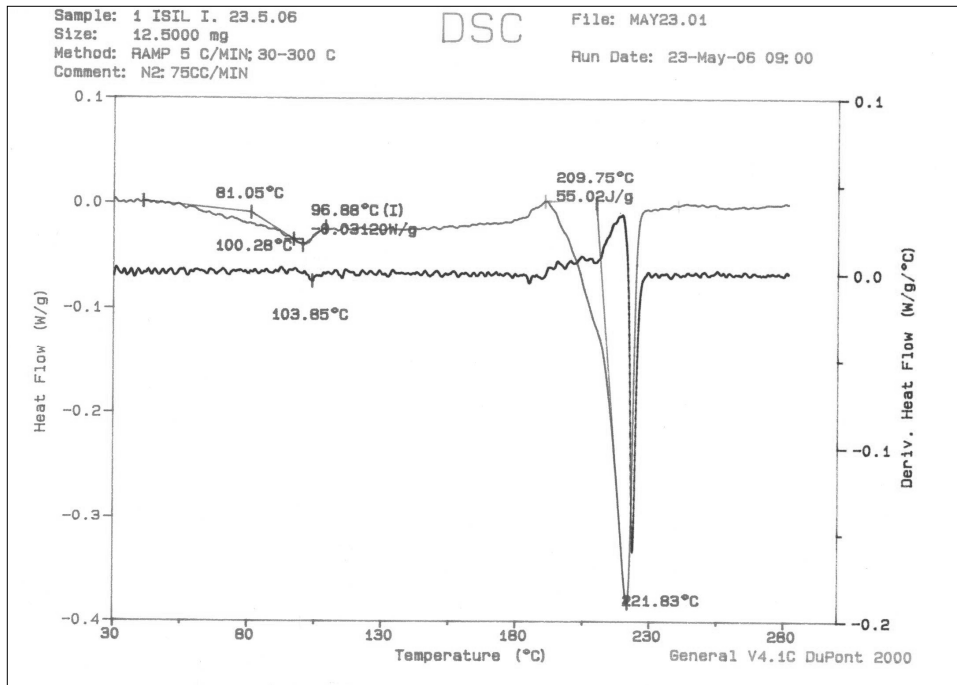


Figure A.24 DSC thermogram of polyamide-6/Cloisite® 15A/E-GMA (PI-C) nanocomposite

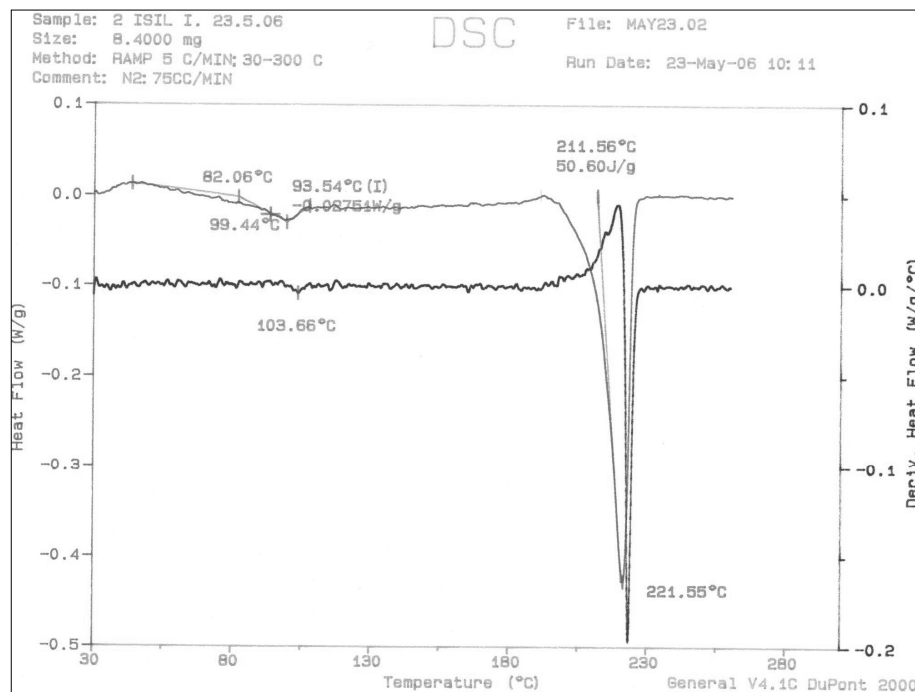


Figure A.25 DSC thermogram of polyamide-6/Cloisite® 15A/E-GMA (PC-I) nanocomposite

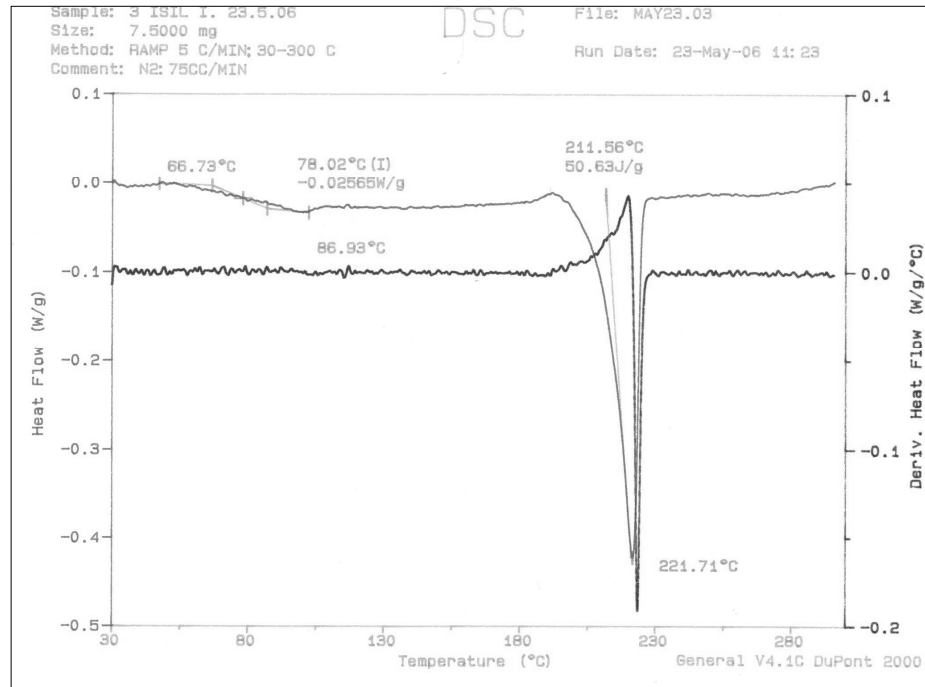


Figure A.26 DSC thermogram of polyamide-6/Cloisite® 15A/E-GMA (IC-P) nanocomposite

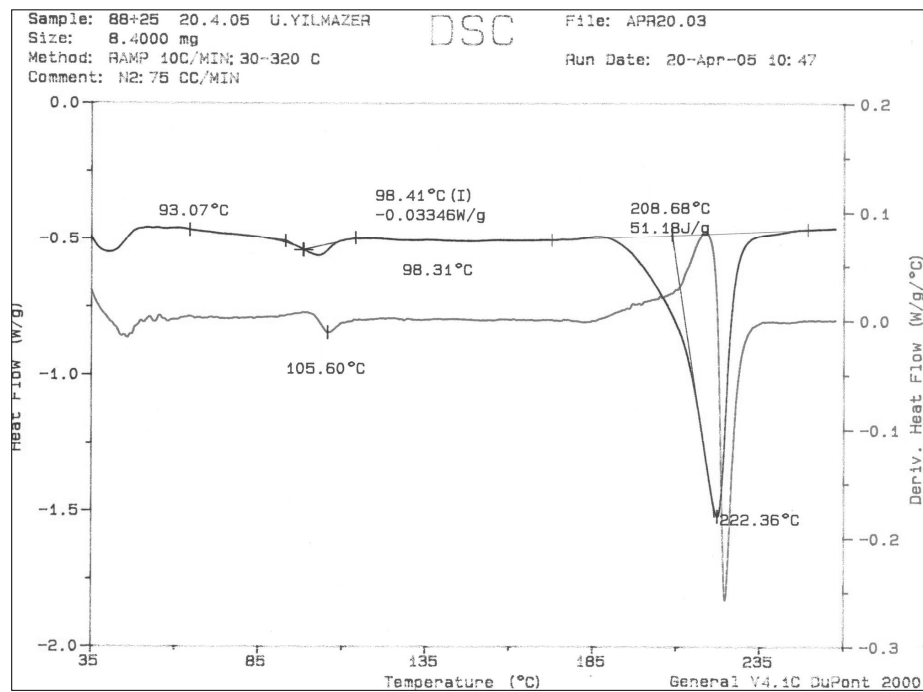


Figure A.27 DSC thermogram of polyamide-6/Cloisite® 25A/E-GMA (All-S) nanocomposite

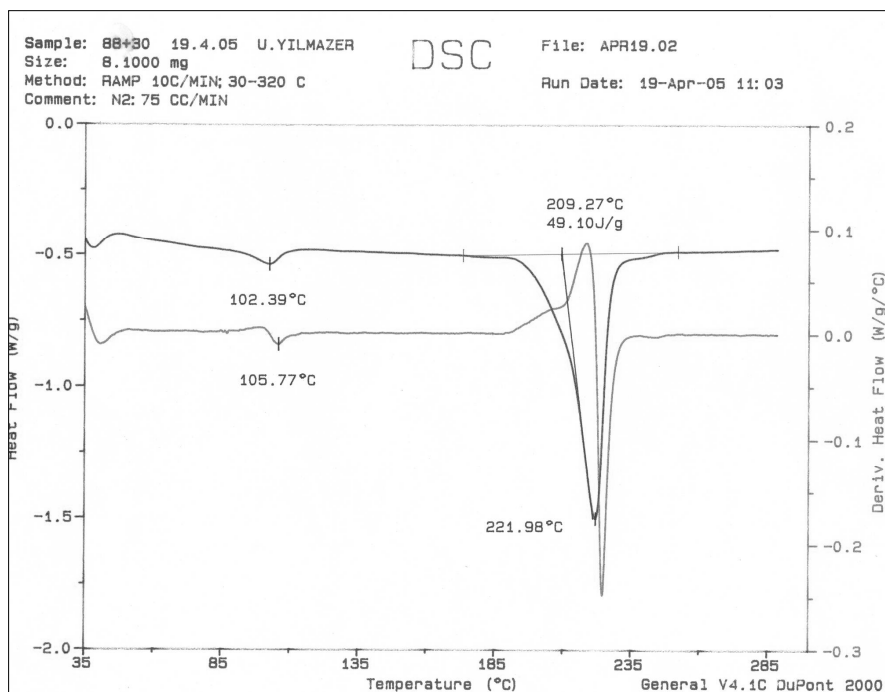


Figure A.28 DSC thermogram of polyamide-6/Cloisite® 30B/E-GMA (All-S) nanocomposite

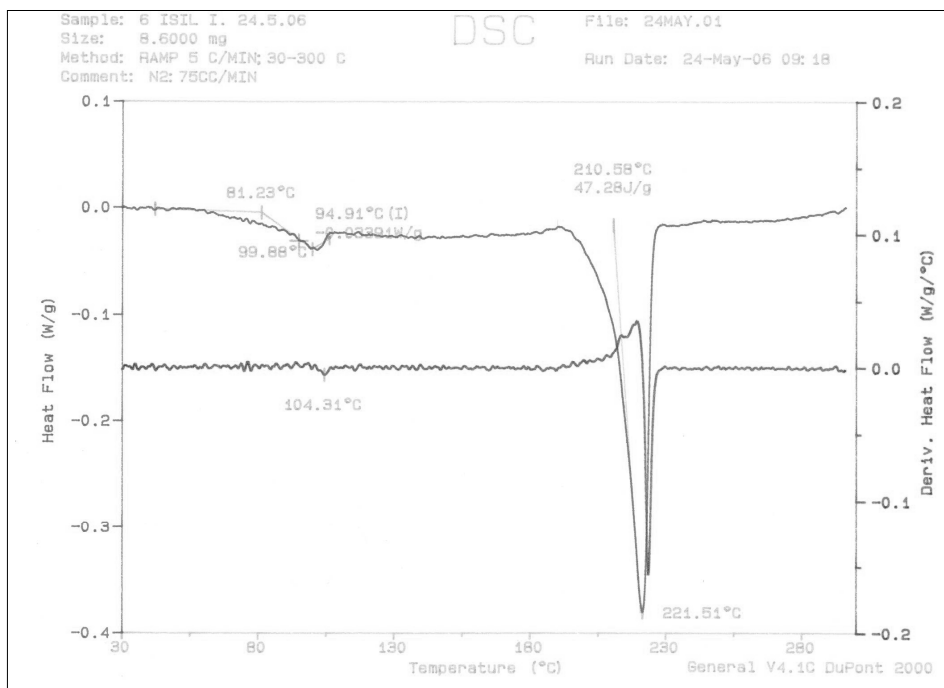


Figure A.29 DSC thermogram of polyamide-6/Cloisite® 30B/E-GMA (PI-C) nanocomposite

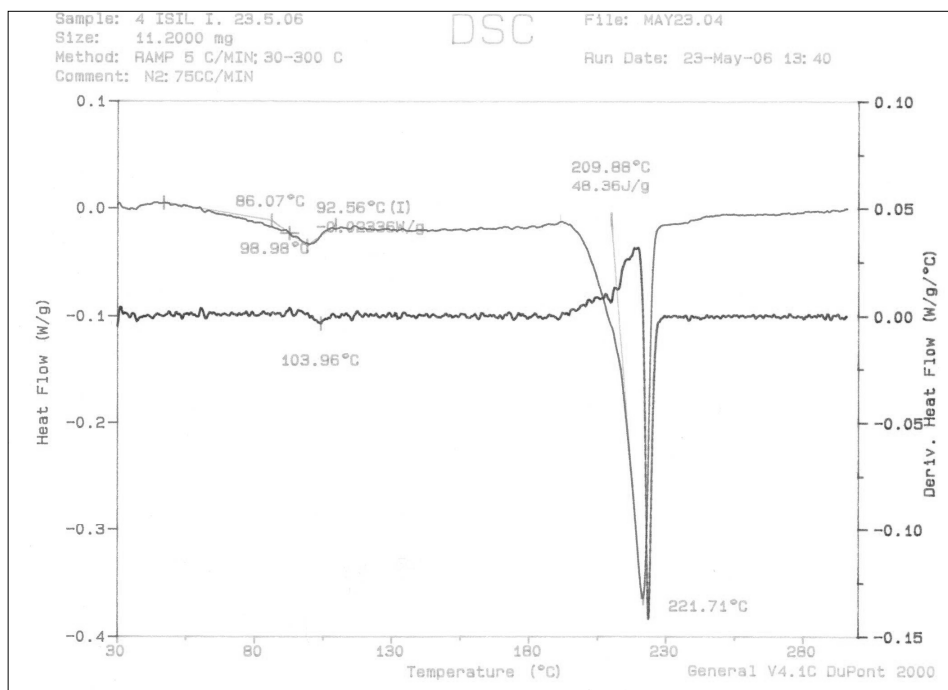


Figure A.30 DSC thermogram of polyamide-6/Cloisite® 30B/E-GMA (PC-I) nanocomposite

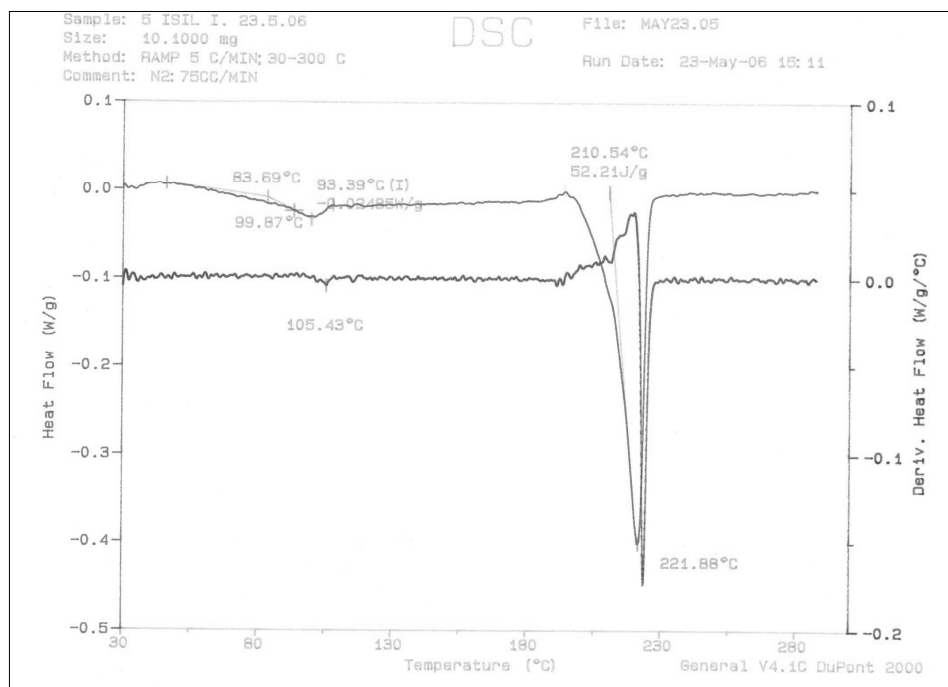


Figure A.31 DSC thermogram of polyamide-6/Cloisite® 30B/E-GMA (IC-P) nanocomposite

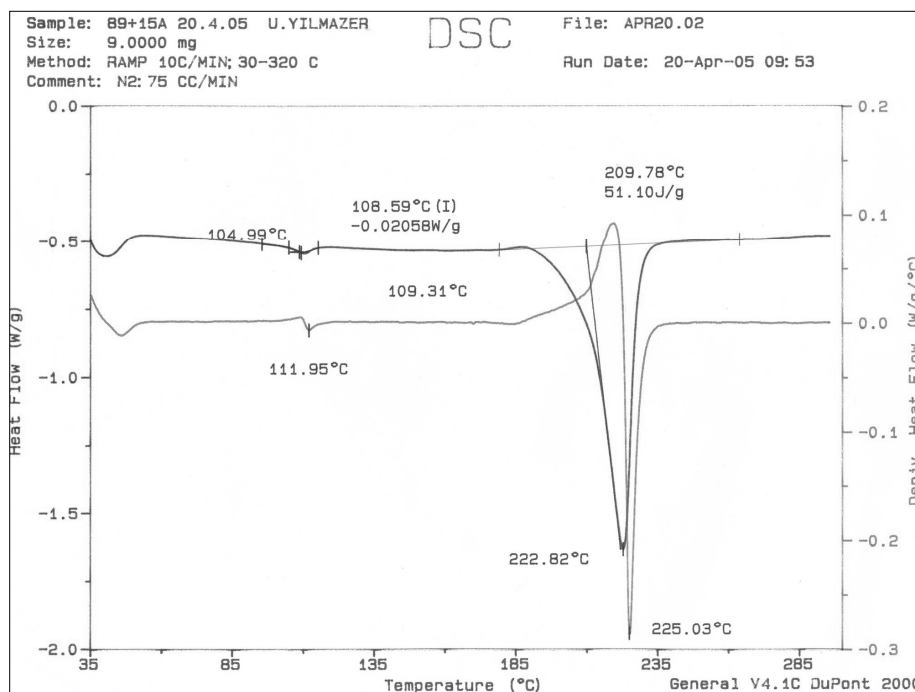


Figure A.32 DSC thermogram of polyamide-6/Cloisite® 15A/E-MA-GMA (All-S) nanocomposite

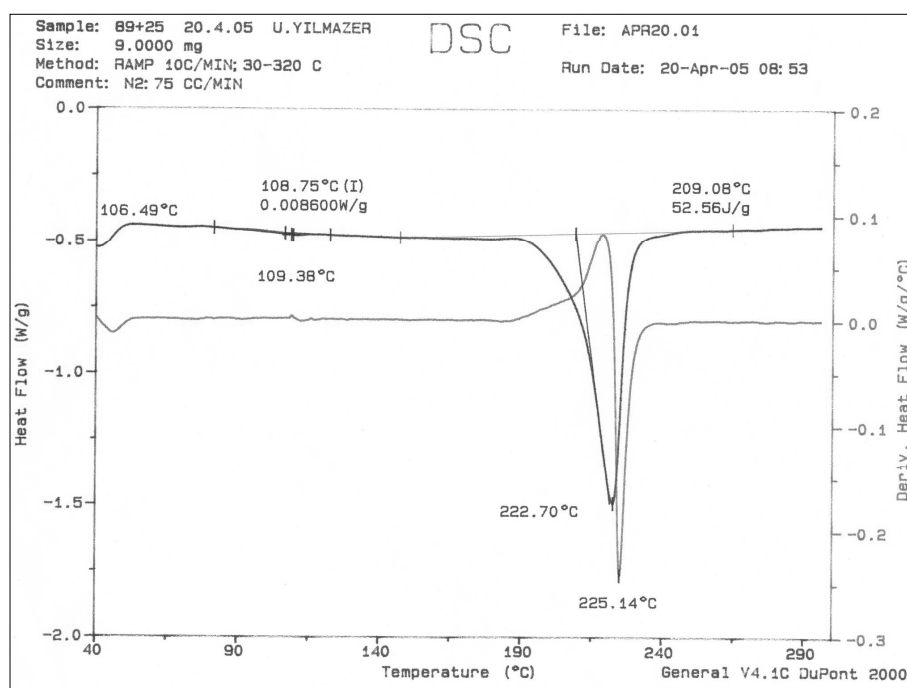


Figure A.33 DSC thermogram of polyamide-6/Cloisite® 25A/E-MA-GMA (All-S) nanocomposite

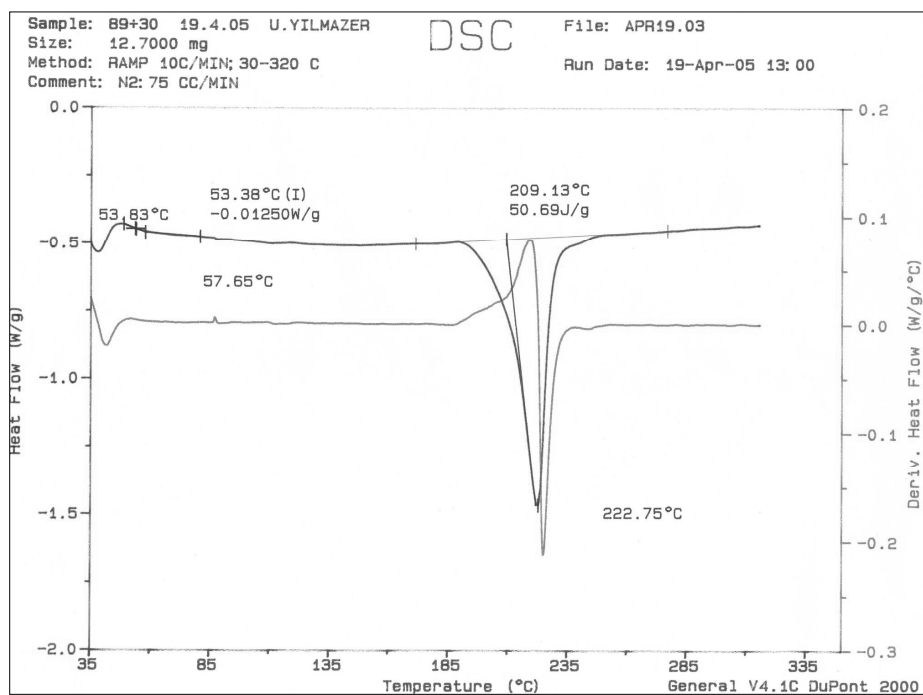


Figure A.34 DSC thermogram of polyamide-6/Cloisite® 30B/E-MA-GMA (All-S) nanocomposite

APPENDIX B

TGA ANALYSIS

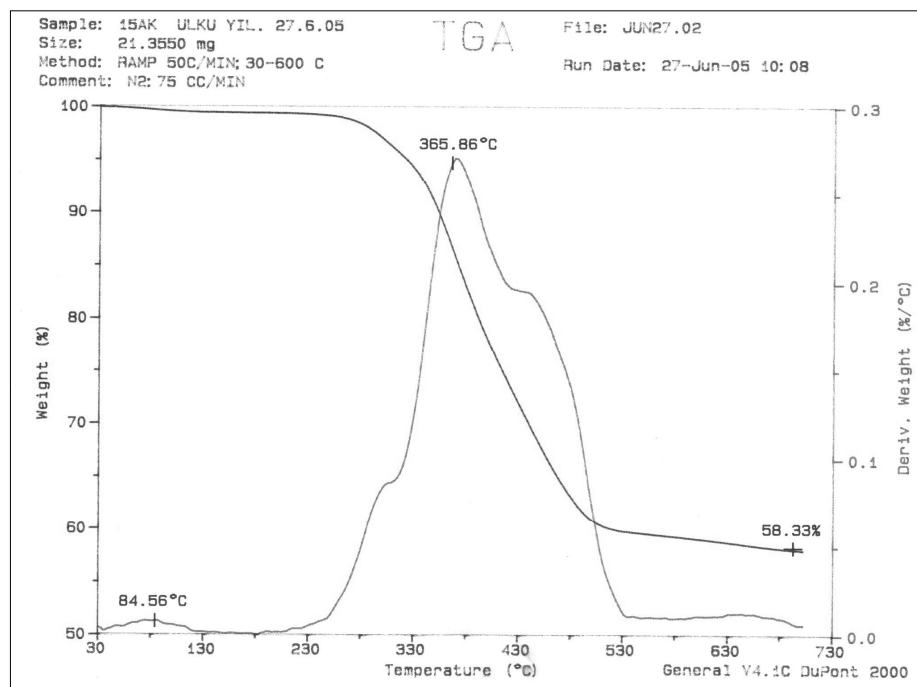


Figure B.1 TGA thermogram of Cloisite® 15A organoclay

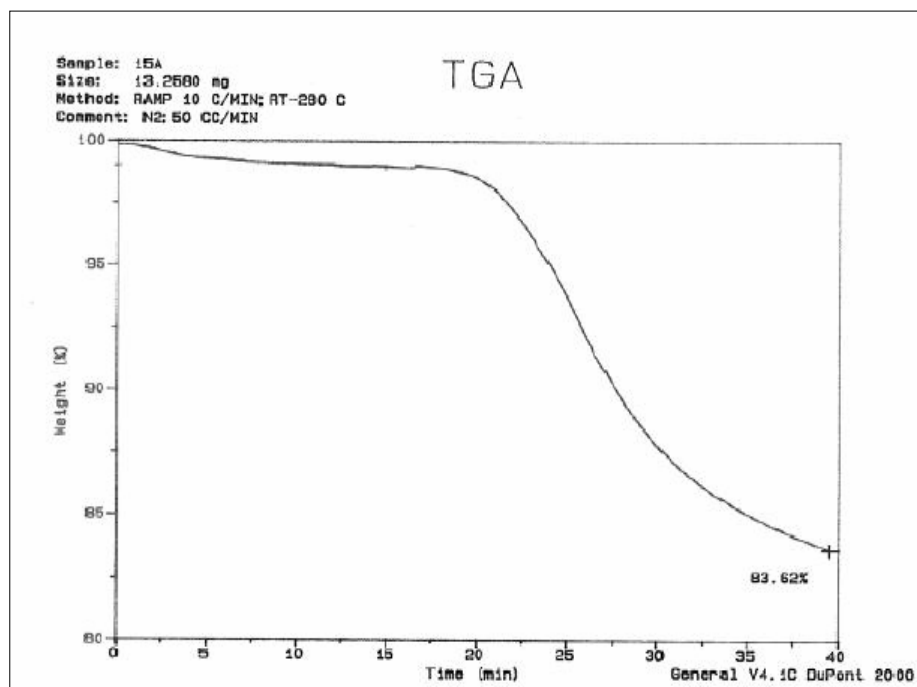


Figure B.2 Isothermal TGA thermogram of Cloisite® 15A organoclay

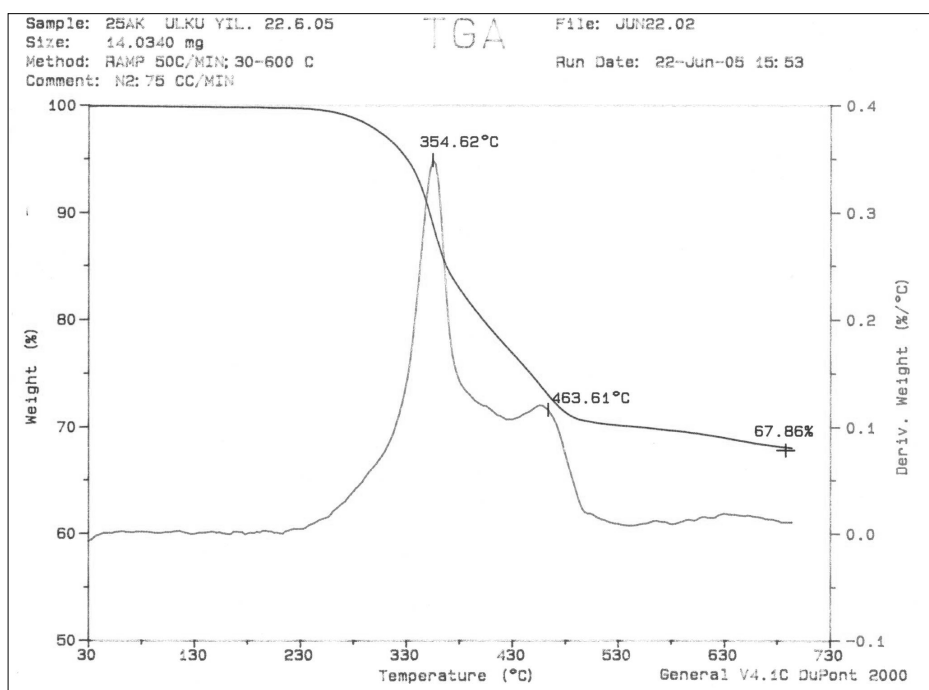


Figure B.3 TGA thermogram of Cloisite® 25A organoclay

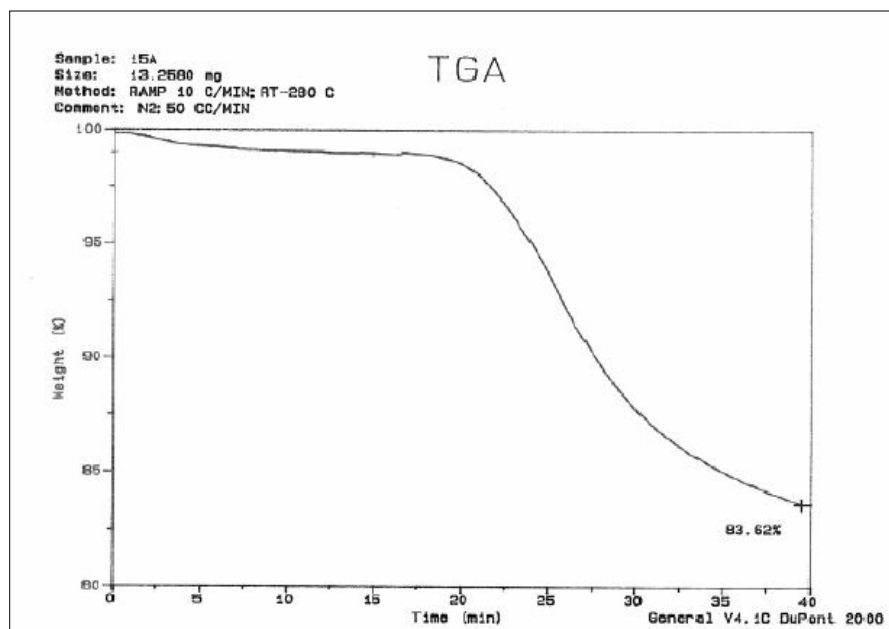


Figure B.4 Isothermal TGA thermogram of Cloisite® 25A organoclay

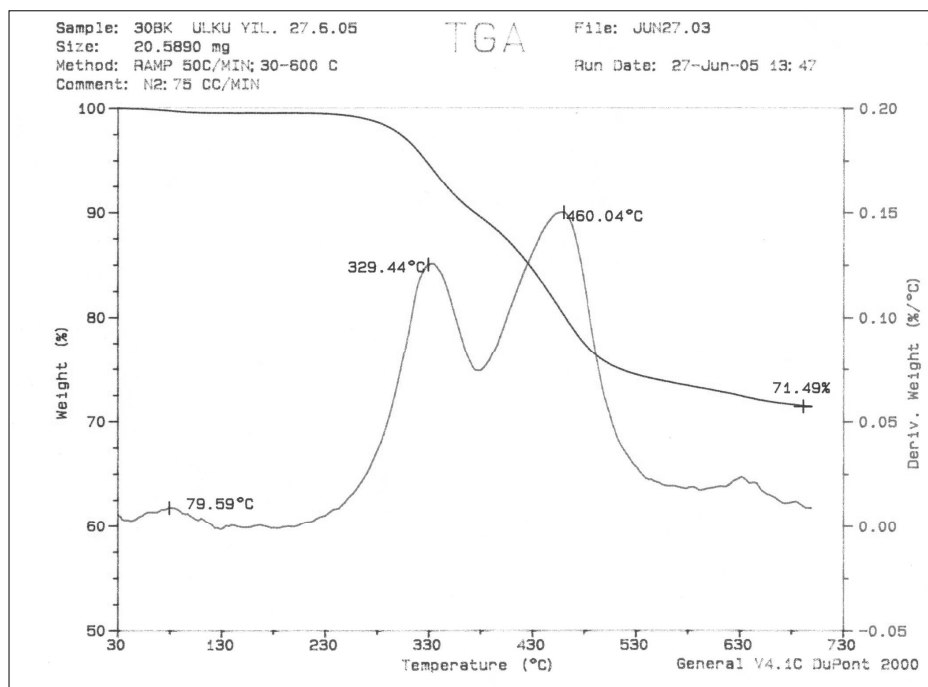


Figure B.5 TGA thermogram of Cloisite® 30B organoclay

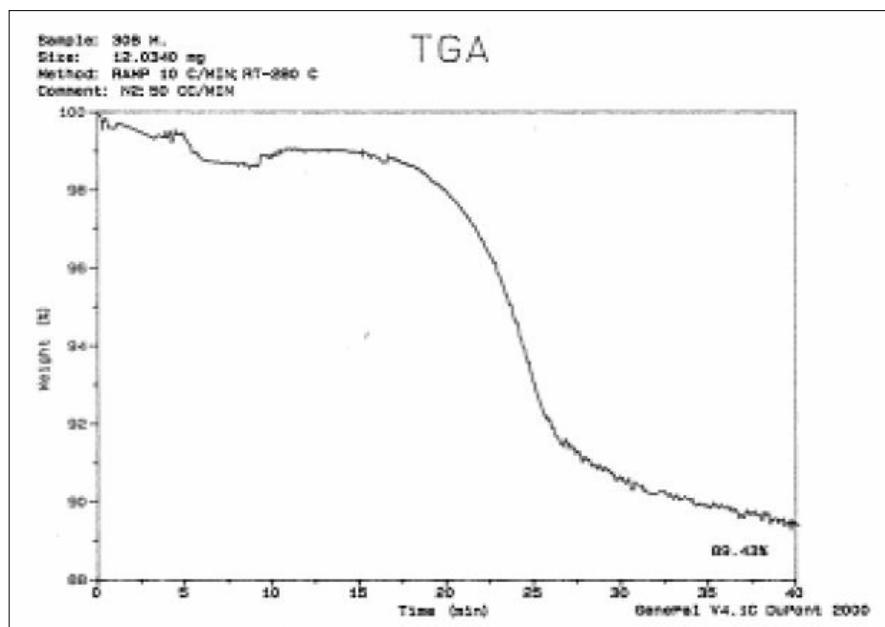


Figure B.6 Isothermal TGA thermogram of Cloisite® 30B organoclay

APPENDIX C

MECHANICAL TEST RESULTS

Table C.1 Impact Strength data and standard deviations for all the compositions

Components	Polyamide-6 (wt%)	Impact Strength (kJ/m ²)	Std. Dev.
Polyamide-6	100	6.0	0.9
Polyamide-6/Elastomer Blends			
Polyamide-6/E-BA-MAH	95	7.3	0.9
Polyamide-6/E-BA-MAH	90	10.8	0.7
Polyamide-6/E-BA-MAH	85	11.0	1.1
Polyamide-6/E-GMA	95	12.4	0.3
Polyamide-6/E-GMA	90	13.1	0.7
Polyamide-6/E-GMA	85	18.9	4.2
Polyamide-6/E-MA-GMA	95	13.2	0.9
Polyamide-6/E-MA-GMA	90	15.9	0.7
Polyamide-6/E-MA-GMA	85	65.3	4.0
Polyamide-6/Organoclay Nanocomposites			
Polyamide-6/Cloisite® 15A	98	3.8	0.1
Polyamide-6/Cloisite® 25A	98	3.6	0.3
Polyamide-6/Cloisite® 30B	98	3.9	0.1
Polyamide-6/Organoclay/Elastomer Nanocomposites (All-S)			
Polyamide-6/Cloisite®15A/E-BA-MAH	93	6.0	0.2
Polyamide-6/Cloisite® 25A/ E-BA-MAH	93	5.2	0.3
Polyamide-6/Cloisite® 30B/ E-BA-MAH	93	5.2	0.4
Polyamide-6/Cloisite®15A/ E-GMA	93	8.2	0.1
Polyamide-6/Cloisite®25A/ E-GMA	93	5.4	0.1
Polyamide-6/Cloisite®30B/ E-GMA	93	7.1	0.5
Polyamide-6/Cloisite®15A/E-MA-GMA	93	7.3	0.9
Polyamide-6/Cloisite®25A/E-MA-GMA	93	7.2	0.5
Polyamide-6/Cloisite®30B/E-MA-GMA	93	6.6	0.5
Polyamide-6/Organoclay/Elastomer Nanocomposites (Mixing Orders)			
Polyamide-6/Cloisite®15A/E-BA-MAH(PI-C)	93	5.2	0.2
Polyamide-6/Cloisite®15A/E-BA-MAH(PC-I)	93	5.5	0.1
Polyamide-6/Cloisite®15A/E-BA-MAH(IC-P)	93	6.0	0.4
Polyamide-6/Cloisite®25A/E-BA-MAH(PI-C)	93	3.7	0.6
Polyamide-6/Cloisite®25A/E-BA-MAH(PC-I)	93	5.2	0.8
Polyamide-6/Cloisite®25A/E-BA-MAH(IC-P)	93	4.7	1.0
Polyamide-6/Cloisite®15A/E-GMA(PI-C)	93	7.1	0.8
Polyamide-6/Cloisite®15A/E-GMA(PC-I)	93	5.8	0.2
Polyamide-6/Cloisite®15A/E-GMA(IC-P)	93	5.6	0.2
Polyamide-6/Cloisite®30B/E-GMA(PI-C)	93	6.1	0.6
Polyamide-6/Cloisite®30B/E-GMA(PC-I)	93	7.6	0.3
Polyamide-6/Cloisite®30B/E-GMA(IC-P)	93	6.8	0.7

Table C.2 Toughness data and standard deviations for all the compositions

Components	Polyamide-6 (wt%)	Toughness (MPa)	Std. Dev.
Polyamide-6	100	6580.9	758.1
Polyamide-6/Elastomer Blends			
Polyamide-6/E-BA-MAH	95	9110.6	1864.2
Polyamide-6/E-GMA	95	5697.4	566.3
Polyamide-6/E-MA-GMA	95	285.3	120.8
Polyamide-6/Organoclay Nanocomposites			
Polyamide-6/Cloisite® 15A	98	8846.9	3187.7
Polyamide-6/Cloisite® 25A	98	10820.7	1056.9
Polyamide-6/Cloisite® 30B	98	9110.6	900.8
Polyamide-6/Organoclay/Elastomer Nanocomposites (All-S)			
Polyamide-6/Cloisite®15A/E-BA-MAH	93	9005.5	1366.5
Polyamide-6/Cloisite® 25A/ E-BA-MAH	93	10611.2	524.9
Polyamide-6/Cloisite® 30B/ E-BA-MAH	93	2613.3	297.9
Polyamide-6/Cloisite®15A/ E-GMA	93	6573.3	1878.9
Polyamide-6/Cloisite®25A/ E-GMA	93	2148.9	176.5
Polyamide-6/Cloisite®30B/ E-GMA	93	5749.2	1729.6
Polyamide-6/Cloisite®15A/E-MA-GMA	93	1642.2	560.1
Polyamide-6/Cloisite®25A/E-MA-GMA	93	174.9	9.5
Polyamide-6/Cloisite®30B/E-MA-GMA	93	859.5	129.4

Table C.3 Tensile strength data and standard deviations for all the compositions

Components	Polyamide-6 (wt%)	Tensile Strength (MPa)	Std. Dev.
Polyamide-6	100	67.6	1.1
Polyamide-6/Elastomer Blends			
Polyamide-6/E-BA-MAH	95	62.0	1.9
Polyamide-6/E-BA-MAH	90	47.4	1.9
Polyamide-6/E-BA-MAH	85	43.9	0.9
Polyamide-6/E-GMA	95	62.2	1.2
Polyamide-6/E-GMA	90	54.7	0.1
Polyamide-6/E-GMA	85	49.2	0.9
Polyamide-6/E-MA-GMA	95	56.9	1.2
Polyamide-6/E-MA-GMA	90	52.5	0.5
Polyamide-6/E-MA-GMA	85	47.9	0.4
Polyamide-6/Organoclay Nanocomposites			
Polyamide-6/Cloisite® 15A	98	65.7	2.0
Polyamide-6/Cloisite® 25A	98	70.5	0.9
Polyamide-6/Cloisite® 30B	98	69.4	0.7
Polyamide-6/Organoclay/Elastomer Nanocomposites (All-S)			
Polyamide-6/Cloisite®15A/E-BA-MAH	93	63.8	1.2
Polyamide-6/Cloisite® 25A/ E-BA-MAH	93	62.6	0.5
Polyamide-6/Cloisite® 30B/ E-BA-MAH	93	56.4	0.6
Polyamide-6/Cloisite®15A/ E-GMA	93	59.4	0.5
Polyamide-6/Cloisite®25A/ E-GMA	93	56.3	0.9
Polyamide-6/Cloisite®30B/ E-GMA	93	55.2	0.5
Polyamide-6/Cloisite®15A/E-MA-GMA	93	58.1	3.5
Polyamide-6/Cloisite®25A/E-MA-GMA	93	58.6	3.1
Polyamide-6/Cloisite®30B/E-MA-GMA	93	52.7	4.7
Polyamide-6/Organoclay/Elastomer Nanocomposites (Mixing Orders)			
Polyamide-6/Cloisite®15A/E-BA-MAH(PI-C)	93	47.6	3.1
Polyamide-6/Cloisite®15A/E-BA-MAH(PC-I)	93	54.6	7.8
Polyamide-6/Cloisite®15A/E-BA-MAH(IC-P)	93	34.5	1.9
Polyamide-6/Cloisite®25A/E-BA-MAH(PI-C)	93	55.6	9.3
Polyamide-6/Cloisite®25A/E-BA-MAH(PC-I)	93	42.8	1.4
Polyamide-6/Cloisite®25A/E-BA-MAH(IC-P)	93	37.7	4.3
Polyamide-6/Cloisite®15A/E-GMA(PI-C)	93	52.6	3.3
Polyamide-6/Cloisite®15A/E-GMA(PC-I)	93	37.3	3.8
Polyamide-6/Cloisite®15A/E-GMA(IC-P)	93	56.9	1.5
Polyamide-6/Cloisite®30B/E-GMA(PI-C)	93	49.8	8.5
Polyamide-6/Cloisite®30B/E-GMA(PC-I)	93	39.4	3.8
Polyamide-6/Cloisite®30B/E-GMA(IC-P)	93	45.2	9.3

Table C.4 Young's Modulus data and standard deviations for all the compositions

Components	Polyamide-6 (wt%)	Young's Modulus (MPa)	Std. Dev.
Polyamide-6	100	1640.2	0.1
Polyamide-6/Elastomer Blends			
Polyamide-6/E-BA-MAH	95	1639.2	0.2
Polyamide-6/E-BA-MAH	90	1627.2	39.5
Polyamide-6/E-BA-MAH	85	1390.2	34.2
Polyamide-6/E-GMA	95	1636.0	83.3
Polyamide-6/E-GMA	90	1690.4	20.2
Polyamide-6/E-GMA	85	1602.9	21.3
Polyamide-6/E-MA-GMA	95	1629.6	20.2
Polyamide-6/E-MA-GMA	90	1690.7	35.5
Polyamide-6/E-MA-GMA	85	1660.3	0.5
Polyamide-6/Organoclay Nanocomposites			
Polyamide-6/Cloisite® 15A	98	2038.3	99.4
Polyamide-6/Cloisite® 25A	98	2236.4	0.1
Polyamide-6/Cloisite® 30B	98	2049.9	0.1
Polyamide-6/Organoclay/Elastomer Nanocomposites (All-S)			
Polyamide-6/Cloisite®15A/E-BA-MAH	93	1974.1	131.5
Polyamide-6/Cloisite® 25A/ E-BA-MAH	93	1537.5	0.1
Polyamide-6/Cloisite® 30B/ E-BA-MAH	93	1447.2	0.3
Polyamide-6/Cloisite®15A/ E-GMA	93	1994.4	84.2
Polyamide-6/Cloisite®25A/ E-GMA	93	1728.1	143.5
Polyamide-6/Cloisite®30B/ E-GMA	93	1696.8	63.8
Polyamide-6/Cloisite®15A/E-MA-GMA	93		
Polyamide-6/Cloisite®25A/E-MA-GMA	93		
Polyamide-6/Cloisite®30B/E-MA-GMA	93		
Polyamide-6/Organoclay/Elastomer Nanocomposites (Mixing Orders)			
Polyamide-6/Cloisite®15A/E-BA-MAH(PI-C)	93	1820.8	63.1
Polyamide-6/Cloisite®15A/E-BA-MAH(PC-I)	93	1890.7	19.4
Polyamide-6/Cloisite®15A/E-BA-MAH(IC-P)	93	1831.1	21.5
Polyamide-6/Cloisite®25A/E-BA-MAH(PI-C)	93	1490.2	32.1
Polyamide-6/Cloisite®25A/E-BA-MAH(PC-I)	93	1528.4	0.9
Polyamide-6/Cloisite®25A/E-BA-MAH(IC-P)	93	1484.4	24.8
Polyamide-6/Cloisite®15A/E-GMA(PI-C)	93	1780.0	39.9
Polyamide-6/Cloisite®15A/E-GMA(PC-I)	93	1828.7	35.2
Polyamide-6/Cloisite®15A/E-GMA(IC-P)	93	1826.5	23.6
Polyamide-6/Cloisite®30B/E-GMA(PI-C)	93	1799.1	50.6
Polyamide-6/Cloisite®30B/E-GMA(PC-I)	93	1863.9	31.8
Polyamide-6/Cloisite®30B/E-GMA(IC-P)	93	1816.8	30.6

Table C.5 Elongation at Break data and standard deviations for all the compositions

Components	Polyamide-6 (wt%)	Elongation at Break (%)	Std. Dev.
Polyamide-6	100	136.5	12.3
Polyamide-6/Elastomer Blends			
Polyamide-6/E-BA-MAH	95	100.4	22.6
Polyamide-6/E-BA-MAH	90	155.9	11.2
Polyamide-6/E-BA-MAH	85	160.6	10.3
Polyamide-6/E-GMA	95	137.7	23.6
Polyamide-6/E-GMA	90	164.7	27.1
Polyamide-6/E-GMA	85	140.8	6.2
Polyamide-6/E-MA-GMA	95	36.59	4.0
Polyamide-6/E-MA-GMA	90	135.5	16.7
Polyamide-6/E-MA-GMA	85	177.5	44.2
Polyamide-6/Organoclay Nanocomposites			
Polyamide-6/Cloisite® 15A	98	199.4	4.2
Polyamide-6/Cloisite® 25A	98	190.2	12.6
Polyamide-6/Cloisite® 30B	98	169.8	11.4
Polyamide-6/Organoclay/Elastomer Nanocomposites (All-S)			
Polyamide-6/Cloisite®15A/E-BA-MAH	93	168.9	16.7
Polyamide-6/Cloisite® 25A/ E-BA-MAH	93	191.8	8.9
Polyamide-6/Cloisite® 30B/ E-BA-MAH	93	52.4	7.2
Polyamide-6/Cloisite®15A/ E-GMA	93	149.3	33.3
Polyamide-6/Cloisite®25A/ E-GMA	93	54.1	11.6
Polyamide-6/Cloisite®30B/ E-GMA	93	98.0	23
Polyamide-6/Cloisite®15A/E-MA-GMA	93	45.2	3.3
Polyamide-6/Cloisite®25A/E-MA-GMA	93	38.4	8.1
Polyamide-6/Cloisite®30B/E-MA-GMA	93	30.2	7.4
Polyamide-6/Organoclay/Elastomer Nanocomposites (Mixing Orders)			
Polyamide-6/Cloisite®15A/E-BA-MAH(PI-C)	93	125.3	12.7
Polyamide-6/Cloisite®15A/E-BA-MAH(PC-I)	93	130.1	8.9
Polyamide-6/Cloisite®15A/E-BA-MAH(IC-P)	93	140.7	6.3
Polyamide-6/Cloisite®25A/E-BA-MAH(PI-C)	93	150.5	3.6
Polyamide-6/Cloisite®25A/E-BA-MAH(PC-I)	93	182.8	6.6
Polyamide-6/Cloisite®25A/E-BA-MAH(IC-P)	93	168.4	5.2
Polyamide-6/Cloisite®15A/E-GMA(PI-C)	93	152.3	24.6
Polyamide-6/Cloisite®15A/E-GMA(PC-I)	93	145.6	7.1
Polyamide-6/Cloisite®15A/E-GMA(IC-P)	93	163.9	15.4
Polyamide-6/Cloisite®30B/E-GMA(PI-C)	93	85.1	15.6
Polyamide-6/Cloisite®30B/E-GMA(PC-I)	93	90.2	6.2
Polyamide-6/Cloisite®30B/E-GMA(IC-P)	93	102.5	26.4

Table C.6 Flexural Strength data and standard deviations for all the compositions

Components	Polyamide-6 (wt%)	Flexural Strength (MPa)	Std. Dev.
Polyamide-6	100	96.3	1.3
Polyamide-6/Elastomer Blends			
Polyamide-6/E-BA-MAH	95	91.6	0.9
Polyamide-6/E-BA-MAH	90	60.5	0.2
Polyamide-6/E-BA-MAH	85	57.2	0.6
Polyamide-6/E-GMA	95	86.3	0.7
Polyamide-6/E-GMA	90	57.9	0.2
Polyamide-6/E-GMA	85	54.5	0.2
Polyamide-6/E-MA-GMA	95	81.9	0.8
Polyamide-6/E-MA-GMA	90	58.3	0.1
Polyamide-6/E-MA-GMA	85	53.9	0.2
Polyamide-6/Organoclay Nanocomposites			
Polyamide-6/Cloisite® 15A	98	101.6	0.9
Polyamide-6/Cloisite® 25A	98	110.5	0.7
Polyamide-6/Cloisite® 30B	98	106.1	0.3
Polyamide-6/Organoclay/Elastomer Nanocomposites (All-S)			
Polyamide-6/Cloisite®15A/E-BA-MAH	93	95.9	0.4
Polyamide-6/Cloisite® 25A/ E-BA-MAH	93	99.0	0.6
Polyamide-6/Cloisite® 30B/ E-BA-MAH	93	84.9	1.3
Polyamide-6/Cloisite®15A/ E-GMA	93	87.0	0.6
Polyamide-6/Cloisite®25A/ E-GMA	93	82.3	1.4
Polyamide-6/Cloisite®30B/ E-GMA	93	82.6	0.9
Polyamide-6/Cloisite®15A/E-MA-GMA	93	88.1	0.9
Polyamide-6/Cloisite®25A/E-MA-GMA	93	86.2	0.7
Polyamide-6/Cloisite®30B/E-MA-GMA	93	97.1	0.8
Polyamide-6/Organoclay/Elastomer Nanocomposites (Mixing Orders)			
Polyamide-6/Cloisite®15A/E-BA-MAH(PI-C)	93	141.8	2.1
Polyamide-6/Cloisite®15A/E-BA-MAH(PC-I)	93	139.3	0.1
Polyamide-6/Cloisite®15A/E-BA-MAH(IC-P)	93	137.6	3.0
Polyamide-6/Cloisite®25A/E-BA-MAH(PI-C)	93	149.3	1.9
Polyamide-6/Cloisite®25A/E-BA-MAH(PC-I)	93	133.7	0.9
Polyamide-6/Cloisite®25A/E-BA-MAH(IC-P)	93	132.2	0.3
Polyamide-6/Cloisite®15A/E-GMA(PI-C)	93	118.6	1.3
Polyamide-6/Cloisite®15A/E-GMA(PC-I)	93	139.9	1.9
Polyamide-6/Cloisite®15A/E-GMA(IC-P)	93	133.2	0.3
Polyamide-6/Cloisite®30B/E-GMA(PI-C)	93	119.8	1.7
Polyamide-6/Cloisite®30B/E-GMA(PC-I)	93	129.2	0.5
Polyamide-6/Cloisite®30B/E-GMA(IC-P)	93	110.6	1.2

Table C.7 Flexural Modulus data and standard deviations for all the compositions

Components	Polyamide-6 (wt%)	Flexural Modulus (MPa)	Std. Dev.
Polyamide-6	100	2627.7	69.6
Polyamide-6/Elastomer Blends			
Polyamide-6/E-BA-MAH	95	2402.2	19.1
Polyamide-6/E-BA-MAH	90	1931.4	32.7
Polyamide-6/E-BA-MAH	85	1405.2	27.7
Polyamide-6/E-GMA	95	2207.2	1.5
Polyamide-6/E-GMA	90	2208.8	14.1
Polyamide-6/E-GMA	85	1891.8	18.8
Polyamide-6/E-MA-GMA	95	2265.1	42.0
Polyamide-6/E-MA-GMA	90	2063.1	59.9
Polyamide-6/E-MA-GMA	85	1902.2	8.1
Polyamide-6/Organoclay Nanocomposites			
Polyamide-6/Cloisite® 15A	98	2910.9	58.3
Polyamide-6/Cloisite® 25A	98	2945.4	77.1
Polyamide-6/Cloisite® 30B	98	3064.6	85.6
Polyamide-6/Organoclay/Elastomer Nanocomposites (All-S)			
Polyamide-6/Cloisite®15A/E-BA-MAH	93	2659.4	1.5
Polyamide-6/Cloisite® 25A/ E-BA-MAH	93	2897.2	18.2
Polyamide-6/Cloisite® 30B/ E-BA-MAH	93	2386.2	6.4
Polyamide-6/Cloisite®15A/ E-GMA	93	2347.9	6.2
Polyamide-6/Cloisite®25A/ E-GMA	93	2302.3	60.3
Polyamide-6/Cloisite®30B/ E-GMA	93	2291.5	32.1
Polyamide-6/Cloisite®15A/E-MA-GMA	93	2596.6	23.9
Polyamide-6/Cloisite®25A/E-MA-GMA	93	2568.6	54.4
Polyamide-6/Cloisite®30B/E-MA-GMA	93	2774.4	39.3
Polyamide-6/Organoclay/Elastomer Nanocomposites (Mixing Orders)			
Polyamide-6/Cloisite®15A/E-BA-MAH(PI-C)	93	2879.1	46.8
Polyamide-6/Cloisite®15A/E-BA-MAH(PC-I)	93	2842.1	26.9
Polyamide-6/Cloisite®15A/E-BA-MAH(IC-P)	93	2890.5	77.4
Polyamide-6/Cloisite®25A/E-BA-MAH(PI-C)	93	3372.5	162.4
Polyamide-6/Cloisite®25A/E-BA-MAH(PC-I)	93	2527.8	99.9
Polyamide-6/Cloisite®25A/E-BA-MAH(IC-P)	93	2500.3	69.7
Polyamide-6/Cloisite®15A/E-GMA(PI-C)	93	2333.1	65.5
Polyamide-6/Cloisite®15A/E-GMA(PC-I)	93	2817.1	100.6
Polyamide-6/Cloisite®15A/E-GMA(IC-P)	93	2706.2	41.9
Polyamide-6/Cloisite®30B/E-GMA(PI-C)	93	2221.4	83.7
Polyamide-6/Cloisite®30B/E-GMA(PC-I)	93	2483.8	82.5
Polyamide-6/Cloisite®30B/E-GMA(IC-P)	93	2150.9	35.4

APPENDIX D

RHEOLOGICAL PROPERTIES

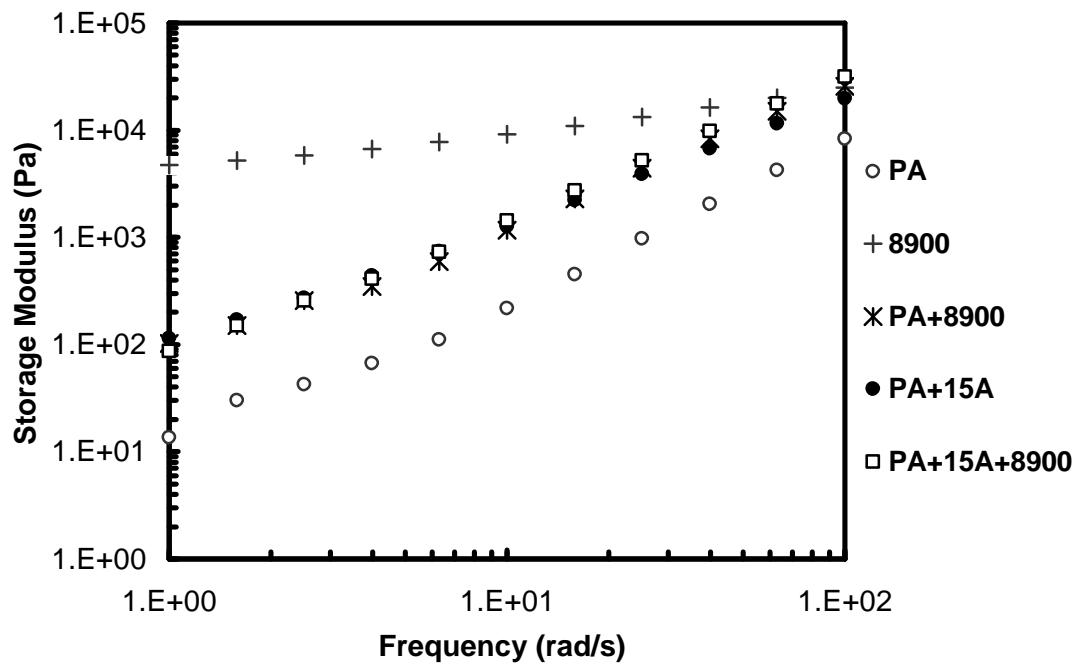


Figure D.1 Influence of frequency on storage modulus for polyamide-6/Cloisite® 15A/E-MA-GMA nanocomposite

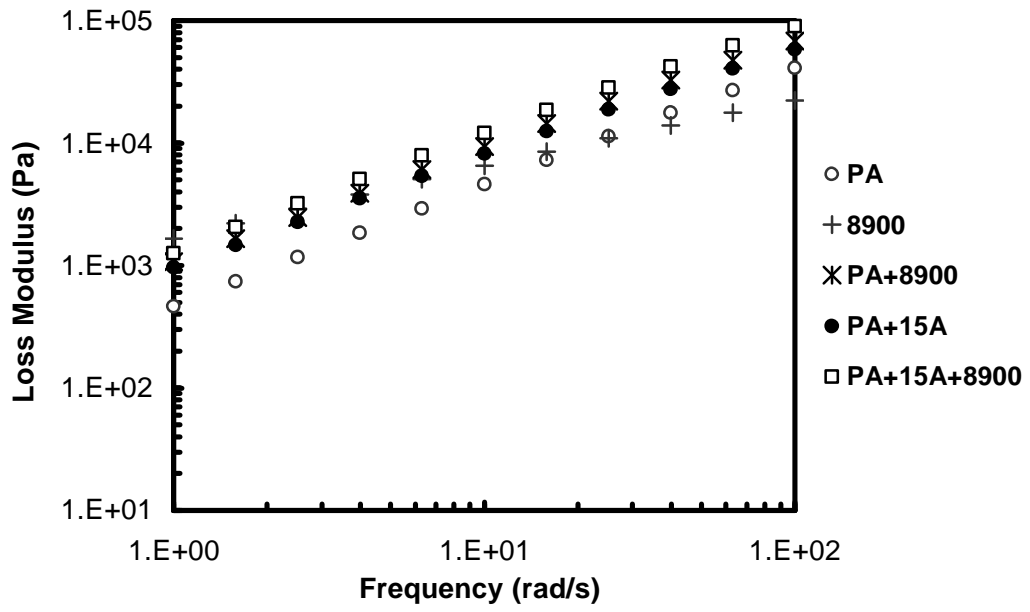


Figure D.2 Influence of frequency on loss modulus for polyamide-6/Cloisite® 15A/E-MA-GMA nanocomposite

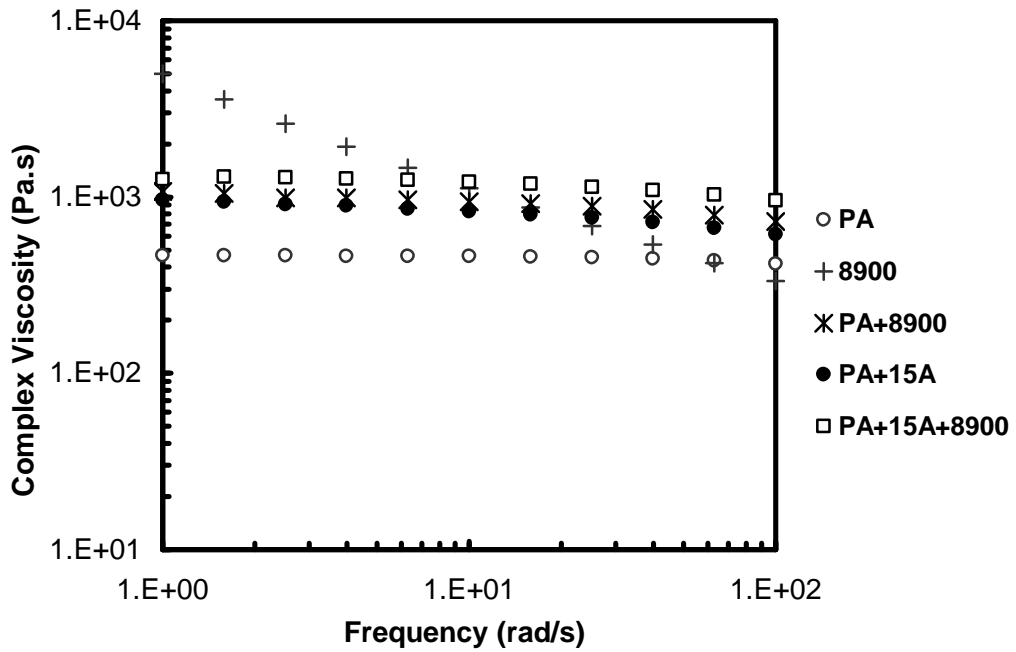


Figure D.3 Influence of frequency on complex viscosity for polyamide-6/Cloisite® 15A/E-MA-GMA nanocomposite

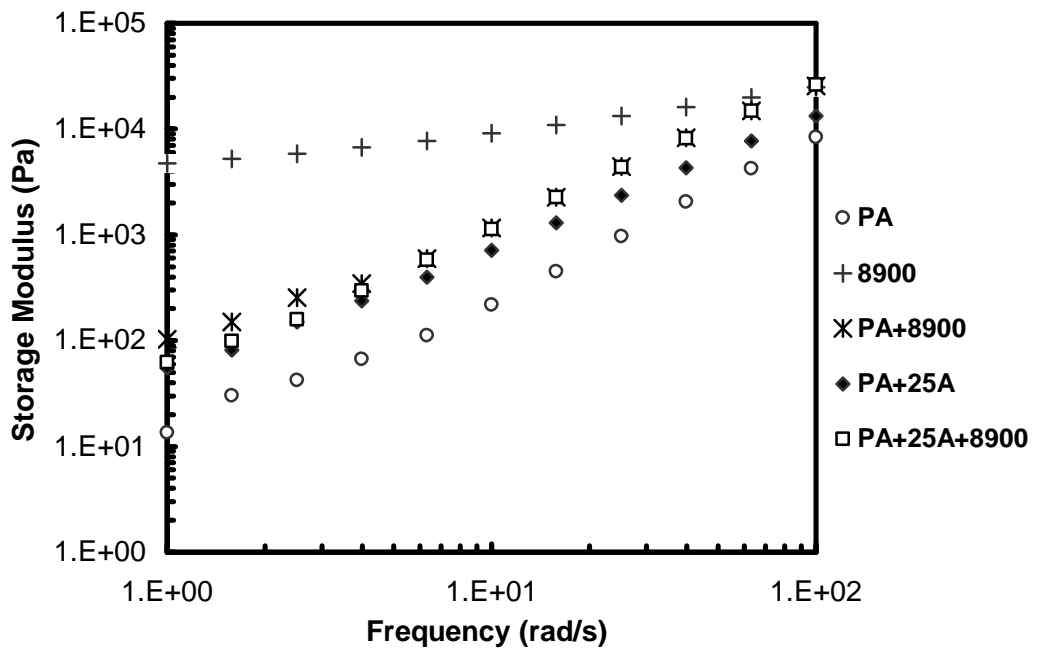


Figure D.4 Influence of frequency on storage modulus for polyamide-6/Cloisite® 25A/E-MA-GMA nanocomposite

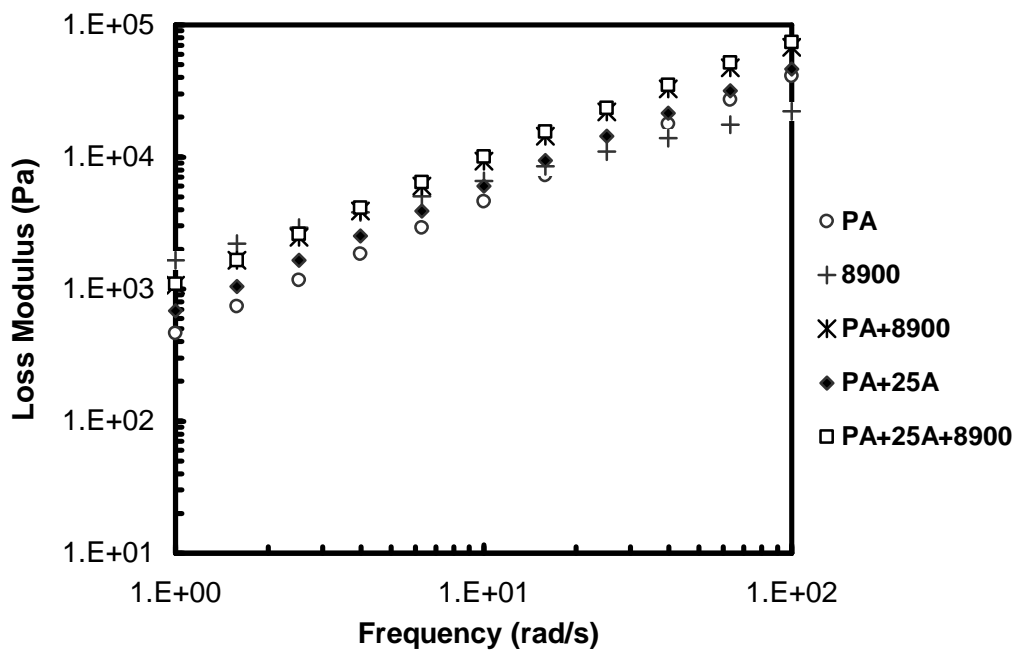


Figure D.5 Influence of frequency on loss modulus for polyamide-6/Cloisite® 25A/E-MA-GMA nanocomposite

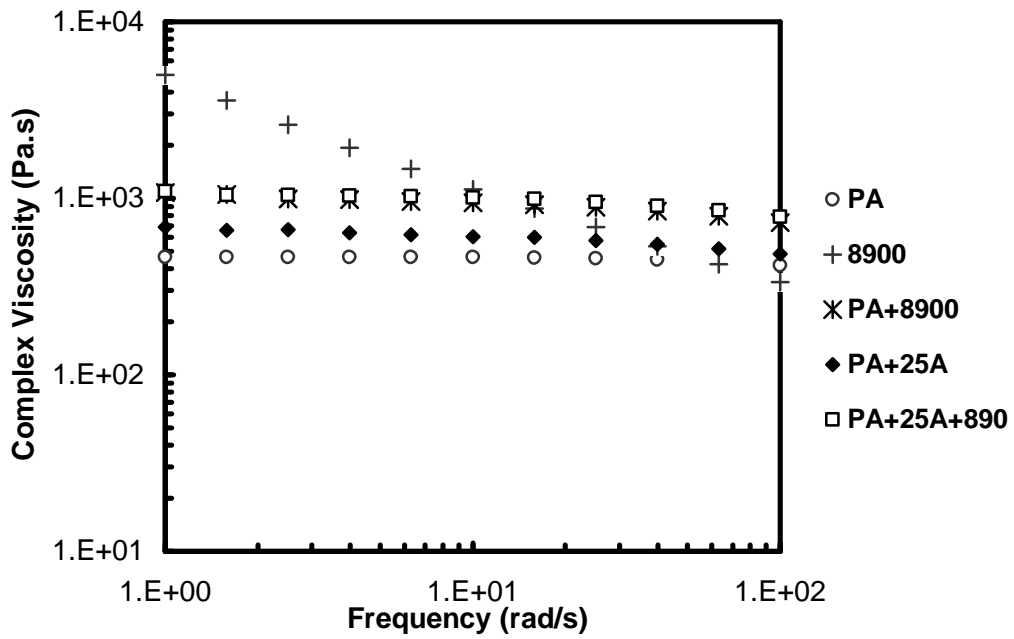


Figure D.6 Influence of frequency on complex viscosity for polyamide-6/Cloisite® 25A/E-MA-GMA nanocomposite

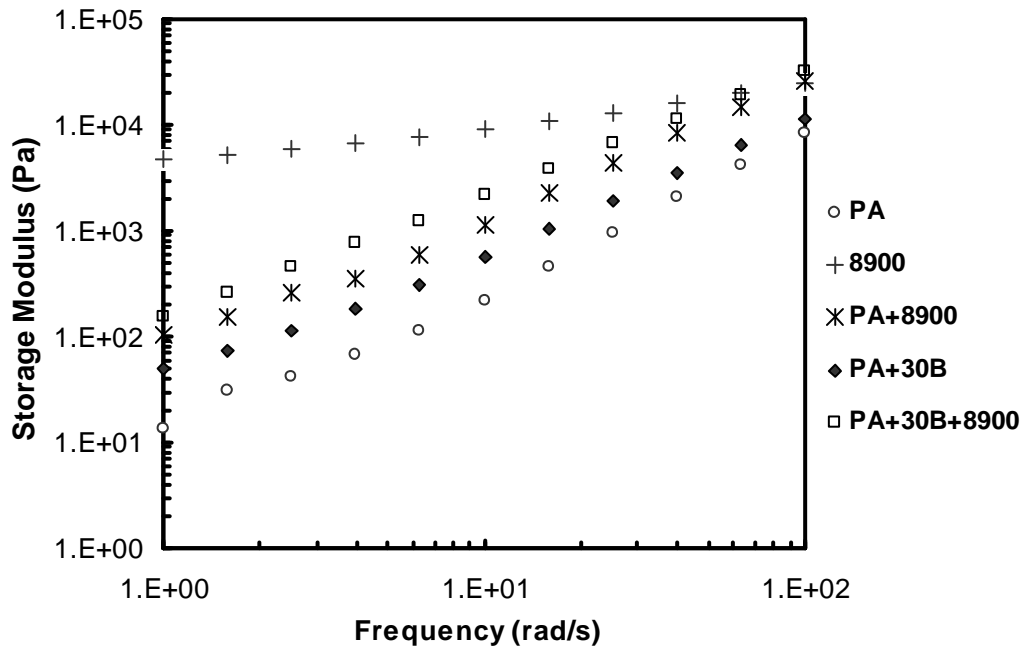


Figure D.7 Influence of frequency on storage modulus for polyamide-6/Cloisite® 30B/E-MA-GMA nanocomposite

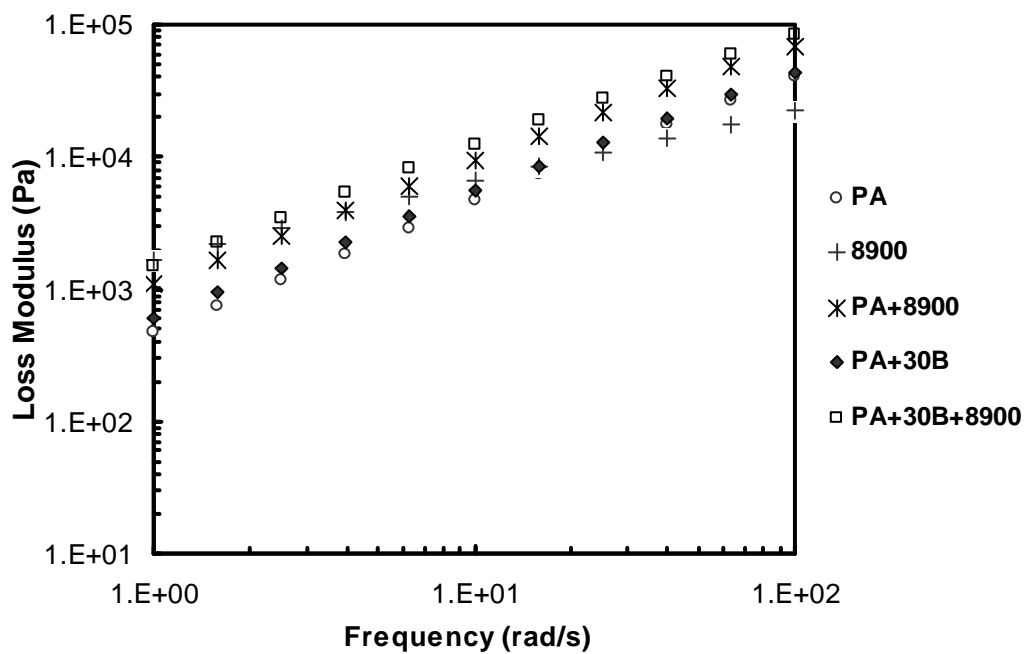


Figure D.8 Influence of frequency on loss modulus for polyamide-6/Cloisite® 30B/E-MA-GMA nanocomposite

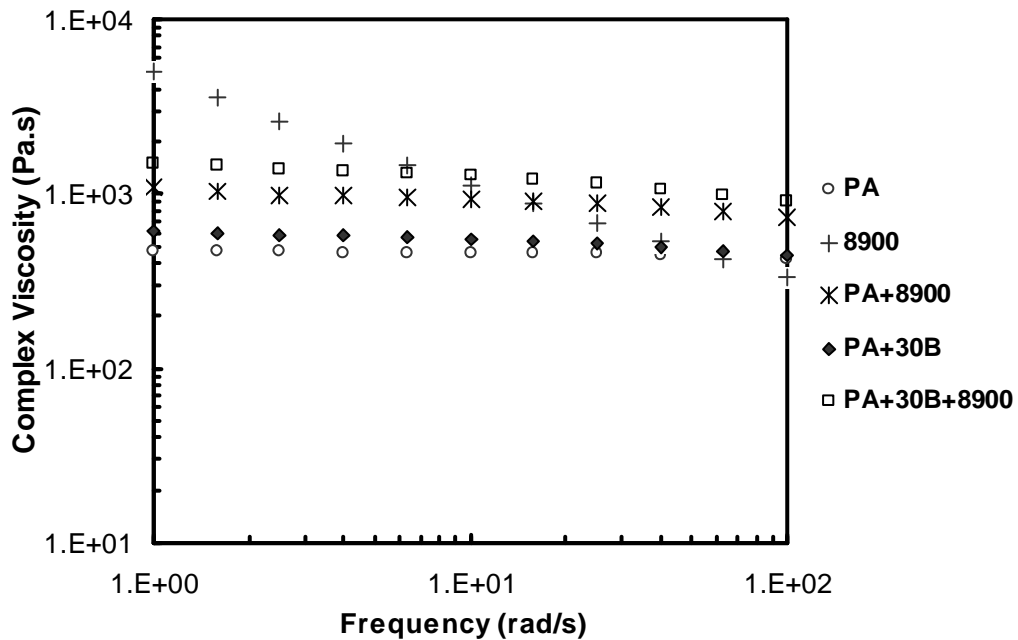


Figure D.9 Influence of frequency on complex viscosity for polyamide-6/Cloisite® 30B/E-MA-GMA nanocomposite

CIRRICULUM VITAE

PERSONEL INFORMATION

Surname, Name: Işık, Işıl
Nationality: Turkish (TC)
Date and Place of Birth: 19 May 1978, Ankara
Marital Status: Single
Phone: +90 312 210 43 90
Fax: +90 312 210 26 00
email: iisil@metu.edu.tr

EDUCATION

Degree	Institution	Year Of Graduation
MS	METU Chemical Engineering	2002
BS	Gazi University, Chemical Engineering	2000
High School	Anadolu High School, Isparta	1996

WORK EXPERIENCE

Year	Place	Enrollment
2002-Present	METU Department of Chemical Engineering	Research Assistant

FOREIGN LANGUAGES

Advanced English, Basic German, Basic Russian

PUBLICATIONS

National and International Congresses

Poster Presentations

Isik, I., Yilmazer, U., Bayram, G., **Impact Modification of Nanocomposites With an Epoxy Matrix**, MRS Materials Research Society, Fall Meeting, December 2-6, 2002 Boston, Massachusetts, USA

Isik, I., Yilmazer, U., Bayram, G., **Flexural Properties and Morphology of Impact Modified Epoxy-Organoclay Nanocomposites**, ANTEC Annual Technical Conference, May 12-15, 2004, Chicago, Illinois, USA

Oral Presentations

Isik, I., Yilmazer, U., Bayram, G., **Epoksi Matrisli Nanokompozitlerin Darbe Dayanımının Geliştirilmesi**, UKMK-5 V. National Chemical Engineering Congress, September 2-5, 2002 Ankara, Turkey

Isik, I., Yilmazer, U., Bayram, G., **Synthesis and characterization of Impact Modified Epoxy-Clay Nanocomposites**, EMCC-3, The 3rd Chemical Engineering Conference for Collaborative Research in Eastern Mediterranean, May 13-15, 2003, Thessaloniki, Greece

Isik, I., Yilmazer, U., Bayram, G., **Polyol Modified Epoxy-Montmorillonite Nanocomposites**, ANTEC Annual Technical Conference, May 4-8, 2003, Nashville, Tennessee, USA

Isik, I., Yilmazer, U., Bayram, G., **Impact Modified Polyamide-Organoclay Nanocomposites**, ANTEC Annual Technical Conference, May 7-11, 2006, Charlotte, NC, USA

Isik, I., Yilmazer, U., Bayram, G., **Polyamide-Impact Modifier-Organoclay Nanocomposites**, Polymer Processing Society 22nd Annual Meeting (PPS-22), July 2-6, 2006, Yamagata, Japan

Isik, I., Yilmazer, U., Bayram, G., **Darbe Dayanımı Geliştirilmiş Poliamid 6-Organokil Nanokompozitleri**, I. Ulusal Polimer Kongresi, 21-23 Haziran, 2006 ODTÜ, Ankara, Turkey

Papers

Isik, I., Yilmazer, U., Bayram, **Impact Modified Epoxy/Montmorillonite Nanocomposites: Synthesis and Characterization**, Polymer, 44, (2003), 6371-6377

Isik, I., Yilmazer, U., Bayram, **Impact Modified Polyamide-6/Montmorillonite Nanocomposites: Processing And Characterization**, Polymer Composites (in press)

Research Projects

Isik, I., Yilmazer, U., Bayram, G., **Impact Modified Polyamide-6 Nanocomposites**, OYP-DPT-IM-3 (2002-2007)

Isik, I., Yilmazer, U., Bayram, G., **Impact Modified Polyamide Nanocomposites**, TUBITAK grant number 104M415 (2005-2007)

HOBBIES

Swimming, Latin Dances, Movies, Gourmet